Springer Tracts in Modern Physics
Volume 229

Springer Tracts in Modern Physics

Springer Tracts in Modern Physics provides comprehensive and critical reviews of topics of current interest in physics. The following fields are emphasized: elementary particle physics, solid-state physics, complex systems, and fundamental astrophysics.
Suitable reviews of other fields can also be accepted. The editors encourage prospective authors to correspond with them in advance of submitting an article. For reviews of topics belonging to the above mentioned fields, they should address the responsible editor, otherwise the managing editor.
See also springer.com

Peter Schmüser
Martin Dohlus
Jörg Rossbach

Ultraviolet and Soft X-Ray Free-Electron Lasers

Introduction to Physical Principles, Experimental Results, Technological Challenges

Springer

Peter Schmüser
Institut für Experimentalphysik
Universität Hamburg and DESY
Notkestr. 85
22607 Hamburg
Germany
peter.schmueser@desy.de

Martin Dohlus
DESY
Notkestr. 85
22607 Hamburg
Germany
martin.dohlus@desy.de

Jörg Rossbach
Institut für Experimentalphysik
Universität Hamburg and DESY
Notkestr. 85
22607 Hamburg
Germany
joerg.rossbach@desy.de

P. Schmüser, et al., *Ultraviolet and Soft X-Ray Free-Electron Lasers: Introduction to Physical Principles, Experimental Results, Technological Challenges*, STMP 229 (Springer, Berlin Heidelberg 2008), DOI 10.1007/ 978-3-540-79572-8

ISBN 978-3-540-79571-1 e-ISBN 978-3-540-79572-8

DOI 10.1007/978-3-540-79572-8

ISSN 0081-3869 e-ISSN 1615-0430

Physics and Astronomy Classification Scheme (PACS):
29.20.Ej, 29.27.-a, 29.27.Bd, 41.60.Ap, 41.60.Cr, 52.25.Os, 52.35.Mw

Library of Congress Control Number: 2008930267

Cover design: Integra Software Services Pvt

Printed on acid-free paper

9 8 7 6 5 4 3 2 1

springer.com

This book is dedicated to the memory of the late Björn H. Wiik who has been the driving force behind the superconducting linear collider project TESLA and the ultraviolet and X-ray free-electron laser projects at DESY. His determination, skilfull leadership and constant encouragement have been vital for the success of the superconducting cavity development and the construction of the free-electron laser FLASH.

Preface

The high scientific interest in coherent X-ray light sources has stimulated world-wide efforts in developing X-ray lasers. In this book a particularly promising approach is described, the free-electron laser (FEL), which is pursued worldwide and holds the promise to deliver ultra-bright X-ray pulses of femtosecond duration. Other types of X-ray lasers are not discussed nor do we try a comparison of the relative virtues and drawbacks of different concepts.

The book has an introductory character and is written in the style of a university textbook for the many newcomers to the field of free-electron lasers, graduate students as well as accelerator physicists, engineers and technicians; it is not intended to be a scientific monograph for the experts in the field. Building on lectures by one of us (J. R.) at the CERN Accelerator School, and motivated by the positive response to a series of seminars on "FEL theory for pedestrians", given by P. S. within the framework of the Academic Training Program at DESY, we have aimed at presenting the theory of the low-gain and the high-gain FEL in a clear and concise mathematical language. Particular emphasis is put on explaining and justifying the assumptions and approximations that are needed to obtain the differential equations describing the FEL dynamics. Although we have tried our best to be "simple", the mathematical derivations are certainly not always as simple as one would like them to be. However, we are not aware of any easier approach to the FEL theory. Some of the more involved calculations are put into the appendices.

The starting points are the Maxwell equations and the basic elements of special relativity. We avoid the Hamiltonian formalism in the main text because many potential readers may not be familiar with this powerful formalism. A short introduction into the Hamiltonian treatment of the electron motion in an undulator magnet and its interaction with the radiation field is given in Appendix A. The FEL equations are derived in the framework of classical electrodynamics. Quantum theory is not needed to explain the theoretical basis and the functioning of presently existing or planned FEL facilities.

The differential equations describing the time evolution of the laser light wave are derived in a one-dimensional approximation and turn out to be quite powerful. In this book they are evaluated using rather straightforward programs for computing the FEL gain curve, laser saturation, bandwidth and other quantities of interest. The implications and modifications of the full three-dimensional treatment are discussed.

The available experimental data on high-gain ultraviolet and soft X-ray FELs are presented but the wide field of FELs in the visible and infrared regime is not covered. We apologize for having to omit the important results obtained in this field as well as other interesting developments and refer to the literature quoted in the book and to the Free-Electron Laser (FEL) conferences and the American and European Particle Accelerator conferences (PAC, EPAC) for a complete overview over the rapidly growing FEL activities worldwide.

The international system (SI) of units is used throughout to enable the reader to obtain practical numbers from the equations in the book. Our mathematical codes (written by M. D.) are available on request. The majority of the illustrations and graphical presentations shown in the book have been prepared by us using these codes, except when otherwise noted.

We have benefited a great deal from fruitful discussions with our colleagues at DESY and other laboratories and want to thank them for their advice, in particular Evgueni Saldin, Evgeny Schneidmiller and Mikhail Yurkov. We are very grateful to Erich Lohrmann and Sara Casalbuoni for a thorough reading of an early version of the manuscript and many valuable suggestions, and to Sven Reiche for a critical reading of the complete manuscript and his suggestions for improvement. Bernd Steffen's help with LATEX problems and editing of figures is gratefully acknowledged, as well as Roxana Tarkeshian's help with checking the references. We are particularly grateful to all members of the TESLA collaboration and of the FLASH team for their invaluable contributions to the design, construction and operation of a superconducting free-electron laser in Hamburg.

Hamburg, Germany — *Peter Schmüser*[1]
Martin Dohlus
April 2008 — *Jörg Rossbach*

[1] Corresponding author Peter.Schmueser@desy.de

Contents

1

Introduction

1.1 Overview

The principle of the Free-Electron Laser (FEL) was invented by John Madey in 1971 [1]. The first FEL, operating in the infrared at a wavelength of 12 μm, was built at Stanford University in the 1970s by Madey and coworkers [2, 3]. For many years FELs have played a marginal role in comparison with conventional lasers except at microwave and infrared wavelengths. Only in recent years it has become clear that these devices have the potential of becoming exceedingly powerful light sources in the X-ray regime [4, 5, 6]. The ultraviolet and soft X-ray free-electron laser facility FLASH in Hamburg has been playing a pioneering role in the development of X-ray FELs. The successful operation of FLASH as a user facility, providing radiation pulses of unprecedented brightness and shortness at wavelengths down to 6.5 nm, has paved the way for new FELs in the Ångström regime. As demonstrated by FLASH the short-wavelength FEL pulses have a power in the Gigawatt range and a time duration of only 10–30 femtoseconds. Similarly, the X-ray pulses produced in the Linac Coherent Light Source LCLS [7] in Stanford (USA) and in the European facility XFEL [8] in Hamburg (Germany) will be far shorter than the pulses from most existing X-ray sources, and their peak brilliance will be about eight orders of magnitude higher. The high pulse energy and the femtosecond duration of the X-ray pulses as well as their coherence open entirely new fields of research, for example structural analysis of individual biomolecules, which are inaccessible at the present third-generation light sources. Alternative concepts of X-ray lasers (see e.g. [9, 10, 11, 12]) are not discussed in this book.

In this introductory chapter a comparison is made between conventional quantum lasers and free-electron lasers. Chapter 2 deals with undulator radiation which is intimately related to FEL radiation. The theory of the low-gain FEL is derived in Chap. 3. The high-gain FEL theory is treated in Chap. 4 in the one-dimensional approximation. A set of coupled first-order equations is derived as well as a third-order differential equation which permit deep

P. Schmüser, et al.: *Introduction*, STMP **229**, 1–10 (2008)
DOI 10.1007/978-3-540-79572-8_1

insight into the physics of the FEL. The third-order equation is valid in the so-called *linear regime* of the FEL where the output field depends linearly on the input field. We often call this the *exponential gain regime* since here the FEL power grows exponentially with the distance traveled in the undulator. The coupled first-order equations are more general and encompass in addition the *nonlinear regime* in which the FEL power goes into saturation.

Numerous applications of the high-gain FEL equations follow in Chap. 5 illustrating the power of the high-gain theory. The refinements of the one-dimensional theory are discussed in Chap. 6, these comprise electron beam energy spread, space charge forces, finite electron beam radius, betatron oscillations, optical diffraction, and slippage effects in short electron bunches.

Special emphasis is put on the principle of Self-Amplified Spontaneous Emission (SASE). The SASE mechanism is illustrated in Chap. 7 with numerical simulations and experimental data. SASE-FELs are frequently considered the fourth generation of accelerator-based light sources. In contrast to existing synchrotron radiation light sources, which are mostly storage rings equipped with undulators, the SASE FEL requirements on the electron beam quality in terms of small beam cross section, high charge density and low energy spread are so demanding that only linear accelerators can be used to provide the drive beam.

The free-electron laser FLASH is described in Chap. 8 in some detail to give an impression of the complexity of such an accelerator-based light source. The last chapter gives an outlook on the physical and technological challenges associated with FELs in the Ångström regime and discusses the layout of the LCLS, the first X-ray FEL to go into operation.

A short introduction into the Hamiltonian treatment of electron motion in an undulator and the coupling between electron and light wave is given in Appendix A, see also [13, 14]. In Appendix B we prove that the high-gain FEL theory reduces to the simpler low-gain theory if the undulator magnet is short and the increase in light intensity per undulator passage is small. The generalization of the coupled first-order equations to non-periodic cases is discussed in Appendix C. The concepts of Gaussian beam optics are presented in Appendix D since Gaussian modes are not only important for conventional laser beams but also for FEL beams. The eigenmode approach for solving the FEL equations is explained in Appendix E, and it is applied to the one-dimensional and the three-dimensional case. Appendix F deals with an important feature of SASE FELs, namely the current modulation resulting from shot noise in the electron beam. The gamma distribution describing the statistical properties of SASE FEL radiation is derived in Appendix G. In the last Appendix H we summarize our conventions and list frequently used symbols, their dimension in SI units, their physical meaning, and the defining equation resp. the chapter where the quantity is introduced. Important formulas are put into boxes.

Since the invention of the free-electron laser, an enormous amount of work has been done in this field. Useful reviews of the work up to 1990 can be found in the Laser Handbook, Vol. 6 - *Free Electron Lasers* [15]. The articles

by Murphy and Pellegrini [16] and by Colson [17] present good introductions into the physics of the low-gain and the high-gain FEL. For additional reading we refer to the other articles in the handbook and to the books by Brau [18] and by Freund and Antonsen [19] and to an article by O'Shea and Freund [20]. A useful account of the progress in FEL physics and technology up to 2004 is presented in two articles by Pellegrini and Reiche [21, 22]; see also the literature quoted therein. The FEL theory is thoroughly treated on a high mathematical level in the book *The Physics of Free Electron Lasers* by Saldin, Schneidmiller and Yurkov [23]. An excellent review of the current status of X-ray free-electron laser theory is found in an article by Huang and Kim [24].

1.2 Electron Accelerators as Short-Wavelength Light Sources

In the bending magnets of a high-energy electron synchrotron or storage ring the relativistic electrons are accelerated toward the center of the ring and emit *synchrotron radiation* tangentially to the circular orbit [25, 26, 27, 28]. Usually different electrons in a bunch radiate independently, so the radiation is incoherent. The frequency spectrum is continuous and extends from zero to frequencies beyond the *critical frequency* ω_c

$$\omega_c = \frac{3c\gamma^3}{2R} \ . \tag{1.1}$$

Here R is the radius of curvature in the bending magnet, γ is the Lorentz factor

$$\boxed{\gamma = \frac{1}{\sqrt{1-(v/c)^2}} = \frac{W}{m_e c^2}} \tag{1.2}$$

and W the total relativistic energy of the electron[1]. The radiated power in a bending magnet of field B is

$$\boxed{P_{\mathrm{syn}} = \frac{e^4\gamma^2 B^2}{6\pi\varepsilon_0 c\, m_e^2} = \frac{e^2 c\,\gamma^4}{6\pi\varepsilon_0 R^2} \ .} \tag{1.3}$$

Most of the power is contained inside a narrow cone of opening angle $1/\gamma$ which is centered around the instantaneous tangent to the circular orbit.
In modern synchrotron light sources the radiation used for research is produced in wiggler or undulator magnets which are periodic arrangements of many short dipole magnets of alternating polarity. The electrons move on a sinusoidal orbit through such a magnet (Fig. 1.1), the overall deflection of the beam is zero. Undulator radiation is far more useful than bending-magnet

[1] The total relativistic energy of the electron is denoted by W in this book since we reserve the letter E for electric fields.

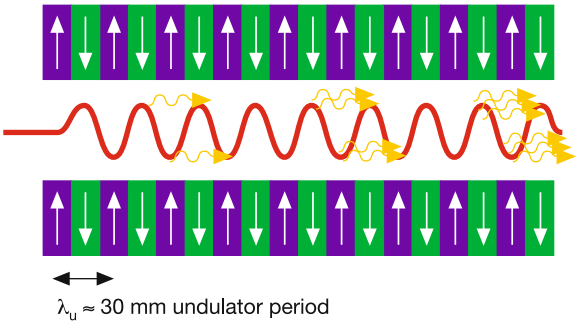

Fig. 1.1. Schematic representation of electron motion in a planar undulator and the emission of undulator radiation. For simplicity the alternating magnetic field and the sine-like electron orbit have been drawn in the same plane. The amplitude of the sinusoidal orbit is exaggerated, in reality it is only a few μm

radiation because it consists of narrow spectral lines and is concentrated in a narrow angular cone along the undulator axis. The fundamental wavelength can be roughly estimated from the following consideration. Call λ_u the period of the magnet arrangement. In a coordinate system moving with the speed of the beam the relativistic length contraction reduces the period to $\lambda_u^* = \lambda_u/\gamma$, and the electrons oscillate at a correspondingly higher frequency $\omega^* = 2\pi c/\lambda_u^*$ and emit radiation just like an oscillating dipole. For an observer in the laboratory who is looking against the electron beam the radiation appears strongly blue-shifted by the relativistic Doppler effect. The wavelength in the laboratory system is $\lambda_\ell \approx \lambda_u^*/(2\gamma) \approx \lambda_u/(2\gamma^2)$. For example, at an electron energy of 500 MeV the radiation wavelength is more than a million times shorter than the undulator period.

A more accurate treatment, taking into account the sinusoidal shape of the electron trajectory and the fact that the longitudinal velocity of the electrons is lower than their total velocity, leads to the formula

$$\boxed{\lambda_\ell = \frac{\lambda_u}{2\gamma^2}\left(1 + \frac{K^2}{2}\right) \quad \text{with} \quad K = \frac{eB_0\lambda_u}{2\pi m_e c}\,.} \tag{1.4}$$

The dimensionless quantity K is called the *undulator parameter*, and B_0 is the peak magnetic field on the undulator axis. The undulator parameter is in the order of 1. The proof of formula (1.4) is presented in Chap. 2. Equation (1.4), which is also valid for the FEL, describes the fundamental wavelength $\lambda_1 \equiv \lambda_\ell$. Note that the radiation in forward direction contains odd higher harmonics with the wavelengths

$$\lambda_m = \frac{\lambda_\ell}{m}\,, \quad m = 1, 3, 5, .. \tag{1.5}$$

The wavelength of undulator radiation can be varied at will, simply by changing the electron energy $W = \gamma\, m_e c^2$.

It is interesting to note that the power radiated by a relativistic electron in an undulator is the same as that in a bending magnet with a magnetic field $B = B_0/\sqrt{2}$, however, the intensity is concentrated in a narrow spectral range. Different electrons radiate independently which means that the total energy produced by a bunch of N_e electrons is just N_e times the radiation energy of one electron. Coherent radiation with an intensity scaling quadratically with the number of electrons would happen for electron bunches shorter than the light wavelength, a condition that is never satisfied in practice in the optical, ultraviolet and X-ray regime.

1.3 Free-Electron Lasers and Quantum Lasers

The next big improvement in the performance of accelerator-based light sources is given by the Free-Electron Laser. The main components of an FEL are an accelerator providing a bunched relativistic electron beam and an undulator magnet. In an FEL a huge number of electrons radiate coherently because there exists a process of self-organization on the scale of the light wavelength, the so-called microbunching. The radiation power scales then quadratically with the number of these particles. For a typical number of 10^6 electrons in a coherence region the FEL will yield a million times higher light output than an undulator.

1.3.1 Stimulated and Spontaneous Emission

The word LASER is an acronym for Light Amplification by Stimulated Emission of Radiation. A conventional laser (Fig. 1.2) consists of three basic components: the laser medium with at least three energy levels, an energy pump which creates a population inversion, and an optical resonator. The axis of the optical cavity defines the direction of the photons to better than 1 mrad typically. In a mono-mode laser exactly one optical eigenmode of the cavity is excited. The photons in this mode have all the same frequency ω, the same direction (described by the wave vector $\boldsymbol{k} = (k_1, k_2, k_3)$), the same polarization and the same phase. These quantum numbers characterize a well-defined quantum state which we denote by the Dirac ket vector $|a\rangle$. Photons have spin 1 and obey the Bose-Einstein statistics; they have a strong tendency to occupy the same quantum state.

Inside the resonator there are many atoms in the excited state E_2 which can emit radiation of frequency $\omega = (E_2 - E_1)/\hbar$ by going into the ground state E_1. In the beginning of the lasing process zero photons are present in the quantum state $|a\rangle$. Call p_{spon} the probability that an atom emits its photon by spontaneous emission into this quantum state. This photon will travel back and forth between the mirrors and will remain in the cavity. However, any other photon, emitted with the same probability p_{spon} into a quantum state $|b\rangle$ with a direction different from the resonator axis, will immediately

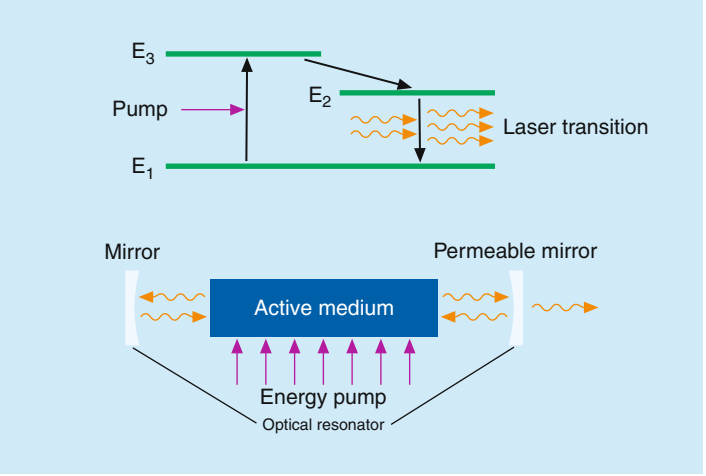

Fig. 1.2. Principle of a quantum laser where the electrons are bound to atomic, molecular or solid-state energy levels ("bound-electron laser")

escape from the optical resonator. Therefore, the number of photons in state $|a\rangle$ increases with time. If already n photons are present in state $|a\rangle$, the probability that photon number $(n+1)$ will also go into this state is $(n+1)$ times larger than the probability p_{spon} for emission into any other state $|b\rangle$:

$$p_n = (n+1)p_{\text{spon}} \; . \tag{1.6}$$

Here the factor n stands for the stimulated emission, induced by the already existing photons in the quantum state $|a\rangle$, and the factor 1 stands for the spontaneous emission which has the same probability p_{spon} for any final state allowed by energy conservation. This equation, which can be derived in quantum field theory, is the physical basis of the laser. The lasing process starts from *noise*, namely spontaneous emission by the excited atoms, and the stimulated emission results in an exponential growth of the light intensity.

One can understand within the framework of quantum mechanics that the probability for stimulated emission is proportional to the number of photons already present. The usual method to compute optical transitions in quantum mechanics is by means of perturbation theory. The electron in the atom is described by a wave function obeying the Schrödinger equation. The transition from the ground state to an excited state or vice versa is caused by a perturbing Hamiltonian which is basically the potential energy of the electron in the field of an external light wave. This electromagnetic field, however, is treated as a classical quantity, using the laws of classical electrodynamics. The matrix element for the transition between two states of the atom is found to

be proportional to the electric field E_0 of the light wave, and the transition probability, which can be calculated using Fermi's Golden Rule, is proportional to E_0^2. The field energy inside the volume V of the optical resonator is

$$\frac{\varepsilon_0}{2} E_0^2 V = n\,\hbar\omega \tag{1.7}$$

where n is the number of photons in the optical cavity. Hence the probability for stimulated emission is indeed proportional to the number n of already existing photons in the quantum state $|a\rangle$.

The Origin of Spontaneous Emission

The two radiative processes which are accessible to quantum mechanical perturbation theory are the absorption of radiation and the stimulated emission of radiation, and both have the same probability. The factor "1" in (1.6) corresponds to the spontaneous emission which cannot be explained in quantum mechanics nor in classical electrodynamics. For a theoretical explanation of spontaneous emission not only the electron but also the radiation field must be "quantized". This leads to Quantum Electrodynamics, the quantum field theory of electromagnetic interactions. In quantum field theory, the ground state, although usually called the "vacuum", is by no means the same as the empty set in mathematics. On the contrary, the ground state is full of activity: all the time short-lived virtual photons and particle-antiparticle pairs are created and annihilated. These so-called vacuum fluctuations have a theoretically well-understood and experimentally verified influence on atomic energy levels. The spontaneous emission of radiation by an excited atom or by an electron moving through an undulator may be interpreted as emission that is stimulated by vacuum fluctuations.

1.3.2 Is the FEL Really a Laser?

The electrons in a conventional quantum laser are bound to atomic, molecular or solid-state energy levels, so one may call this device a *bound-electron laser*, in contrast to the free-electron laser where the electrons move in vacuum.

In a free-electron laser (Fig. 1.3) the role of the active laser medium and the energy pump are both taken over by the relativistic electron beam. An FEL operating at infrared and optical wavelengths can be equipped with an optical resonator, but this is no longer possible if the wavelength is decreased below 100 nm, because here the reflectivity of metals and other mirror coatings drops quickly to zero at normal incidence. In the extreme-ultraviolet and X-ray regime a large laser gain has to be achieved in a single passage of a very long undulator magnet. The principle of Self Amplified Spontaneous Emission (SASE) allows to realize high-gain FELs at these short wavelengths.

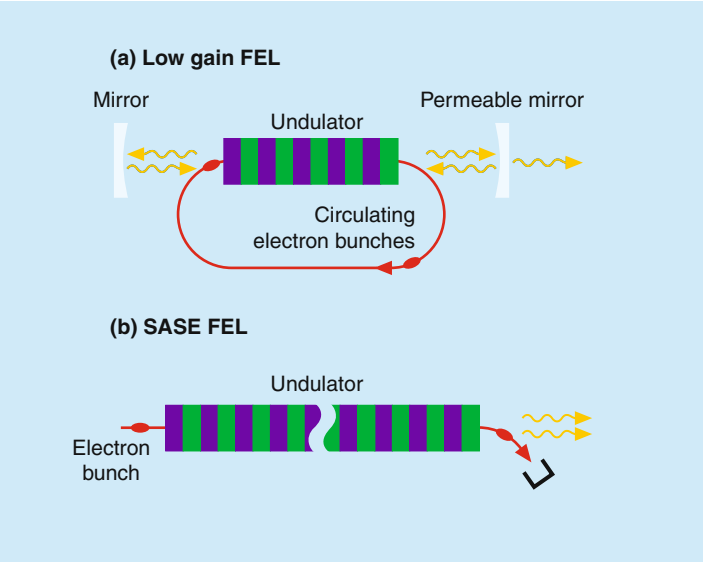

Fig. 1.3. Principle of free-electron laser. For visible or infrared light an optical resonator can be used. A increase in light intensity of a few % per passage of a short undulator magnet is sufficient to achieve laser saturation within many round trips. In the ultraviolet and X-ray region one can apply the mechanism of Self-Amplified Spontaneous Emission where a large laser gain is achieved in a single passage of a very long undulator

We will see in the chapter on the low-gain FEL theory that the coupling between the electrons and an already existing light wave in the undulator is proportional to the electric field E_0 of the light wave, and the laser gain is proportional to E_0^2, i.e. to the number of photons in the light wave. Hence one is well justified to speak of *light amplification by stimulated emission of radiation* when talking about a free-electron laser. Moreover, the light emerging from an FEL has the same properties as conventional laser light, it is nearly monochromatic, polarized, extremely bright, tightly collimated, and possesses a high degree of transverse coherence.

The equations of the free-electron laser can be derived from classical relativistic electrodynamics without using the methods of quantum theory. Unlike for optical transitions in atoms, the computation of the power radiated in an undulator or an FEL needs no quantum mechanical matrix elements but can be traced back to the classical Larmor formula for radiation by an accelerated charge. Of course, when the number of photons is of interest or the change in energy and momentum which an electron experiences upon the emission of a photon, the fundamental Planck relation $E = \hbar\omega$ must be used. A genuine quantum theoretical treatment of the FEL [29, 30, 31] is only needed under extreme conditions which are not fulfilled in presently existing or planned FEL facilities.

References

1. Madey, J.M.J.: Stimulated emission of bremsstrahlung in a periodic magnetic field. J. Appl. Phys. **42**, 1906 (1971) 1
2. Elias, L.R, et al.: Observation of stimulated emission of radiation by relativistic electrons in a spatially periodic transverse magnetic field. Phys. Rev. Lett. **36**, 717 (1976) 1
3. Deacon, D.A.G., et al., First operation of a free-electron laser. Phys. Rev. Lett. **38**, 892 (1977) 1
4. Pellegrini, C.: Progress towards a soft X-Ray FEL. Nucl. Instr. Meth. **A 272**, 364 (1988) 1
5. Pellegrini, C., Stöhr, J.: X-ray free-electron lasers – principles, properties and applications. Nucl. Instr. Meth. **A 500**, 33 (2003) 1
6. Pellegrini, C. et al., The SLAC soft X-ray high power FEL. Nucl. Instr. Meth. **A 341**, 326 (1994) 1
7. The LCLS Design Study Group: LCLS Design Study Report. http://www-ssrl.slac.stanford.edu/lcls/ 1
8. Brinkmann, R., et al.: TESLA XFEL: First stage of the X-ray laser laboratory – Technical design report. http://www.xfel.net 1
9. Nickles, P.V., et al.: Short Pulse X-Ray Laser at 32.6 nm Based on Transient Gain in Ne-like Titanium. Phys. Rev. Lett. **78**, 2748 (1997) 1
10. Nickles, P.V., Sandner, W. and Janulewicz, K.A.: X-ray lasers, Landoldt-Börnstein - Group VIII Advanced Materials and Technologies, p. 203, Springer, Berlin, Heidelberg, (2008) 1
11. Rocca, J.J.: Table-top soft x-ray lasers. Rev. Scient. Instrum. **70**, 3799 (1999) 1
12. Zeitoun, P., et al.: A high-intensity highly coherent soft X-ray femtosecond laser seeded by a high harmonic beam. Nature **431**, 426 (2004) 1
13. Dattoli, G., Renieri, A., Romanelli, F.: Progress in the Hamiltonian picture of the free-electron laser. IEEE J. Quantum Electron. **17**, 1371 (1981) 2
14. Bonifacio, R., Casagrande F., Pellegrini, C.: Hamiltonian model of a free-electron laser. Opt. Comm. **61**, 55 (1987) 2
15. Colson, W.B., Pellegrini, C., Renieri, A. (eds.) Laser Handbook Vol. 6, *Free Electron Lasers*. North Holland, Amsterdam, Oxford, New York, Tokyo (1990) 2
16. Murphy, J.B., Pellegrini, C.: Introduction to the physics of the free electron laser. Laser Handbook vol. 6, p. 11 (1990) 3
17. Colson, W.B.: Classical free electron laser theory. Laser Handbook vol. 6, p. 115 (1990) 3
18. Brau, C.A.: Free-Electron Lasers. Academic Press, Boston (1990) 3
19. Freund, H.P., Antonsen, T.M.: Principles of Free-Electron Lasers. Chapman & Hall, London (1996) 3
20. O'Shea P., Freund, H.P.: Free-electron lasers: Status and applications. Science **292**, 1853 (2001) 3
21. Pellegrini, C., Reiche, S.: The development of X-ray free-electron lasers, IEEE J. Quantum Electron. **10**(6), 1393 (2004) 3
22. Pellegrini, C., Reiche, S.: Free-Electron Lasers. The Optics Encyclopedia, p. 1111 Wiley-VCH (2003) 3
23. Saldin, E.L., Schneidmiller, E.A., Yurkov, M.V.: The Physics of Free Electron Lasers. Springer, Berlin, Heidelberg (2000) 3
24. Huang, Z., Kim, K.-J. Review of x-ray free-electron laser theory. Phys. Rev. ST Accel. Beams **10**, 034801 (2007) 3

25. Jackson, J.D.: Classical Electrodynamics. 3rd ed. John Wiley, New York (1999) 3
26. Duke, P.J.: Synchrotron Radiation: Production and Properties. Oxford University Press Oxford (2000) 3
27. Wiedemann, H.: Particle Accelerator Physics II, 2nd ed., Springer, Berlin (1999) 3
28. Clarke, J.A.: The Science and Technology of Undulators and Wigglers. Oxford University Press Oxford (2004) 3
29. Bonifacio, R., Casagrande, F.: Instabilities and quantum initiation in the free-electron laser. Opt. Comm. **50**, 251 (1984) 8
30. Dattoli, G., Renieri, A.: The quantum-mechanical analysis of the free electron laser. Laser Handbook vol. 6 (1990) 8
31. Schroeder, C.B., Pellegrini, C., Chen, P.: Quantum effects in high-gain free-electron lasers. Phys. Rev. E **64**, 056502 (2001) 8

2

Undulator Radiation

2.1 Magnetic Field of a Planar Undulator

The motion of an electron in a planar undulator magnet is shown schematically in Fig. 2.1. The undulator axis is along the direction of the beam (z direction), the magnetic field points in the y direction (vertical). The period λ_u of the magnet arrangement is in the order of 30 mm. For simplicity we assume that the horizontal width of the pole shoes is larger than λ_u, then one can neglect the x dependence of the field in the vicinity of the tightly collimated electron beam. In the vacuum chamber of the electron beam we have $\boldsymbol{\nabla}\times\boldsymbol{B} = 0$, hence the magnetic field can be written as the gradient of a scalar magnetic potential

$$\boldsymbol{B} = -\nabla\Phi_{\mathrm{mag}} \; .$$

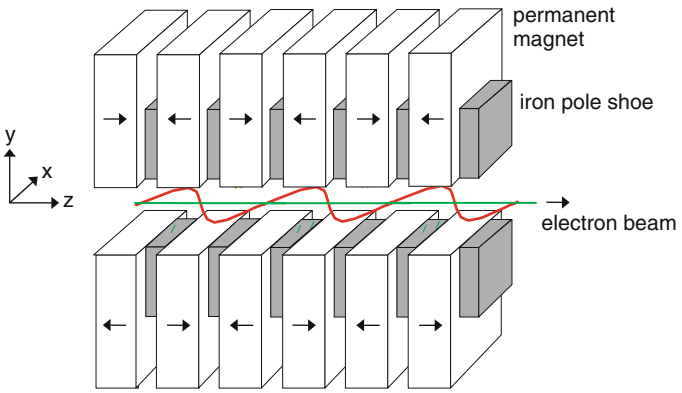

Fig. 2.1. Schematic view of a planar undulator magnet with alternating polarity of the magnetic field and of the sine-like trajectory of the electrons. In the magnet shown here the field is produced by permanent magnets that are placed between iron pole shoes. The distance between two equal poles is called the undulator period λ_u. A typical value is $\lambda_u = 30$ mm

P. Schmüser, et al.: *Undulator Radiation*, STMP **229**, 11–22 (2008)
DOI 10.1007/978-3-540-79572-8_2

The potential Φ_{mag} fulfills the Laplace equation

$$\nabla^2 \Phi_{\mathrm{mag}} = 0 \,.$$

The field on the axis is approximately harmonic. Making the ansatz

$$\Phi_{\mathrm{mag}}(y,z) = f(y)\sin(k_u z) \quad \Rightarrow \quad \frac{d^2 f}{dy^2} - k_u^2 f = 0\,, \qquad k_u = \frac{2\pi}{\lambda_u}$$

we obtain for the general solution

$$f(y) = c_1 \sinh(k_u y) + c_2 \cosh(k_u y) \,.$$

The vertical field is

$$B_y(y,z) = -\frac{\partial \Phi_{\mathrm{mag}}}{\partial y} = -k_u(c_1 \cosh(k_u y) + c_2 \sinh(k_u y))\sin(k_u z) \,.$$

B_y has to be symmetric with respect to the plane $y = 0$ hence $c_2 = 0$. We set $k_u c_1 = B_0$ and obtain $B_y(0,z) = -B_0 \sin(k_u z)$. So the potential is

$$\Phi_{\mathrm{mag}}(x,y,z) = \frac{B_0}{k_u}\, \sinh(k_u y)\sin(k_u z) \,. \tag{2.1}$$

For $y \neq 0$ the magnetic field has also a longitudinal component B_z.

$$\begin{aligned} B_x &= 0 \\ B_y &= -B_0 \cosh(k_u y)\sin(k_u z) \\ B_z &= -B_0 \sinh(k_u y)\cos(k_u z) \,. \end{aligned} \tag{2.2}$$

In the following we restrict ourselves to the symmetry plane $y = 0$ and use the idealized field

$$\boxed{\boldsymbol{B} = -B_0 \sin(k_u z)\, \boldsymbol{e}_y} \tag{2.3}$$

where $\boldsymbol{e}_y$ is the unit vector in y direction.

2.2 Electron Motion in an Undulator

2.2.1 Trajectory in First Order

We call $W = W_{kin} + m_e c^2 = \gamma m_e c^2$ the total relativistic energy of the electron. The transverse acceleration by the Lorentz force is

$$\gamma m_e \dot{\boldsymbol{v}} = -e\boldsymbol{v} \times \boldsymbol{B} \,. \tag{2.4}$$

This results in two coupled equations

$$\ddot{x} = \frac{e}{\gamma m_e} B_y \dot{z} \qquad\qquad \ddot{z} = -\frac{e}{\gamma m_e} B_y \dot{x} \tag{2.5}$$

which are solved iteratively. To obtain the first-order solution we observe that $v_z = \dot{z} \approx v = \beta\, c = const$ and $v_x \ll v_z$. Then $\ddot{z} \approx 0$ and the solution for $x(t)$ and $z(t)$ is

$$x(t) \approx \frac{eB_0}{\gamma m_e \beta c k_u^2} \sin(k_u \beta c t)\ , \qquad z(t) \approx \beta c t \tag{2.6}$$

if the initial conditions

$$x(0) = 0\,, \quad \dot{x}(0) = \frac{eB_0}{\gamma m_e k_u}$$

are realized by a suitable beam steering system in front of the undulator[1] (the undulator magnet starts at $z = 0$). The electron travels on the sine-like trajectory

$$x(z) = \frac{K}{\beta\gamma k_u} \sin(k_u z)\ . \tag{2.7}$$

In this equation we have introduced the important dimensionless *undulator parameter*

$$\boxed{K = \frac{eB_0}{m_e c k_u} = \frac{eB_0 \lambda_u}{2\pi m_e c} = 0.934 \cdot B_0\,[\mathrm{T}] \cdot \lambda_u\,[\mathrm{cm}]\ .} \tag{2.8}$$

The transverse velocity is

$$v_x(z) = \frac{K\, c}{\gamma} \cos(k_u z)\ . \tag{2.9}$$

It is a general property of the radiation emitted by relativistic electrons in a magnetic field that at large distance most of the intensity is concentrated in a narrow cone of opening angle $1/\gamma$, see e.g. [2]. The cone is centered around the instantaneous tangent to the particle trajectory. The direction of the tangent varies along the sinusoidal orbit in the undulator magnet, the maximum angle with respect to the axis being

$$\theta_{max} \approx \left[\frac{dx}{dz}\right]_{max} = \frac{K}{\beta\gamma} \approx \frac{K}{\gamma}\ . \tag{2.10}$$

If this directional variation is less than $1/\gamma$ the radiation field contributions from various sections of the trajectory overlap in space and interfere with each other. The consequence is, as will be shown in the next sections, that the radiation spectrum in forward direction is not continuous but nearly monochromatic (more precisely, it is composed of a narrow spectral line at a well-defined

[1] In practice the initial conditions can be realized by augmenting the undulator with a quarter period preceding the periodic structure and by displacing the electron orbit at $z = -\lambda_u/4$ by $x(-\lambda_u/4) = -K/(\beta\gamma k_u)$ with the help of two dipole magnets. A similar arrangement at the rear end restores the beam orbit downstream of the undulator. For an illustration see [1].

frequency and its odd higher harmonics). This is the characteristic feature of undulator radiation. The condition is

$$\theta_{max} \leq \frac{1}{\gamma} \quad \Rightarrow \quad K \leq 1 \,. \tag{2.11}$$

If however the maximum angle θ_{max} exceeds the radiation cone angle $1/\gamma$ by a large factor, which is the case for $K \gg 1$, one speaks of a wiggler magnet. Wiggler radiation consists of many densely spaced spectral lines forming a quasi-continuous spectrum which resembles the spectrum of ordinary synchrotron radiation in bending magnets. We will not discuss it any further in this book.

2.2.2 Motion in Second Order

Due to the sinusoidal trajectory the z component of the velocity is not constant. It is given by

$$v_z = \sqrt{v^2 - v_x^2} \approx c \left(1 - \frac{1}{2\gamma^2}\left(1 + \gamma^2 v_x^2/c^2\right)\right) \,.$$

Inserting for $v_x = \dot{x}(t)$ the first-order solution, the z velocity becomes

$$v_z(t) = \left(1 - \frac{1}{2\gamma^2}\left(1 + \frac{K^2}{2}\right)\right) c - \frac{cK^2}{4\gamma^2}\cos(2\omega_u t) \tag{2.12}$$

with the abbreviation $\omega_u = \bar{\beta} c k_u$. The average longitudinal speed is

$$\boxed{\bar{v}_z = \left(1 - \frac{1}{2\gamma^2}\left(1 + \frac{K^2}{2}\right)\right) c \equiv \bar{\beta}\, c \,.} \tag{2.13}$$

The particle trajectory in second order is described by the equations

$$\boxed{x(t) = \frac{K}{\gamma k_u}\sin(\omega_u t) \,, \qquad z(t) = \bar{v}_z t - \frac{K^2}{8\gamma^2 k_u}\sin(2\omega_u t) \,.} \tag{2.14}$$

The motion in a helical undulator is treated in Sect. 4.9 and Appendix A.

2.3 Emission of Radiation

2.3.1 Radiation in a Moving Coordinate System

Consider a coordinate system (x^*, y^*, z^*) moving with the average z velocity of the electrons:

$$\bar{v}_z \equiv \bar{\beta} c \,, \quad \bar{\gamma} = \frac{1}{\sqrt{1 - \bar{\beta}^2}} \approx \frac{\gamma}{\sqrt{1 + K^2/2}} \,. \tag{2.15}$$

The Lorentz transformation from the moving system to the laboratory system reads

$$t^* = \bar{\gamma}(t - \bar{\beta}z/c) \approx \bar{\gamma}t(1 - \bar{\beta}^2) = t/\bar{\gamma}$$
$$x^* = x = \frac{K}{\gamma k_u} \sin(\omega_u t)$$
$$z^* = \bar{\gamma}(z - \bar{\beta}ct) \approx -\frac{K^2}{8\gamma k_u \sqrt{1 + K^2/2}} \sin(2\omega_u t).$$

The electron orbit in the moving system is thus

$$x^*(t^*) = a \sin(\omega^* t^*) \ , \quad z^*(t^*) = -a \frac{K}{8\sqrt{1 + K^2/2}} \sin(2\omega^* t^*) \tag{2.16}$$

with the amplitude $a = K/(\gamma k_u)$ and the frequency

$$\omega^* = \bar{\gamma}\omega_u = \bar{\gamma}\bar{\beta}\, c\, k_u \approx \frac{\gamma\, c\, k_u}{\sqrt{1 + K^2/2}} \ .$$

Note that $\omega_u t = \omega^* t^*$. The motion is depicted in Fig. 2.2. It is mainly a transverse harmonic oscillation with the frequency $\omega^* = \bar{\gamma}\omega_u$. Superimposed is a small longitudinal oscillation with twice that frequency. If we ignore the longitudinal oscillation for the time being, the electron will emit dipole radiation in the moving system with the frequency $\omega^* = \bar{\gamma}\omega_u$ and the wavelength $\lambda_u^* = \lambda_u/\bar{\gamma}$.

The radiation power from an accelerated charge is given by the well-known Larmor formula

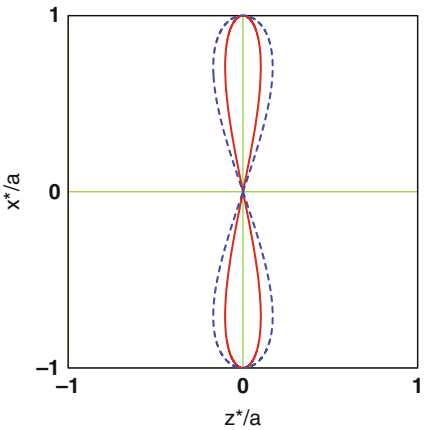

Fig. 2.2. The electron trajectory in the moving coordinate system for an undulator parameter of $K = 1$ (*continuous red curve*) or $K = 5$ (*dashed blue curve*). The curve has the shape of the number 8. For $K \gg 1$ the excursion in longitudinal direction is $z^*_{\max}/a = \sqrt{2}/8 = 0.18$. For $K \to 0$ the longitudinal width shrinks to zero

$$P = \frac{e^2}{6\pi\varepsilon_0 c^3}\,\dot{\boldsymbol{v}}^2 \tag{2.17}$$

see Jackson [2] or any other textbook on classical electrodynamics. For an oscillating charge, $\dot{\boldsymbol{v}}^2$ must be averaged over one period. The Larmor formula is applicable for an oscillating dipole which is either at rest or moving at non-relativistic speeds. This condition is satisfied in the moving coordinate system. Ignoring the longitudinal oscillation the acceleration has only an x component

$$\dot{v}_x^* = \frac{d^2x^*}{dt^{*2}} = -\frac{K}{\gamma k_u}\,\omega^{*2}\sin(\omega^* t^*) = -\frac{K\gamma c^2 k_u}{1+K^2/2}\,\sin(\omega^* t^*)\;.$$

Then the time-averaged square of the acceleration becomes

$$\left\langle \dot{\boldsymbol{v}}^2 \right\rangle = \frac{K^2\gamma^2 c^4 k_u^2}{(1+K^2/2)^2}\,\frac{1}{2}\;.$$

The total radiation power in the moving system is thus

$$P^* = \frac{e^2 c\,\gamma^2 K^2 k_u^2}{12\pi\varepsilon_0 (1+K^2/2)^2}\;. \tag{2.18}$$

2.3.2 Transformation of Radiation into Laboratory System

The radiation characteristics of an oscillating dipole which is either at rest or moving at relativistic speed is depicted in Fig. 2.3. With increasing Lorentz factor γ the radiation becomes more and more concentrated in the forward direction. To compute the light wavelength in the laboratory system as a function of the emission angle θ with respect to the beam axis it is appropriate to apply the Lorentz transformation

$$\hbar\omega^* = \bar{\gamma}(E_{ph} - \bar{\beta}\,c\,p_{ph}\cos\theta) = \bar{\gamma}\hbar\omega_\ell(1-\bar{\beta}\cos\theta)$$

which expresses the photon energy $\hbar\omega^*$ in the moving system in terms of the photon energy $E_{ph} = \hbar\omega_\ell$ and the photon momentum $p_{ph} = \hbar\omega_\ell/c$ in the laboratory system. The light frequency in the laboratory system is thus

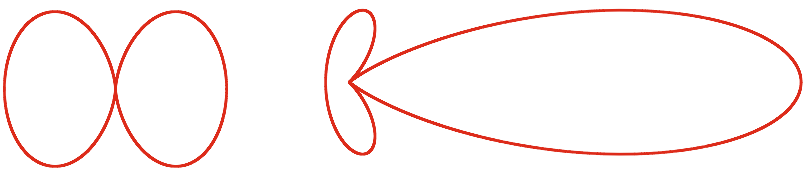

Fig. 2.3. Radiation characteristics in the laboratory system of an oscillating dipole at rest (*left*) or moving horizontally at a speed of $v = 0.9\,c$ (*right*). The dipole oscillates in vertical direction

$$\omega_\ell = \frac{\omega^*}{\bar{\gamma}\,(1-\bar{\beta}\cos\theta)} \quad \Rightarrow \quad \lambda_\ell = \frac{2\pi c}{\omega_\ell} \approx \lambda_u\,(1-\bar{\beta}\cos\theta)\;.$$

Using $\bar{\beta} = \left(1 - \frac{1}{2\bar{\gamma}^2}\,(1+K^2/2)\right)$ and $\cos\theta \approx 1-\theta^2/2$ (the typical angles are $\theta \leq 1/\gamma \ll 1$) we find that the wavelength of undulator radiation near $\theta = 0$ is in good approximation

$$\boxed{\lambda_\ell = \frac{\lambda_u}{2\gamma^2}\left(1 + \frac{K^2}{2} + \gamma^2\theta^2\right)\;.} \tag{2.19}$$

The radiation is linearly polarized with the electric vector in the plane of the wavelike electron trajectory.

T. Shintake has written a computer code in which the electric field pattern of a relativistic electron moving through the undulator is computed [3]. The field lines are shown in Fig. 2.4. One can clearly see the optical wavefronts and the dependence of the wavelength on the emission angle.

The total radiation power is relativistically invariant [2]. This can be seen as follows. Since we have ignored the longitudinal oscillation of the electron its longitudinal coordinate and momentum are zero in the moving system

$$z^* = 0\,, \quad p_z^* = 0\;.$$

Then the Lorentz transformations of time and electron energy read

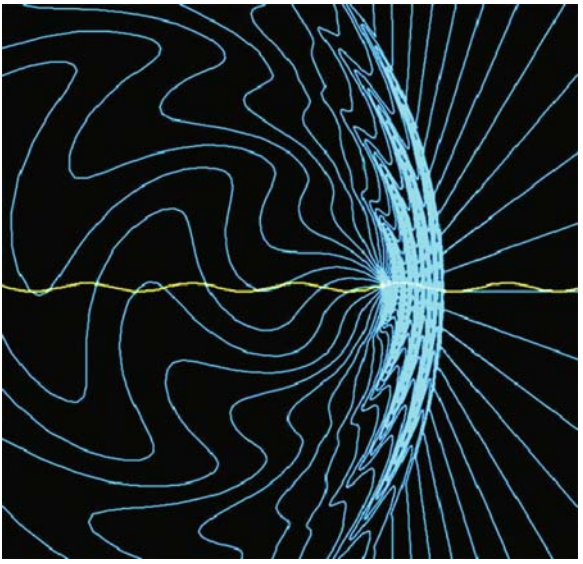

Fig. 2.4. Undulator radiation of an electron with $v = 0.9\,c$. The undulator parameter is $K = 1$. The wavy curve indicates the electron trajectory in the undulator. (Courtesy T. Shintake)

$$t = \bar{\gamma}\, t^* \,, \quad W = \bar{\gamma}\, W^*$$

so the radiation power in the laboratory system becomes

$$P = -\frac{dW}{dt} = -\frac{dW^*}{dt^*} = P^* \,.$$

The undulator radiation power per electron in the laboratory system is therefore

$$P_1 = \frac{e^2 c\, \gamma^2 K^2 k_u^2}{12\pi\varepsilon_0 (1 + K^2/2)^2} \,. \tag{2.20}$$

Since this formula has been derived neglecting the influence of the longitudinal oscillation it describes only the power P_1 contained in the first harmonic. The total power of spontaneous undulator radiation, summed over all harmonics and all angles, is equal to the synchrotron radiation power in a bending magnet whose field strength is $B = B_0/\sqrt{2}$.

$$\boxed{P_{\text{spont}} = \frac{e^4 \gamma^2 B_0^2}{12\pi\varepsilon_0 c\, m_e^2} = \frac{e^2 c\, \gamma^2 K^2 k_u^2}{12\pi\varepsilon_0} \,.} \tag{2.21}$$

This is easy to understand because the undulator field varies as $B(z) = -B_0 \sin(k_u z)$ and hence $\langle B^2 \rangle = B_0^2/2$. Formula (2.21) is valid for any value of K and thus also applicable for wiggler radiation. With increasing undulator parameter K the ratio P_1/P_{spont} drops, hence the fraction of power contained in the first harmonic decreases.

2.4 Lineshape and Spectral Energy of Undulator Radiation

An important property of undulator radiation is that it consists of narrow spectral lines. How wide is such a line? In this section we consider the first harmonic only and look in forward direction. An electron passing through an undulator with N_u periods produces a wave train with N_u oscillations (Fig. 2.5) and a time duration of $T = N_u \lambda_1 / c$. The electric field of the light wave is written as

$$E_\ell(t) = \begin{cases} E_0 \exp(-i\,\omega_1 t) & \text{if } -T/2 < t < T/2 \\ 0 & \text{otherwise} \end{cases} \tag{2.22}$$

Due to its finite length, this wave train is not monochromatic but contains a frequency spectrum which is obtained by Fourier transformation

$$\begin{aligned} A(\omega) &= \int_{-\infty}^{+\infty} E_\ell(t) e^{i\omega t} dt = E_0 \int_{-T/2}^{+T/2} e^{-i(\omega_1 - \omega)t} dt \\ &= 2E_0 \cdot \frac{\sin((\omega_1 - \omega)T/2)}{\omega_1 - \omega} \,. \end{aligned} \tag{2.23}$$

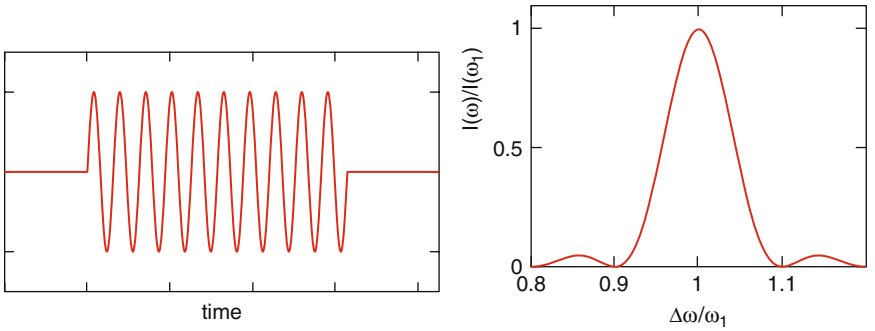

Fig. 2.5. A finite wave train with 10 oscillations and the lineshape function of forward undulator radiation (i.e. the intensity as a function of frequency) in a magnet with $N_u = 10$ periods. Only the first harmonic is considered here

The spectral intensity is

$$I(\omega) \propto |A(\omega)|^2 \propto \left(\frac{\sin \xi}{\xi}\right)^2 \quad \text{with} \quad \xi = \frac{(\omega_1 - \omega)T}{2} = \pi\, N_u\, \frac{\omega_1 - \omega}{\omega_1}\ . \quad (2.24)$$

It has a maximum at $\omega = \omega_1$ and a full width at half maximum of

$$\Delta\omega \approx \frac{\omega_1}{N_u}\ . \quad (2.25)$$

The lineshape function for a wave train with 10 oscillations is shown in Fig. 2.5.

The angular width of the first harmonic around $\theta = 0$ can be estimated as follows. We know from (2.19) that the frequency decreases with increasing emission angle θ:

$$\omega_1(\theta) = \omega_1(0) \cdot \frac{1 + K^2/2}{1 + K^2/2 + \gamma^2\theta^2}\ .$$

The intensity drops to zero when $\delta\omega_1 = \omega_1(0) - \omega_1(\theta)$ exceeds the bandwidth following from (2.24). The root-mean-square value is found to be [4]

$$\sigma_\theta \approx \frac{1}{\gamma} \cdot \sqrt{\frac{1 + K^2/2}{2N_u}} \approx \frac{1}{\gamma} \cdot \frac{1}{\sqrt{N_u}} \quad \text{for} \quad K \approx 1\ . \quad (2.26)$$

Obviously, the first harmonic of undulator radiation is far better collimated than synchrotron radiation: the typical opening angle $1/\gamma$ is multiplied by the factor $1/\sqrt{N_u} \ll 1$. It is important to realize that this tight collimation of the first harmonic applies only if one requests that the frequency stays within the bandwidth. If one drops the restriction to a narrow spectral line and accepts the entire angular-dependent frequency range as well as the higher harmonics, the cone angle of undulator radiation becomes for $K > 1$, using (2.10)

$$\theta_{\text{cone}} \approx \frac{K}{\gamma}\ . \quad (2.27)$$

2.5 Higher Harmonics

To understand the physical origin of the higher harmonics of undulator radiation we follow the argumentation in the excellent book *The Science and Technology of Undulators and Wigglers* by J.A. Clarke [5]. In the forward direction ($\theta = 0$) only odd higher harmonics are observed while the off-axis radiation contains also the even harmonics. How can one explain this observation?

Consider a detector with a small aperture centered at $\theta = 0$ which is placed in the far-field at large distance from the undulator. The electrons moving on a sinusoidal orbit with maximum angle of K/γ emit their radiation into a cone of opening angle $1/\gamma$. If the undulator parameter is small, $K \ll 1$, the radiation cone points always toward the detector and therefore the radiation from the entire trajectory is detected. One observes a purely sinusoidal electric field which has only one Fourier component at the fundamental harmonic ω_1, see Fig. 2.6 (top). The situation changes if the undulator parameter is significantly larger than 1, because then the angular excursion of the electron is much larger than the cone angle $1/\gamma$ and the radiation cone sweeps back and forth across the aperture, so the detector receives its light only from short sections of the electron trajectory. The radiation field seen by the detector consists therefore of narrow pulses of alternating polarity as sketched in the bottom part of Fig. 2.6. The frequency spectrum contains many higher harmonics. In forward direction only the odd harmonics occur because the positive and negative pulses are symmetric in shape and uniformly spaced. When the detector is

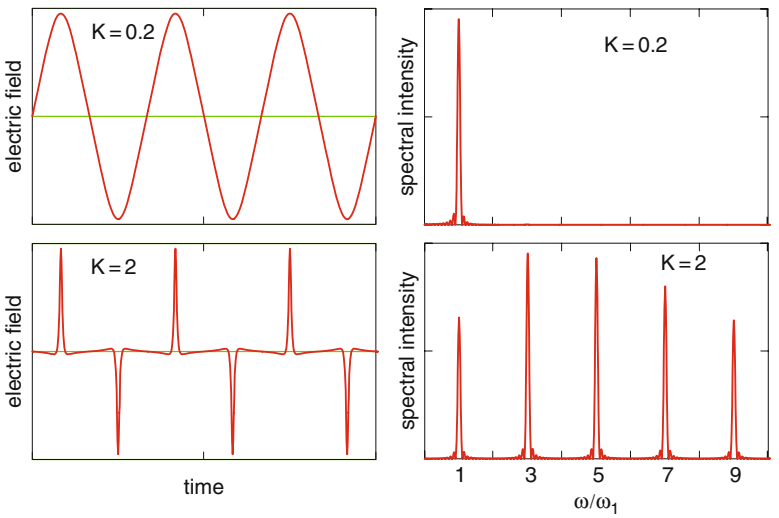

Fig. 2.6. Schematic view of the electric light-wave field seen by a small detector in forward direction and the corresponding frequency spectrum. *Top*: small undulator parameter $K = 0.2$, *bottom*: undulator parameter $K = 2$

placed at a finite angle $\theta > 0$, the field pulses are no longer equally spaced and the radiation spectrum contains the even harmonics as well (see [5] for an illustration).

The wavelength of the mth harmonic as a function of the angle θ is

$$\lambda_m(\theta) = \frac{1}{m}\,\frac{\lambda_u}{2\gamma^2}\,(1 + K^2/2 + \gamma^2\theta^2)\,, \quad m = 1,\ 2,\ 3,\ 4, \ldots\ . \tag{2.28}$$

In forward direction only the odd harmonics are observed with the wavelengths

$$\boxed{\lambda_m = \frac{1}{m}\,\frac{\lambda_u}{2\gamma^2}\,(1 + K^2/2)\,, \quad m = 1,\ 3,\ 5, \ldots} \tag{2.29}$$

so $\lambda_3 = \lambda_1/3$, $\lambda_5 = \lambda_1/5$. We will present an alternative derivation of (2.29) in Chap. 3.

The spectral energy density per electron of the radiation emitted in forward direction (emission angle $\theta = 0$) is for the mth harmonic [4, 5, 6]

$$\frac{d^2U_m}{d\Omega d\omega} = \frac{e^2\gamma^2\, m^2K^2}{4\pi\varepsilon_0 c(1 + K^2/2)^2} \cdot \frac{\sin^2(\pi N_u(\omega - \omega_m)/\omega_1)}{\sin^2(\pi(\omega - \omega_m)/\omega_1)} \cdot |JJ|^2$$

$$JJ = J_n\left(\frac{m\,K^2}{4 + 2K^2}\right) - J_{n+1}\left(\frac{m\,K^2}{4 + 2K^2}\right)\ , \quad m = 2n + 1\ . \tag{2.30}$$

Here $\omega_m = m\,\omega_1 \equiv m\,\omega_\ell$ is the (angular) frequency of the mth harmonic. The harmonic index m is related to the index n by $m = 2n + 1$ and takes on the odd integer values $m = 1, 3, 5, \ldots$ for $n = 0, 1, 2, \ldots$. The J_n are the Bessel functions of integer order.

The absolute bandwidth at $\theta = 0$ is the same for all harmonics

$$\Delta\omega_1 = \Delta\omega_3 = \Delta\omega_5 \ldots$$

but the fractional bandwidth drops as $1/m$

$$\frac{\Delta\omega_m}{\omega_m} = \frac{1}{mN_u} \tag{2.31}$$

because the wave train comprises now mN_u oscillations in an undulator with N_u periods. The angular width is [4]

$$\sigma_{\theta,\,m} \approx \frac{1}{\gamma} \cdot \sqrt{\frac{1 + K^2/2}{2mN_u}} \approx \frac{1}{\gamma} \cdot \frac{1}{\sqrt{mN_u}} \quad \text{for} \quad K \approx 1\ . \tag{2.32}$$

The corresponding solid angle

$$\Delta\Omega_m = 2\pi\sigma^2_{\theta,\,m} \approx \frac{2\pi}{\gamma^2} \cdot \frac{1}{m\,N_u}$$

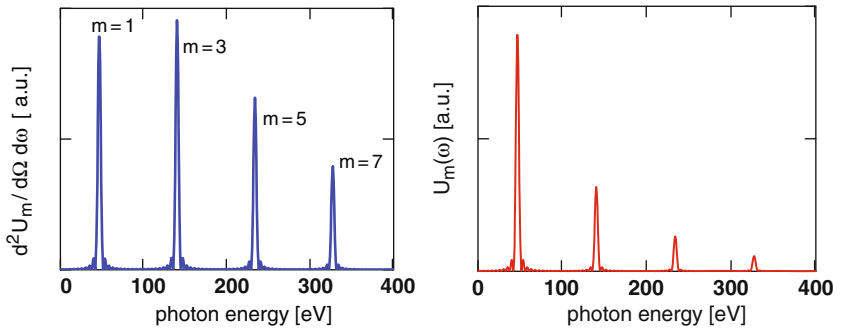

Fig. 2.7. *Left*: Example of a computed photon energy spectrum of undulator radiation for an undulator with 10 periods. Plotted is the differential spectral energy density $d^2U_m/d\Omega d\omega$ at $\theta = 0$. The units are arbitrary. *Right*: the spectral energy $U_m(\omega)$ of the m^{th} harmonic that is emitted into the solid angle $\Delta\Omega_m$. The electron Lorentz factor is $\gamma = 1000$, the undulator has the period $\lambda_u = 25$ mm and the parameter $K = 1.5$. Note that the energy ratios U_m/U_1 depend only on the harmonic index m and the undulator parameter K, but not on γ nor on λ_u

decreases as $1/m$ with increasing harmonic order. Within the solid angle $\Delta\Omega_m$ the angular-dependent frequency shift is less than the bandwidth. Of practical interest is the spectral energy contained in this solid angle:

$$U_m(\omega) = \frac{d^2U_m}{d\Omega d\omega}\,\Delta\Omega_m \qquad m = 1, 3, 5, \ldots \ . \tag{2.33}$$

This spectral energy is shown in Fig. 2.7 for $m = 1, 3, 5, 7$ for a short undulator with ten periods and $K = 1.5$.

The angular dependence of the spectral energy is derived in [5]. For emission angles $\theta \neq 0$ the radiation will contain all higher harmonics ($m = 1, 2, 3, 4, \ldots$), as mentioned above.

References

1. Wille, K.: The Physics of Particle Accelerators. An Introduction. Oxford University Press, Oxford (2001) 13
2. Jackson, J.D.: Classical Electrodynamics, 3rd ed., John Wiley, New York (1999) 13, 16, 17
3. Shintake, T.: New real-time simulation technique for synchrotron and undulator radiation. Proceedings of LINAC2002, Geongju, Korea (2002) 17
4. Wiedemann, H.: Particle Accelerator Physics II, 2nd ed., Springer, Berlin (1999) 19, 21
5. Clarke, J.A.: The Science and Technology of Undulators and Wigglers. Oxford University Press, Oxford (2004) 20, 21, 22
6. Duke, P.J: Synchrotron Radiation: Production and Properties. Oxford University Press, Oxford (2000) 21

3

Low-Gain FEL Theory

The schematic setup of a low-gain FEL is shown in Fig. 3.1. The main components are

- an electron storage ring in which relativistic electron bunches carry out many revolutions or a linear accelerator providing a long periodic train of bunches,
- a short undulator magnet,
- an optical cavity.

We assume the presence of an initial light wave with wavelength λ_ℓ which may be provided either by an external source such as an optical laser, or by the spontaneously emitted undulator radiation which is captured in the optical cavity. Following the terminology in laser physics, one speaks of an FEL amplifier if the lasing process is initiated by seed radiation, and of an FEL oscillator if the lasing process starts from spontaneous radiation. The bunches make very many passages through the undulator. Upon each passage the light intensity grows by only a few per cent, which is the reason why

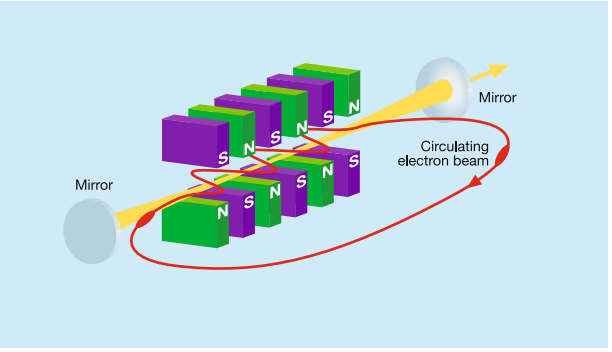

Fig. 3.1. Principle of a low-gain FEL oscillator equipped with an optical resonator. In this example the undulator is inserted in a storage ring

P. Schmüser, et al.: *Low-Gain FEL Theory*, STMP **229**, 23–36 (2008)
DOI 10.1007/978-3-540-79572-8_3

such a device is called a *low-gain FEL*. The small gain per undulator passage, however, does not prevent the FEL from reaching very high output powers (in the order of Gigawatts) if the electron beam makes a sufficiently large number N of passages and if the lifetime of the optical eigenmode (being proportional to the quality factor of the optical cavity) is long enough:

$$P_{\text{out}} = P_{\text{in}}(1+\delta)^N \ . \tag{3.1}$$

Here P_{in} is the input power and δ the relative increase per turn. Note that δ will decrease when the FEL saturation power is approached.

3.1 Energy Exchange Between Electron Beam and Light Wave

We consider here the case of an FEL amplifier which is seeded by an external laser. For simplicity, the light wave co-propagating with the relativistic electron beam is described by a plane electromagnetic wave

$$E_x(z,t) = E_0 \cos(k_\ell z - \omega_\ell t + \psi_0) \quad \text{with} \quad k_\ell = \omega_\ell/c = 2\pi/\lambda_\ell \ . \tag{3.2}$$

(In reality the seed laser will be a pulsed laser to achieve sufficient instantaneous power. Likewise, the FEL light is concentrated in a short pulse that is traveling back and forth between the mirrors of the optical resonator). The time derivative of the electron energy $W = \gamma m_e c^2$ is

$$\frac{dW}{dt} = \boldsymbol{v} \cdot \boldsymbol{F} = -e v_x(t) E_x(t) \ . \tag{3.3}$$

Energy conservation tells us that the light wave gains energy if $dW/dt < 0$. Hence the x component of the electron velocity and the electric vector E_x of the light wave must point in the same direction to get an energy transfer from the electron to the light wave[1]. Suppose this is the case at some position z_0 in

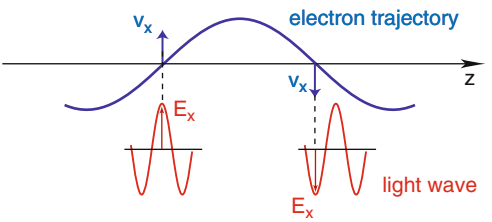

Fig. 3.2. Condition for sustained energy transfer from electron to light wave: the light wave has to advance by $\lambda_\ell/2$ per half period of the electron trajectory

[1] We remark that in Chap. 4 the inhomogeneous wave equation will be used to compute the energy exchange between the electron beam and the FEL wave.

the undulator (see Fig. 3.2). Now a problem arises. The light wave, traveling with the speed c along the z axis, will obviously slip forward with respect to the electron whose average speed in z direction is $\bar{v}_z = c\left(1-(2+K^2)/(4\gamma^2)\right)$ according to (2.13). This speed is definitely less than c because the electrons are massive particles and thus slower than light, but more importantly, because they travel on a sinusoidal orbit which is longer than the straight path of the photons.

The question is then: how is it at all possible to achieve a steady energy transfer from the electron beam to the light wave along the entire undulator? The answer is that the phase of the light wave has to slip by the right amount, and this proper slippage is only possible for certain wavelengths. Figure 3.2 illustrates that the transverse velocity v_x and the field E_x remain parallel if the light wave advances by half an optical wavelength $\lambda_\ell/2$ in a half period of the electron trajectory. The difference of the electron and light travel times for a half period of the undulator is

$$\Delta t = t_{\rm el} - t_{\rm light} = \left[\frac{1}{\bar{v}_z} - \frac{1}{c}\right] \frac{\lambda_u}{2} \,.$$

The condition for sustained energy transfer is thus

$$c\,\Delta t = \lambda_\ell/2 \,.$$

Inserting Δt allows us to compute the light wavelength. In good approximation it is given by

$$\lambda_\ell = \frac{\lambda_u}{2\gamma^2}\left(1+\frac{K^2}{2}\right) \,. \tag{3.4}$$

We remark that slippages by $3\lambda_\ell/2, 5\lambda_\ell/2\ldots$ are also possible leading to odd higher harmonics $(\lambda_\ell/3\,,\ \lambda_\ell/5\ldots)$ of the FEL radiation. Note however that $c\,\Delta t = 2\lambda_\ell/2,\ 4\lambda_\ell/2\ldots$ yields zero net energy transfer from the electron to the light wave: the even harmonics $(\lambda_\ell/2\,,\ \lambda_\ell/4\ldots)$ are not present.

Quantitative Treatment

The energy transfer per unit time from an electron to the light wave is described by the equation

$$\begin{aligned}\frac{dW}{dt} &= -ev_x(t)E_x(t) = -e\frac{cK}{\gamma}\cos(k_u z)E_0\cos(k_\ell z-\omega_\ell t+\psi_0)\\ &= -\frac{ecKE_0}{2\gamma}\left[\cos((k_\ell+k_u)z-\omega_\ell t+\psi_0)+\cos((k_\ell-k_u)z-\omega_\ell t+\psi_0)\right]\\ &\equiv -\frac{ecKE_0}{2\gamma}\,\cos\psi - \frac{ecKE_0}{2\gamma}\,\cos\chi \,. \end{aligned}\tag{3.5}$$

Due to the fact that the electron bunch is far longer than the light wavelength, $L_b \gg \lambda_\ell$, we must admit that the light wave may be phase-shifted against the

sinusoidal trajectory of an arbitrary electron by an arbitrary phase ψ_0. Now we consider the first term in (3.5). It is customary in FEL physics to call the argument ψ of the first cosine function the *ponderomotive phase*:

$$\boxed{\psi \equiv (k_\ell + k_u)z - \omega_\ell t + \psi_0 \; .} \tag{3.6}$$

The position z of the electron is a function of time t according to (2.14), so we can write the ponderomotive phase as a function of the single variable t:

$$\psi(t) \equiv (k_\ell + k_u)z(t) - \omega_\ell t + \psi_0 \; . \tag{3.7}$$

The first term in (3.5) will provide a continuous energy transfer from the electron to the light wave if $\psi(t)$ is constant along the undulator (independent of time), the optimum value being $\psi = 0$ resp. $\psi = \pm n\, 2\pi$. The condition $\psi = const$ can only be fulfilled for a certain wavelength. To find this we insert $z(t)$ from (2.14) but neglect for the time being the longitudinal oscillation, hence we put $z(t) = \bar{v}_z\, t$.

$$\psi(t) = (k_\ell + k_u)\bar{v}_z\, t - \omega_\ell t + \psi_0 = const \;\; \Leftrightarrow \;\; \frac{d\psi}{dt} = (k_\ell + k_u)\bar{v}_z - k_\ell c = 0 \; . \tag{3.8}$$

Insertion of $\bar{v}_z$ permits us to compute the light wavelength, which is in good approximation

$$\boxed{\lambda_\ell = \frac{\lambda_u}{2\gamma^2}\left(1 + \frac{K^2}{2}\right) \; .} \tag{3.9}$$

This is a very important result: The condition for sustained energy transfer all along the undulator yields the same light wavelength as is observed in undulator radiation at $\theta = 0$. This fact is the reason why spontaneous undulator radiation can serve as *seed radiation* in a low-gain FEL amplifier or a SASE FEL.

Now we look at the second cosine function in (3.5). Here the argument cannot be kept constant since from

$$\chi(t) \equiv (k_\ell - k_u)\bar{v}_z t - \omega_\ell t + \psi_0 = const \tag{3.10}$$

we would get

$$k_\ell(1 - \bar{\beta}) = -k_u \bar{v}_z / c \quad \Rightarrow \quad k_\ell < 0$$

which means that the light wave propagates in negative z direction. Writing ψ as a function of $z = \bar{v}_z\, t$ we can immediately verify that

$$\chi(z) = \psi(z) - 2k_u z \; .$$

So for $\psi(z) = const$, which happens if (3.9) is fulfilled, the second cosine function behaves as $\cos(2k_u z)$, i.e. it makes two oscillations per undulator period and cancels out. This is shown in Fig. 3.3. Neglecting the rapidly oscillating term, (3.5) reduces to

$$\frac{dW}{dt} = -\frac{ecKE_0}{2\gamma}\cos\psi \; . \tag{3.11}$$

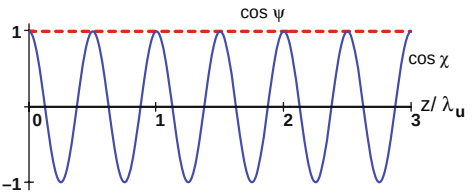

Fig. 3.3. The z dependencies of the terms $\cos\psi$ and $\cos\chi$

3.2 Internal Bunch Coordinate

The ponderomotive phase ψ has an intuitive interpretation: it can be transformed into a longitudinal coordinate ζ inside the bunch.

$$\boxed{\zeta = \frac{\psi + \pi/2}{k_\ell + k_u} \approx \frac{\psi + \pi/2}{2\pi}\,\lambda_\ell\ .} \tag{3.12}$$

This is schematically shown in Fig. 3.4. We define a reference position $\zeta = \zeta_r = 0$ by the condition that the energy exchange between electron and light wave is zero; this corresponds to an initial phase $\psi_0 = -\pi/2$, see Fig. 3.5. The z position of this *reference electron* and its ponderomotive phase have the time dependencies

$$z_r(t) = \bar{v}_z t\ , \quad \psi_r(t) = (k_\ell + k_u) z_r(t) - \omega_\ell t - \pi/2\ .$$

For an arbitrary electron the position along the undulator is

$$z(t) = z_r(t) + \zeta(t) = \bar{v}_z t + \zeta(t)$$

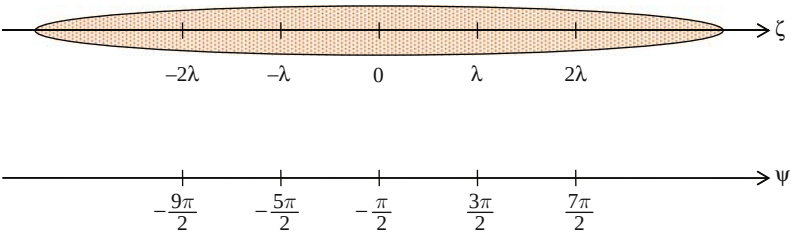

Fig. 3.4. Definition of the internal longitudinal bunch coordinate ζ. The light wavelength is written here as λ instead of λ_ℓ. The ponderomotive phase is $\psi = 2\pi\,\zeta/\lambda - \pi/2$. The reference position $\zeta_r = 0$ corresponds to an initial phase $\psi_0 = -\pi/2$ in (3.5), (3.6) and vanishing energy exchange between electron and light wave. The reference position moves with the average electron speed $\bar{v}_z$ along the z axis of the undulator. Note that the length scale of the coordinate ζ refers to the laboratory system and not to the co-moving coordinate system of the relativistic bunch. Hence there is no relativistic length expansion

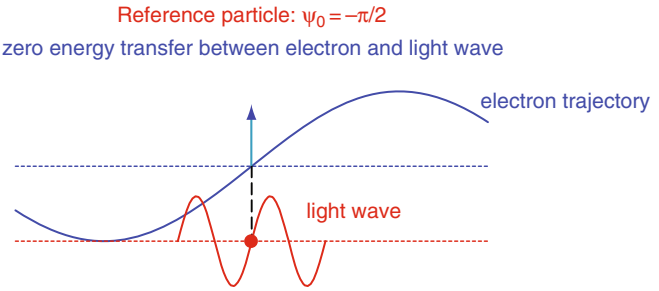

Fig. 3.5. Ponderomotive phase $\psi_0 = -\pi/2$ corresponding to vanishing energy exchange between electron and light wave

and the ponderomotive phase is

$$\psi(t) = (k_\ell + k_u)(\bar{v}_z t + \zeta(t)) - \omega_\ell t - \pi/2 \; .$$

At time $t = 0$ we get

$$\psi_0 \equiv \psi(0) = (k_\ell + k_u)\zeta(0) - \pi/2 \; .$$

Hence the initial distance ζ_0 of an arbitrary electron from the reference electron is related to its initial phase ψ_0 by:

$$\zeta_0 = \zeta(0) = \frac{\psi_0 + \pi/2}{k_\ell + k_u} \approx \frac{\psi_0 + \pi/2}{2\pi}\,\lambda_\ell \; . \tag{3.13}$$

The meaning of the ponderomotive phase is illustrated in Figs. 3.5 and 3.6. The general electron will be at an initial position $\zeta_0 \neq 0$ in the bunch and it will thus possess an initial phase $\psi_0 \neq -\pi/2$. When this phase is chosen as $\psi_0 = 0$ (see the left part of Fig. 3.6), we get $\psi = 0$ all along the undulator since $\psi = const = \psi_0$ if the light wavelength obeys the basic equation (3.9). Hence there will be sustained energy transfer from the electron to the light wave, which

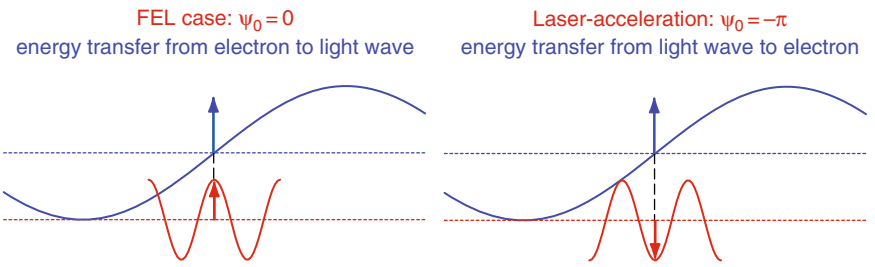

Fig. 3.6. *Left*: ponderomotive phase $\psi_0 = 0$ for optimum energy transfer from electron to light wave (FEL operation). *Right*: phase $\psi_0 = -\pi$ for optimum energy transfer from light wave to electron (acceleration of particles by a laser field). This is sometimes called an inverse FEL

is the optimal working condition for the FEL. Choosing $\psi_0 = -\pi$, we obtain maximum energy transfer from the light wave to the electron, corresponding to particle acceleration by a laser field (right part of Fig. 3.6).

3.3 The FEL Pendulum Equations

We treat the low-gain FEL as a laser amplifier and assume that the lasing process in the undulator is initiated by an incident monochromatic light wave of amplitude E_0 and wavelength λ_ℓ. We define the *resonance electron energy* $W_r = \gamma_r\, m_e c^2$ by the equation

$$\boxed{\lambda_\ell = \frac{\lambda_u}{2\gamma_r^2}\left(1 + \frac{K^2}{2}\right) \quad \Rightarrow \quad \gamma_r = \sqrt{\frac{\lambda_u}{2\lambda_\ell}\left(1 + \frac{K^2}{2}\right)}\,.} \tag{3.14}$$

W_r is sometimes also called the *reference energy*. Its meaning is that electrons with the energy W_r would emit undulator radiation with just the incident wavelength λ_ℓ.

Let now the electron energy W be slightly different from W_r and define the relative energy deviation

$$\boxed{\eta = \frac{W - W_r}{W_r} = \frac{\gamma - \gamma_r}{\gamma_r} \qquad |\eta| \ll 1\,.} \tag{3.15}$$

The Lorentz factor γ and the ponderomotive phase ψ of an electron will both change due to the interaction with the radiation field. In contrast to this the electric field amplitude E_0 grows so slowly in a low-gain FEL that it can be considered as roughly constant during one passage of the undulator. The time derivative of the ponderomotive phase is no longer zero for $\gamma \neq \gamma_r$:

$$\frac{d\psi}{dt} = (k_\ell + k_u)\bar{v}_z - \omega_\ell \approx k_u c - \frac{k_\ell c}{2\gamma^2}\left(1 + \frac{K^2}{2}\right)$$

where we have inserted $\bar{v}_z$ from (2.13). According to (3.14) we can write

$$k_u c = \frac{k_\ell c}{2\gamma_r^2}\left(1 + \frac{K^2}{2}\right)$$

and obtain

$$\frac{d\psi}{dt} = \frac{k_\ell c}{2}\left(1 + \frac{K^2}{2}\right)\left(\frac{1}{\gamma_r^2} - \frac{1}{\gamma^2}\right)\,.$$

From this follows in good approximation, using (3.15) and the fact that γ differs very little from γ_r :

$$\boxed{\frac{d\psi}{dt} = 2k_u c\,\eta\,.} \tag{3.16}$$

The time derivative of the relative energy deviation η is according to (3.5)

$$\boxed{\frac{d\eta}{dt} = -\frac{eE_0K}{2m_ec\gamma_r^2}\cos\psi\ .} \tag{3.17}$$

The two equations (3.16) and (3.17) are called the FEL pendulum equations. They are of fundamental importance for both the low-gain FEL and the high-gain FEL.

In order to stress the similarity with the mathematical pendulum it is convenient to introduce a shifted phase variable[2] ϕ by

$$\phi = \psi + \pi/2 \quad \Rightarrow \quad \cos\psi = \sin\phi\ . \tag{3.18}$$

The two coupled first-order differential equations (3.16) and (3.17) read then

$$\frac{d\phi}{dt} = 2k_uc\,\eta\ , \qquad \frac{d\eta}{dt} = -\frac{eE_0K}{2m_ec\gamma_r^2}\,\sin\phi\ . \tag{3.19}$$

Combining them we arrive at the second-order pendulum equation of the low-gain FEL

$$\ddot{\phi} + \Omega^2\sin\phi = 0 \quad \text{with} \quad \Omega^2 = \frac{eE_0Kk_u}{m_e\gamma_r^2} \tag{3.20}$$

which is mathematically fully equivalent to the second-order differential equation of a mathematical pendulum. We point out that this equation is not applicable in the high-gain FEL theory because the growth of the electric field has been neglected in the derivation of (3.20).

3.4 Phase Space Representation and FEL Bucket

3.4.1 Phase Space Trajectories

There is a close analogy between the dynamics of a low-gain FEL and the motion of a mathematical pendulum which is treated in Appendix A. The first-order differential equations are

FEL	$\dfrac{d\phi}{dt} = 2k_uc\cdot\eta$	$\dfrac{d\eta}{dt} = -\dfrac{eE_0K}{2m_ec\gamma_r^2}\cdot\sin\phi$
pendulum	$\dfrac{d\phi}{dt} = \dfrac{1}{m\ell^2}\cdot L$	$\dfrac{dL}{dt} = -m\,g\,\ell\cdot\sin\phi$

Owing to the same mathematical structure of the two sets of coupled equations we can describe the FEL by a Hamiltonian, too. In analogy with (A.5) the Hamiltonian of the low-gain FEL is given by

[2] The shifted phase ϕ is only needed for our comparison between FEL and pendulum. It will not be used in the other chapters.

$$H(\phi,\eta) = k_u c\,\eta^2 + \frac{eE_0K}{2m_e c\gamma_r^2}\,(1-\cos\phi)\ . \tag{3.21}$$

The equations (3.19) are an immediate consequence of the Hamilton equations

$$\frac{d\phi}{dt} = \frac{\partial H}{\partial \eta} = 2k_u c\,\eta\ , \qquad \frac{d\eta}{dt} = -\frac{\partial H}{\partial \phi} = -\frac{eE_0K}{2m_e c\gamma_r^2}\sin\phi\ . \tag{3.22}$$

The trajectories in the (ϕ,η) phase space are the curves of a constant Hamiltonian: $H = const.$ The region of bounded motion (periodic oscillation in case of the pendulum) is separated from the region of unbounded motion (rotation of pendulum, see Appendix A) by a curve called the *separatrix*. The equation of the FEL separatrix is in analogy to (A.7)

$$\eta_{\rm sep}(\phi) = \pm\sqrt{\frac{eE_0K}{k_u m_e c^2\gamma_r^2}}\,\cos(\phi/2)\ . \tag{3.23}$$

The phase space trajectory of an electron in an FEL can be easily constructed by writing the coupled differential equations (3.22) as difference equations and solving these in small time steps. An electron at the reference position would have zero energy exchange with the light wave as illustrated in Fig. 3.5. If moreover the energy of the reference electron is chosen as $W = W_r = \gamma_r m_e c^2$ (hence $\eta = 0$), then the equations (3.22) show that the phase space coordinates of this reference electron will be stationary during the motion through the undulator. The point $(\phi,\eta) = (0,0)$ is therefore a fixpoint in the phase space diagram.

The phase space trajectories for 15 electrons of different initial phases ϕ_0 are shown in Fig. 3.7 for the two cases $\gamma = \gamma_r$ and $\gamma > \gamma_r$. When the electrons are on resonance, $\gamma = \gamma_r$, the net energy transfer is zero since there are as many electrons which supply energy to the light wave as there are electrons which remove energy from the wave. For $\gamma > \gamma_r$, however, the phase space picture clearly shows that there is a positive net energy transfer from the electron beam to the light wave. This will be computed in the next section.

3.4.2 Definition of the FEL Bucket

The particle dynamics in a low-gain FEL has some similarity with the longitudinal dynamics in a proton storage ring. When the proton beam has been accelerated to the design energy the phase of the radio-frequency (RF) in the accelerating cavities is adjusted such that the bunch receives zero energy gain on average. The energy of a "reference" particle at the bunch center will remain constant. However, individual protons inside the bunch will either be accelerated or decelerated depending on their position relative to the reference particle. The particles carry out longitudinal oscillations about the reference position and energy oscillations about the reference energy. The phase space picture looks exactly alike the FEL phase space diagrams in Fig. 3.7.

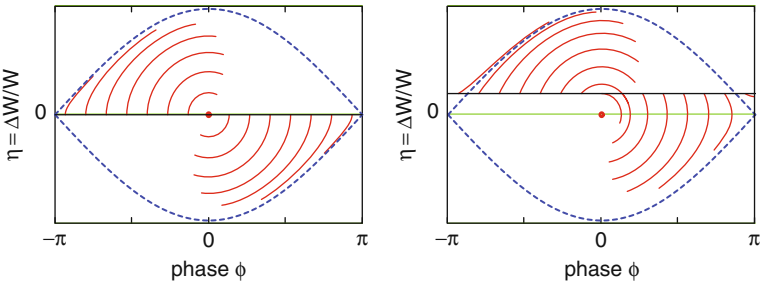

Fig. 3.7. Phase space trajectories for 15 electrons of different initial phases ϕ_0. *Left picture*: electrons are on resonance, $\gamma = \gamma_r$, $\eta = 0$. The electrons with negative initial phases $-\pi < \phi_0 < 0$ withdraw energy from the light wave while those with positive initial phases $0 < \phi_0 < \pi$ supply energy to the light wave. From the symmetry it is obvious that the net energy transfer from the ensemble of electrons to the light wave is zero for $\gamma = \gamma_r$. The particle at the center $(\phi, \eta) = (0, 0)$ does not move at all, so $(0, 0)$ is a fixpoint. The separatrix (3.23) is drawn as a dashed curve. *Right picture*: $\gamma > \gamma_r$, $\eta > 0$. Now there are more particles losing energy than gaining energy, so the net energy transfer from the electron beam to the light wave is positive (in this example there are seven electrons inside the separatrix that lose energy and five electrons that gain energy). Note that for $\eta > 0$ the fixpoint is not occupied by a particle, and that moreover the first and the last particle are outside the separatrix and carry out an unbounded motion

The proton bunches are contained in the potential minima of the Hamiltonian, the so-called *RF buckets*. By analogy we call the area enclosed by the separatrix (3.23) the *FEL bucket*. The phase space picture in Fig. 3.7 can be periodically repeated (making the replacement $\phi \to \phi \pm n\,2\pi$). Hence there will be very many FEL buckets for a long electron bunch.

Written in terms of the ponderomotive phase $\psi = \phi - \pi/2$ the equation of the separatrix reads

$$\eta_{\mathrm{sep}}(\psi) = \pm\sqrt{\frac{eE_0K}{k_u m_e c^2 \gamma_r^2}}\,\cos\left(\frac{\psi - \psi_b}{2}\right) \tag{3.24}$$

where

$$\psi_b = -\pi/2 \pm n\,2\pi \tag{3.25}$$

is the phase of the bucket center. The energy exchange between electron and light wave vanishes at the bucket center (see also Fig. 3.5).

It is interesting to note that the frequency of the longitudinal oscillations in a storage ring (the so called synchrotron oscillations) is quite small: in the 920 GeV proton storage ring HERA at DESY, for example, the particles carry out less than 0.001 longitudinal oscillation per revolution. The circumference of the machine is 6.2 km. In a similar manner the phase space motion of the electrons in the FEL is very slow. To see this we rewrite the first pendulum equation in the form

$$\frac{d\psi}{dz} \approx \frac{d\psi}{c\,dt} = \frac{4\pi}{\lambda_u}\,\eta\ .$$

In an undulator of 1 m length and with a period of $\lambda_u = 0.025\,\mathrm{m}$ the phase advance is only $\Delta\psi = 0.16\pi$ for a typical fractional energy deviation $\eta = 0.001$.

3.5 FEL Gain and Madey Theorem

We have seen in the previous section that the energy transfer between the electron beam and the light wave depends on the relative energy deviation $\eta = (\gamma - \gamma_r)/\gamma_r$. Figure 3.7 shows quite clearly that the light wave gains energy when η is positive but remains invariant for $\eta = 0$. Likewise, the light wave loses energy when η is negative. Now we look for a quantitative description. The FEL gain function is defined as the relative energy increase of the light wave during one passage of the undulator

$$G = \frac{\Delta W_\ell}{W_\ell}\ .$$

Treating the phase space motion of the electrons by second-order perturbation theory it can be shown (see e.g. [1]) that the gain function[3] is given by the expression

$$\boxed{G(\xi) = -\frac{\pi\, e^2 \widehat{K}^2 N_u^3 \lambda_u^2\, n_e}{4\varepsilon_0 m_e c^2 \gamma_r^3} \cdot \frac{d}{d\xi}\left(\frac{\sin^2\xi}{\xi^2}\right)\ .} \tag{3.26}$$

Here n_e is the number of electrons per unit volume, N_u the number of undulator periods and $\widehat{K}$ the modified undulator parameter defined in (3.31) below. The dimensionless variable $\xi = \pi N_u\,(\omega_1 - \omega)/\omega_1$ is a measure of the frequency deviation from the initial frequency ω_1. Equation (3.26) is the *Madey theorem* which states that the FEL gain curve is proportional to the negative derivative of the line-shape curve of undulator radiation [2]. We omit here the somewhat cumbersome proof of the Madey theorem because we will demonstrate in Chap. 5 and Appendix B that (3.26) can be obtained by taking the low-gain limit of the more general high-gain FEL theory.

In (3.26) the frequency ω is taken as the independent variable. In practice the equation is often applied in a different way. The initial frequency $\omega_1 \equiv \omega_\ell$ is fixed by an external seed laser or by the eigenmode of the optical resonator. The electron energy $W = \gamma m_e c^2$, however, may differ from the resonance energy $W_r = \gamma_r m_e c^2$ defined in (3.14). Then we can rewrite the quantity ξ in the form

$$\xi = \pi N_u\,\frac{\omega_1 - \omega}{\omega_1} \approx 2\pi N_u \frac{\gamma - \gamma_r}{\gamma_r} = 2\pi N_u \eta \tag{3.27}$$

[3] This is the traditional definition of the gain function in FEL theory. In the terminology of electronic amplifiers as well as of standard laser physics the gain should be defined as $gain = G + 1$ because unity gain means that the output signal is equal to the input signal.

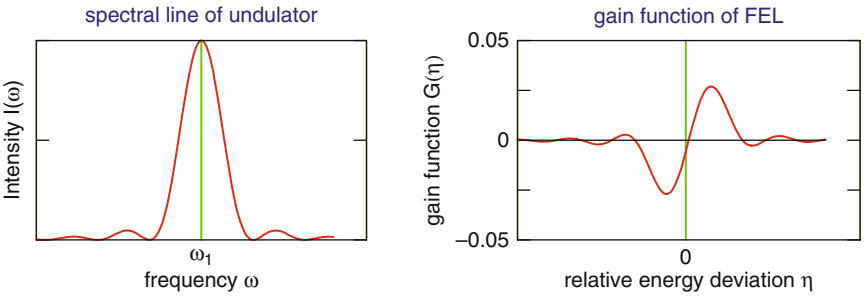

Fig. 3.8. *Left*: the line-shape curve $I(\omega)$ for the first harmonic $\omega_1 \equiv \omega_\ell$ of undulator radiation. *Right*: a typical gain function $G(\eta)$ of the low-gain FEL

which means that the equation (3.26) represents the FEL gain curve as a function of the relative energy deviation η. Electrons with positive η enhance the intensity of the light wave, while those with negative η reduce it. An illustration is given in Fig. 3.8.

3.6 Higher Harmonics and Modified Undulator Parameter

In the previous sections we have only considered the average longitudinal speed $\bar{v}_z$ of the particles in the computation of the energy exchange between electron and light wave. Now the longitudinal oscillation of $z(t)$ is explicitly taken into account, see (2.14)

$$z(t) = \bar{v}_z t - \frac{cK^2}{8\gamma^2\omega_u} \sin(2\omega_u t) \; .$$

We insert this into (3.5), choosing $\psi_0 = 0$ to simplify the notation:

$$\frac{dW}{dt} = -\frac{ecKE_0}{2\gamma} \left[\cos(k_\ell z(t) - \omega_\ell t + k_u \bar{v}_z t) + \cos(k_\ell z(t) - \omega_\ell t - k_u \bar{v}_z t)\right] \; .$$

An approximation has already been made here: $k_u z(t) \approx k_u \bar{v}_z t$, which is justified since $k_u \ll k_\ell$ and the amplitude of the oscillating term in $z(t)$ is small. At this place it is convenient to write the cosine functions as the real part of the complex exponential function of the form

$$\exp\left[ik_\ell(\bar{\beta} - 1)c\,t \pm ik_u \bar{v}_z\, t\right] \cdot \exp\left[-i\,\frac{K^2 k_\ell}{8\gamma^2 k_u}\,\sin(2\omega_u t)\right] \; .$$

The second exponential can be expanded into a Fourier-Bessel series

$$\exp(iY\sin\Phi) = \sum_{n=-\infty}^{\infty} J_n(Y)\exp(in\Phi) \qquad (3.28)$$

$$\text{with} \quad Y = -\frac{K^2 k_\ell}{8\gamma^2 k_u}\,, \quad \Phi = 2\omega_u t = 2\bar{v}_z k_u t\,.$$

The two cosine terms in (3.5) yield now

$$\left[\sum_{n=-\infty}^{\infty} J_n(Y)\exp(i[2n+1]k_u\bar{v}_z t) + \sum_{m=-\infty}^{\infty} J_m(Y)\exp(i[2m-1]k_u\bar{v}_z t)\right] \times \exp(ik_\ell[\bar{\beta}-1]ct)\,.$$

In the second sum we make the replacement $m \to (n+1) \;\Rightarrow\; (2m-1) \to (2n+1)$. Then both sums can be combined into one sum. Taking the real part, the energy change of the electron becomes

$$\frac{dW}{dt} = -\frac{ecKE_0}{2\gamma}\sum_n [J_n(Y) + J_{n+1}(Y)]\cos[(k_\ell + (2n+1)k_u)\bar{v}_z t - k_\ell c\,t]\,.$$

The condition for continuous energy transfer from the electron to the light wave is for the term with index n

$$(k_\ell + [2n+1]k_u)\bar{v}_z - k_\ell c = 0 \quad \Rightarrow \quad k_u = \frac{1}{2n+1}\cdot\frac{k_\ell}{2\gamma^2}\left(1+\frac{K^2}{2}\right)\,.$$

Since the light wavelength must be positive only the non-negative integers $n = 0, 1, 2, \ldots$ are allowed. Therefore the FEL wavelengths of the harmonics $m = 2n+1$ are in good approximation given by the expression

$$\boxed{\lambda_m = \frac{1}{m}\cdot\frac{\lambda_u}{2\gamma^2}\left(1+\frac{K^2}{2}\right) \quad m = 1,\,3,\,5,\ldots\,.} \qquad (3.29)$$

We see that only the odd higher harmonics are present. This equation is equally valid for undulator radiation in forward direction, see (2.29).

The energy transfer from electron to light wave is described by the equation

$$\frac{dW}{dt} = -\frac{ecKE_0}{2\gamma}\sum_{n=0}^{\infty}[J_n(Y_n) + J_{n+1}(Y_n)]\cos[(k_\ell + (2n+1)k_u)\bar{v}_z t - k_\ell c\,t]$$

$$\text{with} \quad Y_n = -\frac{(2n+1)K^2}{4+2K^2}\,. \qquad (3.30)$$

The sum extends over all integers $n \geq 0$.

The oscillatory term in the longitudinal velocity of the electrons leads not only to the generation of odd higher harmonics but has also an influence on the

fundamental harmonic $m = 1$. From (3.30) follows that the coupling between the charged particle and the electromagnetic wave is changed by the factor $[J_0(Y_0) + J_1(Y_0)]$ if the longitudinal oscillation is taken into consideration. We can absorb this correction factor into a modified undulator parameter[4]

$$\boxed{\widehat{K} = K \cdot \left[J_0\left(\frac{K^2}{4+2K^2}\right) - J_1\left(\frac{K^2}{4+2K^2}\right)\right] .} \tag{3.31}$$

Here we have used the facts that J_0 is an even function and J_1 is an odd function. For $K = 1$ the modified undulator parameter is $\widehat{K} = 0.91$.

References

1. Wille, K.: The Physics of Particle Accelerators. An Introduction. Oxford University Press, Oxford (2001) 33
2. Madey, J.M.J.: Relationship between mean radiated energy, mean squared radiated energy and spontaneous power spectrum in a power series expansion of the equation of motion in a free electron laser. Nuovo Cimento **50B**, 64 (1979) 33

[4] In the FEL literature the modified undulator parameter is often written in the form $K \cdot JJ$ or $K \cdot A_{JJ}$.

4

One-Dimensional Theory of the High-Gain FEL

4.1 General Principles of High-Power FELs

There are basically two ways to build a high-power FEL. At infrared and optical wavelengths an optical resonator is utilized and the FEL radiation pulse passes a short undulator magnet very many times in close spatial overlap with an electron bunch. In each passage the light intensity grows by just a few per cent but after very many round trips a large overall amplification is achieved. A striking example is the infrared FEL at the Thomas Jefferson Laboratory in Newport News, Virginia, USA where an average FEL beam power of more than 10 kW has been achieved at wavelengths of 6 resp. 1.6 μm [1]. It is even possible to reach laser saturation in an FEL equipped with an optical cavity, but one has to realize that near saturation the initially uniform particle distribution inside the bunch acquires the microbunch structure discussed below. When such a bunch traverses the bending magnets of a storage ring the microbunches will be washed out, so a recirculated bunch entering the undulator will essentially be a "fresh" bunch without a microstructure at the level of the optical wavelength.

In the vacuum ultraviolet and X-ray region an optical resonator cannot be realized due to the lack of mirrors, and thus the light amplification must be achieved in a single pass through a very long undulator magnet. Here the low-gain FEL theory is obviously inadequate and one has to admit that the amplitude of the light wave grows considerably during the motion through the undulator. This growth and the development of a microbunch structure at the level of the optical wavelength are the essential new features of the high-gain FEL theory. The regime of microbunching and saturation is inaccessible to the low-gain FEL theory.

P. Schmüser, et al.: *One-Dimensional Theory of the High-Gain FEL*, STMP **229**, 37–60 (2008)
DOI 10.1007/978-3-540-79572-8_4

4.2 Microbunching

The essential advantage of high-gain FEL radiation as compared to undulator radiation is its much higher intensity because a large number of electrons radiate coherently. The intensity of the radiation field grows quadratically with the number of coherently acting particles: $I_N = N^2 I_1$. If it were possible to concentrate all electrons of a bunch into a region far smaller than the light wavelength then these N particles would radiate like a "point macroparticle" with charge $Q = -Ne$. The problem is, however, that this concentration of some 10^9 electrons into a tiny volume is totally unfeasible, even the shortest conceivable particle bunches are much longer than the wavelength of an X-ray FEL. The way out of this dilemma is given by the process of *microbunching* which is based on the following principle: electrons losing energy to the light wave travel on a sinusoidal trajectory of larger amplitude than electrons gaining energy from the light wave (compare (2.14)). The result is a modulation of the longitudinal velocity which eventually leads to a concentration of the electrons in slices which are shorter than the optical wavelength λ_ℓ. These *microbunches* are close to the positions where maximum energy transfer to the light wave can happen according to Fig. 3.2 (we will prove this statement in Sect. 5.6.2). A numerical simulation of the microbunching process is shown in Fig. 4.1. The particles within a microbunch radiate like a single particle of high charge. The resulting strong radiation field enhances the microbunching even further and leads to an exponential growth of the radiation power. In Fig. 4.2 experimental data at a wavelength of 98 nm are shown. They agree very well with the theoretical prediction.

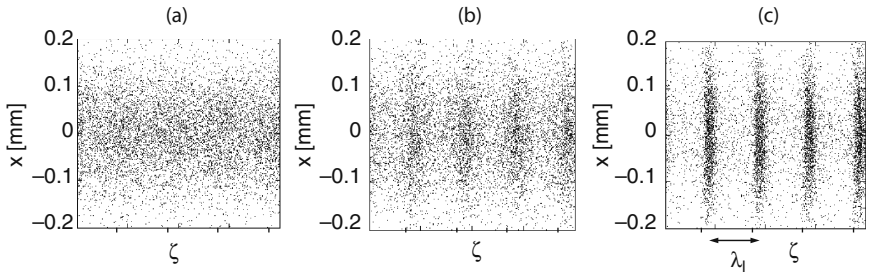

Fig. 4.1. Numerical simulation of microbunching. The particles are plotted as dots in a (x, ζ) plane where x is the horizontal displacement from the undulator axis and ζ the longitudinal internal bunch coordinate. (**a**) Initial uniform distribution, (**b**) beginning of microbunching, (**c**) fully developed microbunches with a periodicity of the light wavelength λ_ℓ . (Courtesy S. Reiche)

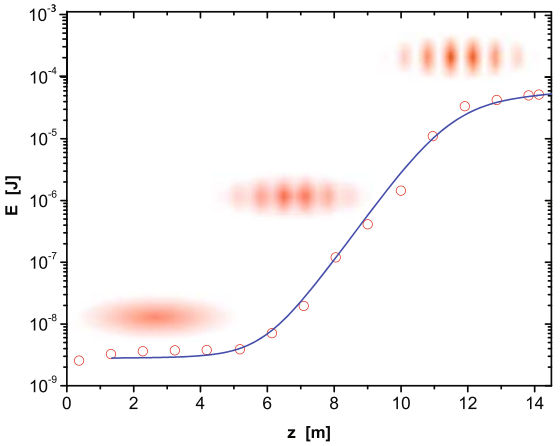

Fig. 4.2. The exponential growth of the FEL pulse energy as a function of the length z traveled in the undulator. The data (*open circles*) were obtained at the SASE FEL of the TESLA Test Facility [2], the electron energy was 245 MeV. The progressing microbunching is indicated schematically. Laser saturation sets in for $z \geq 12\,\mathrm{m}$. Here the microbunches are fully developed and no further increase in laser power can be expected

4.3 Basic Elements of the One-Dimensional FEL Theory

We restrict ourselves here to the one-dimensional FEL theory where a dependency of the bunch charge density and the electromagnetic fields on the transverse coordinates x, y is neglected. This is justified if the electron beam possesses a homogeneous charge density and if its radius r_b is sufficiently large. A lower limit for r_b will be derived in Sect. 6.2. The electron bunches are treated as being very long, the effects occurring at the head or tail of a bunch are ignored. Betatron oscillations and diffraction of the light wave are disregarded as well. The influence of these effects will be investigated in Chap. 6. The full three-dimensional treatment of the FEL is quite complicated and cannot be carried through by analytical methods.

In this chapter we use complex notation to simplify the mathematics and designate complex quantities with a tilde. For example, the electric field of the light wave inside the undulator is written in the form

$$\boxed{\tilde{E}_x(z,t) = \tilde{E}_x(z)\exp[i(k_\ell z - \omega_\ell t)]} \tag{4.1}$$

with a complex amplitude function $\tilde{E}_x(z)$. The actual field is obtained by taking the real part of this equation

$$E_x(z,t) = \Re\{\tilde{E}_x(z)\exp[i(k_\ell z - \omega_\ell t)]\}\,. \tag{4.2}$$

The analytic description of a high-gain FEL amounts to a self-consistent treatment of

- the coupled pendulum equations (3.16, 3.17), describing the phase-space motion of the particles under the influence of the electric field of the light wave,
- the inhomogeneous wave equation for the electric field of the light wave,
- the evolution of a microbunch structure coupled with longitudinal space charge forces.

The charge density is initially distributed uniformly along the bunch. During the passage through the undulator, the interaction with the periodic light wave will gradually produce a periodic density modulation. In analogy with the treatment of longitudinal instabilities in circular accelerators [3] we anticipate the microbunching effect by assuming that the initially uniform charge distribution acquires a small modulation which is periodic in the internal bunch coordinate ζ with the period given by the light wavelength λ_ℓ. From (3.12) follows then a periodicity in the ponderomotive phase variable ψ with the period 2π. Hence we express the electric charge density in the form

$$\tilde{\rho}(\psi, z) = \rho_0 + \tilde{\rho}_1(z) e^{i\psi} \quad \text{with} \quad \psi = \frac{\zeta}{\lambda_\ell} \cdot 2\pi - \frac{\pi}{2} \,. \tag{4.3}$$

The real charge density is of course given by

$$\rho(\psi, z) = \rho_0 + \Re\left(\tilde{\rho}_1(z) e^{i\psi}\right) \,.$$

The complex amplitude $\tilde{\rho}_1 = \tilde{\rho}_1(z)$ grows while the bunch moves through the undulator. From $j_z = v_z \rho$ follows that the current density acquires a similar modulation:

$$\boxed{\tilde{j}_z(\psi, z) = j_0 + \tilde{j}_1(z)\, e^{i\psi} = j_0 + \tilde{j}_1(z)\, \exp[i(k_\ell + k_u)z - i\omega_\ell t] \,.} \tag{4.4}$$

In the high-gain FEL theory there is a slight difference in the definition of the phase ψ as compared to the low-gain case, see equation (3.6). The incident light wave is taken as the reference, so we choose $\psi_0 = 0$, and the initial positions ζ_n of the electrons inside the bunch are specified by assigning a start phase ψ_n to each particle (see Sects. 4.6 and 5.6).

In this chapter we ignore the oscillatory part in the longitudinal velocity and put

$$\boxed{z(t) = \bar{v}_z t = \bar{\beta} c\, t \,, \quad \bar{\beta} = \left(1 - \frac{1}{2\gamma^2}\left(1 + \frac{K^2}{2}\right)\right) \,.} \tag{4.5}$$

Higher harmonics are therefore not considered in our treatment of the high-gain FEL, but the modified undulator parameter $\widehat{K}$ from (3.31) is used wherever appropriate, see Sect. 4.5. When the electron beam is on resonance

(we will see in Chap. 5 that a high-gain FEL is always operated close to $\gamma = \gamma_r$) we obtain to a good approximation

$$k_\ell + k_u = k_\ell/\bar{\beta}$$

where we have used the equations (2.13) and (3.14). Hence the current density can be written as

$$\tilde{j}_z(\psi, z) = j_0 + \tilde{j}_1(z)\, \exp\left(i\, k'[z - \bar{v}_z t]\right) \quad \text{with} \quad k' = (k_\ell/\bar{\beta})\ . \tag{4.6}$$

From this equation it is evident that the current modulation moves along the z direction with the same speed $\bar{v}_z = \bar{\beta}\, c$ as the electron bunch, except for a very slight slippage which is due to the phase evolution of $\tilde{j}_1(z)$. This will be studied in Sect. 5.6.2.

The periodic charge density modulation leads to repulsive space charge forces with the same periodicity. These longitudinal forces counteract the microbunching effect and tend to smear out any structure in the longitudinal charge distribution. Hence we have to consider these two opposing effects in describing the evolution of the microbunch structure.

The question arises whether it is really justified to assume the existence of an initial periodic density modulation. We can convince ourselves that this is indeed the case. The argument is as follows. The electrons in a bunch entering the undulator are in general randomly distributed along the bunch axis. In Appendix F we show that the random longitudinal distribution has a non-vanishing Fourier component at the optical wavelength λ_ℓ . This Fourier component will be strongly amplified in the FEL gain process. Of course one might as well make a Fourier expansion with another wavelength as the period. It will turn out, however, that the FEL gain is large only in a narrow interval around the optical wavelength (see Sect. 5.2), while the gain becomes negligible if λ is very different from λ_ℓ . Hence the Fourier components at other wavelengths will in general not be amplified but retain their small initial values.

Some care is needed in applying the Maxwell equations in the 1D FEL theory because these are intrinsically three-dimensional. For example, the first Maxwell equation in its integral form states that the flux of the electric field through the closed surface of a volume is given by the enclosed electric charge:

$$\oint \boldsymbol{E} \cdot \boldsymbol{dS} = Q/\varepsilon_0\ .$$

An interesting consequence is that the internal longitudinal Coulomb force in highly relativistic bunches can be neglected if the bunch length is much larger than its radius (an intuitive explanation is that all particles have velocities very close to c and do not "see" each other). Mathematically we demonstrate this as follows. In the rest frame of the electrons the bunch length appears stretched by the Lorentz factor $\bar{\gamma} \gg 1$ and is thus very much larger than the bunch radius which remains invariant: $L_b^* = \bar{\gamma}\, L_b \gg r_b^* = r_b$. Consequently,

the flux of the electric field through a cylindrical surface enclosing the bunch is mainly in radial direction, the flux through the end faces of the cylinder is almost negligible. Therefore the electric field in the rest frame of the bunch is radial, and it preserves this feature after Lorentz back-transformation into the laboratory system.

In the 1D FEL theory described in this chapter the bunches are assumed to be very long. Then the longitudinal electric field can be neglected as long as the charge distribution remains homogeneous. However, as soon as the periodic charge density modulation sets in at the very tiny scale of the light wavelength, which in the co-moving coordinate frame corresponds to a periodic modulation at the scale of $\lambda_u^* = \lambda_u/\bar{\gamma} \ll L_b^*$, a periodic longitudinal Coulomb field will arise.

4.4 Electromagnetic Fields

4.4.1 Radiation Field

The wave equation for the electric field $\boldsymbol{E}$ of the light wave reads

$$\left[\boldsymbol{\nabla}^2 - \frac{1}{c^2}\frac{\partial^2}{\partial t^2}\right]\boldsymbol{E} = \mu_0 \frac{\partial \boldsymbol{j}}{\partial t} + \frac{1}{\varepsilon_0}\boldsymbol{\nabla}\rho \tag{4.7}$$

with the current density $\boldsymbol{j}$ and the electric charge density ρ. In the one-dimensional approximation the equation for the x component becomes in complex notation

$$\left[\frac{\partial^2}{\partial z^2} - \frac{1}{c^2}\frac{\partial^2}{\partial t^2}\right]\tilde{E}_x(z,t) = \mu_0 \frac{\partial \tilde{j}_x}{\partial t} \tag{4.8}$$

where $\tilde{j}_x$ is the x component of the current density resulting from the sinusoidal motion of the electron bunch in the undulator. The derivative $\partial\rho/\partial x$ is not present in the 1D theory[1].

We assume that the lasing process in the undulator is initiated (*seeded*) by an incident electromagnetic wave $E_x(z,t)$ with horizontal polarization. In the low-gain FEL, an approximate solution of the wave equation is

$$E_x(z,t) = E_0 \cos(k_\ell z - \omega_\ell t + \psi_0)$$

with a constant amplitude E_0 of the light wave (in reality the amplitude grows by a few per cent during one passage of a short undulator). For the high-gain FEL, however, we have to admit that the amplitude of the light grows considerably along the undulator. Hence we assume a solution of the form

[1] The derivative $\partial\rho/\partial x$ plays no role in the 3D theory either, see Appendix E and [4], if one considers only the first harmonic. However, this term becomes important for higher harmonics.

$$\tilde{E}_x(z,t) = \tilde{E}_x(z)\exp[i(k_\ell z - \omega_\ell t)] \tag{4.9}$$

with a complex amplitude $\tilde{E}_x(z)$ which will be a function of the path length z in the undulator. The initial phase ψ_0 is put to zero, see the previous section. The phase of $\tilde{E}_x(z)$ may vary with z which means that the phase velocity of the FEL light wave may differ slightly from the phase velocity c of a plane electromagnetic wave. This effect will be studied in Chap. 6. Inserting (4.9) into the wave equation yields

$$\left[2\,i\,k_\ell \tilde{E}'_x(z) + \tilde{E}''_x(z)\right]\exp[i(k_\ell z - \omega_\ell t)] = \mu_0 \frac{\partial \tilde{j}_x}{\partial t}\ . \tag{4.10}$$

To proceed further we make the *slowly varying amplitude* (SVA) approximation in order to be able to drop the second derivative $\tilde{E}''_x$. The amplitude $\tilde{E}_x(z)$ is assumed to be a smooth function of z which varies slowly in the sense that the change within one undulator period λ_u is small. Then the change within one light wavelength is even much smaller. This implies that the first derivative of the field is also small

$$\left|\tilde{E}'_x(z)\right| \lambda_\ell \ll \left|\tilde{E}_x(z)\right| \quad \Rightarrow \quad \left|\tilde{E}'_x(z)\right| \ll k_\ell \left|\tilde{E}_x(z)\right|\ . \tag{4.11}$$

Nevertheless, the first derivative, characterizing the slope of the function $\tilde{E}_x(z)$, must of course be retained in order to describe the growth of the FEL power as a function of undulator length. The change of the slope, however, will be extremely small in one undulator period λ_u and practically negligible in one optical wavelength

$$\left|\tilde{E}''_x(z)\right| \lambda_\ell \ll \left|\tilde{E}'_x(z)\right| \quad \Rightarrow \quad \left|\tilde{E}''_x(z)\right| \ll k_\ell \left|\tilde{E}'_x(z)\right|\ . \tag{4.12}$$

Hence one can safely omit the second derivative of the field in (4.10). The differential equation of the slowly varying amplitude reads in the SVA approximation

$$\frac{d\tilde{E}_x}{dz} = -\frac{i\mu_0}{2k_\ell}\cdot\frac{\partial \tilde{j}_x}{\partial t}\cdot\exp[-i(k_\ell z - \omega_\ell t)]\ . \tag{4.13}$$

Now a connection is made between the longitudinal and transverse components of the current density. This relation is given by the motion of the particles in the undulator. From

$$\tilde{j}_x = \tilde{\rho} v_x\ , \quad \tilde{j}_z = \tilde{\rho} v_z$$

follows

$$\tilde{j}_x = \tilde{j}_z\, v_x/v_z\ .$$

The x component of the electron velocity in a planar undulator is taken from (2.9). We get

$$\tilde{j}_x = \tilde{j}_z \frac{v_x}{v_z} \approx \tilde{j}_z \frac{v_x}{c} = \tilde{j}_z\,\frac{K}{\gamma}\cos(k_u z)\ . \tag{4.14}$$

This relation between the currents in x and z direction is put into (4.13):

$$\frac{d\tilde{E}_x}{dz} = -\frac{i\mu_0 K}{2k_\ell \gamma} \cdot \frac{\partial \tilde{j}_z}{\partial t} \exp[-i(k_\ell z - \omega_\ell t)] \cos(k_u z) \; .$$

The current density

$$\tilde{j}_z(\psi, z) = j_0 + \tilde{j}_1(z) \exp(i\psi) = j_0 + \tilde{j}_1(z) \exp[i(k_\ell z - \omega_\ell t) + ik_u z]$$

has to be partially differentiated with respect to time

$$\left[\frac{\partial \tilde{j}_z}{\partial t}\right]_{z=const} = -i\omega_\ell \, \tilde{j}_1 \exp[i(k_\ell z - \omega_\ell t) + ik_u z] \; .$$

The derivative of the transverse field becomes

$$\begin{aligned} \frac{d\tilde{E}_x}{dz} &= -\frac{\mu_0 cK}{2\gamma} \, \tilde{j}_1 \exp[i(k_\ell z - \omega_\ell t) + ik_u z] \exp[-i(k_\ell z - \omega_\ell t)] \, \frac{e^{ik_u z} + e^{-ik_u z}}{2} \\ &= -\frac{\mu_0 cK}{4\gamma} \, \tilde{j}_1 \, \{1 + \exp(i2k_u z)\} \, . \end{aligned}$$

The phase factor $\exp[i2k_u z]$ carries out two oscillations per undulator period λ_u and averages to zero (see also Fig. 3.3). So within the SVA approximation we can express the derivative of the transverse field in terms of the modulation amplitude of the current density by

$$\frac{d\tilde{E}_x}{dz} = -\frac{\mu_0 cK}{4\gamma_r} \cdot \tilde{j}_1 \; . \tag{4.15}$$

In this equation we have replaced γ by γ_r because a high-gain FEL is always operated close to resonance (see Sect. 5.1).

4.4.2 Space Charge Field

The longitudinal space charge field created by the modulated charge density (4.3) is computed using the Maxwell equation $\boldsymbol{\nabla} \cdot \boldsymbol{E} = \rho/\varepsilon_0$. According to the discussion in Sect. 4.3 the homogeneous part ρ_0 of the charge density can be disregarded. The periodic part of the charge density generates a periodic longitudinal field according to the equation

$$\frac{\partial \tilde{E}_z(z,t)}{\partial z} = \frac{\tilde{\rho}_1(z)}{\varepsilon_0} \exp[i((k_\ell + k_u)z - \omega_\ell t)] \; . \tag{4.16}$$

Writing

$$\tilde{E}_z(z,t) = \tilde{E}_z(z) \exp[i((k_\ell + k_u)z - \omega_\ell t)]$$

the derivative of the field with respect to z is in the SVA approximation

$$\frac{\partial \tilde{E}_z(z,t)}{\partial z} \approx i\,(k_\ell + k_u)\tilde{E}_z(z)\exp[i((k_\ell + k_u)z - \omega_\ell t)]$$

since for a slowly varying amplitude

$$\left|\frac{d\tilde{E}_z(z)}{dz}\right| \ll (k_\ell + k_u)\left|\tilde{E}_z(z)\right| \ .$$

Comparing with (4.16) and using $k_u \ll k_\ell$ we obtain for the complex amplitude of the longitudinal electric field

$$\boxed{\tilde{E}_z(z) \approx -\frac{i}{\varepsilon_0 k_\ell}\,\tilde{\rho}_1(z) \approx -\frac{i\mu_0 c^2}{\omega_\ell}\cdot\tilde{j}_1(z)\ .} \tag{4.17}$$

Combining (4.17) and (4.15) allows us to relate the longitudinal field to the derivative of the transverse field

$$\tilde{E}_z(z) = i\,\frac{4\gamma_r c}{\omega_\ell K}\cdot\frac{d\tilde{E}_x}{dz}\ . \tag{4.18}$$

4.5 Corrections Due to the Longitudinal Oscillation

In the previous section we have disregarded the longitudinal oscillation of the electrons during their motion through the undulator. We know from Sect. 3.6 that this oscillation leads to a modification of the energy transfer from the electron to the light wave, see (3.30). The modified undulator parameter defined in (3.31)

$$\widehat{K} = K\cdot\left[J_0\left(\frac{K^2}{4+2K^2}\right) - J_1\left(\frac{K^2}{4+2K^2}\right)\right]$$

enters the energy-transfer equation (3.17) which has to read

$$\boxed{\frac{d\eta}{dt} = -\frac{eE_0\widehat{K}}{2m_e c\gamma_r^2}\cos\psi\ .} \tag{4.19}$$

Moreover, $\widehat{K}$ appears in the longitudinal component of electron-beam current density. Therefore in the equations (4.15) and (4.18) the replacement $K \to \widehat{K}$ must be made:

$$\boxed{\frac{d\tilde{E}_x}{dz} = -\frac{\mu_0 c\widehat{K}}{4\gamma_r}\cdot\tilde{j}_1\ .} \tag{4.20}$$

$$\boxed{\tilde{E}_z(z) = i\,\frac{4\gamma_r c}{\omega_\ell\widehat{K}}\cdot\frac{d\tilde{E}_x}{dz}\ .} \tag{4.21}$$

On the other hand, the FEL wavelength equations (3.9) and (3.29) remain unchanged, so they contain the unmodified undulator parameter K.

4.6 The Coupled First-Order Equations

In Sect. 3.4 we have studied how an ensemble of electrons moves in the (ψ, η) phase space due to the interaction with the field of the light wave. The time derivative of an electron's ponderomotive phase (or, alternatively, of its position ζ inside the bunch) is given by the first pendulum equation (3.16). Replacing the time t by the longitudinal coordinate z according to $z(t) = \bar{\beta} c\, t$, we get

$$\frac{d\psi}{dz} = 2k_u \eta \qquad (\bar{\beta} \approx 1) \; . \tag{4.22}$$

The change in the relative energy deviation η is described by the second pendulum equation (4.19)

$$\frac{d\eta}{dz} = -\frac{eE_0 \widehat{K}}{2m_e c^2 \gamma_r^2} \cos\psi \; .$$

In case of the low-gain FEL the electric field amplitude E_0 of the light wave is treated as a constant but now we have to take into account the z dependence of the field. In our present complex notation we rewrite the second pendulum equation as

$$\left[\frac{d\eta}{dz}\right]_{\ell} = -\frac{e\widehat{K}}{2m_e c^2 \gamma_r^2} \, \Re(\tilde{E}_x e^{i\psi}) \; .$$

At this place it is mandatory to take the real part because the relative energy deviation is always a real quantity. The index "ℓ" indicates the coupling to the light wave. One has to add the energy change due to the interaction between the electron and the space charge (sc) field. The rate of change of the electron energy due to the longitudinal force is

$$\frac{dW}{dt} = \bar{v}_z F_z = -e\, \bar{v}_z \Re(\tilde{E}_z e^{i\psi}) \; .$$

Using $z = \bar{v}_z t$ we find then

$$\left[\frac{d\eta}{dz}\right]_{sc} = -\frac{e}{m_e c^2 \gamma_r} \, \Re(\tilde{E}_z e^{i\psi}) \; .$$

Combining the two effects yields

$$\frac{d\eta}{dz} = -\frac{e}{m_e c^2 \gamma_r} \Re\left\{ \left(\frac{\widehat{K}\tilde{E}_x}{2\gamma_r} + \tilde{E}_z \right) e^{i\psi} \right\} \; . \tag{4.23}$$

Our goal is now to study the phase space motion of the electrons in a similar manner as in the low-gain case, but to take explicitly into account the growth of the field amplitude $\tilde{E}_x(z)$ of the light wave and the evolution of the space charge field $\tilde{E}_z(z)$. Both are related to the modulation amplitude $\tilde{j}_1(z)$ of the electron beam current density by the equations (4.20) and (4.17):

$$\frac{d\tilde{E}_x}{dz} = -\frac{\mu_0 c\widehat{K}}{4\gamma_r} \cdot \tilde{j}_1(z)\,, \quad \tilde{E}_z(z) = -\frac{i\mu_0 c^2}{\omega_\ell} \cdot \tilde{j}_1(z)\,. \tag{4.24}$$

The obvious task is to compute $\tilde{j}_1$ for a given arrangement of electrons in phase space. To this end we subdivide the electron bunch into longitudinal slices of length λ_ℓ. Since the bunch is much longer than the light wavelength, there will be very many of these slices (in fact infinitely many in the periodic 1D theory where one neglects the beginning and the end of the bunch). Each slice has an area $A_b = \pi r_b^2$ where r_b is the radius of the bunch. Written in terms of the ponderomotive phase these are slices of length 2π. In the slice $0 \le \psi < 2\pi$ we have N electrons with the phases ψ_n $(n = 1...N)$. Treating the electrons as point-like particles the longitudinal distribution can be expressed in the form

$$S(\psi) = \sum_{n=1}^{N} \delta(\psi - \psi_n) \qquad \psi,\, \psi_n \in [0, 2\pi]\,. \tag{4.25}$$

In this chapter and in Chap. 5 we restrict ourselves to the special cases that the initial state is characterized either by a perfectly uniform longitudinal distribution of the electrons in the bunch or by a density distribution that is periodic in ψ with the period 2π. To this end we continue the function (4.25) periodically so that is is defined for all $|\psi| < \infty$. We call this the periodic model. The more realistic case of a random longitudinal particle distribution will be investigated in the chapter on the SASE FEL and in Appendix F. The uniformity (resp. periodicity) implies that the function $S(\psi)$ can be expanded in a real Fourier series

$$\begin{aligned} S(\psi) &= \frac{a_0}{2} + \sum_{k=1}^{\infty} [a_k \cos(k\,\psi) + b_k \sin(k\,\psi)] \qquad (4.26)\\ a_k &= \frac{1}{\pi}\int_0^{2\pi} S(\psi)\cos(k\,\psi)d\psi \quad k = 0, 1, 2\ldots\\ b_k &= \frac{1}{\pi}\int_0^{2\pi} S(\psi)\sin(k\,\psi)d\psi \quad k = 1, 2\ldots \end{aligned}$$

Defining the complex Fourier coefficients $c_k = a_k - ib_k$ one can rewrite $S(\psi)$ in the form

$$S(\psi) = \frac{c_0}{2} + \Re\left\{\sum_{k=1}^{\infty} c_k \exp(i\,k\,\psi)\right\}\,. \tag{4.27}$$

The complex Fourier coefficients are given by

$$c_k = \frac{1}{\pi}\int_0^{2\pi} S(\psi)\exp(-i\,k\,\psi)d\psi\,. \tag{4.28}$$

In order to find the relation between the Fourier coefficients and the current density we look first at the dc part of the current density which is proportional

to the zeroth Fourier coefficient $c_0/2 \equiv a_0/2 = N/(2\pi)$. From $j_0 = -e\,c\,n_e$ and $n_e = N/(A_b\lambda_\ell)$ follows then

$$j_0 = -e\,c\,\frac{2\pi}{A_b\lambda_\ell}\cdot\frac{c_0}{2}\,.$$

Remember that n_e is the number of electrons per unit volume, N the number of electrons in a slice of area A_b and length λ_ℓ, and j_0 the dc current density in [A/m^2].

The modulation current $\tilde{j}_1$ is proportional to the coefficient of the first harmonic $k = 1$

$$c_1 = \frac{1}{\pi}\int_0^{2\pi}\left(\sum_{n=1}^{N}\delta(\psi-\psi_n)\right)\exp(-i\,\psi)d\psi = \frac{1}{\pi}\sum_{n=1}^{N}\exp(-i\psi_n)\,.$$

By analogy with j_0 we obtain

$$\tilde{j}_1 = -e\,c\,\frac{2\pi}{A_b\lambda_\ell}\cdot c_1 = -e\,c\,\frac{2\pi}{A_b\lambda_\ell}\cdot\frac{1}{\pi}\sum_{n=1}^{N}\exp(-i\psi_n) = j_0\frac{2}{N}\sum_{n=1}^{N}\exp(-i\psi_n)\,. \tag{4.29}$$

Now we have collected all equations that are needed to compute numerically the time evolution of our system. (We remind the reader that our time variable is here the path length z in the undulator magnet which is related to the normal time t by $z = \bar{v}_z t$).

The complete set of coupled first-order equations in the periodic model is

$$\frac{d\psi_n}{dz} = 2k_u\eta_n\,, \quad n = 1...N \tag{4.30a}$$

$$\frac{d\eta_n}{dz} = -\frac{e}{m_e c^2\gamma_r}\Re\left\{\left(\frac{\widehat{K}\tilde{E}_x}{2\gamma_r} - \frac{i\mu_0 c^2}{\omega_\ell}\cdot\tilde{j}_1\right)\exp(i\psi_n)\right\} \tag{4.30b}$$

$$\tilde{j}_1 = j_0\,\frac{2}{N}\sum_{n=1}^{N}\exp(-i\psi_n) \tag{4.30c}$$

$$\frac{d\tilde{E}_x}{dz} = -\frac{\mu_0 c\widehat{K}}{4\gamma_r}\cdot\tilde{j}_1\,. \tag{4.30d}$$

The equations (4.30) describe the time evolution of the ponderomotive phase ψ_n and the relative energy deviation $\eta_n = (\gamma_n - \gamma_r)/\gamma_r$ of the nth electron ($n = 1...N$), as well as the time evolution of the modulated current density $\tilde{j}_1$ and the amplitude of the light wave $\tilde{E}_x$. Since N is a large number we are confronted with a true many-body problem for which no analytical solution

exists. The set of $2N + 2$ coupled differential and algebraic equations can be solved by numerical integration as will be discussed in Sect. 5.4.

We point out that the coupled equations in the form (4.30) are restricted to uniform or periodic initial particle distributions. They are well suited for a simulation of the saturation process in an FEL amplifier that is seeded by monochromatic light, but a SASE FEL cannot be handled because here the initial particle distribution is random. Now we describe briefly how the periodic model can be generalized. The main changes are:

(a) The initial phase space distribution must be specified for the whole bunch and not just for one period of length λ_ℓ.
(b) The electron beam current is a function of z, like $\tilde{j}_1(z)$, but depends in addition on the internal bunch coordinate $\zeta = z - \bar{\beta}\, c\, t = z - \bar{v}_z t$. The current density is therefore written as

$$\tilde{j}_z = j_0(\zeta) + \widehat{j}_1(z, \zeta) \exp(i\, \psi) \; .$$

(c) To describe variations of the electric field inside the FEL pulse we introduce an internal longitudinal coordinate

$$u = z - c\, t = \left(1 - \frac{c}{\bar{v}_z}\right) z + \frac{c}{\bar{v}_z}\, \zeta$$

and make the ansatz

$$\tilde{E}_x(z, t) = \widehat{E}(z, u) \exp[i(k_\ell z - \omega_\ell t)]$$

in which the complex amplitude function $\widehat{E}(z, u)$ depends on the position z in the undulator, like $\tilde{E}_x(z)$, but also on the internal FEL pulse coordinate $u = z - ct$.

The detailed treatment is found in Appendix C where also a non-periodic form (C.7) of the coupled equations is presented.

4.7 The Third-Order Equation of the High-Gain FEL

The main physics of the high-gain FEL is contained in the coupled first-order equations presented in the previous section, but unfortunately these equations possess no analytical solution. If we make the additional assumption that the periodic density modulation remains small it is possible to eliminate the quantities ψ_n and η_n characterizing the particle dynamics in the bunch and derive a differential equation containing only the electric field amplitude $\tilde{E}_x(z)$ of the light wave. This equation has the great advantage that it can be solved analytically.

4.7.1 Particle Distribution Function

In a one-dimensional description of particle motion in an accelerator we have to specify two quantities for each particle in a bunch: (1) its internal position inside the bunch, we choose the distance ζ from a reference position $\zeta_r = 0$, and (2) its relative deviation η from the reference energy. These two quantities, which are conjugate variables in a Hamiltonian description of the FEL, define the so-called *longitudinal phase space*. The ponderomotive phase is related to the longitudinal coordinate of an electron inside the bunch, compare (3.12):

$$\psi = \frac{2\pi\zeta}{\lambda_\ell} - \frac{\pi}{2} \,. \tag{4.31}$$

Furthermore, it is customary in accelerator physics to replace the independent variable time t by the path length z along the nominal beam orbit. The equations of the one-dimensional high-gain FEL can therefore be written in terms of the variables (ψ, η, z) where z plays the role of a quasi time.

The ensemble of particles can be described by a distribution function $F(\psi, \eta, z)$ in the (ψ, η) phase space. The number of electrons in a phase space volume element $(d\psi\, d\eta)$ is

$$dn_e = n_e\, F(\psi, \eta, z) d\psi\, d\eta \tag{4.32}$$

where n_e is the particle density in the bunch (the number of particles per unit volume). The distribution function is normalized to unity:

$$\frac{1}{2\pi} \int_0^{2\pi} \left(\int F(\psi, \eta, z)\, d\eta \right) d\psi = 1 \,. \tag{4.33}$$

A microscopic expression for the distribution function is presented in [4].

From our assumption of a periodically modulated charge distribution follows that there will be a periodic term in the distribution function, too. Hence we write in complex notation

$$F(\psi, \eta, z) = \Re\left\{ \tilde{F}(\psi, \eta, z) \right\} = F_0(\eta) + \Re\left\{ \tilde{F}_1(\eta, z) \cdot e^{i\psi} \right\} \,. \tag{4.34}$$

The modulation amplitude must remain small to justify the approximations which will be made in the derivation of the third-order equation, $\left|\tilde{F}_1(\eta, z)\right| \ll |F_0(\eta)|$. An example for a periodically modulated particle distribution function is presented in Fig. 4.3.

For the unperturbed term F_0 we assume a narrow distribution in the relative energy deviation, for example a Gaussian

$$F_0(\eta) = \frac{1}{\sqrt{2\pi}\,\sigma_\eta} \exp\left(-\frac{(\eta - \eta_0)^2}{2\sigma_\eta^2} \right) \qquad \text{with} \quad \eta_0 = \frac{W_0 - W_r}{W_r} \,. \tag{4.35}$$

Note that in general the mean value W_0 of the electron energy may differ slightly from the resonance energy W_r which is defined by the wavelength

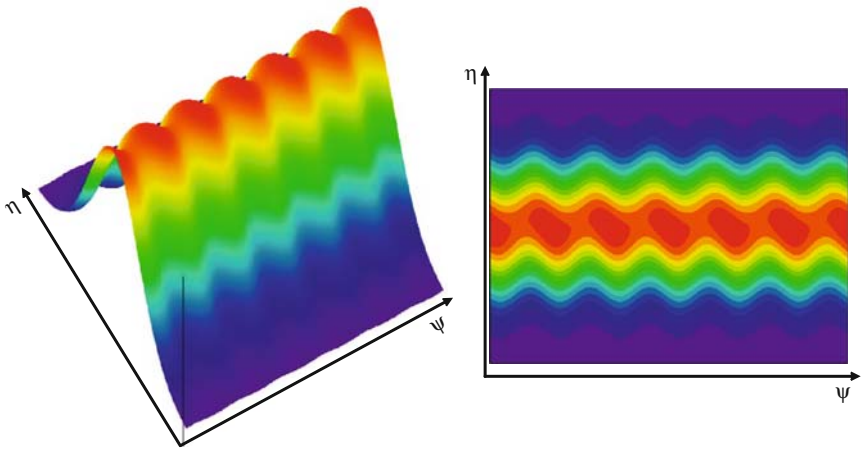

Fig. 4.3. Illustration of a periodically modulated charge density. The particle distribution function is plotted as a function of the ponderomotive phase ψ and the relative energy deviation from resonance $\eta = (W - W_r)/W_r$. Note that in the beginning the periodic modulation is mainly an energy modulation which results from the energy exchange between the electrons and the periodic light wave. The relation between the particle distribution function and the charge density can be found in (4.37)

λ_ℓ of the incident light wave according to (3.14). The variance σ_η is usually small, $\sigma_\eta \leq 10^{-4} \ldots 10^{-3}$ for the electron beam in a linac-driven FEL. Hence the relative energy deviation is restricted to a narrow range $|\eta| < \delta$, where $0 < \delta \ll 1$ is chosen such that $F_0(\eta)$ vanishes identically for all $|\eta| \geq \delta$.
The integral over the unmodulated part of the distribution function yields 1

$$\int_{-\delta}^{\delta} F_0(\eta) d\eta = 1 \,. \tag{4.36}$$

The relation between distribution function and charge resp. current density is

$$\tilde{\rho}_1(z) = \rho_0 \int_{-\delta}^{\delta} \tilde{F}_1(\eta, z) d\eta \,, \quad \tilde{j}_1(z) = j_0 \int_{-\delta}^{\delta} \tilde{F}_1(\eta, z) d\eta \,. \tag{4.37}$$

4.7.2 Vlasov Equation

According to the Liouville Theorem of Hamiltionian mechanics, the phase space volume occupied by an ensemble of particles is conserved along the particle trajectory. This leads to a generalized continuity equation which is called the *Vlasov equation* (see for example [3])

$$\frac{dF}{dz} = \frac{\partial F}{\partial z} + \frac{\partial F}{\partial \psi}\frac{d\psi}{dz} + \frac{\partial F}{\partial \eta}\frac{d\eta}{dz} = 0 \,. \tag{4.38}$$

Note that ψ, η and z are real variables. Inserting (4.34) one obtains

$$\frac{dF}{dz} = \Re\left\{\left(\frac{\partial \tilde{F}_1}{\partial z} + i\,\tilde{F}_1 \frac{d\psi}{dz}\right) e^{i\psi}\right\} + \left(\frac{dF_0}{d\eta} + \Re\left\{\frac{\partial \tilde{F}_1}{\partial \eta}\, e^{i\psi}\right\}\right) \frac{d\eta}{dz} = 0\,.$$

The derivative of $\tilde{F}_1$ with respect to η will be neglected here since we assume a small modulation amplitude, $\left|\tilde{F}_1(z,\eta)\right| \ll |F_0(\eta)|$. Using the pendulum equations (4.22) and (4.23) we obtain

$$\Re\left\{\left(\frac{\partial \tilde{F}_1}{\partial z} + i\,2k_u\eta\tilde{F}_1 - \frac{e}{m_e c^2 \gamma_r}\frac{dF_0}{d\eta}\left[\frac{\widehat{K}}{2\gamma_r}\tilde{E}_x + \tilde{E}_z\right]\right) e^{i\psi}\right\} = 0\,. \tag{4.39}$$

This equation is certainly fulfilled if we can find a function $\tilde{F}_1$ obeying the more demanding equation

$$\frac{\partial \tilde{F}_1}{\partial z} + i\,2k_u\eta\tilde{F}_1 - \frac{e}{m_e c^2 \gamma_r}\frac{dF_0}{d\eta}\left[\frac{\widehat{K}}{2\gamma_r}\tilde{E}_x + \tilde{E}_z\right] = 0\,.$$

To this end we replace the longitudinal space charge field by the derivative of the transverse field according to (4.21) and construct a solution of the following equation

$$\frac{\partial \tilde{F}_1}{\partial z} + i\,2k_u\eta\tilde{F}_1 = \frac{e}{m_e c^2 \gamma_r}\,[\ldots]\,\frac{dF_0}{d\eta} \tag{4.40}$$

with

$$[\ldots] = \left[\frac{\widehat{K}}{2\gamma_r}\tilde{E}_x + \tilde{E}_z\right] = \left[\frac{\widehat{K}}{2\gamma_r}\tilde{E}_x + i\frac{4\gamma_r c}{\omega_\ell \widehat{K}}\,\frac{d\tilde{E}_x}{dz}\right]\,. \tag{4.41}$$

The differential equation (4.40) is of the type

$$y' + i\alpha y(z) = f(z)$$

with the general solution

$$y(z) = \int_0^z f(s)\exp(-i\alpha\cdot(z-s))ds + c_1\exp(-i\alpha\, z)$$

with an arbitrary constant c_1. Since the beam is unmodulated at the entrance to the undulator we request $\tilde{F}_1(0) = 0$ and thus $c_1 = 0$, so we obtain

$$\tilde{F}_1(\eta, z) = \frac{e}{m_e c^2 \gamma_r}\int_0^z [\ldots]\,\frac{dF_0}{d\eta}\exp\left[-i\,2k_u\eta\cdot(z-s)\right]ds\,. \tag{4.42}$$

4.7.3 Integro-Differential Equation

The time evolution of the radiation field amplitude is described by the differential equation (4.20)

$$\frac{d\tilde{E}_x}{dz} = -\frac{\mu_0 c\widehat{K}}{4\gamma_r}\tilde{j}_1 = \frac{\mu_0 c^2 \widehat{K} n_e e}{4\gamma_r}\int_{-\delta}^{\delta} \tilde{F}_1(\eta, z)d\eta \,. \tag{4.43}$$

Inserting $\tilde{F}_1(\eta, z)$ from (4.42) we get

$$\frac{d\tilde{E}_x}{dz} = \frac{\mu_0 \widehat{K} n_e e^2}{4m_e\gamma_r^2}\int_0^z \left\{ [\ldots] \int_{-\delta}^{\delta} \frac{dF_0}{d\eta} \exp(-i2k_u\eta \cdot (z-s))d\eta \right\} ds$$

Integrating by parts over η, using $F_0(\pm\delta) = 0$, yields an integro-differential equation

$$\boxed{\frac{d\tilde{E}_x}{dz} = i\,k_u \frac{\mu_0 \widehat{K} n_e e^2}{2m_e\gamma_r^2}\int_0^z \left[\frac{\widehat{K}}{2\gamma_r}\tilde{E}_x + i\frac{4\gamma_r c}{\omega_\ell \widehat{K}}\frac{d\tilde{E}_x}{dz}\right] h(z-s)ds} \tag{4.44}$$

$$\text{with} \quad h(z-s) = \int_{-\delta}^{\delta} (z-s)\, \exp\left[-i\,2k_u\eta \cdot (z-s)\right] F_0(\eta)d\eta \,.$$

The two-dimensional problem in the variables (η, z) has now been reduced to a one-dimensional problem in z.

4.7.4 Third-Order Equation

The integro-differential equation (4.44) can be simplified if we assume a monoenergetic beam of energy $W = W_0$. Then

$$h(z-s) = (z-s)\, \exp\left[-i\,2k_u\eta_0\,(z-s)\right] \quad \text{with} \quad \eta_0 = (W_0 - W_r)/W_r$$

and (4.44) becomes

$$\frac{d\tilde{E}_x}{dz} = i\,k_u \frac{\mu_0 \widehat{K} n_e e^2}{2m_e\gamma_r^2}\int_0^z [\ldots]\,(z-s)\, \exp\left[-i\,2k_u\eta_0\,(z-s)\right] ds \,. \tag{4.45}$$

In the following we write η instead of η_0, dropping the subscript. Equation (4.45) is of the type

$$y(z) = \int_0^z f(s)(z-s)\exp[-i\alpha\,(z-s)]ds \,.$$

It is easy to verify that the function $y(z)$ fulfills the differential equation

$$y'' + 2i\alpha y' - \alpha^2 y = f \,.$$

Applied to (4.45) this yields

$$\tilde{E}_x''' + 4ik_u\eta\tilde{E}_x'' - 4k_u^2\eta^2\tilde{E}_x' = i\,k_u\frac{\mu_0\widehat{K}n_e e^2}{2m_e\gamma_r^2}\left[\frac{\widehat{K}}{2\gamma_r}\tilde{E}_x + i\frac{4\gamma_r c}{\omega_\ell\widehat{K}}\,\tilde{E}_x'\right] .$$

Ordering terms we obtain finally the well-known third-order differential equation of the high-gain FEL

$$\frac{d^3\tilde{E}_x(z)}{dz^3} + 4ik_u\eta\frac{d^2\tilde{E}_x(z)}{dz^2} + \left(k_p^2 - 4k_u^2\eta^2\right)\frac{d\tilde{E}_x(z)}{dz} - i\Gamma^3\tilde{E}_x(z) = 0 . \quad (4.46)$$

Two new coefficients appear in this equation which depend on the beam properties and the layout of the undulator and which have both the dimension of an inverse length. The first one is called the *gain parameter* Γ, the second one is often called the *space charge parameter* k_p

$$\boxed{\Gamma = \left[\frac{\mu_0\widehat{K}^2e^2k_un_e}{4\gamma_r^3m_e}\right]^{1/3} , \quad k_p = \sqrt{\frac{2k_u\mu_0n_ee^2c}{\gamma_rm_e\omega_\ell}} = \sqrt{\frac{2\lambda_\ell}{\lambda_u}}\cdot\frac{\omega_p^*}{c} .} \quad (4.47)$$

The space charge parameter is related to the plasma frequency ω_p^* in the relativistic electron bunch

$$\omega_p^* = \sqrt{\frac{n_e^*e^2}{\varepsilon_0m_e}} = \sqrt{\frac{n_ee^2}{\gamma_r\varepsilon_0m_e}} . \quad (4.48)$$

(When computing the plasma frequency in the relativistic bunch one has to take into account that the particle density in the rest frame of the bunch is $n_e^* = n_e/\gamma_r$ due to Lorentz expansion of the bunch length). We will see in Chap. 6 that space charge forces can be neglected if k_p is small in comparison with the gain parameter Γ.

It is instructive to rewrite the third-order equation in the form

$$\frac{\tilde{E}_x'''}{\Gamma^3} + 2i\,\frac{2k_u}{\Gamma}\,\eta\,\frac{\tilde{E}_x''}{\Gamma^2} + \left(\frac{k_p^2}{\Gamma^2} - \left(\frac{2k_u}{\Gamma}\,\eta\right)^2\right)\frac{\tilde{E}_x'}{\Gamma} - i\,\tilde{E}_x = 0 .$$

The coefficient of the relative energy deviation $\eta = (W - W_r)/W_r$ is $2k_u/\Gamma$. This motivates the introduction of a new quantity which is called the FEL parameter (or Pierce parameter)

$$\boxed{\rho_{\text{FEL}} = \frac{\Gamma}{2k_u} = \frac{1}{4\pi\sqrt{3}}\cdot\frac{\lambda_u}{L_{\text{g0}}}} \quad (4.49)$$

where L_{g0} is the power gain length defined below in (4.53). With the dimensionless FEL parameter the third-order equation reads

$$\boxed{\frac{\tilde{E}_x'''}{\Gamma^3} + 2i\,\frac{\eta}{\rho_{\mathrm{FEL}}}\,\frac{\tilde{E}_x''}{\Gamma^2} + \left(\frac{k_p^2}{\Gamma^2} - \left(\frac{\eta}{\rho_{\mathrm{FEL}}}\right)^2\right)\frac{\tilde{E}_x'}{\Gamma} - i\,\tilde{E}_x = 0\,.} \tag{4.50}$$

The form (4.50) of the third-order equation shows quite clearly that significant changes must be expected if the fractional energy deviation comes in the order of the FEL parameter. This will be studied in Chap. 5. We will also show that the FEL parameter is closely related to two important properties of a high-gain FEL: its bandwidth and its saturation power.

4.8 Analytic Solution of the Third-Order Equation

The linear third-order differential equation (4.50) can be solved analytically using the trial function $\tilde{E}_x(z) = Ae^{\alpha z}$. We consider first the special case $\eta = 0$, which means that the electron energy is equal to the resonant energy ($W = W_r$), and assume in addition $k_p = 0$ (the plasma frequency becomes small for low electron density n_e or for very large γ_r). Then one obtains

$$\alpha^3 = i\,\Gamma^3$$

with the three solutions

$$\alpha_1 = (i + \sqrt{3})\Gamma/2\,, \quad \alpha_2 = (i - \sqrt{3})\Gamma/2\,, \quad \alpha_3 = -i\Gamma\,. \tag{4.51}$$

The first solution has a positive real part and leads to an exponential growth of the field $\tilde{E}_x(z)$, while the other two eigenvalues correspond to exponentially damped or oscillatory eigenfunctions. For sufficiently large z the power of the light wave grows as

$$P(z) \propto \exp(2\,\Re\{\alpha_1\}) = \exp(\sqrt{3}\Gamma z) \equiv \exp(z/L_{\mathrm{g0}}) \tag{4.52}$$

where we have defined the *power gain length* by[2]

$$\boxed{L_{\mathrm{g0}} = \frac{1}{\sqrt{3}\Gamma} = \frac{1}{\sqrt{3}}\left[\frac{4\gamma_r^3 m_e}{\mu_0 \widehat{K}^2 e^2 k_u n_e}\right]^{1/3}\,.} \tag{4.53}$$

The index "0" in formula (4.53) indicates that L_{g0} is the idealized gain length of the one-dimensional theory assuming a mono-energetic beam and neglecting space charge forces. The power gain length L_g of a realistic FEL will in general be larger because beam energy spread, space charge, betatron oscillations and optical diffraction tend to weaken the exponential gain with the unfortunate consequence that the undulator length must be increased if one wants to

[2] Some authors define the *field gain length* which is a factor of two larger than the power gain length.

preserve the FEL gain and aims at laser saturation. This will be investigated in Chap. 6. The general definition of the power gain length is

$$L_g = P\left(\frac{dP}{dz}\right)^{-1} . \tag{4.54}$$

In the general case $\eta \neq 0$ and $k_p \neq 0$ the linear third-order differential equation is again solved by assuming a z dependence of the form $\exp(\alpha z)$. The resulting cubic equation for the exponent α has three solutions $\alpha_1, \alpha_2, \alpha_3$ which are computed in Appendix E. The general solution of (4.50) can be written as a linear combination of the three eigenfunctions $V_j(z) = \exp(\alpha_j z)$:

$$\tilde{E}_x(z) = c_1 V_1(z) + c_2 V_2(z) + c_3 V_3(z) \qquad V_j(z) = \exp(\alpha_j z) . \tag{4.55}$$

For the first and second derivative we obtain

$$\begin{aligned} \tilde{E}'_x(z) &= c_1\alpha_1 V_1(z) + c_2\alpha_2 V_2(z) + c_3\alpha_3 V_3(z) \\ \tilde{E}''_x(z) &= c_1\alpha_1^2 V_1(z) + c_2\alpha_2^2 V_2(z) + c_3\alpha_3^2 V_3(z) . \end{aligned}$$

Since $V_j(0) = 1$ the coefficients c_j can be computed by specifying the initial conditions for $\tilde{E}_x(z)$, $\tilde{E}'_x(z)$ and $\tilde{E}''_x(z)$ at the beginning of the undulator at $z = 0$. The initial values can be expressed in matrix form by

$$\begin{pmatrix} \tilde{E}_x(0) \\ \tilde{E}'_x(0) \\ \tilde{E}''_x(0) \end{pmatrix} = \boldsymbol{\mathcal{A}} \cdot \begin{pmatrix} c_1 \\ c_2 \\ c_3 \end{pmatrix} \quad \text{with} \quad \boldsymbol{\mathcal{A}} = \begin{pmatrix} 1 & 1 & 1 \\ \alpha_1 & \alpha_2 & \alpha_3 \\ \alpha_1^2 & \alpha_2^2 & \alpha_3^2 \end{pmatrix} . \tag{4.56}$$

The coefficient vector is then computed as

$$\begin{pmatrix} c_1 \\ c_2 \\ c_3 \end{pmatrix} = \boldsymbol{\mathcal{A}}^{-1} \cdot \begin{pmatrix} \tilde{E}_x(0) \\ \tilde{E}'_x(0) \\ \tilde{E}''_x(0) \end{pmatrix} . \tag{4.57}$$

To be more specific we go back to the simple case $\eta = 0$ and $k_p = 0$. Then the eigenvalues are given by (4.51) and the matrix $\boldsymbol{\mathcal{A}}$ and its inverse assume the forms

$$\boldsymbol{\mathcal{A}} = \begin{pmatrix} 1 & 1 & 1 \\ (i+\sqrt{3})\Gamma/2 & (i-\sqrt{3})\Gamma/2 & -i\Gamma \\ (i+\sqrt{3})^2\Gamma^2/4 & (i-\sqrt{3})^2\Gamma^2/4 & -\Gamma^2 \end{pmatrix} , \tag{4.58}$$

$$\boldsymbol{\mathcal{A}}^{-1} = \frac{1}{3} \cdot \begin{pmatrix} 1 & (\sqrt{3}-i)/(2\Gamma) & (-i\sqrt{3}+1)/(2\Gamma^2) \\ 1 & (-\sqrt{3}-i)/(2\Gamma) & (i\sqrt{3}+1)/(2\Gamma^2) \\ 1 & i/\Gamma & -1/\Gamma^2 \end{pmatrix} . \tag{4.59}$$

Let now the FEL process be started by an incident plane light wave of wavelength λ_ℓ and amplitude E_{in}

$$E_x(z,t) = E_{\rm in}\cos(k_\ell z - \omega_\ell t) \quad \text{with} \quad k_\ell = \omega_\ell/c = 2\pi/\lambda_\ell$$

which to a good approximation happens when the FEL is *seeded* by an external laser. The initial density modulation is assumed to be zero: $\tilde{j}_1(0) = 0$ so $\tilde{E}_x'(0) = 0$ from (4.20). Also the second derivative of the field vanishes at $z = 0$. Hence the initial condition is

$$\begin{pmatrix} \tilde{E}_x(0) \\ \tilde{E}_x'(0) \\ \tilde{E}_x''(0) \end{pmatrix} = \begin{pmatrix} E_{\rm in} \\ 0 \\ 0 \end{pmatrix} . \tag{4.60}$$

From (4.57) we find that all three coefficients have the same value, $c_j = E_{\rm in}/3$. So the field of the FEL wave is

$$\tilde{E}_x(z) = \frac{E_{\rm in}}{3}\left[\exp((i+\sqrt{3})\Gamma z/2) + \exp((i-\sqrt{3})\Gamma z/2) + \exp(-i\Gamma z)\right] . \tag{4.61}$$

The first term in the square bracket exhibits exponential growth, the second term carries out a damped oscillation and the third term oscillates as a function of the position z along the undulator axis. So after a certain distance the first term will dominate and the FEL field will grow as

$$\left|\tilde{E}_x(z)\right| \approx \frac{E_{\rm in}}{3}\exp(\sqrt{3}\Gamma z/2) \equiv \frac{E_{\rm in}}{3}\exp(z/(2L_{\rm g0})) .$$

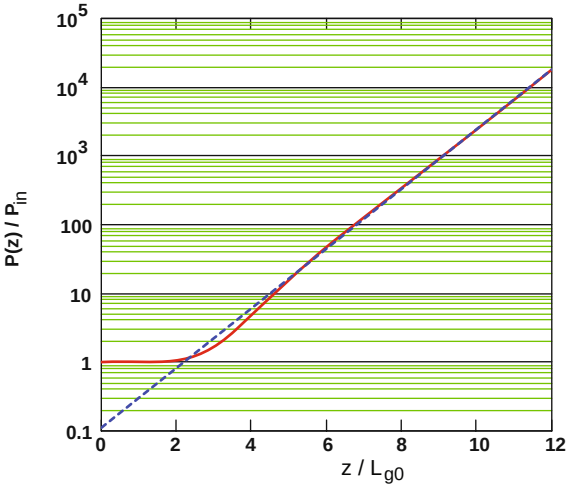

Fig. 4.4. Computed power rise in a high-gain FEL. The lasing process is started by incident *seed radiation*, the input light wave is a plane wave with power $P_{\rm in}$. The electron beam is mono-energetic and on resonance, i.e. $\eta = 0$. The solid curve shows the normalized FEL power $P(z)/P_{\rm in}$ as a function of $z/L_{\rm g0}$. The dashed line is the exponential function $f(z) = (P_{\rm in}/9)\exp(z/L_{\rm g0})$

The FEL power as function of z is plotted in Fig. 4.4. Due to the presence of the other two terms it stays almost constant in the so-called "lethargy regime" ($0 \le z \le 2L_{\mathrm{g0}}$ in the present example) and grows then asymptotically as

$$P(z) \cong \frac{P_{\mathrm{in}}}{9} \exp(z/L_{\mathrm{g0}}) \quad \text{for} \quad z \ge 2L_{\mathrm{g0}} \tag{4.62}$$

where P_{in} is the power of the incident seed light wave at $z = 0$. The starting value of the exponential function is one ninth of the incident power P_{in}. This behavior is quite typical for seeded high-gain FELs.

4.9 High-Gain FEL with Helical Undulator

We present here without proof a short description of the electron motion in a helical undulator and the emission of circularly polarized radiation. Some of the results are derived in Appendix A.

A helical undulator can be thought of as a long dipole magnet that is twisted about its axis. The idealized field (valid near the axis) for a right-handed screw sense is

$$\boldsymbol{B} = -B_0 \left[\cos(k_u z)\boldsymbol{e}_x + \sin(k_u z)\boldsymbol{e}_y\right] \tag{4.63}$$

where $\boldsymbol{e}_x$ and $\boldsymbol{e}_y$ are the unit vectors in x resp. y direction. Note that this field is only approximate and does not obey the Maxwell equations. The electron moves on a helical trajectory of radius

$$r_{\mathrm{hel}} = \frac{K}{\gamma k_u} \, .$$

The longitudinal speed is constant and given by

$$v_z \approx v_0 \equiv c \left[1 - \frac{1}{2\gamma^2}\left(1 + K^2\right)\right] \, . \tag{4.64}$$

The wavelength of helical undulator radiation is

$$\lambda_\ell = \frac{\lambda_u}{2\gamma^2}\left(1 + K^2\right) \, . \tag{4.65}$$

The radiation produced in the undulator field (4.63) has positive helicity and its electric vector can be written in the form (see Appendix A)

$$\boldsymbol{E}(z,t) = E_0 \left[\cos(k_\ell z - \omega_\ell t)\boldsymbol{e}_x - \sin(k_\ell z - \omega_\ell t)\boldsymbol{e}_y\right] \tag{4.66}$$

If the helical magnet is twisted like a left-handed screw the circularly polarized radiation will have negative helicity.

In Table 4.1 we compare important high-gain FEL equations which are different for planar and helical undulators. The main change concerns the

Table 4.1. Comparison of FELs with planar resp. helical undulator

Planar undulator	Helical undulator
$\lambda_\ell = \frac{\lambda_u}{2\gamma^2}\left(1+\frac{K^2}{2}\right) \quad K = \frac{eB_0\lambda_u}{2\pi m_e c}$	$\lambda_\ell = \frac{\lambda_u}{2\gamma^2}\left(1+K^2\right) \quad K = \frac{eB_0\lambda_u}{2\pi m_e c}$
In equations below use $\widehat{K}$	For helical undulator always use K
$\widehat{K} = K\cdot\left[J_0\left(\frac{K^2}{4+2K^2}\right) - J_1\left(\frac{K^2}{4+2K^2}\right)\right]$	
$\frac{d\eta}{dz} = -\frac{e}{m_e c^2\gamma_r}\Re\left\{\left(\frac{\widehat{K}\tilde{E}_x}{2\gamma_r}+\tilde{E}_z\right)e^{i\psi}\right\}$	$\frac{d\eta}{dz} = -\frac{e}{m_e c^2\gamma_r}\Re\left\{\left(\frac{K}{2\gamma_r}(\tilde{E}_x \pm i\,\tilde{E}_y)+\tilde{E}_z\right)e^{i\psi}\right\}$
	$\tilde{E}_y = \mp i\,\tilde{E}_x$
	$\Rightarrow \frac{d\eta}{dz} = -\frac{e}{m_e c^2\gamma_r}\Re\left\{\left(\frac{K\tilde{E}_x}{\gamma_r}+\tilde{E}_z\right)e^{i\psi}\right\}$
$\frac{d\tilde{E}_x}{dz} = -\frac{\mu_0 c\widehat{K}}{4\gamma}\cdot\tilde{j}_1$	$\frac{d\tilde{E}_x}{dz} = -\frac{\mu_0 cK}{4\gamma}\cdot\tilde{j}_1$
$\tilde{E}_z(z) = i\,\frac{4\gamma c}{\omega_\ell\widehat{K}}\cdot\frac{d\tilde{E}_x}{dz}$	$\tilde{E}_z(z) = i\,\frac{4\gamma c}{\omega_\ell K}\cdot\frac{d\tilde{E}_x}{dz}$
$\frac{\partial\tilde{F}_1}{\partial z} = -i\,2k_u\eta\tilde{F}_1 + \frac{e}{m_e c^2\gamma_r}\left[\frac{\widehat{K}}{2\gamma_r}\tilde{E}_x+\tilde{E}_z\right]\frac{dF_0}{d\eta}$	$\frac{\partial\tilde{F}_1}{\partial z} = -i\,2k_u\eta\tilde{F}_1 + \frac{e}{m_e c^2\gamma_r}\left[\frac{K}{\gamma_r}\tilde{E}_x+\tilde{E}_z\right]\frac{dF_0}{d\eta}$
$\Gamma = \left[\frac{\mu_0\widehat{K}^2 e^2 k_u n_e}{4\gamma_r^3 m_e}\right]^{1/3}$	$\Gamma = \left[\frac{\mu_0 K^2 e^2 k_u n_e}{2\gamma_r^3 m_e}\right]^{1/3}$

undulator parameter: $\widehat{K}$ has to be replaced by K when going from a planar to a helical undulator. Moreover one has to keep in mind that the electric vector of the radiation field has two components which couple both to the electron and double the energy transfer. They are related by $\tilde{E}_y = \mp i\,\tilde{E}_x$.

The space charge parameter k_p remains invariant, and the third-order equation retains its form (4.50) if the correct value of the gain parameter Γ is used.

References

1. FEL at Jefferson Lab, see www.jlab.org/FEL/ 37
2. Ayvazyan, V., et al.: Generation of GW radiation pulses from a VUV free-electron laser operating in the femtosecond regime. Phys. Rev. Lett. **88**, 104802 (2002) 39
3. Edwards, D.A., Syphers, M.J.: An Introduction to the Physics of High Energy Accelerators. John Wiley, New York (1993) 40, 51
4. Huang, Z., Kim, K.-J. Review of x-ray free-electron laser theory. Phys. Rev. ST Accel. Beams **10**, 034801 (2007) 42, 50

General Reading

5. Murphy, J.B., Pellegrini, C.: Introduction to the physics of the free electron laser. In: Colson, W.B., Pellegrini, C., Renieri, A. (eds.) Laser Handbook vol. 6, Free Electron Lasers, p. 11–67. North Holland, Amsterdam (1990)
6. Colson, W.B.: Classical free electron laser theory. Laser Handbook vol. 6, p. 115. (1990)
7. Saldin, E.L., Schneidmiller, E.A., Yurkov, M.V.: The Physics of Free Electron Lasers. Springer, Berlin, Heidelberg (2000)

5

Discussion of the High-Gain FEL Equations

In the first part of this chapter we want to exploit the third-order differential equation for the amplitude of the FEL wave in order to gain a deeper understanding of the properties and peculiarities of high-gain Free-Electron Lasers. It will turn out that a remarkable number of predictions can be deduced from the analytic description of the high-gain FEL although we have made rather simplifying assumptions in deriving (4.50), for example by neglecting any dependencies on the transverse coordinates x and y. The coupled first-order equations are evaluated in the second part. They contain even more physics. We will apply them to study the saturation regime and the evolution of microbunching. In the model calculations discussed in this chapter we investigate the amplifier mode of the high-gain FEL and consider either a perfectly uniform initial particle distribution, in which case the lasing process has to be started by an incident light wave, or we assume a density modulation of the electron bunch which is periodic in the optical wavelength. Then no "seed light" is needed. The startup from "noise" via the SASE mechanism will be investigated in Chap. 7.

5.1 Gain Function in the High-Gain Regime

5.1.1 Third-Order Equation with Energy Detuning

The third-order equation (4.50) has been derived in the previous chapter within the one-dimensional (1D) approximation of the high-gain FEL theory, and we have constructed the solution for the simplest case of a monoenergetic electron beam ($\sigma_\eta = \sigma_W/W_r = 0$) whose energy obeys the FEL resonance condition $\eta = 0 \Rightarrow W = W_r = \gamma_r m_e c^2$. The third-order equation can also be solved for a beam energy $W \neq W_r$. The procedure is as follows. In the first step the three complex eigenvalues α_j are calculated, using the methods described in Appendix E. These eigenvalues are functions of the energy

P. Schmüser, et al.: *Discussion of the High-Gain FEL Equations*, STMP **229**, 61–81 (2008)
DOI 10.1007/978-3-540-79572-8_5

detuning $\eta = (W - W_r)/W_r$, see (E.18). Once they are known, the general solution of equation (4.50) can be written in the form

$$\tilde{E}_x(\eta, z) = \sum_{j=1}^{3} c_j(\eta) \exp(\alpha_j(\eta) z) \; . \tag{5.1}$$

The field $\tilde{E}_x$ inside the undulator magnet depends implicitly on the relative energy deviation η through the eigenvalues $\alpha_j(\eta)$. The coefficients c_j are determined by the initial conditions (compare (4.56), (4.57)):

$$\begin{pmatrix} c_1 \\ c_2 \\ c_3 \end{pmatrix} = \boldsymbol{\mathcal{A}}^{-1} \cdot \begin{pmatrix} \tilde{E}_x(0) \\ \tilde{E}'_x(0) \\ \tilde{E}''_x(0) \end{pmatrix} \quad \text{with} \quad \boldsymbol{\mathcal{A}} = \begin{pmatrix} 1 & 1 & 1 \\ \alpha_1 & \alpha_2 & \alpha_3 \\ \alpha_1^2 & \alpha_2^2 & \alpha_3^2 \end{pmatrix} \; . \tag{5.2}$$

From this equation it is clear that the coefficients depend on η as well. Let again the lasing process be started by an incident plane wave of amplitude E_{in}. The gain function $G(\eta, z)$ of an FEL amplifier depends on the relative energy deviation η and the position z in the undulator

$$G(\eta, z) = \left| \frac{\tilde{E}_x(\eta, z)}{E_{\text{in}}} \right|^2 - 1 \tag{5.3}$$

(compare the discussion of the FEL gain function in Chap. 3).

5.1.2 Short Undulator: Low-Gain Limit

We have seen in Fig. 4.4 of the previous chapter that the FEL power stays almost constant in the lethargy regime $0 \le z \le 2\, L_{\text{g0}}$. Therefore we expect the low-gain FEL theory to be applicable here. This is indeed the case. As an illustration we consider an undulator magnet that is shorter than two power gain lengths, say $L_u = L_{\text{g0}}$. The gain curve computed according to (5.3) is compared in Fig. 5.1 with the gain curve obtained in the low-gain theory, using the Madey theorem (3.26). An almost perfect agreement is observed, both in the shape of the gain curve and also in its magnitude. This demonstrates that the low-gain FEL theory is the limiting case of the more general high-gain theory for short undulator magnets. The mathematical proof of this statement is presented in Appendix B.

5.1.3 Long Undulator: High-Gain Regime

For undulator magnets that are longer than several gain lengths we obtain significant differences between the low-gain and the high-gain theory. This is demonstrated in Fig. 5.2 where the gain function is shown at various longitudinal positions inside a long undulator ($L_u \gg L_{\text{g0}}$). In the next section

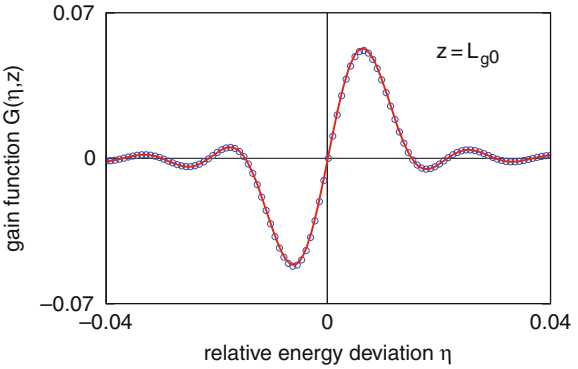

Fig. 5.1. Comparison of the high-gain and the low-gain FEL theory for a short undulator magnet ($L_u = L_{g0}$). The continuous curve shows the gain function $G(\eta, z = L_{g0})$ according to equation (5.3) of the high-gain FEL theory. The circles show the gain function according the low-gain FEL theory, using the Madey theorem (3.26) with the replacement $N_u\lambda_u \to L_{g0}$. Note that the maximum value of the gain function is only 0.05, so one is indeed in the low-gain regime

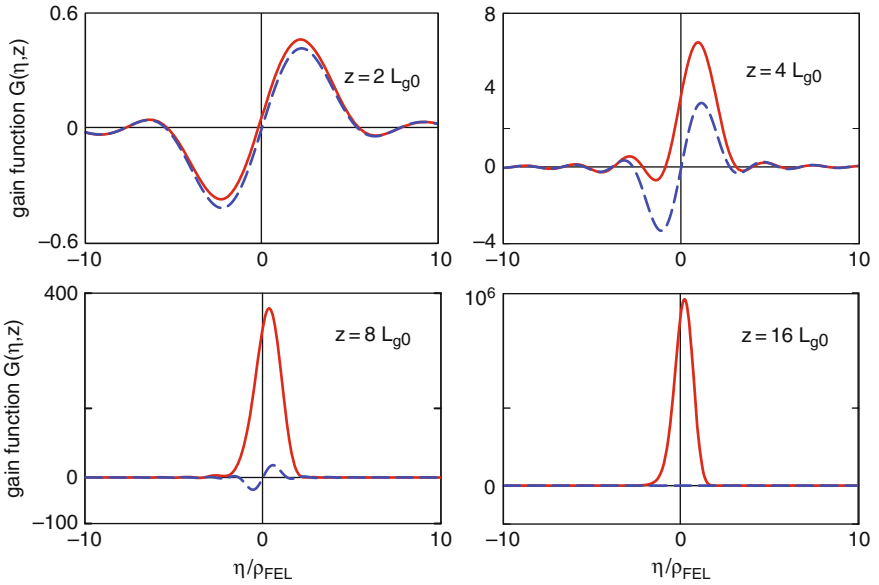

Fig. 5.2. FEL gain function $G(\eta, z)$ plotted vs. η/ρ_{FEL} at various positions in a long undulator: $z = 2L_{g0}, 4L_{g0}, 8L_{g0}, 16L_{g0}$. *Continuous red curves*: computation according to the high-gain theory. *Dashed blue curves*: gain function according to the low-gain theory, using the Madey theorem (3.26). Note the very different vertical scales in the figures

we will see that the width of the gain curve is closely related to the FEL parameter which is the reason why $G(\eta, z)$ is plotted as a function of η/ρ_{FEL}. For a long undulator, the high-gain FEL features a much larger amplification than the low-gain FEL. A very interesting observation is that the maximum amplification happens close to the point $\eta = 0$, i.e. on resonance, where the gain function vanishes in the low-gain theory.

5.2 FEL Bandwidth

The width of the gain curves $G(\eta, z)$ shown in Fig. 5.2 shrinks with increasing undulator length. Which quantity determines the bandwidth of the high-gain FEL amplifier? A good measure for the bandwidth turns out to be the dimensionless FEL parameter defined in the previous chapter

$$\rho_{\mathrm{FEL}} = \frac{1}{4\pi\sqrt{3}} \cdot \frac{\lambda_u}{L_{\mathrm{g0}}} \ .$$

The numerical value of the FEL parameter is typically in the 10^{-3} range. One observes that the FEL gain drops significantly when the relative energy deviation η exceeds the FEL parameter. The full width at half maximum (FWHM) of the gain curves of Fig. 5.2 is about $2\,\rho_{\mathrm{FEL}}$ at $z = 4\,L_{\mathrm{g0}}$ and drops to $\approx 1\,\rho_{\mathrm{FEL}}$ at $z = 16\,L_{\mathrm{g0}}$. These observations show that the high-gain FEL acts as a narrow-band amplifier of variable bandwidth.

5.2.1 Detuning Parameter

The third-order equation describes the FEL process for a given combination of light frequency ω_ℓ and beam energy $W = \gamma m_e c^2$. The eigenvalues α_j depend on the *detuning*. Detuning means a deviation from the resonance condition. We distinguish two important cases:

(1) FEL seeding with a single frequency

In a monochromatically seeded FEL, which we have extensively studied in the previous sections, the incident seed light of frequency ω_ℓ defines the resonant frequency

$$\omega_r \equiv \omega_\ell \tag{5.4}$$

but the electron energy $W = \gamma m_e c^2$ may be different from the resonant energy $W_r = \gamma_r m_e c^2$. In this case the detuning parameter is a function of γ

$$\eta = \eta(\gamma) = \frac{\gamma - \gamma_r}{\gamma_r} \quad \text{with} \quad \gamma_r = \sqrt{\frac{\omega_\ell}{2c\,k_u}\left(1 + \frac{K^2}{2}\right)} \ . \tag{5.5}$$

(2) Seeding with different frequencies or SASE FEL

Suppose several stimulation frequencies $\omega_1, \omega_2, \ldots$ are simultaneously present, either in an incident seed wave or in the Fourier spectrum of the bunch charge distribution. The latter case applies for the SASE FEL. Now it is appropriate to take the electron beam energy W as reference (we disregard energy spread at this point)

$$W \equiv W_r = \gamma_r m_e c^2 \tag{5.6}$$

and define the detuning parameter as a function of frequency

$$\eta = \eta(\omega) = -\frac{\omega - \omega_r}{2\omega_r} \quad \text{with} \quad \omega_r = \frac{2\gamma_r^2 c\, k_u}{1 + K^2/2} \,. \tag{5.7}$$

The factor of two in the denominator is due to the proportionality $\omega_r \propto \gamma_r^2$, and the minus sign comes in because an electron energy higher than the resonance energy in a seeded FEL is equivalent to a light frequency lower than the resonance frequency in a SASE FEL. With (5.7) we have basically translated a frequency deviation of the FEL wave into an equivalent energy deviation of the electron beam.

The coefficients $c_j(\eta_1), c_j(\eta_2), \ldots$ of the eigenfunction expansion are now calculated individually by applying (5.2) for each detuning parameter $\eta_\nu = \eta(\omega_\nu)$. The resulting field is the superposition of the individual contributions

$$\begin{aligned} E_x(z,t) &= \Re\left\{ \sum_\nu \tilde{E}_x^{(\nu)}(z) \exp(i\omega_\nu[z/c - t]) \right\} \\ &= \Re\left\{ \exp(i\omega_r[z/c - t]) \sum_\nu \tilde{E}_x^{(\nu)}(z) \exp(i\Delta\omega_\nu[z/c - t]) \right\} \end{aligned} \tag{5.8}$$

where $\Delta\omega_\nu = \omega_\nu - \omega_r$ is the respective frequency deviation from resonance. The time variable can be eliminated using the relation (compare Appendix C)

$$\zeta(z,t) = z - \bar{\beta}\, c\, t$$

which means that the field can be considered as being a function of the position z in the undulator and the internal coordinate ζ in the bunch:

$$E_x(z,t) = \Re\left\{ \exp(i\omega_r[z/c - t)]) \sum_\nu \widehat{E}^\nu(z, \zeta(z,t)) \right\} \tag{5.9}$$

with the complex field amplitudes

$$\widehat{E}^\nu(z,\zeta) = \tilde{E}_x^\nu(z) \exp(i\Delta\omega_\nu[z/c + (\zeta - z)/(\bar{\beta}\, c)]) \,. \tag{5.10}$$

The current density can be computed by means of (4.20). The method sketched here will be applied in Sect. 5.5 to investigate under which circumstances the superposition principle is applicable in a high-gain FEL.

5.2.2 Analytical Determination of FEL Bandwidth

In order to investigate the relevance of the FEL parameter in a quantitative way we determine the eigenvalues α_j for the case that the beam energy W differs from the resonance energy W_r. In the special case of a mono-energetic beam ($\sigma_\eta = 0$), and for negligible space charge ($k_p = 0$), the three complex eigenvalues $\alpha_j(\eta)$ are computed analytically in Appendix E, see (E.18), (E.19). In the exponential regime the eigenfunction $\exp(\alpha_1 z)$ dominates and the real part of α_1 determines the growth rate of the field $\tilde{E}_x$. The functional dependence $\Re(\alpha_1(\eta))$ is discussed in Appendix E. In the vicinity of $\eta = 0$ the real part of $\alpha_1(\eta)$ can be expanded in a Taylor series

$$\Re\{\alpha_1(\eta)\} \approx \frac{1}{2L_{\mathrm{g0}}}\left(1 - \frac{\eta^2}{9\,\rho_{\mathrm{FEL}}^2}\right) . \tag{5.11}$$

From this follows that the gain curve in the exponential regime can be approximated by a Gaussian[1]

$$G(\eta, z) \propto \exp(z/L_{\mathrm{g0}})\,\exp\left(-\frac{\eta^2 z}{9\,\rho_{\mathrm{FEL}}^2 L_{\mathrm{g0}}}\right) = \exp(z/L_{\mathrm{g0}})\,\exp\left(-\frac{\eta^2}{2\tau^2}\right) \tag{5.12}$$

with a z dependent variance

$$\tau^2 = \frac{9\,\rho_{\mathrm{FEL}}^2 L_{\mathrm{g0}}}{2z} .$$

From (5.7) follows that the rms frequency bandwidth of a SASE FEL is

$$\boxed{\sigma_\omega(z) = \tau(z)\,2\,\omega_\ell = 3\sqrt{2}\,\rho_{\mathrm{FEL}}\omega_\ell\sqrt{\frac{L_{\mathrm{g0}}}{z}} .} \tag{5.13}$$

Note that σ_ω refers to the power of the light wave. The formula is only valid in the exponential regime between about $4\,L_{\mathrm{g0}}$ and the beginning of saturation. The so-defined bandwidth will be used in Chap. 7 to compute the power of a SASE FEL.

5.3 FEL Startup by a Periodically Modulated Electron Beam

Now we want to demonstrate that the FEL process can also be initiated by a periodic charge density modulation in the electron beam, instead of an

[1] In reality the Gaussian is not centered at $\eta = 0$ but is shifted to slightly positive values. This shift, which is due to the energy dependence of the coefficients $c_j(\eta)$, has little effect on the bandwidth and is neglected here.

incident light wave for seeding. Hence we consider a beam current which is modulated periodically in the ponderomotive phase variable ψ according (4.4)

$$j_z = j_0 + \tilde{j}_1(z)\,\exp(i\psi)\ .$$

In the previous chapter we have shown that this leads to a non-vanishing derivative of the transverse electric field, see (4.20). At the entrance of the undulator at $z = 0$ one gets

$$E_0' \equiv \frac{d\tilde{E}_x}{dz}(0) = -\frac{\mu_0 c\widehat{K}}{4\gamma_r}\cdot\tilde{j}_1(0)\ .$$

The second derivative is

$$E_0'' = -\frac{\mu_0 c\widehat{K}}{4\gamma_r}\cdot\tilde{j}_1'(0)$$

so the question arises how to compute the derivative of the current density. For that purpose we use two of the coupled equations (4.30):

$$\tilde{j}_1(z) = j_0\,\frac{2}{N}\,\sum_{n=1}^{N}\exp(-i\psi_n(z)) \quad \text{and} \quad \frac{d\psi_n}{dz} = 2k_u\eta_n\ .$$

Under the assumption that initially all particles have the same energy

$$\eta_1(0) = \eta_2(0) = \ldots\,\eta_N(0) \equiv \eta$$

we obtain

$$\tilde{j}_1'(0) = \left[\sum_{n=1}^{N}\frac{d\tilde{j}_1}{d\psi_n}\frac{d\psi_n}{dz}\right]_{z=0} = -i\,2k_u\eta\tilde{j}_1(0)\ .$$

From this follows

$$E_0'' = i\,2k_u\eta\,\frac{\mu_0 c\widehat{K}}{4\gamma_r}\cdot\tilde{j}_1(0)\ .$$

Hence the initial condition of the third-order equation is

$$\begin{pmatrix}\tilde{E}_x(0)\\ \tilde{E}_x'(0)\\ \tilde{E}_x''(0)\end{pmatrix} = \begin{pmatrix}0\\ E_0'\\ E_0''\end{pmatrix} = \begin{pmatrix}0\\ -1\\ i\,2k_u\eta\end{pmatrix}\frac{\mu_0 c\,\widehat{K}}{4\gamma_r}\,\tilde{j}_1(0)\ . \tag{5.14}$$

It is straightforward to compute the coefficients c_j of the eigenfunction expansion

$$\tilde{E}_z(z) = \sum_j c_j\exp(\alpha_j z)$$

with the help of (5.2). The resulting FEL power as a function of undulator length is shown in Fig. 5.3. At the entrance of the undulator ($z = 0$) the radiation power is of course zero but it rises rapidly with increasing undulator length and approaches the exponential function $\exp(z/L_{g0})$ after about two gain lengths.

A third type of stimulation of the high-gain FEL process is a periodic energy modulation of the incident electron beam.

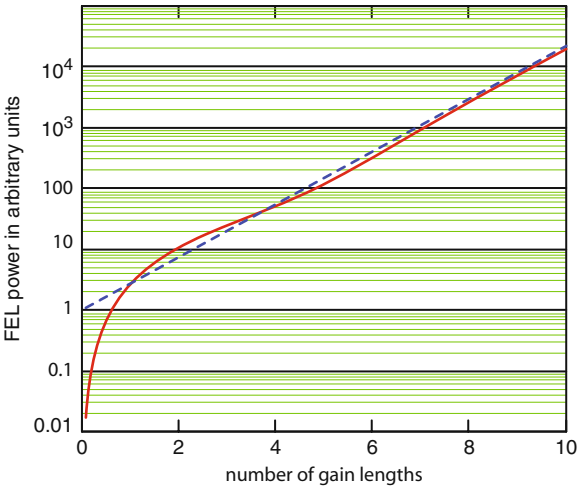

Fig. 5.3. Power rise in a high-gain FEL which is started by a periodic initial electron charge density modulation with the period λ_ℓ. The electron beam is assumed to be mono-energetic and on resonance, i.e. $\eta = 0$. Shown as a dotted line is the exponential function $f(z) = \exp(z/L_{\mathrm{g0}})$

5.4 Laser Saturation

The exponential growth cannot continue indefinitely because the beam energy decreases due to the energy loss by radiation and the modulated current density $\tilde{j}_1$ becomes eventually comparable in magnitude to the dc current density j_0. Moreover, the particles begin to move into the phase space region where energy is taken out of the light wave.

The numerical solution of the coupled differential equations (4.30) will now be applied to study the regime of FEL saturation.

In this calculation we use typical parameters of the extreme-ultraviolet free-electron laser FLASH: Lorentz factor $\gamma = 1000$, number of electrons in the leading spike of the electron bunch $N_e = 10^9$, length of the spike 100 fs, rms bunch radius $\sigma_x = 0.07\,\mathrm{mm}$. This leads to the following values of the relevant FEL quantities: peak current $I_{\mathrm{peak}} = 1600\,\mathrm{A}$, 1D gain length $L_{\mathrm{g0}} = 0.5\,\mathrm{m}$, space charge parameter $k_p = 0.24\,\mathrm{m}^{-1}$, FEL parameter $\rho_{\mathrm{FEL}} = 0.003$. To reach saturation at about 20 gain lengths the field of the seed light wave is chosen as $E_{\mathrm{in}} = 5\,\mathrm{MV/m}$, corresponding to a seed laser power of $P_{\mathrm{in}} \approx 1\,\mathrm{kW}$ for laser pulses that are about 1 ps long. An important practical consideration is that the seed laser beam has to be well focused over the whole extension of the lethargy region, typically over 2–3 gain lengths, to initiate the FEL gain process. Only after this region the exponential amplifications sets in, and then the seed laser beam is no longer needed.

The computed power rise is shown in Fig. 5.4. For $0 \le z \le 16\,L_{\mathrm{g0}}$ one obtains perfect agreement with the eigenfunction approach of the third-order

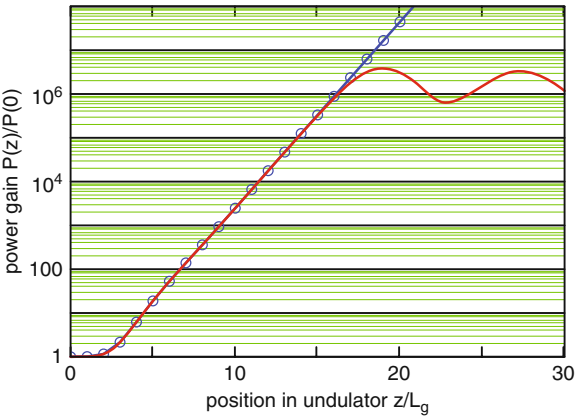

Fig. 5.4. Computed power $P(z)/P_{\rm in}$ as a function of $z/L_{\rm g0}$ in a seeded FEL with typical FLASH parameters, given in the text. The continuous curve shows the result of the numerical integration of the coupled first-order equations. The circles have been computed from the third-order equation (4.50). Here the exponential rise continues beyond 16 gain lengths, however it must be kept in mind that (4.50) is no longer valid in the saturation regime where the modulated current density $\tilde{j}_1$ becomes comparable in magnitude to the dc current density j_0.

equation. In the saturation regime the figure displays an oscillatory behavior of the FEL power which means that energy is pumped back and forth between the electron beam and the light wave. This will be studied in more detail in Chap. 6.

An interesting observation is that different input powers of the seeding wave lead to the same saturation level. This is demonstrated in Fig. 5.5.

The radiation power at saturation can be very roughly estimated as follows. We assume full modulation, i.e. $\left|\tilde{j}_1\right| \approx |j_0|$. The major part of the intensity is generated in the last section of the exponential regime. The field amplitude at saturation is approximately given by the slope of the field gain curve, multiplied with the field gain length (which is twice as large as the power gain length)

$$\left|\tilde{E}_x\right|_{\rm sat} \approx \left|\frac{d\tilde{E}_x}{dz}\right| \cdot 2\,L_{\rm g0} = \frac{\mu_0 c\,\widehat{K}}{4\gamma_r}\;|j_0|\,2\,L_{\rm g0}$$

The saturation power is

$$P_{\rm sat} = \frac{c\varepsilon_0}{2}\left|\tilde{E}_x\right|^2_{\rm sat} A_b \approx \frac{c\varepsilon_0}{2}\left(\frac{\mu_0 c\,\widehat{K}}{4\gamma_r}\right)^2 \frac{I_0^2}{A_b}\,4\,L_{\rm g0}^2$$

where A_b is the beam cross section and $I_0 = |j_0|\;A_b$ is the magnitude of the dc beam current. Introducing the FEL parameter and the power contained in the electron beam

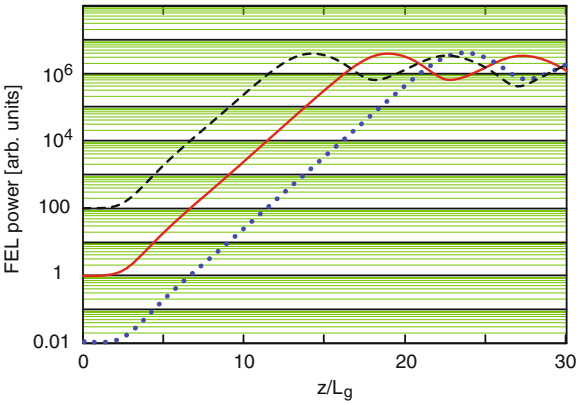

Fig. 5.5. Computed power rise in a high-gain FEL, resulting from the numerical integration of the equations (4.30), for three different power levels of the incident seeding wave. Solid curve: $P_{\rm in} \equiv P_0 \approx 1\,{\rm kW}$, dashed curve: $P_{\rm in} = 100\,P_0$, dotted curve: $P_{\rm in} = 0.01\,P_0$. In the linear regime, comprising the lethargy and the exponential gain regime, the curves differ by factors of 100 which means that the FEL output power depends here linearly on the input power. The saturation level, however, is the same in all three cases, so the saturated FEL is definitely in the nonlinear regime

$$P_{\rm beam} = \frac{\gamma_r m_e c^2 I_0}{e} \tag{5.15}$$

one finds a rule of thumb for estimating for the FEL power at saturation

$$P_{\rm sat} \approx \rho_{\rm FEL}\, P_{\rm beam}\ . \tag{5.16}$$

A better estimate of the saturation power is presented in the next chapter, equation (6.31). The FEL power at saturation is thus in the order of 0.1% of the electron beam power. For typical beam parameters of FLASH one obtains a saturation power of several GW.

5.5 Linear and Nonlinear Regime of a High-Gain FEL

The free-electron laser is an intrinsically nonlinear system. This is immediately evident from one of its basic equations, the pendulum equation

$$\frac{d\eta}{dz} = -\frac{eE_0\widehat{K}}{2m_e c^2\gamma_r^2}\cos\psi\ .$$

In Chap. 4 the single-particle coordinates have been eliminated with the help of a distribution function, and a linearization has been achieved by neglecting the term $d\tilde{F}_1/d\eta$. We have derived the linear third-order differential equation (4.50) for the amplitude of the light wave. The solutions of a linear

differential equation depend linearly on the initial conditions. The same applies for the integro-differential equation (4.44) which is more general than (4.50) as it can be used for a beam with energy spread, too. The linear regime of a high-gain FEL amplifier is characterized by the following features:

(1) The response (output electric field) is proportional to the stimulation (the input field).
(2) The superposition principle applies: the response to a superposition of different stimulations is equal to the superposition of the responses to the individual stimulations.

An illustration of the linear relationship between the input field $E_{\rm in}$ of a monochromatic seed wave and the FEL output field $\tilde{E}_x$ has already been presented in Fig. 5.5 where this linearity is observed over a wide range of z values. The linear relationship is completely lost in the saturation region.

Now we give an example for the superposition principle and study the response of the FEL to a seed radiation containing two different frequencies. According to Sect. 5.2.1 the electron beam energy W defines now the reference frequency:

$$W \equiv W_r = \gamma_r m_e c^2, \quad \omega_r = \frac{2\gamma_r^2 c\, k_u}{1 + K^2/2} \,.$$

We choose symmetrically detuned frequencies for our seed wave

$$\omega_a = \omega_r(1 - \rho_{\rm FEL}), \quad \omega_b = \omega_r(1 + \rho_{\rm FEL})$$

with equal initial amplitudes, $E^a_{\rm in} = E^b_{\rm in} = 5\,{\rm MV/m}$. The coupled first-order equations (C.7) in the non-periodic model are used to compute the individual response functions. We introduce the complex field amplitudes according to (5.10)

$$\begin{aligned} \widehat{E}^a(z,\zeta) &= \tilde{E}^a_x(z)\exp(i\Delta\omega_a[z/c + (\zeta - z)/(\bar{\beta}\, c)]) \\ \widehat{E}^b(z,\zeta) &= \tilde{E}^b_x(z)\exp(i\Delta\omega_b[z/c + (\zeta - z)/(\bar{\beta}\, c)]) \end{aligned} \tag{5.17}$$

which are functions of the position z along the undulator and the position ζ inside the bunch. In the same manner one computes the sum-response function $\widehat{E}^s(z,\zeta)$ corresponding to the simultaneous excitation with two frequencies and the initial field $E^s_{\rm in} = E^a_{\rm in} + E^b_{\rm in}$. A bunch with a flat charge profile and a length of 1000 optical periods has been used in the computation, but for the sake of clarity the effects at the bunch head and tail are ignored here. The result obtained in the linear regime at $z = 15\,{\rm L_{g0}}$ is depicted in Fig. 5.6. One finds that the equation

$$\widehat{E}^s(z,\zeta) = \widehat{E}^a(z,\zeta) + \widehat{E}^b(z,\zeta) \tag{5.18}$$

is satisfied both for the real part and the imaginary part. Incidentally, the curves shown in Fig. 5.6 can also be computed using (5.8), but only in the flat-top region of the bunch and not at the head or the tail.

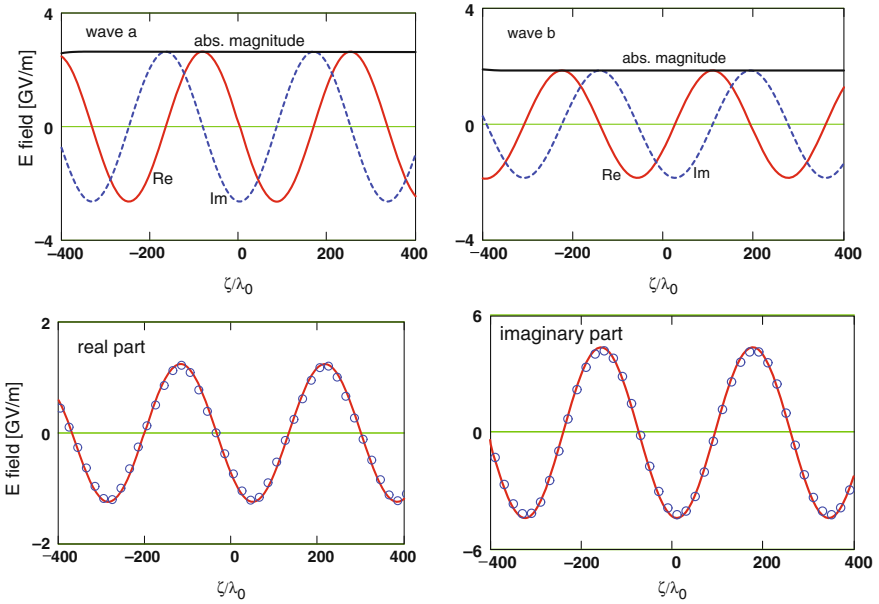

Fig. 5.6. Response of the FEL in the linear regime at $z = 15\,L_{\mathrm{g0}}$. Top left graph: real part, imaginary part and absolute magnitude of the field $\widehat{E}^a(z,\zeta)$ of frequency ω_a, plotted versus ζ/λ_0 (λ_0 denotes the FEL wavelength corresponding to the resonance energy). Top right graph: real part, imaginary part and absolute magnitude of the field $\widehat{E}^b(z,\zeta)$ of frequency ω_b. Bottom left graph: the sum of the real parts $\Re\{\widehat{E}^a(z,\zeta) + \widehat{E}^b(z,\zeta)\}$ of the individual responses is shown as solid red curve, the real part $\Re\{\widehat{E}^s(z,\zeta)\}$ of the sum-response (5.18) is shown as the blue circles. Bottom right graph: same for the imaginary parts

A completely different behavior is found in the nonlinear regime, see Fig. 5.7. While the individual excitations in this example lead still to almost sinusoidal responses the sum-response is strongly distorted and the superposition principle is badly violated. Equation (5.8) is obviously not applicable in the nonlinear regime.

The Figs. 5.6 and 5.7 reveal that the amplitude of the field E^a is larger than that of E^b in spite of the symmetrical detuning. This asymmetry is due to an asymmetric shape of the curve $\Re\{\alpha_1(\eta)\}$, see Fig. 6.1 in the next chapter.

In summary one can say that the third-order differential equation is well suited for the description of the linear regime of the high-gain FEL, comprising the lethargy and the exponential-gain regime. However this equation breaks down in the nonlinear regime where the laser power goes into saturation. The coupled first-order equations encompass both the linear and the nonlinear regime.

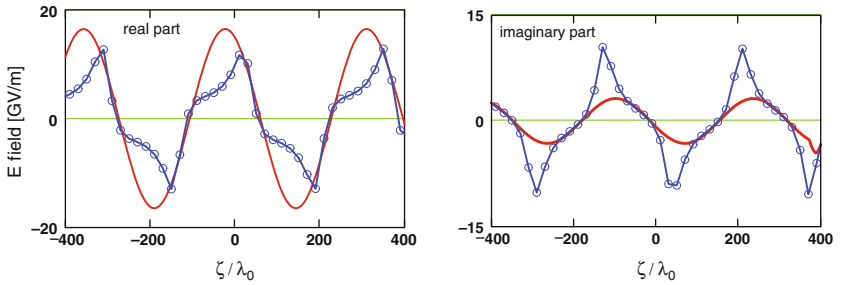

Fig. 5.7. FEL response in the nonlinear regime at $z = 20\,L_{\mathrm{g0}}$. Left graph: the sum of the real parts $\Re\{\widehat{E}^a(z,\zeta) + \widehat{E}^b(z,\zeta)\}$ of the individual responses is shown as solid red curve, the real part of the sum-response $\Re\{\widehat{E}^s(z,\zeta)\}$ is shown by the *blue circles*. Right graph: comparison of the imaginary parts

5.6 Simulation of Microbunching

5.6.1 Evolution of Phase Space Structures

In our next example we demonstrate that the periodic form (4.30) of the coupled first-order equations can be used to study the microbunching effect. Again we use typical parameters of the ultraviolet FEL FLASH. As initial condition for the numerical simulation we take a beam whose mean electron energy W_0 is equal to the resonance energy W_r , hence $\eta_0 = 0$. A total of $N = 50000$ test particles are distributed uniformly in the initial ponderomotive phase variable over an interval of $\Delta\psi_0 = 2\pi$. The distribution is periodically continued to the full range $-\infty < \psi_0 < \infty$ as assumed in the periodic model. A randomly distributed Gaussian energy spread is imposed with $\sigma_\eta = 0.1\,\rho_{\mathrm{FEL}}$. The FEL process is started by a seed laser beam with $E_{\mathrm{in}} = 5\,\mathrm{MV/m}$.

In Fig. 5.8 we show the distribution of the particles in the phase space (ψ, η) shortly after the beginning of the undulator at $z = 0.2\,L_{\mathrm{g0}}$, together with the projection onto the ψ axis. The energy modulation of the electron bunch is very small, well below the rms energy spread σ_η, and the normalized charge density $\rho_n(\psi, z) = |\tilde{\rho}(\psi, z)|\,/\rho_0$ shows no significant deviation from unity. The FEL buckets are centered at nearly the same phase values as they are at the beginning of the undulator at $z = 0$, compare (3.25)

$$\psi_b(0.2\,L_{\mathrm{g0}}) \approx \psi_b(0) = -\pi/2 \pm n\,2\pi\ .$$

The equation of the separatrix is practically the same as in the low-gain case, see (3.24)

$$\eta_{\mathrm{sep}}(\psi) = \pm\sqrt{\frac{e\left|\tilde{E}_x(z)\right|\widehat{K}}{k_u m_e c^2 \gamma_r^2}}\,\cos\left(\frac{\psi - \psi_b(z)}{2}\right)\ . \tag{5.19}$$

Note that due to the initial beam energy spread many particles are outside the FEL bucket, i.e. the area enclosed by the separatrix. With increasing z

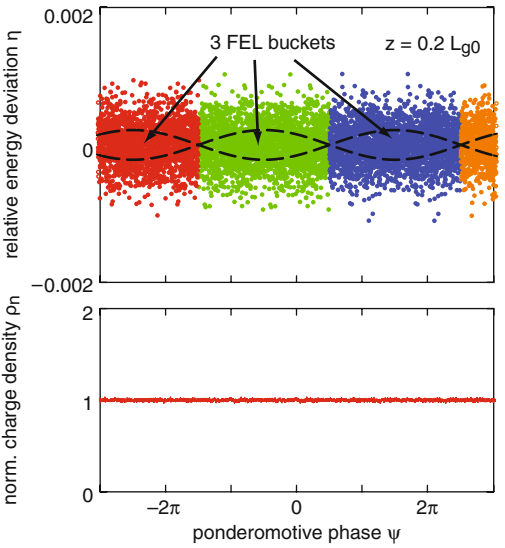

Fig. 5.8. Top: distribution of particles in the (ψ, η) phase space at $z = 0.2\, L_{\mathrm{g0}}$. The separatrix is indicated by the dashed curves. Shown are several adjacent FEL buckets. Bottom: normalized charge density $\rho_n(\psi) = |\tilde{\rho}(\psi)|\,/\rho_0$, plotted as a function of ψ. Remember that the phase ψ corresponds to the internal bunch coordinate according to $\zeta = \lambda_\ell \cdot (\psi + \pi/2)/(2\pi)$

the height of the separatrix grows with the square root of the FEL field, according to (5.19), and most particles are eventually captured in the FEL buckets (this can be seen in Fig. 5.9). Most importantly, the bucket center moves with increasing z toward smaller phase values. The z dependence of the bucket center phase $\psi_b(z)$ will be determined in the next section.

Strong changes in the phase space pictures and the charge density distributions become visible after about 10 gain lengths. At $z \geq 12 L_{\mathrm{g0}}$ one can nicely see the evolution of the microbunch structure, see Fig. 5.9. The microstructure with the periodicity of the light wavelength λ_ℓ is fully developed after 16 power gain lengths.

We make several important observations:

(1) With increasing z the FEL buckets move towards smaller phases and the amplitude of the separatrix grows.
(2) The energy modulation is almost harmonic up to 12–14 gain lengths but acquires unharmonic distortions for $z \geq 14 L_{\mathrm{g0}}$.
(3) Due to the bucket motion many particles do not stay in their original bucket but move into the next one.
(4) The normalized particle density gradually develops narrow peaks which are located in the right half of the respective FEL bucket, i.e. at the phase value where energy transfer from the electrons to the FEL wave will happen.

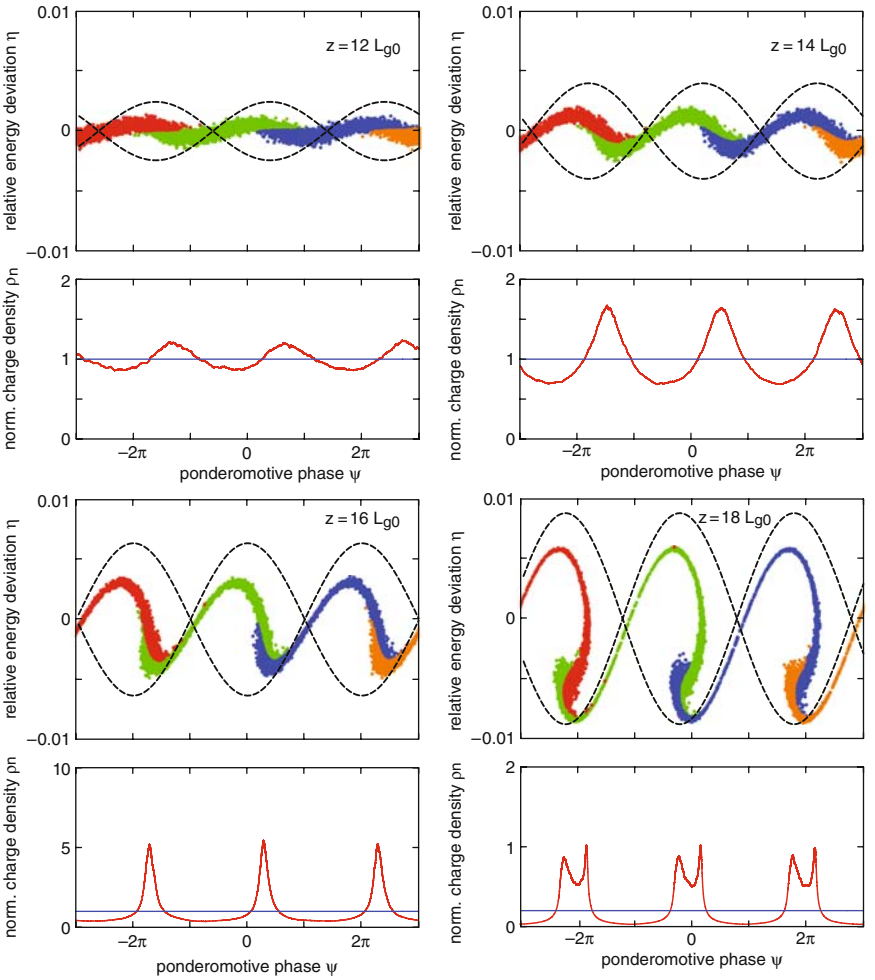

Fig. 5.9. Evolution of the microbunch structure. *Top left*: $z = 12L_{g0}$, *top right*: $z = 14L_{g0}$. *Bottom left*: $z = 16L_{g0}$, *bottom right*: $z = 18L_{g0}$. The upper subplots show the distribution of the particles in the (ψ, η) phase space. The separatrices are indicated by the *dashed curves*. The lower subplots show the normalized particle density as a function of ψ

Deep in the saturation regime the phase space distributions acquire large distortions as shown in Fig. 5.10. Many particles move over into the left halves of the FEL buckets with the consequence that energy is withdrawn from the light wave. This is the reason for the reduction of the FEL power at about 20 gain lengths that is visible in Fig. 5.4. The microbunches develop a substructure. The energy spread of the beam increases considerably with increasing undulator length. The distortions of the particle distribution in phase space and the oscillatory behavior of the FEL gain curve in the saturation regime are well-known from the literature, see e.g. [1], [2].

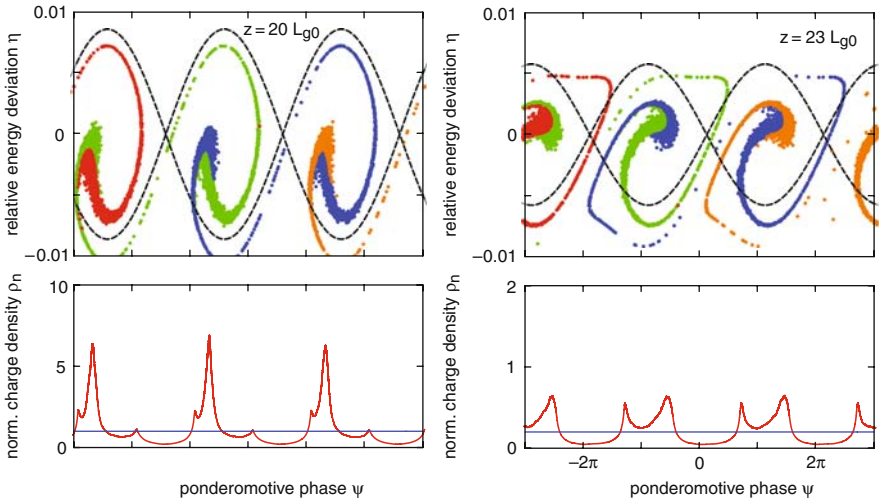

Fig. 5.10. Distortion of the phase space distribution and evolution of substructure of the microbunches deep in the saturation regime at 20 resp. 23 gain lengths

5.6.2 Evolution of Phases in the FEL Gain Process

Phases of Electric Field and Current Density

To determine the phase evolution of the field $\tilde{E}_x(z)$ and the current density $\tilde{j}_1(z)$ in the linear FEL regime we express the slowly varying complex field amplitude as a superposition of the three eigenfunctions of the third-order equation

$$\tilde{E}_x(z) = \frac{E_{\rm in}}{3} \sum_{j=1}^{3} \exp(\alpha_j z) \equiv \left|\tilde{E}_x(z)\right| \exp(i\,\varphi_E(z)) \; . \tag{5.20}$$

In the simplest case $\eta = 0$ and $k_p = 0$ the eigenvalues α_j are given by (4.51). The phase $\varphi_E(z)$ is readily computed from (5.20). The phase of the modulated current density $\tilde{j}_1(z)$ can be related to the phase of $\tilde{E}_x(z)$ by means of (4.20)

$$\tilde{j}_1(z) = -\frac{4\gamma_r}{\mu_0 c\,\widehat{K}}\,\tilde{E}'_x(z) = -\frac{4\gamma_r}{\mu_0 c\,\widehat{K}} \sum_{j=1}^{3} \alpha_j \exp(\alpha_j z) \equiv \left|\tilde{j}_1(z)\right| \exp(i\,\varphi_{j1}(z)) \; . \tag{5.21}$$

The z dependence of the two phases is depicted in Fig. 5.11. The phase of the field grows initially faster than that of the current. The phase difference $\Delta\varphi = [\varphi_E(z) - \varphi_E(0)] - [\varphi_{j1}(z) - \varphi_{j1}(0)]$ grows from $\Delta\varphi = 0$ at small z to $\Delta\varphi = \pi/3$ for $4L_{\rm g0} \le z \le 17\,L_{\rm g0}$. In the saturation regime the coupled first-order equations must be used. One finds a cross-over of the phases at about 20 gain lengths.

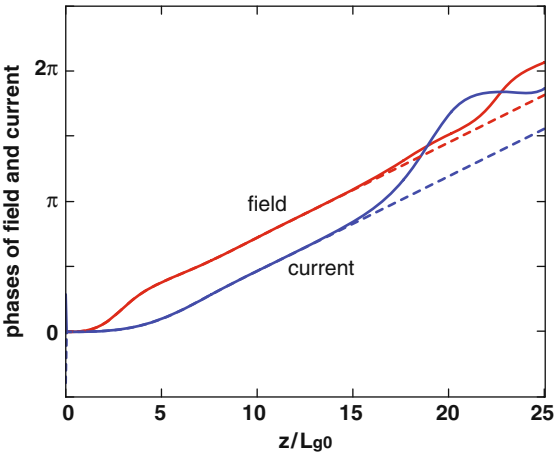

Fig. 5.11. The phase $\varphi_E(z) - \varphi_E(0)$ of the complex field $\tilde{E}_x(z)$ (*solid red curve*) and the phase $\varphi_{j1}(z) - \varphi_{j1}(0)$ of the modulated current density $\tilde{j}_1(z)$ (*solid blue curve*) as a function of z/L_{g0}. The phases have been computed using the coupled first-order equations. In the linear regime there is perfect agreement with the phases derived from (5.20), (5.21). The dashed lines show the extrapolation of the linear theory into the nonlinear regime $z > 17\,L_{g0}$

Bucket Center Phase and Microbunch Phase

In Sect. 4.2 we have discussed the origin of microbunching as being due to a modulation of the longitudinal velocity: particles losing energy to the light wave move on an undulator trajectory of larger amplitude and have a smaller average speed in z direction than particles gaining energy from the light wave. This reasoning is unable to predict the position of the microbunches inside the FEL buckets. Now we address this question which is of crucial importance for the functioning of the high-gain FEL: why are the microbunches located in the right half of the respective FEL bucket where energy is transferred from the electron beam to the light wave, and why not in the left half where energy would be withdrawn from the light wave? The explanation is based on the observation that the FEL bucket center moves in phase space during the exponential gain process. The peak of the charge density modulation moves also but at a slower rate, and the resulting phase difference turns out to be essential.

The second of the coupled first-order equations (4.30) can be utilized to determine the phase evolution of the bucket center. Since the FEL bucket is generated by the light-wave field $\tilde{E}_x$ we consider only the first term in this equation but neglect the second term (the term with $\tilde{j}_1(z)$). For a particle "b" at the bucket center the equation (4.30b) reads then

$$\frac{d\eta_b}{dz} = -\frac{e}{m_e c^2 \gamma_r} \Re \left\{ \frac{\widehat{K}\tilde{E}_x(z)}{2\gamma_r} \exp[i\,\psi_b(z)] \right\} \propto \cos[\varphi_E(z) + \psi_b(z)]$$

where $\varphi_E(z)$ is the z dependent phase of the complex field $\tilde{E}_x(z)$. At $z = 0$ the bucket center is located at

$$\psi_b(0) = -\pi/2 \pm n\,2\pi \ .$$

The energy of particle "b" has to remain invariant if this particle should represent the bucket center for all $z \geq 0$. Hence we request $d\eta_b/dz = 0$ which implies

$$\varphi_E(z) + \psi_b(z) = \text{const} \equiv \varphi_E(0) + \psi_b(0) \ .$$

This leads to the important relation between the bucket center phase and the phase of the complex field amplitude:

$$\psi_b(z) - \psi_b(0) = -(\varphi_E(z) - \varphi_E(0)) \ . \tag{5.22}$$

In a similar way (4.30b) can be utilized to determine the phase evolution of the peak of the charge distribution, i.e. the position of the "microbunch".

In this case the current density term $\tilde{j}_1(z)$ in (4.30b) is relevant because it describes the particle's energy variation due to space charge forces, while the light-wave field term has to be ignored. From the condition $d\eta_c/dz = 0$ we infer that the "microbunch phase" obeys the equation

$$\psi_m(z) - \psi_m(0) = -(\varphi_{j1}(z) - \varphi_{j1}(0)) \ . \tag{5.23}$$

Evolution of Particle Phases in the Gain Process

The phase variation of a selected number of particles in three adjacent FEL buckets is depicted in Fig. 5.12. The ponderomotive phases ψ_n have been computed with the coupled equations (4.30) and are plotted as a function of the distance z traveled in the undulator. The particles are initially on resonance ($W = W_r,\ \eta = 0$). Until about 10 gain lengths the particle phases ψ_n remain almost invariant. We look at the central bucket which is initially at $-3\pi/2 < \psi_0 < \pi/2$. Bucket center phase and microbunch phase are identical here, $\psi_b(0) = \psi_m(0) = -\pi/2$. We observe that the central bucket moves towards negative ψ values and that about half of the particles remain in this bucket while the other half is captured by the next bucket. The microbunching process is thus associated with a mixing of neighboring buckets.

The motion of the central FEL bucket is depicted in Fig. 5.13. One can see very clearly that the bucket moves with respect to the particles. Moreover it becomes evident that the microbunch is formed in the right half of the bucket. This is the explanation for the strong rise of the FEL power.

For $z > 13L_{g0}$ a dramatic variation of the particle phases is observed. They begin to concentrate in narrow bands which are fully developed at 18–20 gain lengths. These bands are the microbunches.

We emphasize again that the phase $\psi_b(z)$ of the bucket center as well as the phase $\psi_m(z)$ of the microbunch move with respect to the particles. In the

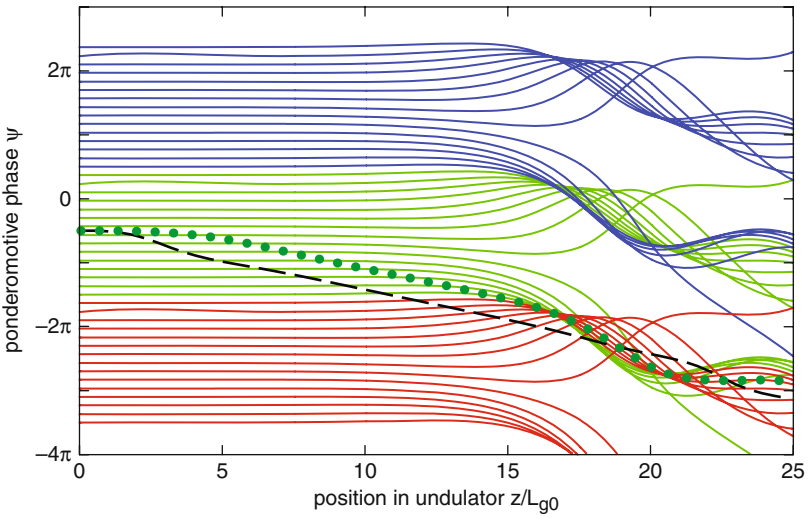

Fig. 5.12. Phase motion of selected particles in three adjacent FEL buckets during the exponential growth and saturation of the FEL power. The beam is monoenergetic and has an initial fractional energy deviation of $\eta = 0$. The dashed curve shows the variation of the FEL bucket center phase $\psi_b(z)$ according to (5.22). The dotted curve shows the motion of the microbunch phase $\psi_m(z)$ as given by (5.23)

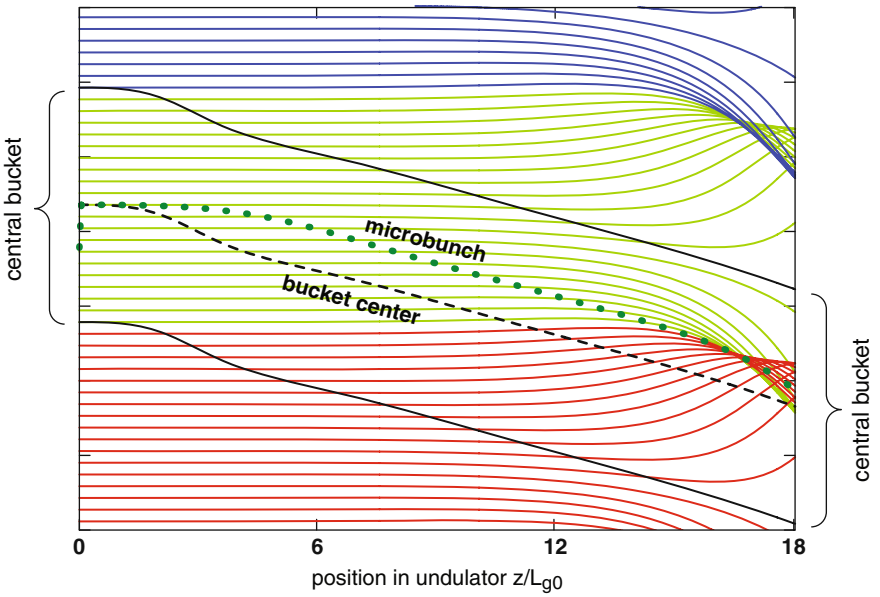

Fig. 5.13. Motion of the central FEL bucket for $0 \leq z \leq 18L_{g0}$

exponential gain regime $4L_{g0} \leq z \leq 17L_{g0}$ we find $\Delta\psi = \psi_m(z) - \psi_b(z) \approx \pi/3$ so the peaks in the charge distribution are in the right half of the respective bucket, as required for energy transfer from the electron beam to the light wave. Above 20 gain lengths, however, the maximum of the charge density has moved to the left half of the bucket, corresponding to energy transfer from the light wave to the electron beam.

It may appear strange at first sight that the particle phases are nearly invariant in the lethargy regime and a large part of the exponential gain regime, while the charge density modulation is moving. This, however, is quite a common phenomenon. In a sound wave in air, for example, the molecules carry

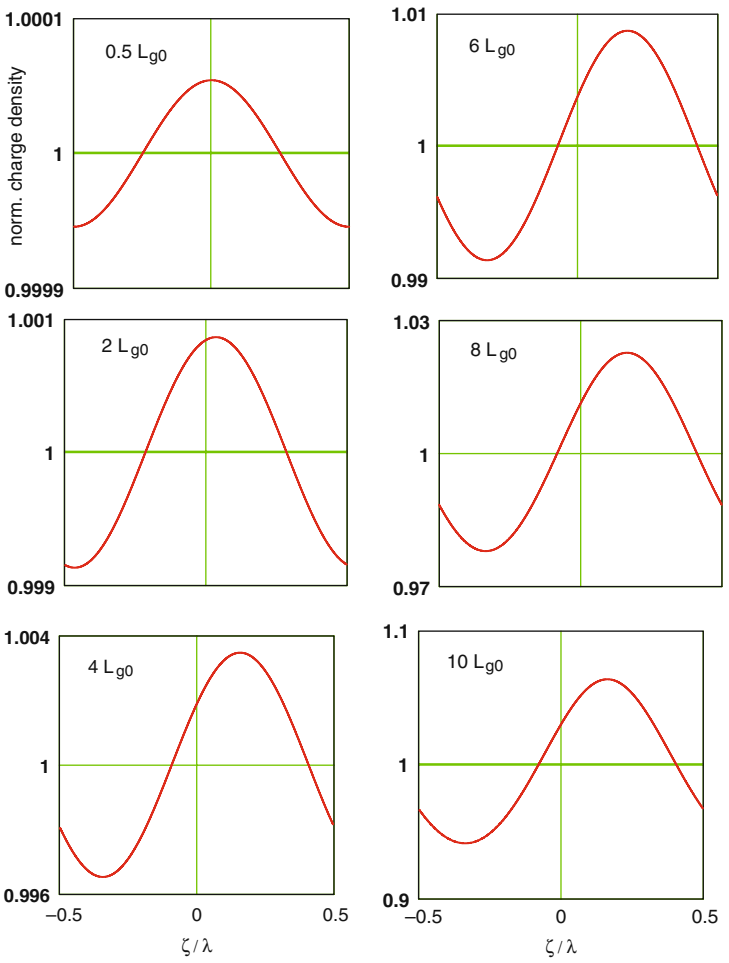

Fig. 5.14. The normalized charge density distribution within the central FEL bucket at $z = 0.5\,L_{g0}, 2\,L_{g0}, 4\,L_{g0}, 6\,L_{g0}, 8\,L_{g0}, 10\,L_{g0}$. Note the rather different vertical scales

out small longitudinal oscillations about stationary positions, but the density fluctuations propagate with the speed of sound. To demonstrate explicitly that a density modulation evolves already quite early in the undulator we show in Fig. 5.14 the normalized charge density within the central FEL bucket at various locations z. At the very beginning the maximum of the charge density is found at the bucket center at $\zeta = 0$, but already after two gain lengths the maximum has moved toward positive ζ values. In the exponential gain regime $4\,L_{\mathrm{g0}} \leq z \leq 17\,L_{\mathrm{g0}}$ the maximum is located at $\zeta \approx \lambda_\ell/6$, corresponding to $\Delta\psi \approx \pi/3$ (compare Figs. 5.14, 5.13).

5.6.3 Higher Harmonics in FEL Radiation

According to Fig. 5.14 the particle density distribution inside the FEL bucket is almost harmonic for $0.5\,L_{\mathrm{g0}} \leq z \leq 10\,L_{\mathrm{g0}}$. At $z \geq 12\,L_{\mathrm{g0}}$ the picture changes. It is evident from Fig. 5.9 that the longitudinal charge distribution has still the periodicity of the fundamental light wavelength $\lambda_1 \equiv \lambda_\ell$ but is no longer a simple harmonic distribution. Its Fourier decomposition will therefore contain higher harmonics. These higher harmonics, however, will not be amplified in our simplified one-dimensional FEL model because we have averaged over the oscillatory part in the longitudinal velocity, compare (4.5). It is possible to generalize the coupled first-order equations in such a way that the odd higher harmonics are incorporated. In three-dimensional FEL codes such as GENESIS the longitudinal oscillation is properly accounted for, and then higher harmonics can be computed as well. There is ample experimental evidence for the existence of higher harmonics, see Chap. 7.

References

1. Murphy, J.B., Pellegrini, C.: Introduction to the physics of the free electron laser, In: Colson, W.B., Pellegrini, C., Renieri, A. (eds.) Laser Handbook, vol. 6, p. 11, North Holland, Amsterdam, Oxford, New York, Tokyo (1990) 75
2. Colson, W.B.: Classical free electron laser theory, Laser Handbook **6**, 115 (1990) 75

6

Refinements of the One-Dimensional FEL Theory

The realistic description of FELs operating in the high-gain regime has to be based on a three-dimensional theory. The dependencies of the electron beam current density and of the light wave on the transverse coordinates x and y must be taken into account. Betatron oscillations of the electrons and diffraction of the light wave play an important role. Moreover, energy spread in the electron beam and the longitudinal slippage of the FEL pulse with respect to the short electron bunch must be considered (in the 1D theory as described in Chaps. 4 and 5 the bunch is treated as being infinitely long, which is far from reality). No analytical methods are known to carry through the full 3D theory and one has to resort to numerical simulation codes such as GINGER [1], GENESIS [2] or FAST [3] which have been developed to a high degree of sophistication. The full three-dimensional treatment of the FEL is beyond the scope of this introductory book, the interested reader is referred to the monograph *The Physics of Free Electron Lasers* by Saldin, Schneidmiller and Yurkov [4] and to the review article *Review of x-ray free-electron laser theory* by Huang and Kim [5] and the literature quoted therein.

In this chapter we consider first the effects that are already present in the 1D theory: energy detuning, beam energy spread and space charge forces, and we analyze their impact on the FEL gain length. Then 3D effects are treated in a somewhat qualitative manner in order to explain the influence of betatron oscillations and optical diffraction on the FEL performance. A simplified three-dimensional model is applied to determine numerically the FEL growth rate parameter and the gain length for a cylindrical electron beam of uniform charge density. In the next section, X-ray FEL parameter studies of other authors are presented which were derived from numerical simulations. Finally, slippage effects in short electron bunches are discussed.

P. Schmüser, et al.: *Refinements of the One-Dimensional FEL Theory*, STMP **229**, 83–101 (2008)
DOI 10.1007/978-3-540-79572-8_6

6.1 Increase of 1D Gain Length by Beam Energy Spread and Space Charge

In Sect. 4.8 the FEL power gain length has been defined in the 1D approximation and for a mono-energetic beam that is on resonance. According to (4.52) the power gain length is related to the real part of the first eigenvalue of the third-order equation:

$$P(z) \propto \exp(2\,\Re\{\alpha_1\}\,z) \equiv \exp(z/L_{\mathrm{g0}})\ . \tag{6.1}$$

We infer that $2\Re\{\alpha_1\}$ is the inverse gain length. This insight allows us to compute the gain length in more general cases.

6.1.1 Energy Detuning

We consider first energy detuning, $W \neq W_r\,, \eta \neq 0$, but keep $\sigma_\eta = 0$ and $k_p = 0$. It is shown in Appendix E how the eigenvalues $\alpha_j = \alpha_j(\eta)$ of the third-order differential equation can be determined for the case $\eta \neq 0$. The real parts of the eigenvalues are depicted in Fig. 6.1.

The real part of the first eigenvalue determines again the growth rate but it is now a function of the relative energy deviation η. According to (6.1) it appears reasonable to define the inverse gain length by the maximum value of $2\Re\{\alpha_1(\eta)\}$. So the gain length is given by the expression

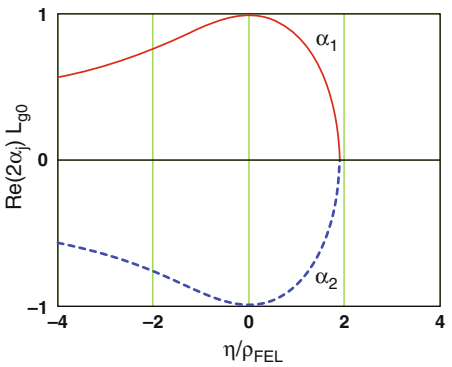

Fig. 6.1. The real part of the first resp. second eigenvalue, multiplied with $2L_{\mathrm{g0}}$, is plotted as a function of η/ρ_{FEL}, the relative energy deviation divided by the FEL parameter. Note that $\Re(\alpha_1)$ (*continuous red curve*) is positive, corresponding to exponential growth of the eigenfunction $V_1(z) = \exp(\alpha_1 z)$. However, the real part vanishes above $\eta \approx 1.88\rho_{\mathrm{FEL}}$ which means that the exponential growth stops if the electron energy W exceeds the resonant energy W_r by more than $\Delta W = 1.88\,\rho_{\mathrm{FEL}}\,W_r$. The real part of α_2 (*dashed blue curve*) is always negative, hence the eigenfunction $V_2(z)$ drops exponentially. Finally, $\Re(\alpha_3) \equiv 0$, so $V_3(z)$ oscillates along the undulator axis

$$\boxed{L_g = \frac{1}{\max\left[2\,\Re\{\alpha_1(\eta)\}\right]}\,.} \tag{6.2}$$

In this special case of a beam without energy spread and space charge we obtain $L_g = L_{g0}$. For the investigation of the general case it is convenient to define a dimensionless "growth rate function" by

$$f_{gr}(\eta) = 2\,\Re\{\alpha_1(\eta)\}\cdot L_{g0}\,. \tag{6.3}$$

The maximum value of the growth rate function is equal to the ratio L_{g0}/L_g:

$$\max\left[2\,\Re\{\alpha_1(\eta)\}\cdot L_{g0}\right] = \frac{L_{g0}}{L_g}\,.$$

6.1.2 Space Charge and Energy Spread

Now we drop the assumption of a mono-energetic beam and admit energy spread $\sigma_\eta > 0$ and space charge $k_p > 0$. The mean beam energy is called W_0, it may be different from the resonance energy ($W_0 \neq W_r\,, \eta_0 \neq 0$). The third-order equation is not suitable for a beam with energy spread but the integro-differential equation (4.44) can be used. It is discussed in Appendix E how the eigenvalue $\alpha_1(\eta_0)$ with positive real part can be determined. The function $\Re\{\alpha_1(\eta_0)\}$ depends on k_p and σ_η. This is shown in Fig. 6.2.

The impact of space charge on the gain length is often rather small. The gain length increases by about 10% if the space charge parameter has the

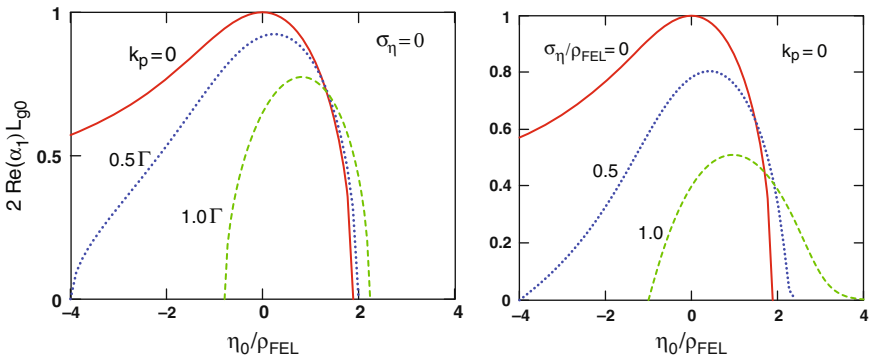

Fig. 6.2. *Left*: the growth rate function $f_{gr}(\eta_0) = 2\,\Re(\alpha_1(\eta_0))L_{g0}$ is plotted versus $\eta_0/\rho_{\mathrm{FEL}}$ for different values of the space charge parameter k_p. *Continuous red curve*: $k_p = 0$, *dotted blue curve*: $k_p = 0.5\,\Gamma$, *dashed green* curve: $k_p = 1.0\,\Gamma$. The energy spread is put to zero.
Right: the growth rate function $f_{gr}(\eta_0) = 2\,\Re(\alpha_1(\eta_0))L_{g0}$ is plotted versus $\eta_0/\rho_{\mathrm{FEL}}$ for different values of the relative beam energy spread $\sigma_\eta = \sigma_W/W_r$. *Continuous red curve*: $\sigma_\eta = 0$, *dotted blue curve*: $\sigma_\eta = 0.5\,\rho_{\mathrm{FEL}}$, *dashed green curve*: $\sigma_\eta = 1.0\,\rho_{\mathrm{FEL}}$. Here the space charge parameter is set to zero

value $k_p = 0.5\,\Gamma$ and by $\approx 30\%$ for $k_p = 1.0\,\Gamma$. The space charge forces can thus be neglected if

$$k_p \ll \Gamma \quad \Leftrightarrow \quad k_p^{-1} \gg L_{\mathrm{g0}}\ . \tag{6.4}$$

At the FLASH facility $k_p \approx 0.2\,\Gamma$, and the increase of the gain length is less than 1%.

The influence of beam energy spread is bigger. For $\sigma_\eta = 0$ the growth rate function has a maximum value of 1 which means that the power gain length L_g is indeed identical to L_{g0} (this case has already been discussed in the previous section). However, for an energy spread of $\sigma_\eta = 0.5\,\rho_{\mathrm{FEL}}$ the maximum drops to 0.8, implying that the gain length is about 25% larger than the ideal 1D gain length, $L_g \approx 1.25\,L_{\mathrm{g0}}$. At $\sigma_\eta = \rho_{\mathrm{FEL}}$ the gain length increases by more than a factor of two. Consequently, the energy spread of the electron beam must be sufficiently small because only the particles inside a narrow energy window contribute constructively to the FEL gain process. A reasonable upper limit for the tolerable rms energy spread is

$$\frac{\sigma_W}{W_r} \equiv \sigma_\eta < 0.5\,\rho_{\mathrm{FEL}}\ . \tag{6.5}$$

At FLASH the beam energy spread is $\sigma_\eta \approx 0.7 \cdot 10^{-3} \approx 0.2\,\rho_{\mathrm{FEL}}$, which means that the increase in gain length due to energy spread is less than 10%. Note, however, that the achievement of a low energy spread is a serious technical challenge for FELs operating in the X-ray regime because the FEL parameter becomes quite small here. For instance, in the X-ray FEL facility LCLS presently under construction at SLAC, the FEL parameter is $\rho_{\mathrm{FEL}} \approx 4 \cdot 10^{-4}$.

It is important to realize that any kind of energy variation inside the electron bunch, and not only the rms energy spread, will have a negative impact on the FEL gain.

6.2 Increase of Gain Length by 3D Effects

Up to now we have neglected the transverse dimensions of the electron beam. In Appendix E the three eigenvalues α_j of the third-order equation are determined for a three-dimensional beam. A cylindrical bunch with radius r_b and homogeneous charge density is considered. The amplitude of the electric field can be expressed by the Bessel function J_0 for $r < r_b$ and the modified Bessel function K_0 for $r > r_b$. The boundary conditions at $r = r_b$ lead to a determinant equation which is solved by numerical iteration and yields the eigenvalues α_j.

Is it possible to establish a criterion under which circumstances the 1D theory is sufficient or if the more complicated 3D treatment is needed? It turns out useful to define a scale parameter for the radial width of the electron beam, namely the geometric means of power gain length and optical wavelength:

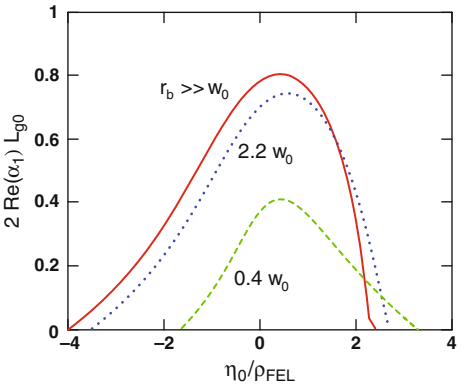

Fig. 6.3. The growth rate function $f_{\rm gr}(\eta_0) = 2\,\Re(\alpha_1(\eta_0))L_{\rm g0}$ plotted vs. $\eta_0/\rho_{\rm FEL}$ for a cylindrical beam with energy spread ($\sigma_\eta = 0.5\,\rho_{\rm FEL}$). *Continuous red curve*: wide beam with a radius $r_b \gg w_0 = \sqrt{L_{\rm g0}\lambda_\ell}$, *dotted blue curve*: narrow beam $r_b = 2.2\,w_0$, *dashed green curve*: very narrow beam, $r_b = 0.4\,w_0$

$$w_0 = \sqrt{L_{\rm g0}\lambda_\ell}\,. \tag{6.6}$$

The growth rate function $f_{\rm gr}(\eta_0) = 2\,\Re(\alpha_1(\eta_0))L_{\rm g0}$ is shown in Fig. 6.3 for a cylindrical beam of constant charge density with three different radii: $r_b \gg w_0$, $r_b = 2.2\,w_0$, and $r_b = 0.4\,w_0$. We present here the computation for a beam with an energy spread of $\sigma_\eta = 0.5\,\rho_{\rm FEL}$. According to Fig. 6.2 the 1D gain length is then $L_g^{\rm 1D} \approx 1.25\,L_{\rm g0}$. From the curves in Fig. 6.3 it is obvious that in case of a "thick" beam the gain length retains its 1D value of about $1.25\,L_{\rm g0}$ while for a very "thin" electron beam ($r_b < \sqrt{L_{\rm g0}\lambda_\ell}$) a considerable further increase in gain length has to be expected, for example by a factor of 2.5 for $r_b = 0.4\,\sqrt{L_{\rm g0}\lambda_\ell}$. Hence the one-dimensional FEL theory is adequate if the criterion

$$r_b \gg \sqrt{L_{\rm g0}\lambda_\ell} \tag{6.7}$$

is satisfied (see also Appendix E.4), but a three-dimensional treatment is needed for beams of small radius. The 1D theory is usually insufficient for a quantitative description of FELs in the UV and X-ray regime.

6.3 Overlap Between Electron and Photon Beam

The amplification process in the high-gain FEL depends critically on a good transverse overlap between electron and photon beam. Intuitively, both beams should have the same cross section to ensure that the energy transfer is optimized all along the undulator. Considering the fact that the typical diameter of a GeV electron beam is below 100 µm the undulator must be manufactured and aligned with great precision such that the deviation of the electrons from

the design orbit is not larger than 10 µm over several gain lengths. This puts stringent requirements on the field quality and mechanical accuracy of the undulator.

6.3.1 Electron Beam Focusing and Emittance

Transverse focusing is mandatory in the long undulator structures of high-gain FELs. The so-called "natural focusing" in an undulator is analogous to the "weak focusing" in circular accelerators [6]. A horizontally deflecting dipole magnet of rectangular shape exerts a weak vertical focusing which is caused by end field effects. A planar undulator is a sequence of short rectangular dipole magnets and provides thus weak focusing in vertical direction. This "natural focusing" has two disadvantages: (1) it acts only in the vertical plane, while the horizontal motion remains unfocused, and (2) it is too weak for short-wavelength FELs. To avoid the first disadvantage Scharlemann [7] proposed to shape the pole faces to be parabolic. In this way, the natural focusing can be distributed equally among both transverse directions. This solution has not been widely pursued because of the mechanical complications and the inability to adjust the beta function to the needs of the FEL. The generally adopted solution is to apply the principle of "strong focusing" [6], known from synchrotrons, by augmenting the undulator system with a periodic lattice of quadrupole lenses of alternating polarity, a so-called FODO lattice where F denotes a focusing quadrupole, D a defocusing quadrupole, and O a drift space or a weakly focusing element such as a bending magnet or an undulator. This FODO lattice can be realized either by superimposing quadrupole fields inside the undulator itself or, more conveniently, by placing electromagnetic quadrupoles between the segments of a long undulator structure. Since these segments are typically 5 m long, the period of the FODO lattice is in the order of 10 m and can be easily tuned to yield beta functions in the range from 5 to 30 m.

The rms horizontal (vertical) width of the electron beam at the position z is computed from

$$\sigma_x^2(z) = \left\langle x^2(z) \right\rangle = \varepsilon_x \beta_x(z)\,, \quad \sigma_y^2(z) = \left\langle y^2(z) \right\rangle = \varepsilon_y \beta_y(z) \tag{6.8}$$

where $\beta_x(z)$ resp. $\beta_y(z)$ is the horizontal resp. vertical beta function inside the undulator and ε_x (ε_y) the horizontal (vertical) emittance. The concept of the beta function is explained in any textbook on accelerator physics, see for example [6]. The brackets in (6.8) indicate an averaging over the betatron oscillation amplitudes and phases in the beam. The mean squared angles are given by [6]

$$\left\langle x'^2 \right\rangle (z) = \frac{1 + (\beta_x'(z)/2)^2}{\beta_x(z)}\, \varepsilon_x\,, \quad \left\langle y'^2 \right\rangle (z) = \frac{1 + (\beta_y'(z)/2)^2}{\beta_y(z)}\, \varepsilon_y\,. \tag{6.9}$$

Here $x' = dx/dz$, $y' = dy/dz$ are the slopes of the particle trajectory in the horizontal resp. vertical plane.

The emittance is, roughly speaking, the product of beam size and beam divergence. The statistical definition is

$$\boxed{\varepsilon_x = \sqrt{\langle x^2\rangle \cdot \langle x'^2\rangle - \langle x \cdot x'\rangle^2}\,, \quad \varepsilon_y = \sqrt{\langle y^2\rangle \cdot \langle y'^2\rangle - \langle y \cdot y'\rangle^2}} \tag{6.10}$$

with the subsidiary condition that the beam is centered in phase space, i.e.

$$\langle x\rangle = \langle x'\rangle = 0\,, \quad \langle y\rangle = \langle y'\rangle = 0\,.$$

In the following rough estimations one can ignore the z dependence of the beta function. Hence we average the beta function over the longitudinal coordinate z, assuming

$$\overline{\beta_x(z)} = \overline{\beta_y(z)} \equiv \beta_{\mathrm{av}}\,. \tag{6.11}$$

Furthermore, we assume a round beam ($\varepsilon_x = \varepsilon_y \equiv \varepsilon$). The emittance shrinks like $1/\gamma$ with increasing electron energy [6]. It is convention to define the normalized emittance by

$$\boxed{\varepsilon_n = \gamma\varepsilon_x\,.} \tag{6.12}$$

In principle ε_n should remain constant all along the accelerator provided collective effects or radiation can be neglected. In practice, space charge forces, radiation effects and wake fields often lead to an emittance growth and a dilution of the particle density in the beam.

Besides determining the beam size and divergence the emittance has an additional influence on the lasing process. The horizontal and vertical betatron oscillations introduce additional transverse velocity components. The average longitudinal speed of a particle carrying out betatron oscillations in the undulator is lower than the speed $\bar{v}_z$ in (2.13)

$$\bar{v}_z^{\beta} \approx \bar{v}_z - \frac{\overline{v_x^2}}{2c} - \frac{\overline{v_y^2}}{2c} = c\left(1 - \frac{1}{2\gamma^2}\left(1 + \frac{K^2}{2}\right)\right) - \frac{\overline{v_x^2}}{2c} - \frac{\overline{v_y^2}}{2c}$$

where the superscript "β" indicates the presence of a betatron oscillation. The averaging over the betatron amplitudes yields

$$\left\langle \overline{v_x^2} \right\rangle \approx c^2 \left\langle \overline{x'^2} \right\rangle \approx c^2\,\frac{\varepsilon_x}{\beta_{\mathrm{av}}}$$

and a corresponding expression holds for v_y^2. The average longitudinal speed in a beam with betatron oscillations is hence given by

$$\left\langle \bar{v}_z^{\beta} \right\rangle = \left(1 - \frac{1}{2\gamma^2}\left(1 + \frac{K^2}{2}\right)\right) c - \frac{\varepsilon_x}{\beta_{\mathrm{av}}}\,c\,. \tag{6.13}$$

Note that three different averaging procedures are applied in this equation: the "bar" in $\bar{v}_z$ denotes the mean longitudinal speed of an electron moving through the undulator on its sinusoidal trajectory, but without betatron oscillation, the

brackets in $\langle \bar{v}_z^{\beta} \rangle$ indicate the averaging over the various betatron amplitudes in a beam, and finally, $\beta_{\rm av}$ is the longitudinal average (6.11) of the beta function.

Concerning the FEL synchronization process, the reduction of the longitudinal speed is equivalent to a reduction of the mean electron beam energy. The equivalent energy reduction is computed as

$$(\delta\gamma)_{\rm eq} = \frac{d\gamma}{d\bar{v}_z}\,\delta\bar{v}_z \approx \frac{\gamma^3\delta\bar{v}_z}{c} = -\frac{\gamma^3\varepsilon_x}{\beta_{\rm av}}\ .$$

Owing to the fact that the particles in the beam have all different betatron oscillation amplitudes one obtains in fact not only a reduction in the longitudinal speed but in addition a smear which is equivalent to an energy spread of the incident beam:

$$(\sigma_\eta)_{\rm eq} = \frac{(\sigma_\gamma)_{\rm eq}}{\gamma_r} \approx \frac{\gamma_r^2\varepsilon_x}{\beta_{\rm av}}\ .$$

The energy spread of the incident beam and the equivalent energy spread caused by betatron oscillations have to be added in quadrature as they stem from statistically independent sources. Requesting that the total energy spread stays below the tolerable value, which according to the inequality (6.5) is about $\rho_{\rm FEL}/2$, we derive an upper limit for the beam emittance:

$$\varepsilon_x < \frac{\beta_{\rm av}}{2\sqrt{2}\,\gamma_r^2}\,\rho_{\rm FEL}\ . \tag{6.14}$$

The magnitude of the transverse velocity can in principle be reduced by choosing a sufficiently large beta function. On the other hand, a larger beta function yields a lower electron density and a longer gain length, so there is an optimum in between. An estimate on this optimum beta function will be given below in (6.30). In the X-ray regime the optimum beta function is in the 10–30 m range.

6.3.2 Optical Diffraction and Gain Guiding

Ideally the photon beam should have the same transverse size as the electron beam. However, like any electromagnetic wave, the FEL wave in the undulator undergoes optical diffraction. Since FEL radiation has a lot of similarity with optical laser beams we use here the Gaussian beam description, see Appendix D. The Rayleigh length z_R is defined as the distance over which the beam cross section grows by a factor of 2 from its minimum value at a beam waist. It is related to the beam waist radius w_0 by

$$z_R = \frac{\pi w_0^2}{\lambda_\ell}\ . \tag{6.15}$$

A typical number is $z_R \approx 1\,\text{m}$ for $w_0 \approx 100\,\mu\text{m}$ and $\lambda_\ell = 30\,\text{nm}$. Moving away from the waist the beam radius grows as

$$w(z) = w_0 \sqrt{1 + \left(\frac{z - z_0}{z_R} \right)^2} \,. \tag{6.16}$$

Note that in Gaussian laser beam optics it is convention to define the radial width by the condition that the intensity of a TEM_{00} beam drops to $1/e^2 = 0.135$ of its value at $r = 0$ (the electric field drops to $1/e$). From this definition follows that the rms radial width of the light beam intensity is

$$\sigma_r(z) = w(z)/2$$

and the Rayleigh length can be written as

$$z_R = \frac{4\pi\sigma_r^2}{\lambda_\ell} \,. \tag{6.17}$$

The diffractive widening of a seed laser beam is not affected by the presence of the electron beam. It is therefore important to realize a sufficiently long Rayleigh length of this beam to obtain efficient seeding in the entire lethargy regime. Once the exponential FEL gain process has started, the additionally created field depends on the transverse dimensions of the electron beam and becomes decoupled from the seed beam.

The FEL beam will also be subject to diffraction, and the resulting widening could readily spoil the good overlap with the electron beam and reduce the energy transfer from the electrons to the light wave. Fortunately there exists an effect counteracting the widening of the FEL beam which is called gain guiding.[1] Gain guiding can be understood as follows. We consider an observation point z_0 in the exponential gain region. Most of the FEL intensity at this point has been produced in the last two or three gain lengths upstream of z_0, and the width of this newly generated radiation is determined by the electron beam width. The more distant contributions are widened by diffraction, however they play a minor role because they are much smaller in amplitude. The overall result is an exponential growth of the central part of the light wave, and this part will retain its narrow width. Nevertheless, diffraction losses will occur. Three-dimensional numerical simulations show indeed that some field energy evades radially from the light beam [10].

Another beneficial effect of gain guiding is the ability of the FEL beam to follow slow, "adiabatic" deviations of the electron beam away from its nominal orbit, which might be caused by spurious magnetic background fields. This guiding is important in the very long undulator magnets of an X-ray FEL.

To provide efficient gain guiding the FEL amplification has to be large enough so that the growth of the light intensity near the optical axis overcompensates the losses by diffraction. A gain length shorter than the Rayleigh length appears thus desirable. This criterion, however, is not easy to fulfill because the gain length depends on the particle density and the rms electron beam radius as

[1] In the FEL literature, another effect named refractive or optical guiding has been discussed, see e.g. [8], [9].

$$L_{\mathrm{g0}} \propto n_e^{-1/3} \propto \sigma_r^{2/3} \; .$$

A very short gain length requires a small transverse beam size, which in turn would lead to a short Rayleigh length if we want to keep the width of the photon beam equal to that of the electron beam. A good compromise is to choose a Rayleigh length that is somewhat larger than the FEL field gain length (or twice the power gain length)

$$z_R \approx 2\, L_{\mathrm{g0}} \quad \Rightarrow \quad \frac{4\pi\sigma_r^2}{\lambda_\ell} \approx \frac{\lambda_u}{2\pi\sqrt{3}\rho_{\mathrm{FEL}}} \; . \tag{6.18}$$

Combining this with (6.8) and (6.14) we can derive an upper limit for the emittance of the electron beam that depends only on the light wavelength.

$$\frac{4\pi\varepsilon_x\beta_{\mathrm{av}}}{\lambda_\ell} \approx \frac{\lambda_u}{2\pi\sqrt{3}\,\rho_{\mathrm{FEL}}} < \frac{\lambda_u}{2\pi\sqrt{3}}\,\frac{\beta_{\mathrm{av}}}{2\sqrt{2}\gamma_r^2\,\varepsilon_x} < \frac{\lambda_\ell}{4\pi}\,\frac{\beta_{\mathrm{av}}}{\varepsilon_x}$$

using $\lambda_u/(2\gamma_r^2) < \lambda_\ell$. So the emittance must be less than about $\lambda_\ell/(4\pi)$.

This rather approximate result can be refined by a more physical argumentation. In Appendix D we show that one can define an emittance for a Gaussian laser beam as the product of rms beam width and divergence:

$$\varepsilon_L = \sigma_x\,\sigma_\theta = \frac{\lambda}{4\pi} \; . \tag{6.19}$$

Requesting that the electron beam emittance does not exceed the light beam emittance leads to the criterion

$$\boxed{\varepsilon \le \frac{\lambda_\ell}{4\pi}} \tag{6.20}$$

which is an extremely demanding requirement on the quality of the electron beam driving an X-ray FEL and cannot be fully satisfied in practice.

6.4 Parametrization of Gain Length in an X-Ray FEL

We have seen above that the power gain length computed in the full three-dimensional theory will be larger than the 1D gain length of a mono-energetic beam. Many effects such as electron beam energy spread and emittance, space charge, finite bunch length and radiation diffraction play a role. Three dimensionless parameters are useful in the characterization of a short-wavelength FEL. Following [11] we write them in the form

$$X_\gamma = \frac{L_{\mathrm{g0}} 4\pi\sigma_\eta}{\lambda_u} \quad \text{energy spread parameter} \tag{6.21a}$$

$$X_d = \frac{L_{\mathrm{g0}}\lambda_\ell}{4\pi\sigma_r^2} \quad \text{diffraction parameter} \tag{6.21b}$$

$$X_\varepsilon = \frac{L_{\mathrm{g0}} 4\pi\varepsilon}{\beta_{\mathrm{av}}\lambda_\ell} \quad \text{angular spread parameter .} \tag{6.21c}$$

From our previous considerations follows that all these parameters should be less than 1. If we insert the FEL parameter (4.49) into the inequality (6.5) we obtain

$$X_\gamma < \frac{1}{\sqrt{3}} \,. \tag{6.22}$$

The diffraction parameter is

$$X_d = \frac{L_{\mathrm{g0}}}{z_R} \approx \frac{1}{2} \tag{6.23}$$

according to (6.18). Finally, using (4.49) and (6.14) the angular spread parameter can be written as

$$X_\varepsilon = \frac{\lambda_u \varepsilon}{\sqrt{3}\,\langle\beta_{\mathrm{av}}\rangle\,\lambda_\ell\,\rho_{\mathrm{FEL}}} < \frac{\lambda_u}{2\sqrt{2}\gamma_r^2}\,\frac{1}{\sqrt{3}\lambda_\ell} < \frac{1}{\sqrt{6}} \tag{6.24}$$

where we have used $\lambda_u/(2\gamma_r^2) < \lambda_\ell$.

M. Xie [11] has expressed the 3D gain length of an X-ray FEL in the form

$$L_g = L_{\mathrm{g0}}(1 + \Lambda) \tag{6.25}$$

where $L_{\mathrm{g0}} = \lambda_u/(4\pi\sqrt{3}\rho_{\mathrm{FEL}})$ is the 1D gain length according to (4.53). Based on three-dimensional numerical studies he obtains a parametrization of the correction term Λ in the form

$$\begin{aligned}\Lambda = {} & a_1 X_d^{a_2} + a_3 X_\varepsilon^{a_4} + a_5 X_\gamma^{a_6} + a_7 X_\varepsilon^{a_8} X_\gamma^{a_9} + a_{10} X_d^{a_{11}} X_\gamma^{a_{12}} \\ & + a_{13} X_d^{a_{14}} X_\varepsilon^{a_{15}} + a_{16} X_d^{a_{17}} X_\varepsilon^{a_{18}} X_\gamma^{a_{19}}\end{aligned} \tag{6.26}$$

with the dimensionless parameters defined in (6.21). The fitted coefficients are

$$\begin{aligned} & a_1 = 0.45, \quad a_2 = 0.57, \quad a_3 = 0.55, \quad a_4 = 1.6, \quad a_5 = 3.0, \\ & a_6 = 2.0, \quad a_7 = 0.35, \quad a_8 = 2.9, \quad a_9 = 2.4, \quad a_{10} = 51, \\ & a_{11} = 0.95, \quad a_{12} = 3.0, \quad a_{13} = 5.4, \quad a_{14} = 0.7, \quad a_{15} = 1.9, \\ & a_{16} = 1140, \quad a_{17} = 2.2, \quad a_{18} = 2.9, \quad a_{19} = 3.2 \,. \end{aligned} \tag{6.27}$$

Quite a different parametrization has been proposed by Saldin et al. [12]. The power gain length[2] is written as

$$L_g = 1.19 \left(\frac{I_A}{I_{\mathrm{peak}}}\right)^{1/2} \frac{(\varepsilon_n \lambda_u)^{5/6}(1 + K^2/2)^{1/3}}{\lambda_\ell^{2/3}\widehat{K}}\,(1 + \delta) \tag{6.28}$$

with

$$\delta = \frac{262\, I_A}{I_{\mathrm{peak}}}\,\frac{\varepsilon_n^{5/4}\sigma_\gamma^2}{\widehat{K}^2(1 + K^2/2)^{1/8}\lambda_\ell^{1/8}\lambda_u^{9/8}} \,. \tag{6.29}$$

[2] Note that in [12] the field gain length is computed which is a factor of two larger than the power gain length.

Here $I_A = 17.5\,\mathrm{kA}$ is the so-called Alvfén current and I_{peak} the peak current in the electron beam. The formula is only valid if the beta function is optimized according to

$$\beta_{\mathrm{opt}} = 15.8 \left(\frac{I_A}{I_{\mathrm{peak}}}\right)^{1/2} \frac{\varepsilon_n^{3/2}\lambda_u^{1/2}}{\widehat{K}\lambda_\ell} (1+8\delta)^{-1/3} \,. \tag{6.30}$$

The two parametrizations (6.25) and (6.28) are in reasonable agreement for the LCLS and the European X-ray FEL while for FLASH the formula by Saldin et al. is not directly applicable because the average beta function in the FLASH undulator is $\beta_{\mathrm{av}} \approx 5\,\mathrm{m}$ and thus much larger than the optimized beta function of 0.9 m as computed from (6.30). Since the quadrupoles in the FLASH undulator are spaced by about 5 m it is impossible to realize a beta function of less than 1 m. The Xie formula (6.26) yields for the FLASH parameters quoted in Chap. 5 a value of $\Lambda = 0.32$ for a beta function $\beta_{\mathrm{av}} = 5\,\mathrm{m}$, so the 3D gain length is about 30% longer than the 1D gain length.

From numerical FEL simulations Kim and Xie [13] derived the following approximate formula for the saturation power

$$P_{\mathrm{sat}} \approx 1.6\,\rho_{\mathrm{FEL}} P_{\mathrm{beam}} \left(\frac{L_{\mathrm{g0}}}{L_g}\right)^2 \,. \tag{6.31}$$

Here P_{beam} is the power of the electron beam.

6.5 FEL Radiation from Short Bunches

In an ultraviolet or X-ray FEL facility the electron bunches must be made very short because otherwise the required high peak current densities cannot be achieved. But also for scientific reasons a short bunch length is desirable since it permits the generation of femtosecond X ray pulses which are indispensable in the study of ultrafast processes.

In the 1D FEL theory of Chap. 4 we have totally disregarded the effects at the head and the tail of the bunch and basically treated the bunches as being infinitely long and having a periodic substructure. Here we consider what happens if the bunch length is finite and amounts to only a few hundred radiation wavelengths.

6.5.1 Velocities

In a high-gain FEL we have to distinguish different velocities which are all lower than the speed c of a plane electromagnetic wave in vacuum: the longitudinal speed $\bar{v}_z$ of the electrons, and the phase and the group velocity of the FEL light wave.

The terms phase and group velocity are familiar from other fields of physics. As an example we take a plane electromagnetic wave, e.g. a light wave

$$E_x(z,t) = A\,\exp[i\,(kz - \omega t)]\ .$$

The phase and group velocities are

$$v_{ph} = \frac{\omega}{k}\ , \quad v_g = \frac{d\omega}{dk}\ .$$

For a light wave in free space the relationship between frequency and wave number is linear, $\omega = c\,k$, so phase and group velocity are equal, $v_{ph} = v_g = c$. The situation is different in a dispersive medium like glass where the refractive index depends on frequency, $n = n(\omega)$. Then the wavelength is $\lambda' = \lambda/n$ and the wave number becomes

$$k' = n\,k = n(\omega)\,\omega/c$$

The phase velocity

$$v_{ph} = \frac{\omega}{k'} = \frac{c}{n} \tag{6.32}$$

is now different from the group velocity

$$v_g = \frac{d\omega}{dk'} = \left(\frac{dk'}{d\omega}\right)^{-1} = c\,\left(n + \omega\,\frac{dn}{d\omega}\right)^{-1}\ . \tag{6.33}$$

The group velocity is relevant for the propagation of wave packets, for example for digital data transmission through a glass fiber.

FEL Phase Velocity

The electron beam generates the FEL wave and has an influence on its propagation. We will see that the phase and group velocities are both less than the speed of light in vacuum and rather different from each other. The phase velocity of the FEL light wave is smaller than c because of the z-dependent phase of the complex field amplitude $\tilde{E}_x$. In the exponential gain regime the field grows as

$$\begin{aligned}\tilde{E}_x(z,t) &= A\,\exp[\alpha_1 z]\,\exp[i\,kz - i\omega t] \\ &= A\,\exp[\Re(\alpha_1)z]\,\exp[i\,(k + \Im(\alpha_1))z - i\omega t] \\ &\equiv A\,\exp[\Re(\alpha_1)z]\,\exp[i\,k'z - i\omega t]\end{aligned} \tag{6.34}$$

where we have written ω and k instead of ω_ℓ and k_ℓ to simplify the notation and introduced a modified wave number k' by

$$k' = k + \Im(\alpha_1)\ . \tag{6.35}$$

The phase velocity is according to (6.32)

$$v_{ph} = \frac{\omega}{k'} = \frac{\omega}{k + \Im(\alpha_1)} \approx c\,\left(1 - \frac{c\,\Im(\alpha_1)}{\omega}\right)\ . \tag{6.36}$$

Assuming for simplicity that we are on resonance ($\eta = 0$) and that space charge can be neglected ($k_p \approx 0$) then $\Im(\alpha_1) = \Gamma/2$, see (4.51). In this case the phase velocity of the FEL wave becomes (writing now again ω_ℓ instead of ω)

$$\boxed{v_{ph} = c\left(1 - \frac{c\,\Gamma}{2\,\omega_\ell}\right) = c\left(1 - \frac{\lambda_\ell}{4\pi\sqrt{3}\,L_{\mathrm{g0}}}\right)\ .} \tag{6.37}$$

The correction term is very small. In an undulator which is $4\pi\sqrt{3} \approx 22$ gain lengths long the FEL wave slips by just one optical wavelength with respect to a plane electromagnetic wave in vacuum. This slow slippage is responsible for the FEL bucket motion shown in Fig. 5.13.

FEL Group Velocity

Of particular interest for a SASE FEL is the velocity of a "spike" in the FEL wave that extends over many optical wavelengths. The spike is represented by a wave packet propagating with the group velocity. The group velocity is according to (6.33)

$$\begin{aligned} v_g = \frac{d\omega}{dk'} &= \left(\frac{dk'}{d\omega}\right)^{-1} = \left(\frac{dk}{d\omega} + \frac{d\Im(\alpha_1)}{d\omega}\right)^{-1} \\ &= \left(\frac{1}{c} + \frac{d\Im(\alpha_1)}{d\omega}\right)^{-1} \approx c\left(1 - c\,\frac{d\Im(\alpha_1)}{d\omega}\right)\ . \end{aligned} \tag{6.38}$$

The derivative $d\Im(\alpha_1)/d\omega$ is computed in Appendix E, see (E.21).

$$\frac{d\Im(\alpha_1)}{d\omega} \approx \frac{2k_u}{3\omega_r}\ .$$

From (6.38) and $c\,k_u = \omega_r(1 + K^2/2)/(2\gamma_r^2)$ follows then that the group velocity is given by the expression

$$\boxed{v_g \approx c\left(1 - \frac{1}{3\gamma_r^2}\left[1 + \frac{K^2}{2}\right]\right)\ .} \tag{6.39}$$

Remarkably, the group velocity of a spike in the electron beam current density is identical with the optical group velocity. The proof is as follows. The current density is

$$\tilde{j}_z(\psi, z) = j_0 + \tilde{j}_1(z)\,\exp(i\,\psi) \quad \text{with} \quad \psi = (k_\ell + k_u)z - \omega_\ell t\ .$$

According to (4.20) the complex amplitude $\tilde{j}_1$ is proportional to the derivative of $\tilde{E}_x$. In the exponential gain regime, the z dependence of $\tilde{j}_1$ is therefore the same as that of $\tilde{E}_x$, namely $\exp(\alpha_1 z)$.

$$\tilde{j}_1 \exp(i\,\psi) \propto \exp[\Re(\alpha_1)z]\, \exp[i\,\Im(\alpha_1)z] \exp[i(k_\ell + k_u)z - i\,\omega_\ell t]$$

The phase of the modulated current density differs from that of the FEL field only by the term $k_u z$. Now $k_u = 2\pi/\lambda_u$ is a constant, independent of frequency. Application of formula (6.38) yields thus the exactly same group velocity as in the FEL wave. This equality has a deep physical relevance: a bump in the electron charge distribution is associated with a corresponding bump in the FEL field due to the FEL gain process, and hence one would expect that both bumps move with the same speed, which they indeed do.

The group velocity is considerably lower than the phase velocity. We have seen above that in an undulator of the length $L_u = 22L_{\mathrm{g0}}$ the phase of a harmonic FEL wave slips by one optical wavelength with respect to a plane electromagnetic wave. In contrast to this an FEL wave packet slips by a few hundred optical wavelengths. On the other hand, the group velocity is larger than the average longitudinal speed of the electrons which is according to (2.13)

$$\bar{v}_z = c\left(1 - \frac{1}{2\gamma_r^2}\left[1 + \frac{K^2}{2}\right]\right) .$$

The difference is

$$\boxed{v_g - \bar{v}_z = \frac{c}{6\gamma_r^2}\left[1 + \frac{K^2}{2}\right] .} \tag{6.40}$$

From this we conclude that spikes (wave packets) in the FEL wave, or spikes in the electron charge distribution, will slip forward inside the electron bunch during the motion through the undulator.

6.5.2 Slippage Effects in Short Bunches

We consider an example which illustrates very nicely the slippage effects occurring in free-electron lasers driven by short electron bunches. The bunch considered has a narrow leading spike and a long tail, which is similar to the shape of the compressed bunch in FLASH. The local current I_0 as a function of the internal bunch coordinate ζ is depicted in Fig. 6.4. The peak current is $I_{\mathrm{peak}} = 1600$ A. We assume that the lasing process is started by seed radiation with an amplitude of $E_0 = 5\,\mathrm{MV/m}$. The simulation of the FEL process is done using the coupled first-order equations (C.7) in their generalized form, including the dependencies on the internal bunch coordinate ζ. The typical FLASH parameters quoted in Chap. 5 are used. At a position of $z = 18\,L_{\mathrm{g0}}$ in the undulator the maximum of the modulation current has almost reached the peak current, but the width of the curve $I_1(t)$ is narrower than the bunch itself which is described by the curve $I_0(t)$. This is due to the fact that the FEL gain depends on the beam current and is suppressed in the tail of the bunch.

In Fig. 6.5 the electric field of the light wave (in units of 10^{10}V/m) and the normalized modulation current I_1/I_{peak} are shown at various positions in

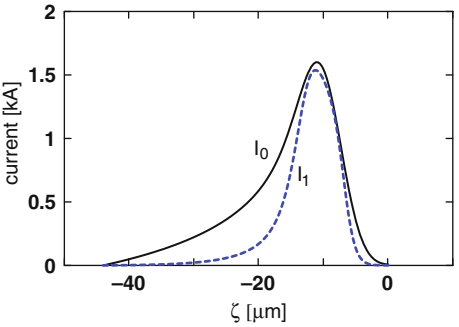

Fig. 6.4. Typical shape of an electron bunch at FLASH. The local "direct current" I_0 is plotted as a function of the internal bunch coordinate ζ (*solid black curve*). The bunch head is on the *right side*. The modulation current I_1 is shown by the *dashed blue curve*. The longitudinal position in the undulator magnet is $z = 18\,L_{\mathrm{g0}}$

the undulator. Close to the end of the exponential gain regime at $z = 18\,L_{\mathrm{g0}}$ the modulation current I_1 has reached the level of the peak current and the electric field of the light wave has grown to 8000 MV/m. Here the longitudinal profile of the field resembles closely the shape of the I_1 distribution inside the bunch, but is a bit narrower than the bunch itself.

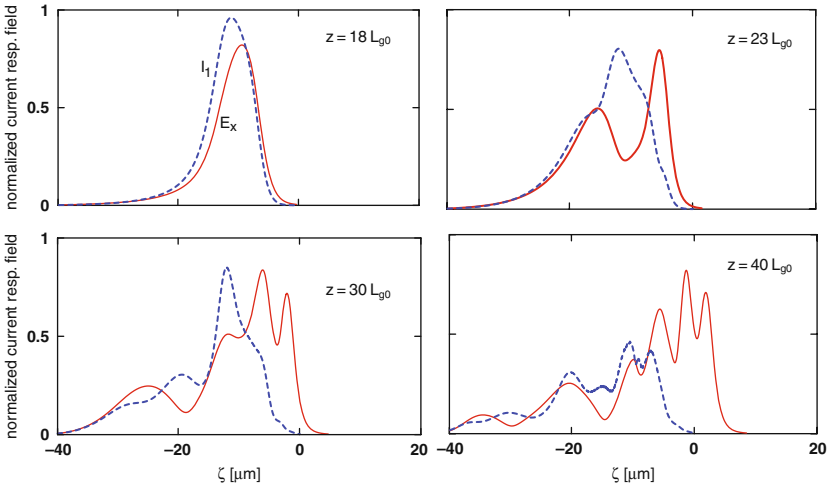

Fig. 6.5. FEL radiation from a FLASH-type electron bunch. The electric field of the FEL wave is plotted as a function of the internal bunch coordinate ζ (*continuous red curves*). The unit is 10^{10} V/m = 10 GV/m. The normalized modulation current I_1/I_{peak} is shown by the *dashed blue curves*. The evolution of modulation current and FEL field is displayed at various longitudinal positions in the undulator magnet: $z = 18\,L_{\mathrm{g0}}, 23\,L_{\mathrm{g0}}, 30\,L_{\mathrm{g0}}, 40\,L_{\mathrm{g0}}$

Next we look into the saturation regime. At $z \geq 20\,L_{g0}$, the modulation current develops a structure with two or more peaks that is quite different from the bunch shape. The electric field amplitude of the light wave is also characterized by a complicated structure. Narrow wave packets of the FEL field escape from the bunch and move away from the bunch head. This is clear evidence for the slippage effect. When an FEL wave packet has slipped away from the bunch it will move with the speed c of light in vacuum, and its magnitude will remain invariant because the overlap with the electron beam is no longer existent and the FEL gain process has come to an end.

It is important to note that the spikes are by no means identical with the microbunches. Rather they are wave packets extending over many optical wavelengths. Inside the bunch they propagate with the FEL group velocity (6.39) and are thus faster than the microbunches which move with a speed that is very close to the average longitudinal speed $\bar{v}_z$ of the electrons (compare Figs. 5.12, 5.13).

Longitudinal Structure of the FEL Pulses

The above figures show that the simulated FEL pulses contain amazingly short wave packets. What is the physical origin of these sharp substructures? We want to demonstrate that this is nothing else but the oscillatory behavior of the FEL power in the saturation regime that we observed earlier in Chap. 5. In order to see this we go back to Fig. 5.4 where the computed FEL power on a logarithmic scale has been plotted against z/L_{g0}. The same data are used to show in Fig. 6.6a the z dependence of the absolute magnitude of the electric light wave field $\left|\tilde{E}_x(z)\right|$ on a linear scale. Here the oscillations reflect obviously the back-and-forth energy exchange between electron bunch and light wave. Converting to the internal bunch coordinate ζ and taking into

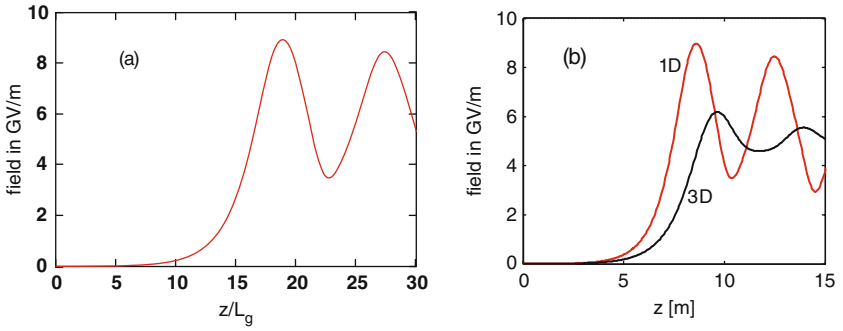

Fig. 6.6. (**a**) The magnitude of the electric light wave field on a linear scale, plotted as a function of the longitudinal position z in the undulator. The parameters are the same as in Fig. 5.4. (**b**) Comparison of the field rise in the 1D and the 3D FEL theory

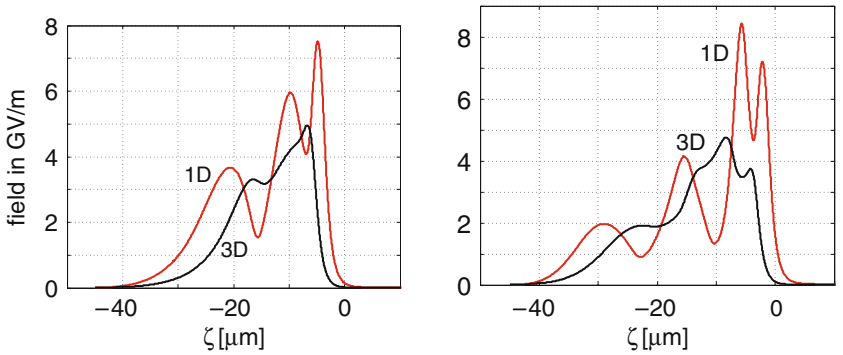

Fig. 6.7. Comparison of the FEL pulse shape in the 1D theory (*red curve*) and the full 3D theory (*black curve*) at two positions in the undulator. We thank Igor Zagorodnov of DESY for carrying out the 3D calculations using the code GENESIS

consideration that bunch head enters the saturation regime earlier than the tail (which implies a sign reversal) one obtains similar sharp time spikes as seen in Fig. 6.5.

The question arises whether these sharp peaks are to be expected in a realistic FEL or whether they are just an artifact of our oversimplified one-dimensional FEL model. The second alternative turns out to be correct. According to computations with three-dimensional FEL codes the gain oscillations in the saturation regime are much less pronounced than predicted by the 1D theory, see Fig. 6.6b. This is in fact easy to understand. In the 1D model the density of the electron beam and the amplitude of the light wave do not depend on the radial coordinate $r = \sqrt{x^2 + y^2}$ while in reality both charge density and field amplitude drop with increasing distance from the beam axis. The reduced coupling strength at $r > 0$ implies that the saturation regime is reached later for off-axis electrons than for on-axis electrons. Consequently, we can expect that the gain oscillations will be smeared out for realistic electron and photon beams. This smearing will also wash out the spike structure of the FEL pulses as demonstrated in Fig. 6.7. In addition, optical diffraction plays a larger role in the saturation regime and reduces the electric field close to the axis.

6.6 Superradiance

Bonifacio and others [14] have predicted the possibility of a reduction of the light pulse length to values below the electron bunch length if the exponential gain regime has been passed. The term *superradiance* is used to describe this pulse shortening regime in which the radiated FEL power is proportional to the square of the number of electrons. In a recent experiment [15] superradiance has been observed in a single-pass high-gain FEL which was seeded by

a titanium-sapphire laser at 800 nm. Using frequency resolved optical gating the FEL pulse duration was measured to be 81.7 fs (rms) while the seed pulse was 150 fs long, and the electron bunch was even more than 1 ps long. In the superradiant regime the FEL power is expected to grow quadratically with the distance z along the undulator.

The interpretation of superradiance is based on the assumption that the radiation pulse slips forward inside the bunch, owing to the fact that the optical group velocity is larger than the longitudinal speed of the electrons, and that this light pulse therefore withdraws energy from "fresh" electrons that have not yet been microbunched.

References

1. Fawley, W.: Report No. LBNL-49625, Lawrence Berkeley Laboratory (2002) 83
2. Reiche, S.: GENESIS 1.3, a fully 3D time-dependent FEL simulation code. Nucl. Instrum. Meth. **A 429**, 243 (1999) 83
3. Saldin, E.L., Schneidmiller, E.A., Yurkov, M.V.: FAST: a three-dimensional timedependent FEL simulation code. Nucl. Instr. Meth. **A 429**, 233 (1999) 83
4. Saldin, E.L., Schneidmiller, E.A., Yurkov, M.V.: The Physics of Free Electron Lasers. Springer, Berlin, Heidelberg (2000) 83
5. Huang, Z., Kim, K.-J.: Review of x-ray free-electron laser theory. Phys. Rev. ST Accel. Beams **10**, 034801 (2007) 83
6. Edwards, D.A., Syphers, M.J.: An Introduction to the Physics of High Energy Accelerators. John Wiley, New York (1993) 88, 89
7. Scharlemann, E.T.: Wiggle plane focusing in linear wigglers. J. Appl. Phys. **58**, 2154 (1985) 88
8. Scharlemann, E.T., Sessler A.M., Wurtele, J.S.: Optical guiding in a free-electron laser. Phys. Rev. Lett. **54**, 1925 (1985) 91
9. Freund H.P., Antonsen, T.M.: Principles of Free-Electron Lasers, 2nd ed., Chapman & Hall, London (1996) 91
10. Huang, Z., Kim, K.-J.: Transverse and temporal characteristics of a high-gain free-electron laser in the saturation regime. Nucl. Instr. Meth. **A 483**, 504 (2002) 91
11. Xie, M.: Exact and variational solutions of 3D eigenmodes in high gain FELs. Nucl. Instr. Meth. **A 445**, 59 (2000) 92, 93
12. Saldin, E.L., Schneidmiller, E.A., Yurkov, M.V.: Design Formulas for VUV and X-Ray FELs, Proc. of FEL Conference. (2004) 93
13. Kim, K.-J., Xie, M.: Self-amplified spontaneous emission for short wavelength coherent radiation. Nucl. Instr. Meth. **A 331**, 359 (1993) 94
14. Bonifacio, R., et al.: Spectrum, temporal structure, and fluctuations in a high-gain free-electron laser starting from noise. Phys. Rev. Lett. **73**, 70 (1994) 100
15. Watanabe, T., et al.: Experimental characterization of superradiance in a single-pass high-gain laser-seeded free-electron laser. Phys. Rev. Lett. **98**, 038402 (2007) 100

7

Self-Amplified Spontaneous Emission

For wavelengths in the ultraviolet and X-ray regime the start-up of the FEL process by seed radiation is not readily done due to the lack of suitable lasers. Seeding by a high harmonic of an optical laser is a widely discussed idea. The process of Self-Amplified Spontaneous Emission SASE permits the startup of lasing at an arbitrary wavelength, without the need of external radiation. The SASE mechanism was proposed and theoretically explored in the early 1980s [1, 2, 3, 4] but it took 20 years before it could be verified experimentally at visible and ultraviolet wavelengths.

The most intuitive explanation of SASE is that the electrons produce spontaneous undulator radiation in the first section of a long undulator magnet which serves then as seed radiation in the main part of the undulator. The FEL can also be started by a periodic charge density modulation in the electron beam, as discussed in Sect. 5.3. The bunches coming from the accelerator do not possess such a modulation at the light wavelength. But due to the fact that they are composed of a large number of randomly distributed electrons a white noise spectrum is generated which has a spectral component within the FEL bandwidth (see Appendix F). This component will be amplified according to Fig. 5.3.

The above two interpretations of SASE are physically equivalent: seeding by spontaneous undulator radiation or FEL start-up by the proper Fourier component of the stochastic density modulation in the electron beam. Randomness is obviously essential in the second model of the SASE process but it is equally important in the first model. It must be noted that the emission of undulator radiation by a bunch much longer than the light wavelength would be impossible if the longitudinal particle distribution were perfectly uniform, in the extreme case, if the electron beam current would be a perfect direct current (dc current). A perfect dc current moving on a sinusoidal orbit through the undulator magnet cannot emit any radiation because there are no oscillating charges. Likewise, a perfect dc current circulating in an electron synchrotron or storage ring would be unable to emit ordinary synchrotron radiation.

P. Schmüser, et al.: *Self-Amplified Spontaneous Emission*, STMP **229**, 103–120 (2008)
DOI 10.1007/978-3-540-79572-8_7

7.1 Computation of the SASE Process in the 1D Theory

7.1.1 Solution of the Third-Order Equation

In this section the equivalent current density modulation $\tilde{j}_1$ arising from the random time distribution of the electrons in the bunch is used as an input for calculating the time evolution of the FEL power by means of the method discussed in Sect. 5.3. The initial conditions are according to (5.14)

$$\begin{pmatrix} \tilde{E}_x(0) \\ \tilde{E}'_x(0) \\ \tilde{E}''_x(0) \end{pmatrix} = \begin{pmatrix} 0 \\ -1 \\ i\,2k_u\eta \end{pmatrix} \frac{\mu_0 c\,\widehat{K}}{4\gamma_r}\,\tilde{j}_1(0)\,.$$

It is convenient to factor out the driving term $\mu_0 c\,\widehat{K}\,\tilde{j}_1(0)/(4\gamma_r)$ by introducing new coefficients d_j

$$\begin{pmatrix} d_1 \\ d_2 \\ d_3 \end{pmatrix} = \begin{pmatrix} 1 & 1 & 1 \\ \alpha_1 & \alpha_2 & \alpha_3 \\ \alpha_1^2 & \alpha_2^2 & \alpha_3^2 \end{pmatrix}^{-1} \cdot \begin{pmatrix} 0 \\ -1 \\ i\,2k_u\eta \end{pmatrix}. \tag{7.1}$$

Then the field amplitude becomes

$$\tilde{E}_x(z) = \sum_{j=1}^{3} d_j \exp(\alpha_j z) \cdot \frac{\mu_0 c\,\widehat{K}}{4\gamma_r}\,\tilde{j}_1(0)\,. \tag{7.2}$$

In Appendix F it will be shown that the equivalent modulated current density resulting from shot noise is given by the formula

$$\tilde{j}_1(0) = \sqrt{\frac{e\,I_0\,\Delta\omega}{\pi}}\,\frac{1}{A_b} \tag{7.3}$$

where I_0 is the absolute magnitude of dc electron beam current, A_b the beam cross section and $\Delta\omega$ the width of the FEL bandwidth curve (assuming a rectangular shape of the bandwidth curve). Using the transmission function (see below) one finds

$$\Delta\omega = \sqrt{2\pi}\,\sigma_\omega\,.$$

First an approximate computation is made with a constant bandwidth. To achieve saturation one needs about 20 gain lengths in FLASH, see Fig. 7.1 below. Using (5.13) we compute then a bandwidth of $\Delta\omega \approx 2.4\,\omega_\ell\,\rho_{\mathrm{FEL}}$. This is substituted in (7.3). The central frequency is taken as $\omega = \omega_r$ hence $\eta = 0$ in (7.1). The FEL power as a function of the position z in the undulator is computed with (7.2).

$$\begin{aligned} P_{\mathrm{cb}}(z) &= \frac{A_b}{\mu_0 c}\left|\tilde{E}_x(z)\right|^2 \\ &= \frac{\mu_0 c\,\widehat{K}^2}{16\gamma_r^2}\left|\sum_j d_j \exp(\alpha_j z)\right|^2 \frac{e\,I_0}{\pi A_b}\,2.4\,\rho_{\mathrm{FEL}}\omega_\ell \end{aligned} \tag{7.4}$$

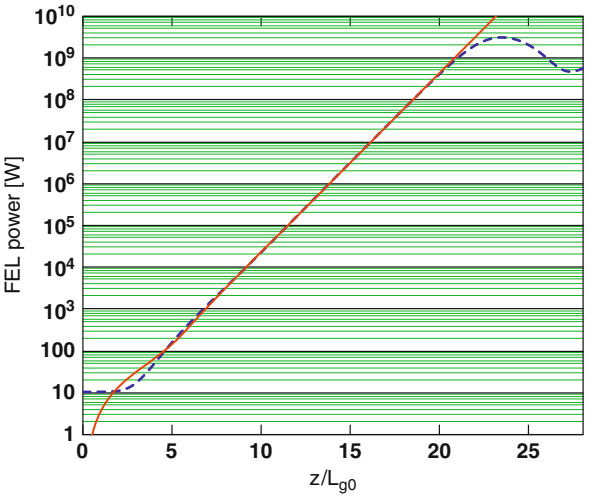

Fig. 7.1. Computed SASE FEL power in FLASH as a function of z/L_{g0} (*continuous red curve*). The startup is provided by the electron current density modulation with the period λ_ℓ which is due to the random distribution of the electrons in the bunch. For comparison the power rise of a seeded FEL is also shown, choosing a seeding field of $E_0 = 0.5$ MV/m (*dashed blue curve*). Here the gain curve has been computed by means of the coupled first-order equations so that the FEL saturation is included

where we have assumed that electron beam and light beam have the same cross section A_b. The subscript "cb" stands for constant bandwidth. The FEL power as a function of z/L_{g0} is shown in Fig. 7.1. It is interesting to compare the power rise curve of a SASE FEL to that of a seeded FEL. The field amplitude E_0 of the seed wave has been adjusted to yield the same power level in the exponential regime as obtained in the SASE FEL. For typical FLASH parameters at an electron energy of 500 MeV we find $E_0 = 0.5$ MV/m. This computation permits us to determine the minimum seed laser field which is needed to be well above the SASE level. In the present example seeding will dominate for an initial field value E_0 exceeding a few MV/m. We come back to this important issue in Sect. 7.1.3.

We learn from Fig. 7.1 that saturation is reached after about 20 gain lengths, so the *saturation length* is

$$L_{\mathrm{sat}} \approx 20 L_{\mathrm{g0}}\,.$$

This is in fact a rather typical number. In Ref. [5] the following formula is given for the saturation length of a SASE X-ray FEL

$$L_{\mathrm{sat}} \approx \frac{\lambda_u}{\rho_{\mathrm{FEL}}} = 4\pi\sqrt{3} L_{\mathrm{g0}} = 21.8\, L_{\mathrm{g0}}\,. \tag{7.5}$$

In the next step we abandon the restriction to a constant bandwidth because in reality the FEL bandwidth is larger in the beginning of the undulator

and drops with increasing z. For example, the bandwidth at $z = 5\,L_g$ is about twice as large as at $z = 20\,L_g$. Therefore the curve in Fig. 7.1 underestimates the FEL power in the first part of the undulator but should be correct near the end of the exponential regime. The variable bandwidth will be taken into account using formula (5.13). The FEL power as a function of the distance z along the undulator axis becomes then

$$P_{\rm vb}(z) = \frac{\mu_0 c\,\widehat{K}^2}{16\gamma_r^2}\,\left|\sum_j d_j \exp(\alpha_j z)\right|^2\,\frac{2\,e\,|I_0|}{\pi A_b}\,6\,\sqrt{\pi}\,\rho_{\rm FEL}\,\omega_\ell\,\sqrt{\frac{L_{\rm g0}}{z}}\,. \qquad (7.6)$$

where the subscript "vb" stands now for variable bandwidth. The FEL power computed with a z dependent bandwidth is higher at low values of $z/L_{\rm g0}$ but approaches the constant-bandwidth curve for $z > 10\,L_{\rm g0}$. In the exponential gain regime $4\,L_{\rm g0} \le z \le L_{\rm sat}$, only the eigenfunction $\exp(\alpha_1 z)$ contributes and the following approximate formula holds

$$P_{\rm vb}(z) \approx \frac{m_e^2 c^4 \gamma_r^2}{3\,\sqrt{\pi}}\,\rho_{\rm FEL}^2\,\omega_\ell\,\exp\left(\frac{z}{L_{\rm g0}}\right)\sqrt{\frac{L_{\rm g0}}{z}}\,. \qquad (7.7)$$

7.1.2 Transmission Function Approach

In the previous section we have implicitly assumed that the eigenvalues α_j are given by their values on resonance ($\eta = 0$), and we have taken into account the bandwidth of the FEL by the multiplicative factor $\Delta\omega$. This is only approximately correct. Now we make a more careful analysis.

We study the SASE mechanism with a mono-energetic electron beam. The detuning parameter is a function of frequency according to (5.7). Our first goal is to compute the eigenvalues α_j for a certain light frequency ω which will in general be different from the resonance frequency ω_r. In the spirit of the argumentation in Sect. 5.2.1 we translate this frequency shift into an equivalent energy shift of the electron beam. The eigenvalues for a beam with energy detuning are given by (E.18) in Appendix E. These eigenvalues depend now implicitly on frequency.

We define a *transmission function* relating current and field in frequency domain

$$H(\omega, z) = \left(\, e^{\alpha_1 z}\; e^{\alpha_2 z}\; e^{\alpha_3 z}\,\right)\cdot\begin{pmatrix} 1 & 1 & 1 \\ \alpha_1 & \alpha_2 & \alpha_3 \\ \alpha_1^2 & \alpha_2^2 & \alpha_3^2 \end{pmatrix}^{-1}\cdot\begin{pmatrix} 0 \\ -1 \\ i\,2k_u\eta \end{pmatrix}\,. \qquad (7.8)$$

The spectral component of the electric field at the position z is

$$\tilde{E}_x(\omega, z) = \frac{\mu_0 c\,\widehat{K}}{4\gamma_r}\,H(\omega, z)J(\omega) \qquad (7.9)$$

where $J(\omega)$ is the spectral current density whose magnitude is

$$|J(\omega)| = \sqrt{\frac{e\,I_0}{\pi}}\,\frac{1}{A_b}$$

according to equation (F.13). The radiated power is

$$P(z) = \frac{A_b}{\mu_0 c}\int_0^\infty \left|\tilde{E}_x(\omega,z)\right|^2 d\omega = \frac{\mu_0 c\,\widehat{K}^2 e\,I_0}{16\pi\gamma_r^2 A_b}\int_0^\infty |H(\omega,z)|^2\,d\omega\,. \qquad (7.10)$$

The power computed from this equation is compared in Fig. 7.2 with the constant-bandwidth formula. The transmission function automatically incorporates the variable bandwidth and yields thus higher FEL power in the first section of the undulator.

7.1.3 Comparison of FEL Startup by Seeding or by SASE

In order to compare the two different startup mechanisms we use (4.57) to determine the coefficients c_j in the eigenfunction expansion

$$\tilde{E}_x(z) = \sum_j c_j \exp(\alpha_j z)$$

according to

$$\begin{pmatrix} c_1 \\ c_2 \\ c_3 \end{pmatrix} = \boldsymbol{\mathcal{A}}^{-1} \cdot \begin{pmatrix} \tilde{E}_x(0) \\ \tilde{E}'_x(0) \\ \tilde{E}''_x(0) \end{pmatrix}.$$

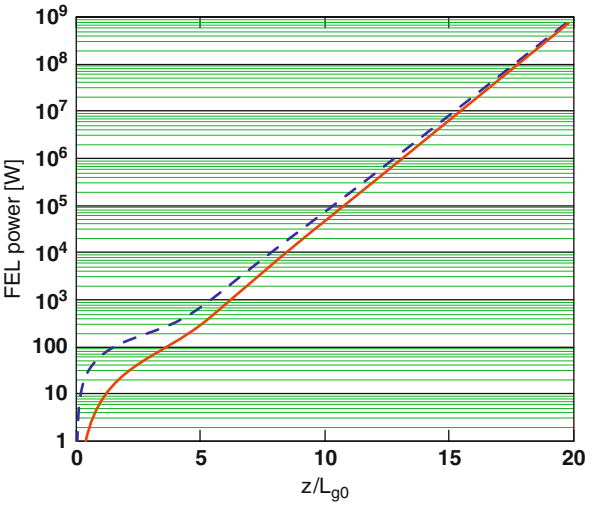

Fig. 7.2. *Dashed blue curve*: Computed SASE FEL power as a function of z/L_{g0} according to (7.10). *Solid red curve*: power $P_{\mathrm{cb}}(z)$ according to the constant-bandwidth formula (7.4)

We take the simplest form of the matrix $\boldsymbol{\mathcal{A}}^{-1}$, see (4.59):

$$\boldsymbol{\mathcal{A}}^{-1} = \frac{1}{3} \cdot \begin{pmatrix} 1 & (\sqrt{3}-i)/(2\Gamma) & (-i\sqrt{3}+1)/(2\Gamma^2) \\ 1 & (-\sqrt{3}-i)/(2\Gamma) & (i\sqrt{3}+1)/(2\Gamma^2) \\ 1 & i/\Gamma & -1/\Gamma^2 \end{pmatrix} . \tag{7.11}$$

In case of seeding by an external laser, corresponding to field stimulation, the initial condition is

$$\begin{pmatrix} \tilde{E}_x(0) \\ \tilde{E}'_x(0) \\ \tilde{E}''_x(0) \end{pmatrix} = E_{\mathrm{in}} \begin{pmatrix} 1 \\ 0 \\ 0 \end{pmatrix}$$

and from (7.11) follows that the c_j are all equal,

$$c_j = \frac{E_{\mathrm{in}}}{3} , \quad j = 1, 2, 3 .$$

In case of SASE we have current stimulation caused by shot noise. Then the initial condition reads

$$\begin{pmatrix} \tilde{E}_x(0) \\ \tilde{E}'_x(0) \\ \tilde{E}''_x(0) \end{pmatrix} = -\frac{\mu_0 c \widehat{K}}{4\gamma_r} \, \tilde{j}_1 \begin{pmatrix} 0 \\ 1 \\ 0 \end{pmatrix}$$

(here we have assumed $\eta = 0$). Applying (7.11) we find

$$|c_j| = \frac{1}{3\Gamma} \, \frac{\mu_0 c \widehat{K}}{4\gamma_r} \, \left|\tilde{j}_1\right| .$$

The equivalent input field is hence

$$E_{\mathrm{equiv}} = \frac{\mu_0 c \widehat{K}}{4\gamma_r \Gamma} \, \left|\tilde{j}_1\right| = \frac{\mu_0 c \widehat{K}}{4\gamma_r \Gamma} \, \frac{\sqrt{e\, I_0 \Delta\omega}}{\sqrt{\pi}\, A_b} . \tag{7.12}$$

With the FLASH parameters used in Sect. 7.1.1 we obtain an equivalent input field of 0.54 MV/m, in good agreement with the value of 0.5 MV/m used in Fig. 7.1. Only in the case that the seeding field E_0 exceeds the equivalent field E_{equiv} by a sufficient margin one can expect that the properties of the FEL output radiation such as pulse length, coherence and bandwidth are determined by the seed radiation rather than by the SASE process. The required seeding field level has to be maintained over a stretch of more than three gain lengths such that the seeded FEL is able to leave the lethargy regime and enter the exponential-gain regime. This is an important constraint on the beam quality and power of the seed radiation which becomes very demanding if one wants to use a high harmonic of optical laser radiation.

7.2 Experimental Results on SASE FEL Radiation

7.2.1 Detection of SASE, Exponential Gain and Saturation

The first experimental demonstration of the SASE mechanism was carried out in the infrared wavelength range [6, 7]. The first successful operation of a SASE FEL in the visible and near-ultraviolet range was accomplished at the low-energy undulator test line LEUTL at Argonne National Laboratory near Chicago, USA [8]. The gain curve measured at 530 nm is shown in Fig. 7.3. Similar data were obtained at 385 nm. The exponential rise and saturation of the FEL intensity is nicely seen both at the visible and the ultraviolet wavelength.

The LEUTL team has made a very nice experimental verification of the microbunching associated with the high-gain FEL process. Coherent optical transition radiation at the FEL wavelength was detected.[1] The data shown

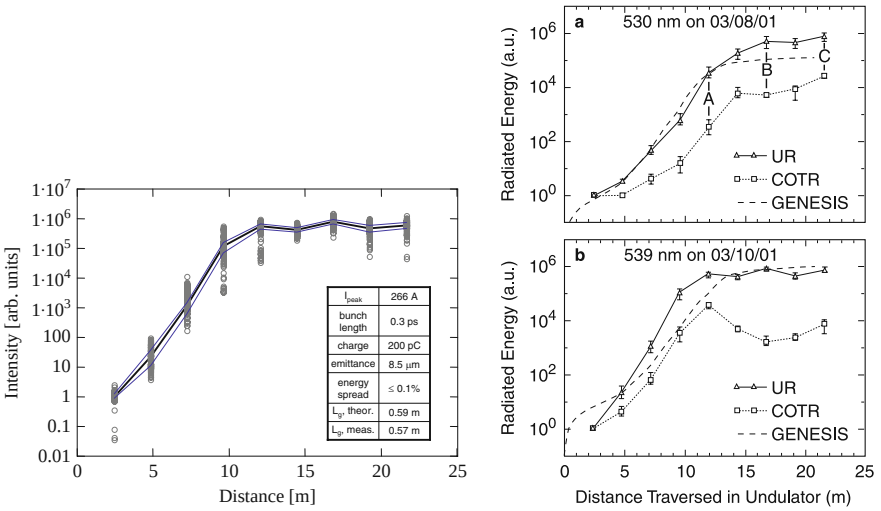

Fig. 7.3. *Left side*: SASE radiation in the low-energy undulator test line LEUTL at 530 nm. The FEL intensity is shown as a function of the distance in the undulator (courtesy S. Milton). *Right side*: energy of SASE FEL radiation (labeled as UR) and of coherent optical transition radiation (COTR) as a function of distance in the undulator [9]. The wavelength was 530 nm resp 539 nm. The *dashed curve* shows the prediction of the FEL code GENESIS. In the COTR measurement the FEL light beam was absorbed by a thin foil which did not disturb the microbunching inside the electron bunch. The radiation screen was mounted downstream of this foil. (Figure reprinted with permission from [9]. Copyright 2002 by the American Physical Society).

[1] Transition radiation is produced when relativistic particles cross the boundary between two media of different refractive indices. The radiation emitted in backward

in Fig. 7.3 demonstrate convincingly the formation of microbunches with the periodicity given by the light wavelength. A similar exponential rise is observed both in the FEL light and in the coherent optical transition radiation.

Shortly afterwards a successful SASE experiment was carried out at DESY in Hamburg, Germany at the vacuum-ultraviolet (VUV) wavelength of 109 nm [10]. In the next series of measurements wavelengths between between 80 and 180 nm were covered and FEL saturation was established [11, 12]. The data at 98 nm have already been presented in Fig. 4.2. These were the first measurements showing FEL saturation in the VUV regime. After an energy upgrade to 700 MeV (1 GeV at a later stage) and an increase of the undulator length from 13.5 to 27 m the FEL was renamed into FLASH. This FEL user facility will be described in Chap. 8. At FLASH lasing has been measured so far at 32, 25, 13.7 and 6.5 nm.

The data at a fundamental wavelength of 13.7 nm [13] are presented in Fig. 7.4. Exponential gain and FEL saturation have been established for the first time in the extreme ultraviolet. Analysis of the exponential part of the gain curve yields a power gain length of $L_g = 1.25 \pm 0.15$ m. Quite remarkable is the observation of the third and fifth harmonic at 4.6 nm resp. 2.75 nm, see

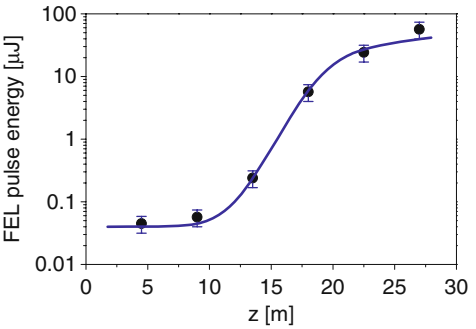

Fig. 7.4. Experimental evidence for exponential gain and FEL saturation in the extreme ultraviolet at $\lambda_\ell = 13.7$ nm [13]. The average light pulse energy is plotted as a function z. Note that this light pulse energy is in fact the sum of the FEL pulse energy and the contribution from spontaneous undulator radiation entering the light detector. The effective undulator length z is varied in the experiment by switching on kicker magnets at selected positions inside the long undulator system, thereby destroying the good overlap between electron and photon beam in the downstream section of the undulator and inhibiting further FEL gain. The intensity of the spontaneous radiation is hardly affected by the induced small orbit distortions

direction is in the visible and infrared range. Optical transition radiation (OTR) is frequently applied at electron accelerators to obtain images of the beam cross section, see Sect. 8.9.2. The radiation is incoherent in most cases because the bunch is much longer than the optical wavelength. Coherent optical transition radiation will be generated if the bunch possesses a periodic density modulation with the period being equal to the optical wavelength.

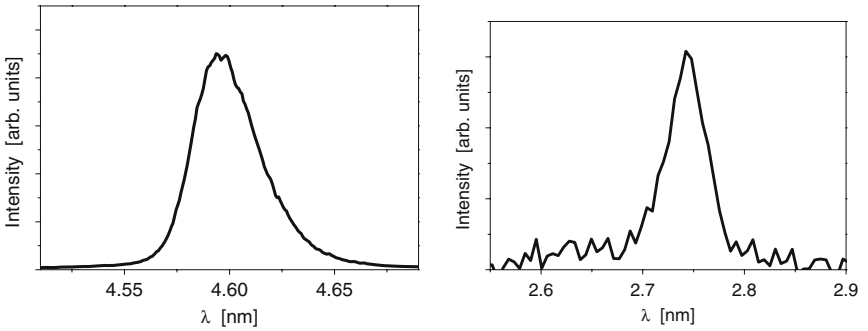

Fig. 7.5. Spectra of the third harmonic (*left*) and fifth harmonic (*right*) of 13.7 nm FEL radiation [13]. For an average pulse energy of 40 µJ at the first harmonic, a pulse energy of 0.25 µJ was measured at the third harmonic (4.6 nm) and of 10 nJ at the fifth harmonic (2.75 nm)

Fig. 7.5. The fifth harmonic is within the so-called *water window*, a spectral region in the extreme ultraviolet where water becomes transparent. Radiation in this region is crucially important for the investigation of biological matter. Higher harmonics of the 32 nm line have also been seen [14] (Fig. 7.6). In this measurement the second harmonic at 15.9 nm was observed, but with a twenty times lower intensity than the third harmonic at 10.5 nm. According to theoretical predictions [15] the contribution of the second harmonic to the total radiation power depends on the ratio of the FEL gain length to the Rayleigh length of the radiation. In the parameter range of FLASH the second harmonic is found to be strongly suppressed [13].

SASE radiation at 840 nm and at the second and third higher harmonic have been reported from the VISA FEL at Brookhaven National Laboratory (BNL), USA [16]. The FEL pulse energy as a function of distance traveled in the undulator exhibits an exponential rise (Fig. 7.7). Both SASE and seeded FEL lasing have been accomplished at wavelengths of 266 and 400 nm in the Deep Ultra-Violet (DUV) FEL at the National Synchrotron Light Source at BNL [17]. SASE radiation at 49 nm was observed in 2006 at the test accel-

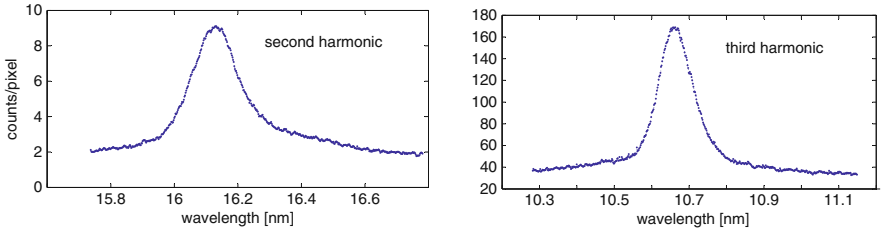

Fig. 7.6. Spectra of the second harmonic (*left*) and third harmonic (*right*) of 32 nm FEL radiation [14]

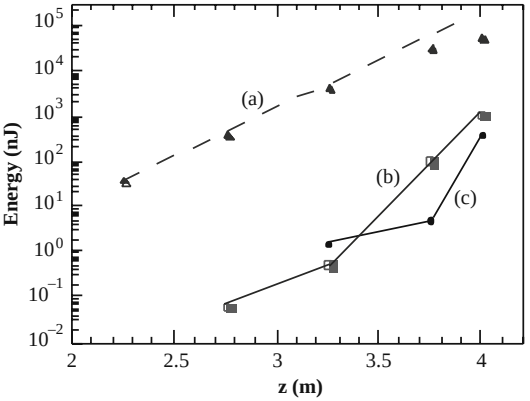

Fig. 7.7. FEL pulse energy vs. distance of the 840 nm FEL radiation at VISA ((Visible to Infrared SASE Amplifier). (**a**) First harmonic, (**b**) second harmonic, (**c**) third harmonic. We thank S. Reiche for providing us with this figure

erator SCSS of the Japanese XFEL project [18], see Fig. 7.8. Saturation has been achieved at 30–60 nm with a pulse energy of 30 μJ (T. Shintake, private communication).

7.2.2 Statistical Properties of SASE radiation

The emission of spontaneous undulator radiation is a stochastic process, and as a consequence SASE FEL radiation, starting from shot noise, has the properties of chaotic light. A characteristic feature are shot-to-shot fluctuations in wavelength. An experimental example is shown in Fig. 7.9. The FEL pulses seen in this figure show 1–3 spikes of variable height. The averaged spectrum of many FEL pulses has a smooth lineshape according to the gain curve discussed in Sect. 5.1.

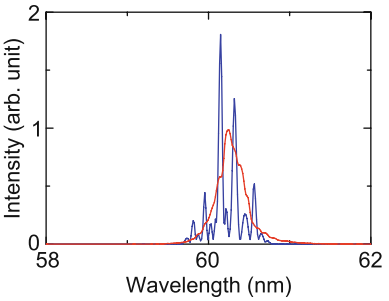

Fig. 7.8. SASE FEL spectrum as measured at SCSS. The *blue curve* shows a single shot spectrum exhibiting several longitudinal modes. The *red curve* is the averaged spectrum from 50 FEL pulses (courtesy M. Yabashi, H. Tanaka)

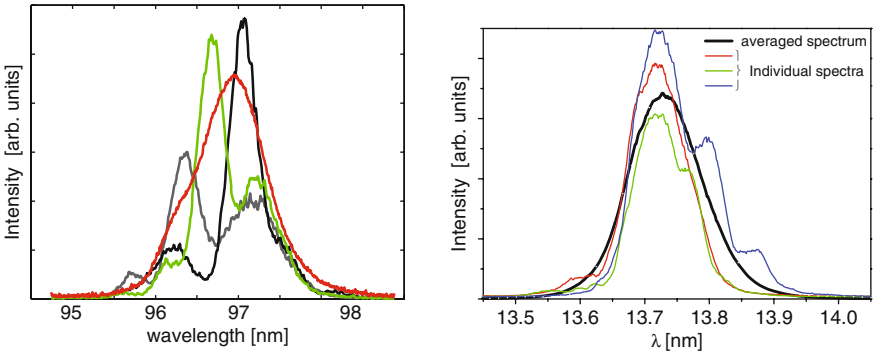

Fig. 7.9. *Left*: The measured spectra of individual SASE FEL pulses at an average wavelength of 97 nm. The single-shot spectra show two to three peaks which fluctuate in size and position from shot to shot. The average spectrum of 100 FEL pulses is wider than the individual spikes. Its shape is determined by the coherence time. *Right*: spectra of individual SASE pulses and the averaged spectrum at 13.7 nm

An important quantity for the characterization of chaotic light is the coherence time, i.e. the time over which there exists a correlation in the field. To determine this quantity we look at the first-order correlation function

$$g(t-t') = \frac{\langle E(t)\rangle \langle E^*(t')\rangle}{|\langle E(t)\rangle|^2} = \frac{\int \left|\tilde{E}(\omega)\right|^2 \exp[-i\,\omega(t-t')]d\omega}{\int \left|\tilde{E}(\omega)\right|^2 d\omega} \tag{7.13}$$

We use (7.9):

$$\tilde{E}_x(\omega, z) = \frac{\mu_0 c\,\widehat{K}}{4\gamma_r} H(\omega, z) J(\omega)$$

to express the field by the transmission function and, using (5.12) and (5.13), we write the transmission function in the approximate form

$$H(\omega) \approx const \cdot \exp\left(-\frac{\omega^2}{2\sigma_\omega^2}\right).$$

The transmission function is thus a Gaussian of variance σ_ω^2. (The z dependence of σ_ω is ignored for the time being). The correlation function becomes

$$g(t-t') = \exp\left(-\frac{\sigma_\omega^2 (t-t')^2}{2}\right).$$

The coherence time is

$$\boxed{\tau_{\text{coh}} = \int (g(t))^2 dt \approx \frac{\sqrt{\pi}}{\sigma_\omega}.} \tag{7.14}$$

Owing to the fact that the rms power bandwidth depends on the longitudinal position in the undulator, see (5.13),

$$\sigma_\omega = \sigma_\omega(z) = 3\sqrt{2}\,\rho_{\text{FEL}}\;\omega_\ell\,\sqrt{\frac{L_{\text{g0}}}{z}}$$

the coherence time will also be a function of z.

Consider now a "flat-top" bunch with a time duration of T_{bunch}. The average number of wave packets (spikes) in the wavelength spectra is

$$M = \frac{T_{\text{bunch}}}{\tau_{\text{coh}}} \tag{7.15}$$

if the bunch duration exceeds the coherence time because each wave packet has a time duration of about τ_{coh} and thus $M = T_{\text{bunch}}/\tau_{\text{coh}}$ non-overlapping wave packets can exist in the bunch. For $T_{\text{bunch}} \le \tau_{\text{coh}}$ only one wave packet can exist and hence $M = 1$. The wave packets are sometimes called the "longitudinal modes". The frequency width of the individual spikes in the spectrum is equal to the Fourier transform limit determined by the bunch duration:

$$\Delta\omega_{\text{spike}} = \frac{2\sqrt{2\ln 2}}{T_{\text{bunch}}}. \tag{7.16}$$

This formula holds for a bunch with a flat time profile.

In the exponential gain regime the radiation pulse energy U_{rad} fluctuates according to the so-called gamma distribution, see Appendix G:

$$p_{_M}(u)du = \frac{M^M\,u^{M-1}}{\Gamma(M)}\exp(-M\,u)du \quad \text{with} \quad u = \frac{U_{\text{rad}}}{\langle U_{\text{rad}}\rangle}\,. \tag{7.17}$$

Here U_{rad} is the energy of an individual radiation pulse, $\langle U_{\text{rad}}\rangle$ the average energy of many pulses and $u = U_{\text{rad}}/\langle U_{\text{rad}}\rangle$ the normalized pulse energy; $\Gamma(M)$ is the gamma function of argument M. The mean value and the variance of the normalized FEL pulse energy are

$$\langle u\rangle = \int_0^\infty u\,p_{_M}(u)du = 1\,, \quad \sigma_u^2 = \left\langle (u - \langle u\rangle)^2\right\rangle = \frac{1}{M}\,. \tag{7.18}$$

As said above, the number of modes is equivalent to the number of spikes seen in the wavelength spectra.

As a nice illustration we show in Figs. 7.10 and 7.11 data obtained at the VUV FEL at DESY at a wavelength of about 97 nm [12]. In a long FEL pulse more wave packets are excited than in a short pulse, and the probability distribution of SASE pulse energy has a correspondingly lower variance. This is indeed verified by the data. When one selects a single longitudinal mode ($M = 1$) by means of a monochromator the probability distribution changes dramatically into a negative-exponential distribution, see Fig. 7.12. We note

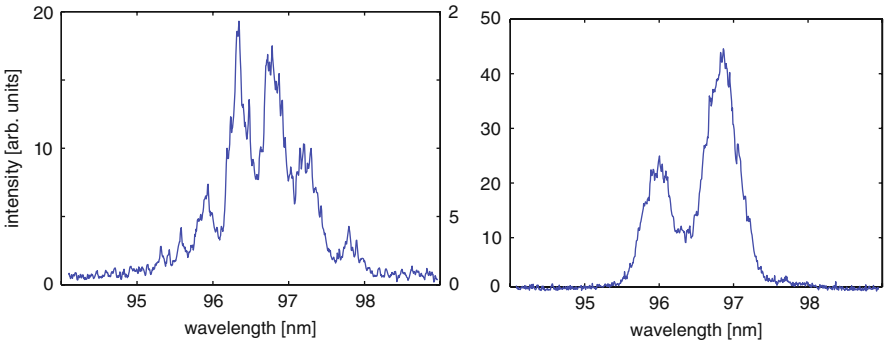

Fig. 7.10. *Left*: single-shot spectrum of a long FEL pulse [12]. The average number of modes is $M = 6$. *Right*: single-shot spectrum of a short FEL pulse. Here the average number of modes is $M = 2.6$

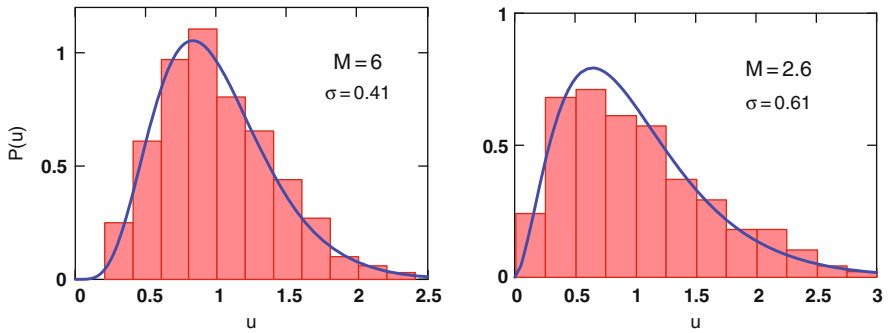

Fig. 7.11. Fluctuation of SASE pulse energy for long and short electron bunches [12]. The mode number is $M = 6$ for the long pulse and the variance is $\sigma_u = 41\%$. For the short pulse one finds $M = 2.6$ and $\sigma_u = 61\%$. The data have been taken in the exponential gain regime. Solid curves: gamma distribution

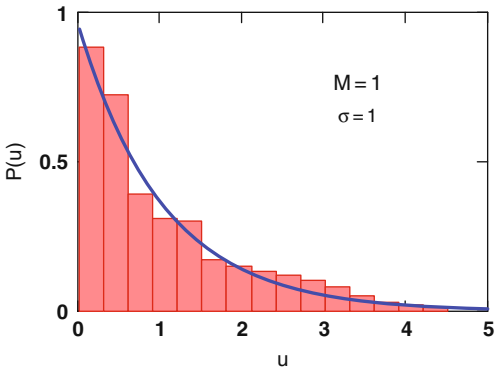

Fig. 7.12. Pulse energy distribution in FEL radiation having passed a monochromator slit [12]. Here $M = 1$ and $\sigma_u = 100\%$

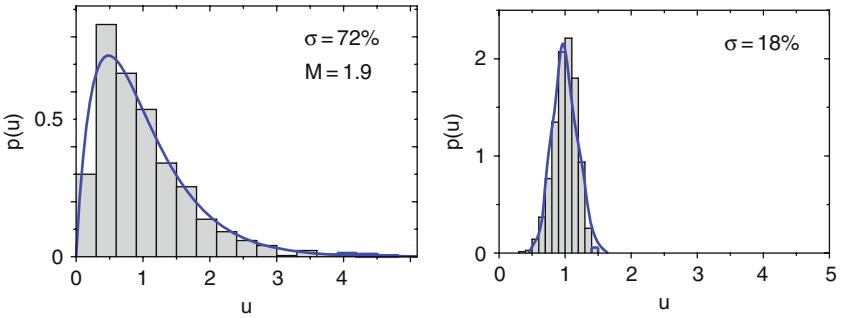

Fig. 7.13. *Left*: measured probability distribution of FEL pulse energy in the exponential regime at a wavelength of 13.7 nm [13]. Solid curve: gamma distribution. The average pulse energy is 1 μJ. *Right*: probability distribution of FEL pulse energy in the saturation regime. Here the gamma distribution is not applicable, the solid curve has been computed with the code FAST. The average pulse energy is 40 μJ.

that the pulse energy fluctuations are quite large in the exponential gain regime, in the order of $60 - 70\%$. This has also been verified in a FLASH measurement at a wavelength of 13.7 nm (Fig. 7.13). From the experimental value $M = 1.9$ and an estimated coherence time of $\tau_{\mathrm{coh}} \approx 4.2 \pm 0.5$ fs one obtains an estimate for the radiation pulse length at the end of the exponential regime of about 8 ± 1 fs [13].

When saturation is reached the gamma distribution is no longer applicable and the fluctuations drop to less than 20%. The regimes of exponential gain and saturation are compared in Fig. 7.13.

A thorough characterization of the 840 nm SASE radiation produced at VISA can be found in [19]. A gain length shorter than 18 cm has been obtained and a gain of 2×10^8 at saturation. For uncompressed bunches the SASE radiation spectra exhibit 4–5 longitudinal modes, and the shot-to-shot intensity fluctuations are described by a gamma distribution with $M = 4.3$, while for compressed bunches only one mode is seen and the observed fluctuations are well fitted with the negative exponential distribution (i.e. the gamma distribution with $M \approx 1$). In another experiment at VISA [20] the microbunching was verified by detecting coherent optical transition radiation at the first and second harmonic of the SASE FEL radiation (at 845 resp. 422 nm).

The spikes in the wavelength spectra have their origin the presence of several wave packets that are separated in time. Consequently, the FEL pulses in time domain will also feature sharp spikes. A direct observation of the temporal spikes has not yet been possible due to the lack of detectors with a time resolution of better than 10 fs. Experiments with such a high time resolution are just on the verge of becoming feasible at free-electron lasers (M. Drescher, private communication). All FEL simulation codes predict the existence of sharp spikes in the time domain. As an example we show in Fig. 7.14 a computation made with the code GENESIS.

The origin of the fluctuations in wavelength and FEL pulse energy in the SASE process is easy to understand. A typical undulator section in which

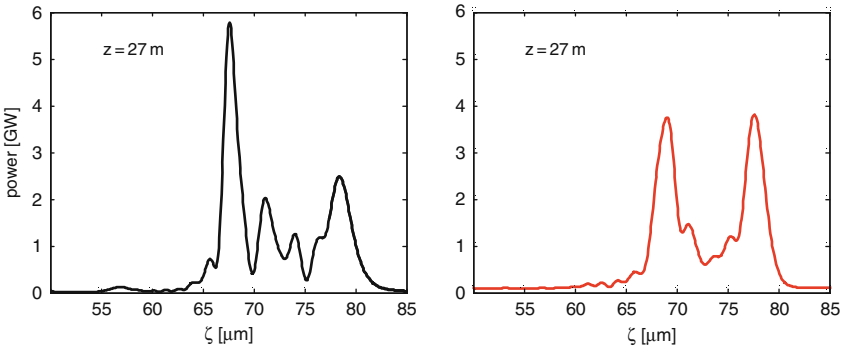

Fig. 7.14. The computed time structure of two different FEL pulses in FLASH at a position of $z = 27\,\mathrm{m}$ in the undulator. We thank Igor Zagorodnov for carrying out the GENESIS calculation

the spontaneous radiation is produced may comprise $N_u \approx 100$ undulator periods. This corresponds to a bandwidth of 1%. If several electrons radiate independently the photon energy may therefore fluctuate by up to ±1%. Moreover, the longitudinal position at which an electron emits its radiation will vary from particle to particle. The radiation which is emitted first will profit most from the exponential amplification while radiation starting at a later position will be lower on the gain curve. In the end, only a few of the initial radiation modes will survive because they absorb the lion's share of the energy extracted from the relativistic electron bunch. Deep in the saturation region all excited modes reach a plateau, and thus the FEL pulse energy variations will be much reduced.

7.2.3 Transverse Coherence

According to Appendix D the fundamental Gaussian mode TEM_{00} has its highest intensity on the beam axis while the higher TEM_{mn} modes extend to larger radial distances and some of them even vanish on the axis. With increasing length in the undulator, the fundamental TEM_{00} mode will therefore grow faster than the other modes, owing to its superior overlap with the electron beam. This process is called mode competition. When the saturation regime is approached the fundamental mode will usually dominate and the FEL radiation will possess a high degree of transverse coherence. This has indeed been verified by double-slit diffraction experiments. The data shown in Fig. 7.15 prove that almost full transverse coherence has been achieved at FEL wavelengths of 100 nm and 7 nm. This feature is of extreme importance for a large class of experiments.

It is interesting to note [5] that a SASE FEL can reach almost full transverse coherence even if the emittance criterion $\varepsilon \leq \lambda_\ell/(4\pi)$ is not fulfilled. Numerical calculations for the Linac Coherent Light Source, made by S. Reiche

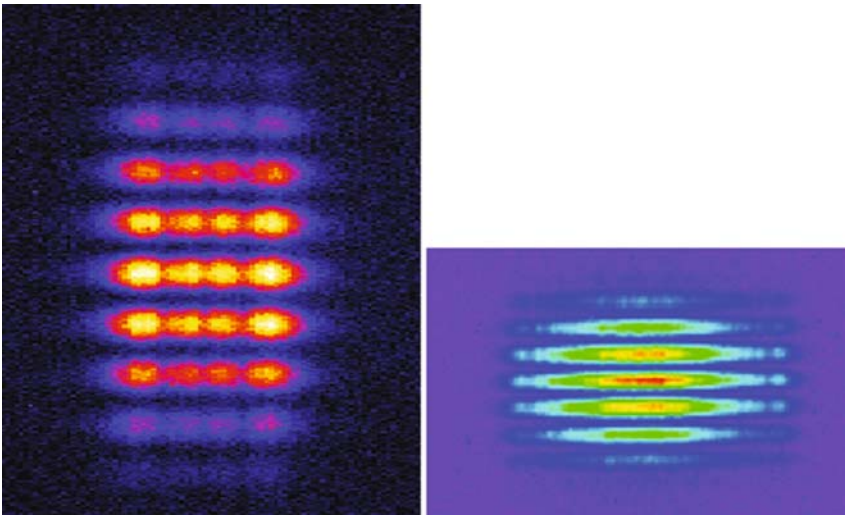

Fig. 7.15. Measured double-slit diffraction patterns. *Left*: at a fundamental wavelength of $\lambda_1 = 100\,\text{nm}$ [21, 22]. The slit separation is 0.5 mm. *Right*: at $\lambda_1 = 7\,\text{nm}$ (courtesy Marion Kuhlmann, DESY)

with his code GENESIS, show that in the early part of the undulator several transverse FEL beam modes will be excited because of too large an electron beam cross section, see the left picture in Fig. 7.16. The fundamental TEM_{00} mode grows faster than the other modes and exceeds their intensity already at 10 gain lengths. At the end of the exponential gain regime ($z = 19\,L_g$) the TEM_{00} mode dominates and the FEL beam has acquired almost full transverse coherence. This is a nice illustration of "mode cleaning".

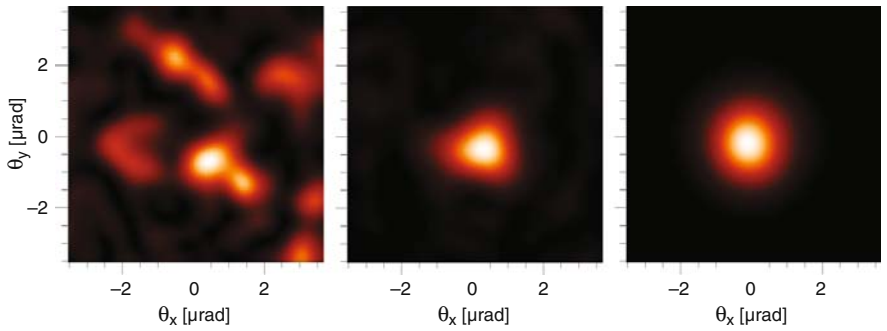

Fig. 7.16. Computed evolution of the transverse angular distribution of the FEL light in the LCLS at different longitudinal positions z in the undulator. *Left*: $z = 4\,L_g$, center: $z = 10\,L_g$, *right*: $z = 19\,L_g$. The gain length is $L_g = 5$ m. We thank S. Reiche for providing us with this figure

Deep in the saturation regime of the fundamental mode, the higher modes are not yet saturated and may continue to grow with increasing z, depending on the beam energy spread in the last section of the undulator. Consequently, the degree of transverse coherence may drop below 90%.

References

1. Kondratenko, A.M., Saldin, E.L.: Generation of coherent radiation by a relativistic electron beam in an undulator. Part. Accel. **10**, 207 (1980) 103
2. Bonifacio, R., Pellegrini, C., Narducci, L.M.: Collective Instabilities and High-Gain Regime in a free electron laser. Opt. Comm. **50**, 373 (1984) 103
3. Kim, K.-J.: Three-dimensional analysis of coherent amplification and self-amplified spontaneous emission in free-electron lasers. Phys. Rev. Lett. **57**, 1871 (1986) 103
4. Kim, K.-J.: An analysis of self-amplified spontaneous emission. Nucl. Instr. Meth. **A 250**, 396 (1986) 103
5. Huang, Z., Kim, K.-J: Review of x-ray free-electron laser theory. Phys. Rev. ST Accel. Beams **10**, 034801 (2007) 105, 117
6. Hogan, M. et al.: Measurements of high gain and intensity fluctuations in a SASE free-electron laser. Phys. Rev. Lett. **80**, 289 (1998) 109
7. Hogan, M., et al.: Measurements of gain larger than 10^5 at 12 μm in a self-amplified spontaneous-emission free-electron laser. Phys. Rev. Lett. **81**, 4867 (1998) 109
8. Milton, S.V., et al.: Exponential gain and saturation of a self-amplified spontaneous emission free-electron laser. Science **292**, 2037 (2001) 109
9. Lumpkin, A.H., et al.: Evidence for microbunching sidebands in a saturated free-electron laser using coherent optical transition radiation. Phys. Rev. Lett. **88**, 234801 (2002) 109
10. Andruszkow, J., et al.: First observation of self-amplified spontaneous emission in a free-electron laser at 109 nm wavelength. Phys. Rev. Lett. **85**, 3825 (2000) 110
11. Ayvazyan, V., et al.: Generation of GW radiation pulses from a VUV free-electron laser operating in the femtosecond regime. Phys. Rev. Lett. **88**, 104802 (2002) 110
12. Ayvazyan, V., et al.: A new powerful source for VUV radiation: Demonstration of exponential growth and saturation at the TTF free-electron laser. Eur. Phys. Journ. **D 20**, 149 (2002) 110, 114, 115
13. FLASH Collaboration, Ackermann, W., et al.: Operation of a free-electron laser from the extreme ultraviolet to the water window, Nature Photonics, June 2007 110, 111, 116
14. Ayvazyan, V., et al.: First operation of a free-electron laser generating GW power radiation at 32 nm wavelength. Eur. Phys. Journ. **D 37**, 297 (2006) 111
15. Geloni, G., Saldin, E.L., Schneidmiller, E.L., Yurkov, M.V.: Exact solution for second harmonic generation in XFELs. Opt. Commun. **271**, 207 (2007) 111
16. Tremaine, A., et al.: Experimental characterization of nonlinear harmonic radiation from a visible self-amplified spontaneous emission free-electron laser at saturation. Phys. Rev. Lett. **88**, 204801 (2002) 111
17. DiMauro, L., et al.: First SASE and seeded FEL lasing of the NSLS DUV FEL at 266 and 400 nm. Nucl. Instr. Meth. **A 507**, 15 (2003) 111

18. Shintake, T.: Status of Japanese XFEL project and SSCS test accelerator, invited paper, FEL Conference, Berlin (2006) 112
19. Murokh, A., et al.: Properties of the ultrashort gain length, self-amplified spontaneous emission free-electron laser in the linear regime and saturation. Phys. Rev. E **67**, 066501 (2003) 116
20. Tremaine, A., et al.: Fundamental and harmonic microbunching in a high-gain self-amplified spontaneous-emission free-electron laser. Phys. Rev. E **66**, 036503 (2002) 116
21. Ischebeck, R.: Transverse coherence of a VUV free electron laser. Ph. D. Thesis, University of Hamburg 2003, DESY-Thesis-2003-033 118
22. Ischebeck, R., et al.: Study of the transverse coherence at the TTF free electron laser. Nucl. Instr. Meth. **A 507**, 175 (2003) 118

Further Reading

23. Lefevre, T., et al.: Self-amplified spontaneous emission and bunching at 3 GHz in a microwave free-electron laser. Phys. Rev. Lett. **82**, 323 (1999)
24. Prazeres, R., et al.: Observation of self-amplified spontaneous emission in the mid-infrared in a free-electron laser. Phys. Rev. Lett. **78**, 2124 (1997)
25. Nguyen, D.C., et al.: First lasing of the regenerative amplifier FEL. Nucl. Instr. Meth. **A 429**, 125 (1999)
26. Babzien, M., et al.: Observation of self-amplified spontaneous emission in the near-infrared and visible wavelengths. Phys. Rev. E **57**, 6093 (1998)
27. Saldin, E.L., Schneidmiller, E.L., Yurkov, M.V.: Statistical properties of the radiation from a SASE FEL operating in the linear regime. Nucl. Instr. Meth. **A 407**, 291 (1998)
28. Bonifacio, R., et al.: Spectrum, temporal structure, and fluctuations in a high-gain free-electron laser starting from noise. Phys. Rev. Lett. **73**, 70 (1994)
29. Saldin, E.L., Schneidmiller, E.L., Yurkov, M.V.: Numerical simulations of the UCLA/LANL/RRCKI/SLAC experiment on a high-gain SASE FEL. Nucl. Instr. Meth. **A 429**, 197 (1999)
30. Yu, L.-H., et al.: First lasing of a high-gain harmonic generation free-electron laser experiment. Nucl. Instr. Meth. **A 445**, 301 (2000)
31. Huang, Z., Kim, K.-J.: Transverse and temporal characteristics of a high-gain free-electron laser in the saturation regime. Nucl. Instr. Meth. **A 483**, 504 (2002)
32. Richter, M., et al.: Measurement of gigawatt radiation pulses from a vacuum and extreme ultraviolet free-electron laser. Appl. Phys. Lett. **83**, 2970 (2003)
33. Krinsky, S., Huang, Z.: Frequency-chirped self-amplified spontaneous emission free-electron lasers. Phys. Rev. ST Accel. Beams **6**, 050702 (2003)

8

The Ultraviolet and Soft X-Ray FEL in Hamburg

8.1 Introductory Remarks

The idea to use a long linear accelerator (linac) for providing the drive beam for an X-ray free-electron laser was conceived at the Stanford Linear Accelerator Center SLAC. In the Linac Coherent Light Source (LCLS) project [1] a 1 km long section of the SLAC electron linac, which has been the major facility for elementary particle physics at Stanford since 1965, will deliver the beam needed in the FEL. The SLAC machine is based on normal-conducting accelerating structures working at 3 GHz. The world's first linear collider SLC was realized utilizing this linac to accelerate electrons and positrons to 46 GeV and collide them after the traversal of an arc to study electro-weak physics at the Z^0 resonance.

Since more than 15 years large groups of particle and accelerator physicists have been working on the development of linear electron-positron colliders in the TeV regime. While at Stanford and in Japan normal-conducting machines were designed the TESLA collaboration decided for superconducting cavities as the acceleration devices. After a decade of intense R&D the collaboration succeeded in raising the accelerating field from a few Megavolts per meter to more than 35 MV/m in multi-cell niobium cavities [2]. The success of the TESLA cavity program was the essential motivation to base the future International Linear Collider ILC on the superconducting TESLA technology.

The TESLA Test Facility TTF was built at DESY with the intention to investigate the performance of superconducting cavities with an accelerated electron beam and to study whether the high beam quality needed in a collider could be achieved. Already at an early stage the decision had been taken to couple the envisaged TESLA collider with an X-ray free-electron laser [3, 4]. As a first test of this concept, the TTF machine was augmented with a 13.5 m long undulator magnet. In February 2000 the worldwide first ultraviolet FEL began its operation at wavelengths between 80 and 180 nm. Meanwhile the TTF linac has been upgraded in two steps to a maximum energy of 1 GeV by adding more cavities, and the undulator was extended to a length of 27 m. The

P. Schmüser, et al.: *The Ultraviolet and Soft X-Ray FEL in Hamburg*, STMP **229**, 121–148 (2008)
DOI 10.1007/978-3-540-79572-8_8

new FEL facility has been named FLASH.[1] The shortest wavelength achieved up to now is 6.5 nm in the first harmonic.

Presently, there are several FEL projects underway all aiming at femtosecond FEL pulses in the UV and soft X-ray regime. They are facing similar scientific and technological challenges as met at FLASH. To some extent the FLASH facility can serve as a blue-print for a new class of accelerator-driven light sources, and the physical considerations and technical solutions described in this chapter are of interest for the envisaged new sources as well.

8.2 Layout of the Free-Electron Laser FLASH

The vacuum-ultraviolet and soft X-ray Free-Electron Laser FLASH is shown schematically in Fig. 8.1. The electron bunches are produced in a laser-driven photo-injector and accelerated to energies between 440 to 1000 MeV by a superconducting linac. The bunch charge is 0.5 to 1 nC. At intermediate energies of typically 125 and 370 MeV the electron bunches are longitudinally compressed, thereby increasing the peak current from initially 50–80 A to approximately 1–2 kA as required for the FEL operation. The 27 m long undulator consists of NdFeB permanent magnets with a fixed gap of 12 mm, a period of $\lambda_u = 27$ mm and a peak magnetic field of $B_0 = 0.47$ T. Finally, a dipole magnet deflects the electron beam into a dump, while the FEL radiation propagates to the experimental hall. The SASE FEL process demands a bunched electron beam of extremely high quality which can be produced only by a linear but not by a circular accelerator. Specifically, high peak current, low emittance, small momentum spread and short bunch length are required.

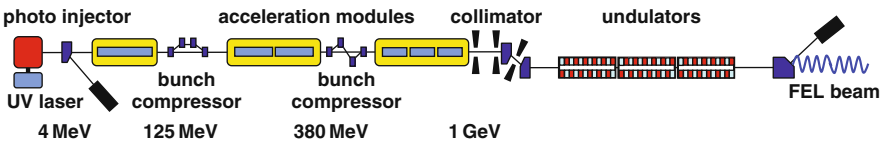

Fig. 8.1. Schematic view of the UV and soft X-ray FEL FLASH at DESY. In 2007 the linac has been upgraded to a maximum energy of 1 GeV. Six acceleration modules are installed, each containing eight superconducting cavities. Two magnetic chicanes are used for longitudinal bunch compression. A collimator removes electron beam halo to prevent radiation damage in the permanent magnets of the undulator

[1] A detailed description of the facility and the scientific program can be found in the brochure "FLASH, the Free-Electron Laser in Hamburg" which can be downloaded from http://pr.desy.de/.

8.3 Electron Source

8.3.1 Layout of the Radio-Frequency Photo-Cathode

The high bunch charge needed in a SASE FEL can be accomplished with photo-cathodes which are illuminated with short ultraviolet laser pulses [5]. The injector at FLASH, shown in Fig. 8.2, consists of a laser-driven photo-cathode which is mounted inside a $1\frac{1}{2}$-cell radio-frequency (RF) cavity. The cathode is made from molybdenum and is coated with a thin Cs_2Te layer to achieve a quantum efficiency for photo-electron emission of typically 5%. The UV laser pulses are generated in a mode-locked solid-state laser system (Nd:YLF) built by the Max Born Institut, Berlin [6, 7]. Another difference to conventional cathodes is the rapid acceleration to relativistic energies which can only be achieved with radio frequency fields and not with a dc electric field. The photo-cathode is located at the backplane of the half-cell where the accelerating field assumes its peak value of about 40 MV/m (60 MV/m in the most recent design). A static magnetic solenoid field is superimposed and provides transverse focusing in order to preserve a small beam cross section. The performance of the electron injector is described in [8]. The pulsed UV laser is synchronized to the 1.3 GHz RF of the linac with a precision of better than 100 fs.

It is impossible to generate the high peak current of several kA immediately in the gun because then huge space charge forces would arise and immediately

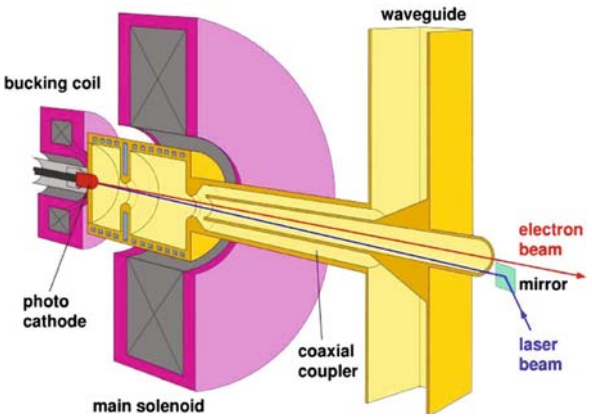

Fig. 8.2. Cut through the electron gun of FLASH. The Cs_2Te photo-cathode is mounted at the backplane of a 1.3 GHz $1\frac{1}{2}$-cell copper cavity. The cavity is excited in a TM_{010}-like mode, the electric field assumes its maximum value at the cathode. The RF power of about 4 MW is guided to the cavity through a wave guide and a coaxial coupler. The UV laser beam is reflected onto the cathode by a small mirror outside the electron beam axis. A solenoid coil provides transverse focusing (see Sect. 8.4.3). A second solenoid, called "bucking coil", compensates the magnetic field in the cathode region where the photo-electrons have very low energy (Courtesy K. Flöttmann)

disrupt the bunch. Therefore bunches with a modest current of some 50 A are produced by laser pulses of 10 ps duration, but even in this case the particles must be accelerated as quickly as ever possible to relativistic energies. In the relativistic regime the repulsive electric forces between the equal charges are largely canceled by the attractive magnetic forces between the parallel currents. Space charge is discussed in the next section.

8.4 Space Charge Effects in FLASH

Space charge forces in the intense electron bunches of a high-gain FEL have a profound influence on the beam dynamics and constitute in fact one of the main performance limitations of an X-ray FEL. We consider first space charge forces in highly relativistic bunches because these are easy to understand, and address then the rather intricate effects that happen in the low-energy electron cloud close to the photo-cathode.

8.4.1 Electric and Magnetic Forces Inside a Relativistic Bunch

We consider for simplicity a bunch of N relativistic electrons which are uniformly distributed in a cylinder of radius r_b and length L_b (measured in the laboratory system). In a co-moving coordinate system, the electrons are at rest and we have a pure Coulomb field inside the bunch. The number of particles and the bunch radius remain invariant ($r_b^* = r_b$) when transforming from the laboratory system to the co-moving coordinate system, but the length is Lorentz-expanded to $L_b^* = \gamma L_b$. For $\gamma \gg 1$ the bunch length L_b^* will be very much larger than the radius, hence one can compute the radial electric field inside the bunch using the approximation of an infinitely long cylindrical charge distribution. The field of an infinitely long charged cylinder has only a radial component

$$\begin{aligned} E_r^*(r) &= \frac{-N\,e}{2\pi\varepsilon_0 L_b^*} \cdot \frac{r}{r_b^2} \quad \text{for} \quad r \le r_b \\ &= \frac{-N\,e}{2\pi\varepsilon_0 L_b^*} \cdot \frac{1}{r} \quad \text{for} \quad r \ge r_b\,. \end{aligned} \tag{8.1}$$

A magnetic field does not exist because the charges are at rest in the co-moving system. Now we transform the field (8.1) into the laboratory system. This yields a radial electric field and an azimuthal magnetic field:

$$E_r(r) = \gamma E_r^*(r) = \frac{-N\,e}{2\pi\varepsilon_0 L_b} \cdot \frac{r}{r_b^2}\,, \quad B_\phi(r) = \frac{v}{c^2}\,E_r(r) \quad \text{for} \quad r \le r_b \tag{8.2}$$

where v is the speed of the electrons. Outside the bunch ($r > r_b$) the fields drop as $1/r$. A test electron inside the bunch experiences a force due to the

radial electric and the azimuthal magnetic field which is computed using the formula

$$\boldsymbol{F} = -e\,(\boldsymbol{E} + \boldsymbol{v} \times \boldsymbol{B})\,.$$

The electric force points radially away from the axis, the magnetic force points inwards but is a bit weaker, hence the overall force points outwards and is thus a defocusing force, given by the expression

$$F_r(r) = \frac{N\,e^2}{2\pi\varepsilon_0 L_b} \cdot \frac{r}{r_b^2} \cdot \left(1 - \frac{v^2}{c^2}\right) = \frac{N\,e^2}{2\pi\varepsilon_0 L_b} \cdot \frac{r}{r_b^2} \cdot \frac{1}{\gamma^2} \quad \text{for} \quad r \le r_b\,. \tag{8.3}$$

The overall force is a factor of $1/\gamma^2$ smaller than the electric force alone and vanishes in the ultra-relativistic limit $\gamma \to \infty$. This "repulsive" total force may lead to a radial blowup of the bunch. The electrons leave the gun with an energy of 4–5 MeV ($\gamma \approx 10$) which is far too low to preserve a small normalized emittance over a large distance. Therefore the first acceleration module, raising the energy to 125 MeV, is mounted directly behind the electron gun.

8.4.2 Partial Compensation of Space Charge Forces by External Focusing

Recognizing that repulsive space charge forces remain an unavoidable problem we may ask the question whether it is possible to counteract these internal forces at least partially by applying an external focusing field. For the cylindrical electron bunch with constant charge density, described in the previous section, this is in fact possible. In such a bunch the total space charge force depends linearly on the displacement r from the axis, see (8.3). A magnetic lens whose field grows linearly with r can indeed exert a focusing force that counteracts the internal force and preserves the emittance.

Now it is important to realize that the transverse intensity distribution in a standard laser beam is described by a Gaussian (see Appendix D). Then the photo-emitted electron bunch will also have a Gaussian transverse density distribution. For such a bunch the total internal force is given by the expression

$$F(r) = \frac{N\,e^2}{2\pi\varepsilon_0 L_b r} \left[1 - \exp\left(-\frac{r^2}{2\sigma^2}\right)\right] \cdot \frac{1}{\gamma^2}\,. \tag{8.4}$$

The radial force inside a bunch with either a constant or a Gaussian charge distribution is depicted in Fig. 8.3. In the Gaussian bunch the force grows almost linearly with r for $0 \le r \le 0.8\sigma$ but then the slope dF/dr levels off, and for $r > 1.8\sigma$ the force even decreases. It is virtually impossible to compensate such a highly nonlinear force by means of an external magnetic field (but of course one can correct for part of it). For this reason the Gaussian charge distribution is quite undesirable in the electron injector region. Great effort is made to shape the UV laser beam toward a flat transverse profile in order to produce cylindrical electron bunches with an approximately constant

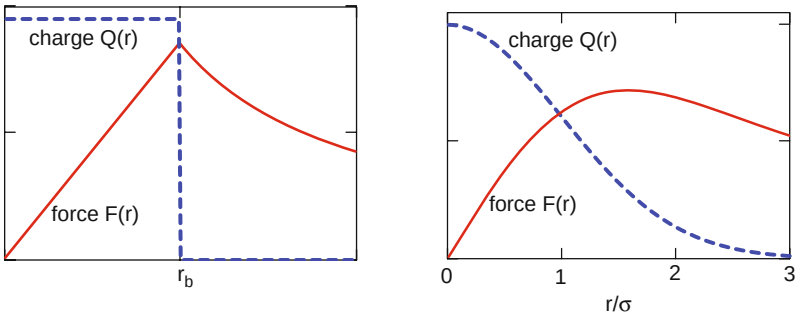

Fig. 8.3. *Left*: charge distribution $Q(r)$ and radial space charge force $F(r)$ in a cylindrical electron bunch with constant charge density and radius r_b . *Right*: charge distribution $Q(r)$ and radial space charge force $F(r)$ in a Gaussian bunch. The units for charge and force are arbitrary

charge density. Also in the longitudinal direction a flat profile is desirable because otherwise the defocusing due to space charge would vary along the bunch while an external focusing force is necessarily the same all along the bunch.

8.4.3 Space Charge in the Electron Gun

The electrons leave the photo-cathode with small velocity and pile up in front of the cathode. The velocity as a function of distance to the cathode is in non-relativistic approximation $v(z) = \sqrt{2e\,E\,z/m_e}$ where E is the accelerating field. Assuming a uniform emission current, i.e. a longitudinally uniform laser pulse profile, the charge density is just inversely proportional to the velocity. In rough approximation the charge density in the vicinity of the cathode can be considered as a superposition of a longer bunch with low charge density and a very short bunch with high charge density. The aspect ratio of the bunch in its rest frame, $a^* = 2r_b/L_b^*$, is close to 1 near the cathode and drops to zero at the relativistic energies. The space charge field of a bunch with a non-vanishing aspect ratio can in general not be described by analytical formulas. Numerical calculations reveal that a bunch with $a^* \approx 1$ and a uniform charge distribution exhibits still a linear relationship between the radial space charge force and the distance r from the axis. The strength of the force, however, depends on the longitudinal position ζ inside the bunch. It is strongest in the center slice and falls off toward the head and tail of the bunch.

The ζ dependence of the radial defocusing force leads to a distortion of the phase space distribution and an associated emittance growth. The stronger defocusing in the center of the bunch as compared to head and tail produces a fan-like structure in phase space, see Fig. 8.4b. The emittance within a short longitudinal slice, the so-called slice-emittance, is not significantly affected by

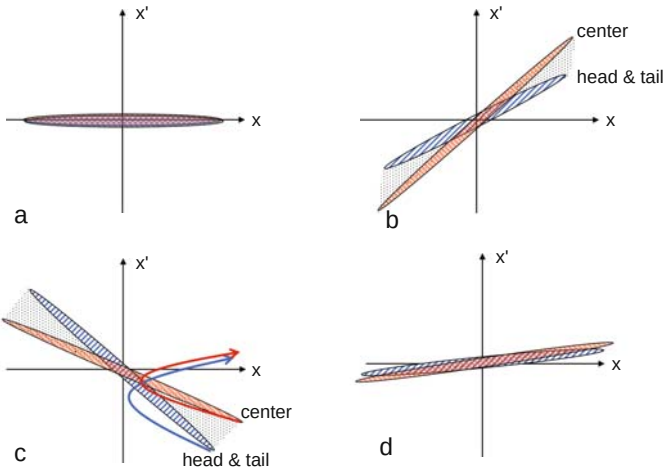

Fig. 8.4. Transverse phase space plots showing schematically the emittance growth due to space charge and its compensation by means of a focusing lens. (**a**) Initial phase space distribution near the photo-cathode. (**b**) Phase space distribution after beam transport to the lens. Not only the two ellipses, representing bunch slices at the center resp. at the head or the tail of the bunch, are filled with particles but also the shaded area between them. This is because the strength of the space charge force varies continuously between center and head of the bunch. (**c**) Rotation of phase space distribution by a focusing lens. (**d**) Shrinkage of the fan-like structure in the drift section behind the lens. We thank Klaus Flöttmann for useful discussions on this subject

the ζ dependence of the radial force, but the orientation of the phase space ellipses of different slices varies with the longitudinal position. Fortunately, the radial blowup of the bunch due to space charge can be counteracted by a clever focusing scheme known as *emittance compensation* [9]. (A more appropriate expression is *emittance-growth compensation* because it is not the emittance as such that is compensated but rather its growth). With the help of a magnetic solenoid field the evolution of the fan-like phase-space structure can be reversed. This is a very complicated mechanism which cannot be explained in terms of linear beam optics alone. The rapid particle acceleration inside the gun and the energy exchange due to longitudinal space charge forces play a role as well.

The mathematical analysis [10] of the emittance-growth compensation process is beyond the scope of this book. Elaborate numerical studies using the code ASTRA [11] and detailed experimental investigations [8] have been carried out for FLASH to optimize the geometry of the solenoid coil arrangement and to determine the proper coil currents.

8.5 Superconducting Linear Accelerator

The electron injector section is followed by six 12.2 m long acceleration modules each containing eight superconducting niobium cavities. The cavities are made from pure niobium and consist of nine cells each. Figure 8.5 shows the layout of the nine-cell TESLA cavity [12]. The basic principles of superconducting cavities for particle acceleration are explained in [13]. An important property of superconductors is that their resistance does not vanish in alternating electromagnetic fields, in contrast to the direct-current case. In a microwave cavity the oscillating magnetic field of the RF wave penetrates into the superconductor down to a depth of about 50 nm (London penetration depth) and induces forced oscillations of the "normal-conducting" electrons, namely those which are not bound in Cooper pairs. The resulting *microwave surface resistance* is many orders of magnitude smaller than in normal copper cavities but nevertheless responsible for significant RF power dissipation at the inner cavity surface. The dissipated power in an RF cavity is given by the formula

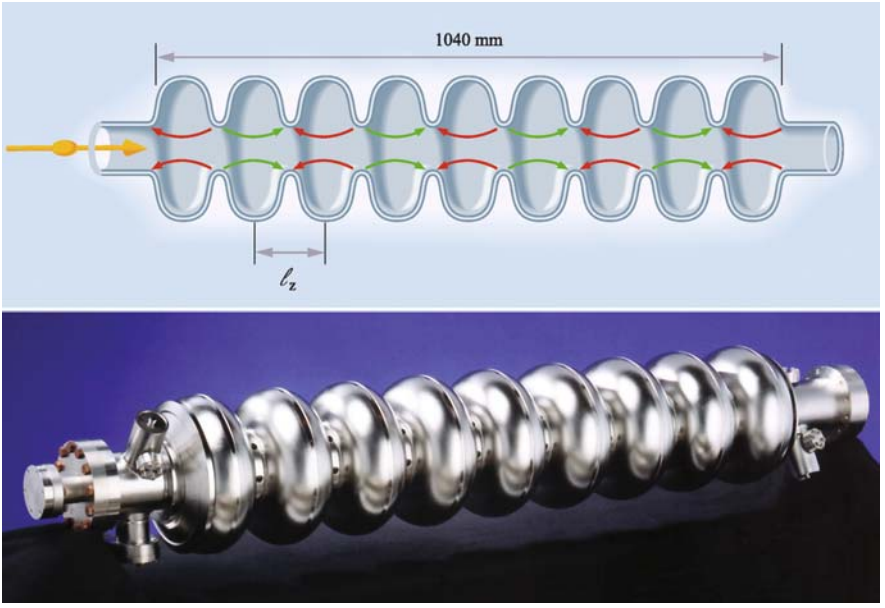

Fig. 8.5. Longitudinal cut and photo of the nine-cell TESLA cavity which is made from pure niobium and cooled by superfluid helium of 2 K. The resonance frequency is $f_0 = 1.3\,\mathrm{GHz}$. The electric field lines are shown at the instant when an electron bunch has just entered the first cell. The length ℓ_c of a cell is chosen such that the field direction has inverted when the relativistic bunch has moved to the next cell. This is fulfilled for a cell length equal to half the RF wave length, $\ell_c = c/(2f_0)$. Thereby it is ensured that the particles receive the same energy gain in each cell

$$P_{\mathrm{diss}} = \frac{R_{\mathrm{surf}}}{2} H_{\mathrm{RF}}^2 S \tag{8.5}$$

where R_{surf} is the microwave surface resistance of the superconductor, H_{RF} the magnitude of the RF magnetic field at the cavity surface, and S the surface area of the cavity. According to the Bardeen-Cooper-Schrieffer (BCS) theory of superconductivity the surface resistance depends exponentially on temperature, see e.g. [13]

$$R_{\mathrm{BCS}} = \frac{A\, f_0^2}{T} \exp\left(-\frac{1.76\, T_c}{T}\right). \tag{8.6}$$

Here T_c is the critical temperature, and A is a coefficient that depends on the London penetration depth and other material properties. The surface resistance of a superconducting cavity can be written as

$$R_{\mathrm{surf}} = R_{\mathrm{BCS}} + R_{\mathrm{res}}$$

with a "residual resistance" of a few nΩ that is caused by surface impurities. The exponential temperature dependence is the reason for cooling the high-field TESLA cavities with superfluid helium at 2 K ($R_{\mathrm{surf}} \approx 10\mathrm{n}\Omega = 10^{-8}\Omega$) instead of using pressurized normal liquid helium at 4.4 K ($R_{\mathrm{surf}} \approx 1000\,\mathrm{n}\Omega$).

The BCS surface resistance scales quadratically with the radio frequency f_0, hence it is advantageous to build superconducting cavities with relatively low resonance frequencies. The value of 1.3 GHz chosen for TESLA is a good compromise between low surface resistance and manageable size of the cavities. The measured surface resistance of the high-purity niobium material used for the TESLA cavities follows the predicted exponential temperature dependence over a wide temperature range. Below 2 K the residual resistance of a few nΩ begins to dominate.

The quality factor of a cavity can be expressed as the ratio of resonance frequency to the width of the resonance curve. It is inversely proportional to the surface resistance.

$$Q_0 = \frac{f_0}{\Delta f} = \frac{G}{R_{\mathrm{surf}}} \tag{8.7}$$

where G is a "geometry factor" that depends only on the shape of the cavity but not on its material. A typical value for a one-cell cavity is $G = 300\,\Omega$. For niobium at 2 K the surface resistance is a few nΩ so the quality factor is $Q_0 > 10^{10}$. In principle the quality factor should stay constant when the field in the cavity is raised from zero to an upper limit which is reached when the RF magnetic field approaches the critical magnetic field of the superconductor. For niobium at 2 Kelvin the critical field is $B_c \approx 200\,\mathrm{mT}$, corresponding to a maximum accelerating field $E_{\mathrm{acc}} \approx 45\,\mathrm{MV/m}$, averaged over the length of the cavity. In practice, however, the excitation curve $Q_0 = Q_0(E_{\mathrm{acc}})$ usually ends at a lower field due to "dirt effects" such as contamination of the inner cavity surface or field emission of electrons. By applying the clean room techniques of the semiconductor industry during the assembly and preparation of

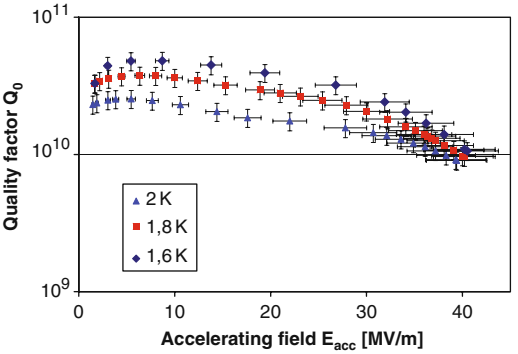

Fig. 8.6. The quality factor of one of the best TESLA nine-cell cavities as a function of the accelerating field E_{acc}. The data were taken at liquid helium temperatures between 1.6 and 2.0 K. In the linac of FLASH the cavities are operated at an average gradient of 20 MV/m (courtesy L. Lilje)

the cavities one can almost achieve the physical limit of the superconducting material, see Fig. 8.6.

In the European X-ray FEL an accelerating field of 21 MV/m is needed to reach an FEL wavelength below 0.1 nm. Although the quality factor exceeds the excellent value of 10^{10} the RF power dissipation in the cavities would be in the order of 100 kilowatts for the whole linac if the cavities were operated in continuous mode. This is far too large for the liquid helium plant because a heat deposition of 100 kW at 2 K requires a primary electric power of almost 100 MW at the refrigerator. The necessary reduction of the cryogenic load is the only (and unfortunate) reason to operate the cavities in pulsed mode with a duty cycle of about one per cent. Continuous operation becomes a realistic option if the accelerating field and the electron beam energy are decreased by a factor of 2.5.

8.6 Bunch Compression

8.6.1 Principle of Longitudinal Compression

We have seen above that the high peak currents of several 1000 A that are needed in linac based UV and X-ray free electron lasers cannot be produced directly in the electron gun because huge space charge forces would destroy the brilliance of the beam within a short distance. Therefore bunches with a peak current of about 50 A are created in the RF photo-injector, accelerated to higher energy and then compressed in length by two orders of magnitude. The electrons in the linac have speeds very close to c, and the velocity differences are too small that a trailing electron would have a chance to catch up with a leading electron if the particles move on a straight line. This possibility is

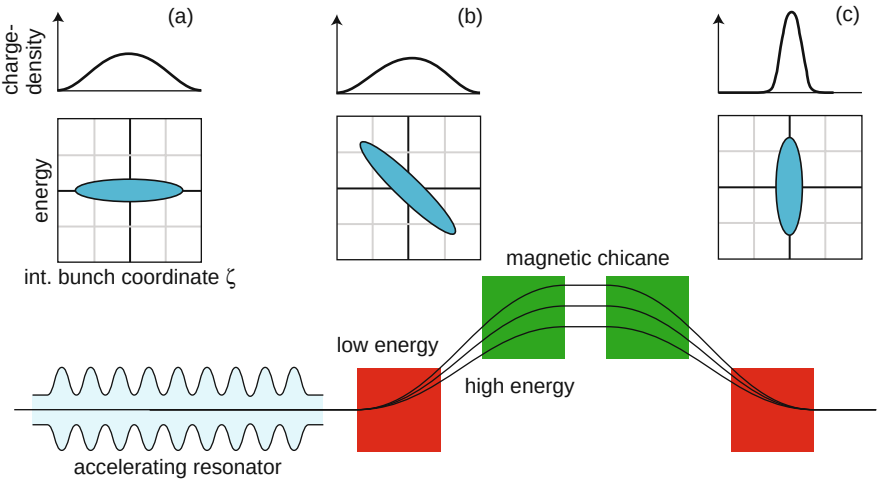

Fig. 8.7. Principle of longitudinal compression of a relativistic electron bunch. The bottom row shows an accelerating cavity and the four dipole magnets of the magnetic chicane. The top figures show the longitudinal bunch charge distribution and the correlation between the internal position ζ of an electron inside the bunch and its relative energy deviation $\eta = (W - W_r)/W_r$ at various positions. (**a**) Before the cavity, (**b**) behind the cavity, (**c**) behind the magnetic chicane. In the RF cavity the particles are accelerated on the slope of the RF wave. Thereby the trailing electrons receive a larger energy gain than the leading ones. In the magnetic chicane the electrons at the tail move on a shorter orbit than those at the head and catch up with them. Note that the ellipse enclosing the beam in the (ζ, η) phase space is transformed by shearing and not by rotation. The enclosed area remains invariant. (Figure adapted from R. Ischebeck [14])

opened if the particles travel through a chicane made of a sequence of bending magnets (such a chicane is shown in Fig. 8.7).

Longitudinal bunch compression is achieved in two steps: first an energy slope is imprinted on the bunch by off-crest acceleration in the first acceleration module, the particles at the head of the bunch receiving a smaller energy gain than those at the tail. Afterwards the particles are passed through a magnetic chicane where the trailing electrons of larger energy travel a shorter distance than the leading ones of smaller energy and are thus enabled to catch up with them. The principle of longitudinal bunch compression is illustrated in Fig. 8.7.

8.6.2 Practical Realization of Bunch Compression

In practice it is not advisable to accomplish the longitudinal bunch compression in a single stage. Such a single-stage compression, leading to peak currents of several 1000 A, would have to take place at rather high energy in order to avoid an emittance blowup due to space charge forces. However in that case

the required energy chirp would introduce a far too large energy spread in the electron beam (remember that a large energy spread reduces the FEL gain as shown in Sect. 6.1). For this reason a two-stage bunch compression system is used in FLASH. The two magnetic chicanes are shown in Fig. 8.1. To realize the energy slope, the RF phases in the acceleration modules preceding the magnetic chicanes are adjusted such that the particles receive their energy gain on the slope of the RF wave. The first compression takes place at 125 MeV, and the second one at 380 MeV. This has considerable advantages over a single-stage system because a large part of the energy chirp is applied at low energy and contributes less to the final energy spread of the beam.

Due to the cosine shape of the RF wave, adding a nonlinear term to the position-energy relationship inside the bunch, and due to collective effects (coherent synchrotron radiation, space charge and wake fields) in the magnetic chicanes the final bunches do not possess the desired narrow shape but consist of a leading spike with a width of less than 100 fs and a tail extending over several picoseconds. Nonlinear dispersion in the chicane contributes also to shape distortions. The leading spike contains 10–20% of the total bunch charge and reaches a peak current in excess of 1000 A which is needed in the high-gain FEL process. In the long tail, the local current is too small to expect any significant FEL gain. The various steps are shown in more detail in Fig. 8.8.

8.6.3 Collective Effects in the Bunch Compression System

While the principle of magnetic bunch compression is easy to understand (there is a lot of resemblance with the compression of laser pulses by the chirping technique) there are subtle details which are special for relativistic electrons. The main problem is that short bunches moving on the curved trajectory through the magnetic chicane will emit coherent synchrotron radiation (CSR) of high intensity. Radiation emitted at the bunch tail takes a shortcut through the vacuum chamber of the magnetic chicane and interacts with the electrons at the bunch head, changing their energy. Also space charge forces have a considerable influence on the shape of the bunches. These interactions and self forces are not present in photon beams. The strong modifications of the bunch shape and the internal energy distribution caused by the collective effects in a 0.5 nC bunch are demonstrated in Fig. 8.9. The bunch shape behind the first bunch compressor is not much affected by the collective effects but behind the second bunch compressor we observe severe distortions in the shape and energy distribution of the bunch. The magnetic deflection in front of the collimator protecting the undulator (see Fig. 8.1) has an additional influence on the bunch shape. Figure 8.10 shows the computed shape of the electron bunch at the entrance of the undulator. A strong energy variation is observed within the leading peak. The energy "chirp" in the lasing portion of the bunch results in an additional broadening of the FEL spectral distribution and a reduction of the FEL gain. The influence of collective effects

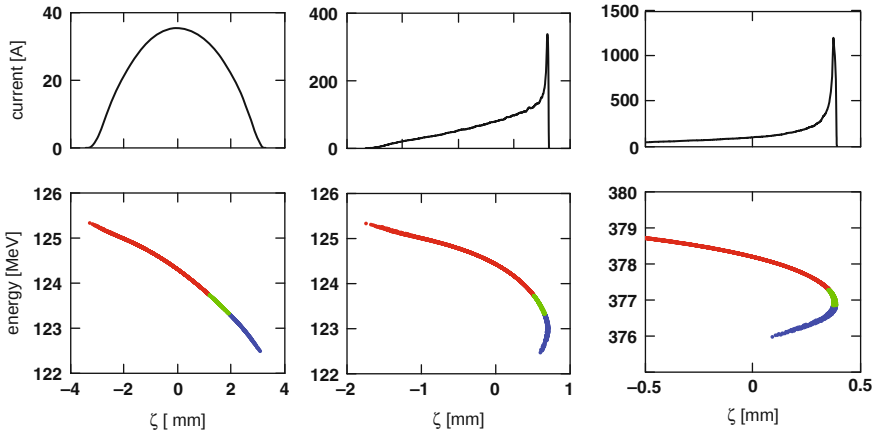

Fig. 8.8. Numerical simulation of bunch compression in FLASH. The mean final beam energy is 377 MeV, the bunch charge is 0.5 nC. The top figures show the dependence of electron beam current on the internal bunch coordinate ζ, the bottom figures show the dependence of electron energy on ζ. *Left*: behind the first acceleration module. The bunch has an rms length of 1.3 mm and the energy varies from 122.3 MeV at the head of the bunch to 125.3 MeV at the tail. The curvature in the energy chirp is visible. *Middle*: behind the first magnetic bunch compressor. The lower energy electrons have collected themselves in a narrow peak at the bunch head, the higher energy particles form a long tail. The peak current has grown from 35 to 350 A. *Right*: behind the second magnetic bunch compressor. Now the peak current has grown to 1250 A. Note that the electrons which where at the front in the left picture are moved backwards in the second bunch compressor due to "overcompression" (*blue color in the plots*)

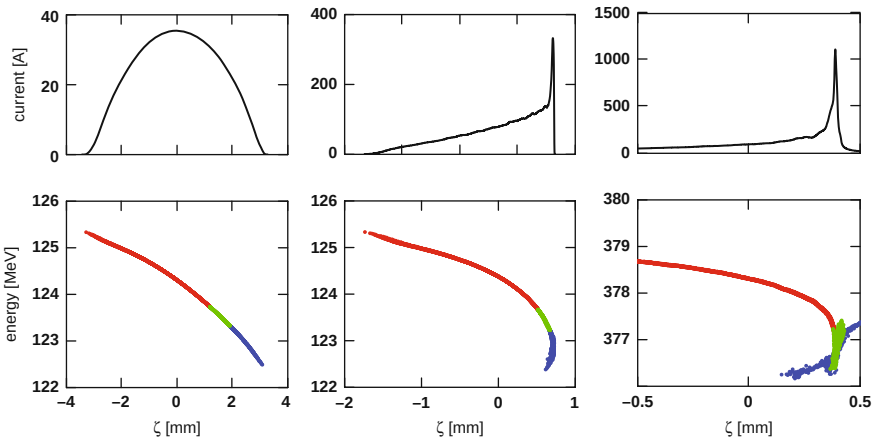

Fig. 8.9. Influence of coherent synchrotron radiation (CSR) and space charge forces on the bunch compression process. The colors indicate the initial positions in the bunch: *blue* head of bunch, *green* middle section, *red* tail

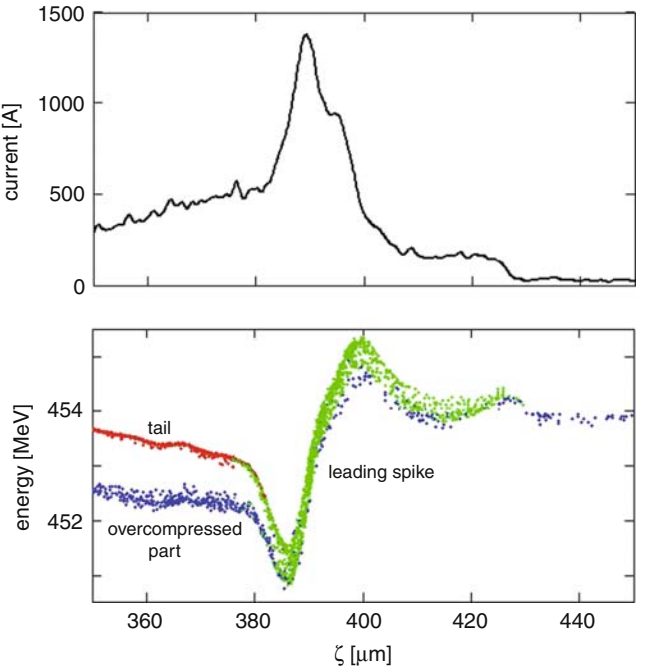

Fig. 8.10. Current profile (*top*) and energy distribution (*bottom*) in the bunch head region for a 0.5 nC bunch entering the undulator. Mean beam energy is 454 MeV

on the beam properties of the SASE FEL in Hamburg has been thoroughly investigated in so-called start-to-end simulations [15].

8.6.4 Linearization of the RF Wave

The FLASH bunch compression system in its present form has the considerable advantage that FEL pulses as short as 10 fs can be produced by the very sharp front spike of the electron bunch. The drawback is that a large fraction of the bunch charge is contained in the tail and does not produce significant FEL radiation.

For FEL users who are not so much interested in the extreme shortness of the FEL pulse but more in its total energy a scheme is under development to supplement the 1.3 GHz cavities with a 3.9 GHz cavity in order to linearize the RF wave. With such a system it should be possible to squeeze almost the entire bunch charge into a single pulse whose length is in the order of 400 fs (FWHM) at peak currents of more than 2500 A at a bunch charge of 1 nC. The computations are shown in Fig. 8.11. In principle, a compression to shorter pulse lengths and higher peak currents appears feasible but great care must be taken to keep space charge and CSR effects at a tolerable level.

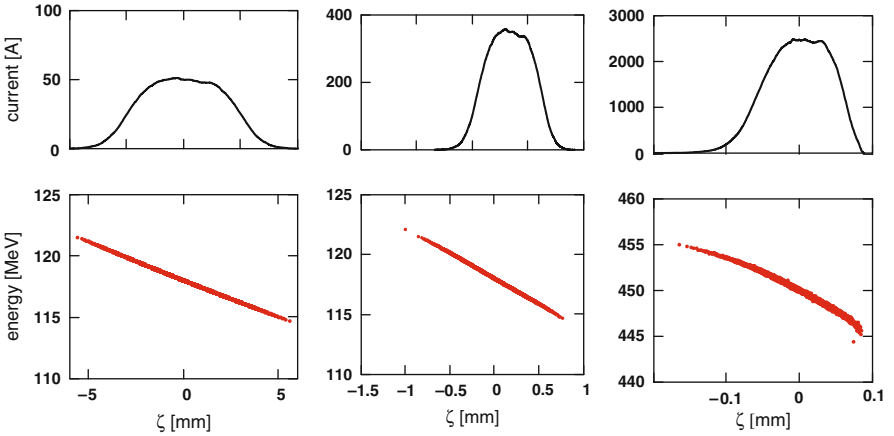

Fig. 8.11. Dependence of beam current and electron energy on the internal bunch coordinate ζ with a third-harmonic cavity for linearizing the energy chirp. *Left*: behind the first acceleration module. The bunch has an almost linear energy-position relationship. *Middle*: behind the first magnetic bunch compressor. Almost all electrons are collected into a narrow pulse with a peak current of 350 A. *Right*: behind the second magnetic bunch compressor. The peak current has grown to 2600 A while the bunch length has shrunk to 120 µm (FWHM), corresponding to a time duration of 400 fs. The bunch charge is 1 nC in this computation. Collective effects have been neglected here

8.7 Undulator Magnet System

The undulators at FLASH [16] are made from iron pole shoes with Nd-FeB permanent magnets in between. The gap height is 12 mm, the period is $\lambda_u = 27\,\text{mm}$ and the peak magnetic field is $B_0 = 0.47\,\text{T}$. To achieve FEL saturation in a single pass the undulator structure must be more than 20 m long for wavelengths in the 10 nanometer regime. The FLASH undulator system consists of six magnets of 4.5 m length each. A photo is shown in Fig. 8.12. An excellent field quality has been achieved in the undulator, after orbit correction the deviation of the electrons from the ideal orbit is about 10 µm. This ensures a good overlap between the electron beam and the light wave which is a prerequisite for achieving a high gain in the lasing process. The field along the axis is purely sinusoidal to a high degree of precision. Due to symmetry only odd higher harmonics are allowed:

$$B_y(z) = -B_0[\sin(k_u z) + b_3 \sin(3k_u z) + b_5 \sin(5k_u z) \ldots] \; .$$

Measurements show that $b_3 < 0.001$ and $b_5 < 0.0005$. In the 60 cm drift space between the segments, quadrupoles are installed for beam focusing as well as beam diagnostics tools.

Fig. 8.12. Photo of a FLASH undulator magnet

8.8 Wake Field Effects

A fast ship moving down a narrow canal produces a wake that is reflected by the shore and acts back on the ship itself or on other ships in the canal. Similar effects happen when intense relativistic particle bunches travel in the vacuum chamber or the cavities of an accelerator. The charged particles generate electromagnetic fields that are modified by the metallic boundaries. These so-called wake fields may act back on the bunch itself or on trailing bunches and perturb the motion of the particles and change their energy distribution. Wake fields are thoroughly treated in the book *Physics of Collective Beam Instabilities in High Energy Accelerators* by A.W. Chao [17].

We consider first the simplest case of an ultra-relativistic bunch traveling on the axis of a smooth cylindrical beam pipe of circular cross section. The walls are assumed to have perfect conductivity. Since for $\gamma \to \infty$ the electric field lines emerging from the bunch are exactly perpendicular to the direction of motion, these field lines enter the metallic wall at right angles and fulfill thus the boundary condition at the interface between vacuum and a perfect conductor. This means that the field pattern inside the beam pipe is not changed by the presence of the metallic wall. In other words: the metallic boundary does not "exist" for the particle bunch, and wake field effects are absent in this case.[2]

[2] In beam pipes of an arbitrary cross section the field pattern will be modified, but wake field effects are still absent if the resistance of the wall vanishes and the particles are ultra-relativistic.

The situation changes if one of the above assumptions is not fulfilled. We consider two important cases

- a finite conductivity of the beam pipe leads to resistive-wall wake fields,
- a variation of the cross section results in geometric wakes.

8.8.1 Resistive-Wall Wake Fields

Resistive-wall wake fields play a role in the 30 m long beam pipe in the undulator system which has a radius of only 5 mm and is made from aluminum. The computed longitudinal wake field for a compressed bunch in FLASH is plotted in Fig. 8.13. The wake field is negative in the bunch head but becomes slightly positive in the tail. This means that the electrons in the bunch head lose energy while those in the tail gain energy. We are mainly interested in the bunch head because it is this region of the bunch that contributes to the SASE FEL process. The energy spread in the bunch head region, induced by resistive wall wake fields, is estimated as

$$\sigma_\eta^{\text{wake}} < 0.1_{\rho_{\text{FEL}}} \ .$$

It is thus uncritical for FLASH but may be a serious concern in an X-ray FEL where the undulator beam pipe is much longer and the FEL parameter significantly smaller than at FLASH. For the XFEL a more careful analysis is required which is beyond the scope of this book.

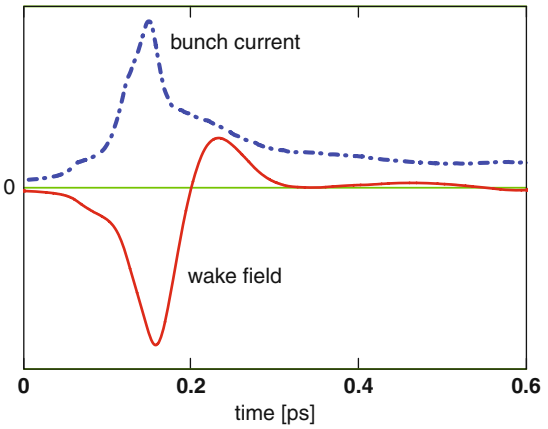

Fig. 8.13. Resistive-wall wake field effect in the aluminum beam pipe of the FLASH undulator. The bunch current as a function of time is shown as a dash-dotted blue curve. The longitudinal electric wake field is shown as a continuous red curve. For a bunch charge of 0.5 nC the maximum bunch current is about 1200 A. The peak value of the wake field amounts to –30 kV/m. The bunch head is at the left side

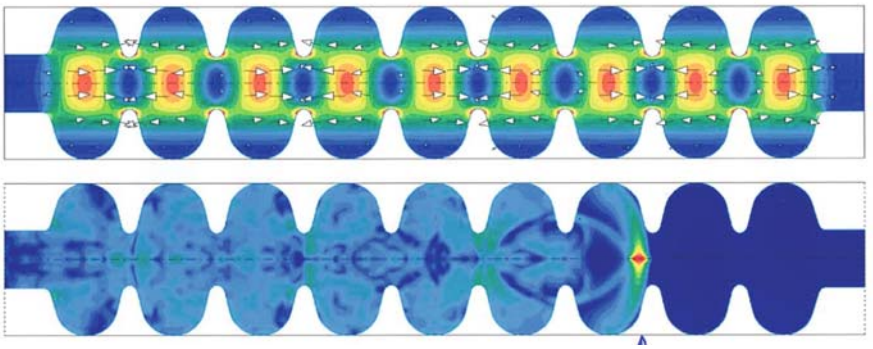

Fig. 8.14. *Top*: the computed field pattern in a nine-cell cavity which is excited to the fundamental TM_{010} mode by a klystron operating at 1.3 GHz. *Bottom*: the wake field pattern generated by a short relativistic electron bunch

8.8.2 Geometric Wakes

Geometric wakes occurring in the nine-cell superconducting cavities are shown in Fig. 8.14. The upper part of the figure shows the field lines and the energy density of the accelerating field that is generated by a klystron, the lower part shows the electromagnetic energy density of the wake fields which are induced by a passing relativistic electron bunch. Many of the induced higher-order eigenmodes of the cavity are coupled out by a specially designed antenna and their energy is absorbed in a dump resistor at room temperature. The very high-frequency modes may leave the cavity and travel along the beam pipe. Damping of the traveling modes is a challenging task in a superconducting linear accelerator.

8.9 Electron Beam Diagnostics

The requirements on electron beam quality are very demanding and in some respects at the limit of present-day technology. High-resolution diagnostic instruments are essential for a detailed understanding of the physical principles of emittance preservation, bunch compression and lasing in the SASE mode. Moreover, they are an indispensable prerequisite for providing the input signals of the feedback systems for beam energy stabilization and bunch compression.

8.9.1 Longitudinal Charge Distribution

We restrict ourselves here to a description of two techniques permitting single-shot direct visualization of longitudinal electron bunch profiles with very high resolution: the transverse deflecting RF structure (TDS) and electro-optic (EO) detection systems.

Transverse Deflecting RF Structure

In the TDS the temporal profile of the electron bunch is transferred to a spatial profile on a view screen by a rapidly varying electromagnetic field, analogous to the sawtooth voltage in conventional oscilloscope tubes but with a thousandfold better time resolution [18, 19]. The TDS at FLASH is a 3.6 m long traveling wave structure operating at 2.856 GHz in which a combination of electric and magnetic fields exerts a transverse force on the electron bunches. The bunches pass the TDS near zero crossing of the RF field (phase zero) and receive no net deflection but are streaked in the transverse direction. A single bunch out of a train can be streaked. With a fast kicker, this bunch is deflected toward an optical transition radiation (OTR) screen viewed by a CCD camera. The other electron bunches are not affected. The time resolution of the TDS installed at FLASH is about 20 fs (rms) if the beam optics is optimized for the measurement. A CCD picture of a streaked electron bunch is shown in Fig. 8.15. The figure shows also the computed temporal charge profile. One observes a sharp peak at the head with a full width at half maximum of 65 fs and a long tail to later times. The sharp peak contains about 20% of the bunch charge, only here the local charge density is high enough to obtain significant gain in the SASE process.

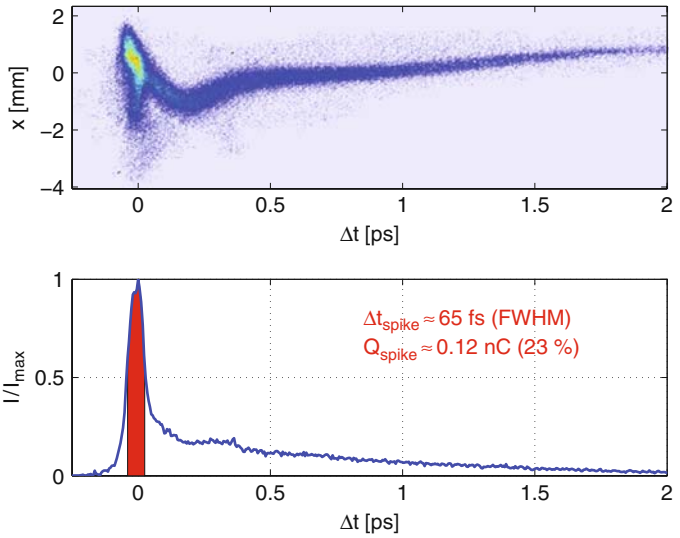

Fig. 8.15. *Top*: Two-dimensional CCD image of a single electron bunch whose time profile is translated into a spatial coordinate on an observation screen. In the photo the bunch is streaked horizontally with the bunch head at the *left side*. *Bottom*: Current as a function of time. The maximum current is $I_{\max} = 1.8\,\mathrm{kA}$ in this measurement [20]

Electro-Optic Detectors

The electro-optic (EO) effect offers the possibility to measure the longitudinal charge distribution in the electron bunches with a resolution of 50 fs. The principle is as follows: the electric field of the relativistic bunch induces an optical birefringence in a crystal such as gallium-phosphide (GaP), which is then probed with femtosecond titanium-sapphire (Ti:Sa) laser pulses. One EO experiment is installed in the FLASH linac in the straight section between the last acceleration module and the undulator. The EO crystal is mounted inside the vacuum chamber of the linac at a distance of 4–5 mm to the electron beam. The linearly polarized Ti:Sa laser pulse enters the chamber at a small angle, crosses the EO crystal and is then coupled out through a quartz window. In the birefringent GaP crystal the laser pulse acquires an elliptical polarization which is transformed into an intensity modulation using a quarter wave plate, a half wave plate and a crossed polarization filter. An experimental challenge is to find and maintain the temporal overlap of the 15 fs long laser pulse and the < 100 fs long electron bunch. The Ti:Sa laser produces a periodic pulse train with a repetition rate of 81 MHz. This frequency is adjusted to exactly 1/16 of the 1300 MHz radio frequency of the linac and then locked to the RF in a phase-locked loop circuit. The measured time jitter is less than 40 fs.

In the electro-optic sampling (EOS) method, which is usually applied in THz physics, the narrow laser pulses are moved in small steps across the wider electron bunches. Thereby the average time profile of many bunches is obtained. Due to time jitter this method is not adequate for the analysis of ultrashort electron bunches. Several single-shot techniques are applied at FLASH permitting the analysis of individual electron bunches, based on spectral, temporal or spatial decoding. The simplest one is the electro-optic spectral decoding (EOSD) method. For this purpose the laser pulse is passed through a dispersive material and stretched (*chirped*) to a length of several ps, longer than the electron bunch. In the chirped pulse the long wavelengths are at the head of the pulse and the short ones at the tail (note that a 15 fs Ti:Sa laser pulse has a bandwidth of 800 ± 30 nm). In the GaP crystal the temporal structure of the electron bunch is imprinted onto the spectral components of the laser pulse. With a diffraction grating and a gated CCD camera the time information can be recovered. The principle is explained in Fig. 8.16.

Typical single-bunch measurements are shown in Fig. 8.17. The data are very useful for accelerator diagnostics. For instance, wrong parameters in the bunch compression scheme are immediately visible from the reconstructed bunch shape. The best achievable rms resolution in the spectral decoding method is about 100 fs.

A better resolution of about 50 fs (rms) is attainable with the technically more involved temporal decoding (EOTD) method. This intrinsic resolution limit has been reached in an experiment which has been carried out [22] in collaboration with a group from the infrared FEL FELIX in the Netherlands. Results are shown in Fig. 8.18.

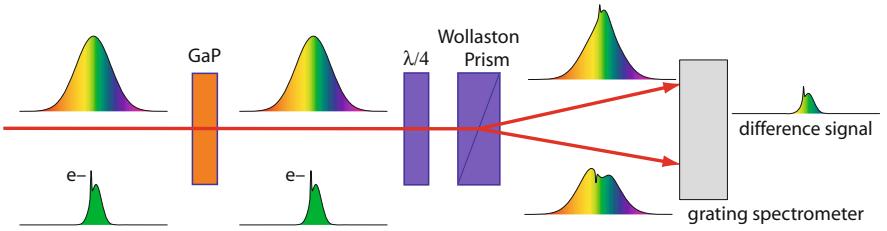

Fig. 8.16. Scheme of the electro-optic reconstruction of the time profile of an electron bunch by spectral decoding [21]. At the top the chirped laser pulse of 1–2 ps length is shown, at the bottom the charge distribution in the electron bunch. In the GaP crystal the electric field distribution is imprinted onto the two polarization components of the laser pulse

The EO experiments are inferior to the TDS in terms of time resolution but have the considerable advantage of being "non-destructive": the same bunch which has been analyzed with the EO system can be used to generate FEL radiation downstream. In contrast to this a bunch that has been streaked by the TDS is too diffuse to produce FEL radiation. Moreover, the EO signals can be utilized as arrival time signals of the FEL pulses in *pump-and-probe* experiments. To fully exploit these capabilities an improved synchronization

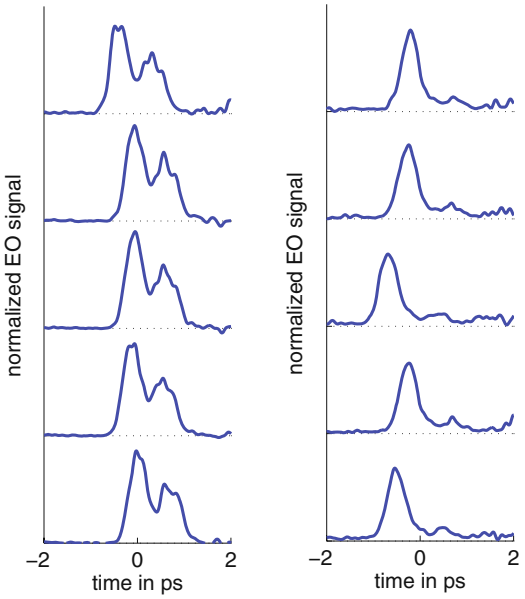

Fig. 8.17. Pulse shape of single electron bunches measured with the spectral decoding method [21]. *Left column*: wrong off-crest phase in the first acceleration module ACC1. The bunches develop a double-peak structure. *Right column*: correct phase in ACC1, leading to optimum compression of the bunch

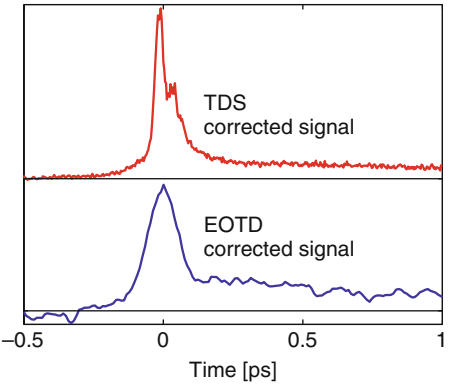

Fig. 8.18. Comparison of two high-resolution measurements on single compressed electron bunches in FLASH. *Top curve*: transverse deflecting structure (TDS), *bottom curve*: electro-optic temporal decoding (EOTD)

system for the accelerating cavities and other time-critical components is under construction, based on periodic infrared lasers pulses that are distributed in the FLASH linac via length-stabilized glass fibers [23, 24]. The measured accuracy in a prototype setup is 10 fs, far better than an electronic signal distribution system using coaxial cables can ever achieve. This optical synchronization system will be absolutely indispensable in the XFEL. Similar systems are developed at other laboratories [25].

Bunch Arrival Time Monitor

A bunch arrival time monitor using the future laser-based synchronization system at FLASH has been developed and tested with a fiber laser [26]. The signal of a beam pick-up antenna with GHz bandwidth is sampled by a periodic pulse train from the fiber laser, using a broadband electro-optical modulator. Bunch arrival time deviations are converted into amplitude modulations of the sampling lasers pulses, which are then detected in a photo-detector. The principle of the monitor is sketched in Fig. 8.19. Data recorded at FLASH are shown in Fig. 8.20. In a train of 30 bunches one observes a systematic variation of the arrival time. The most likely cause is an energy variation in the bunch train which translates into a time variation in the magnetic chicanes of the bunch compressor. There is a good correlation between the arrival times of two bunches within a train. From the scattering around the correlation line the accuracy of the bunch arrival time monitor is estimated at 30 fs (rms). Meanwhile the resolution has been improved to better than 10 fs.

8.9.2 Transverse Emittance

The FEL gain depends critically on a small transverse size of the electron beam all along the undulator. To obtain high efficiency in the SASE process, a tightly

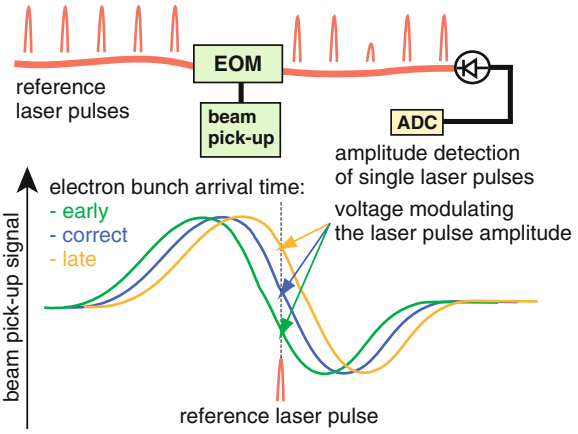

Fig. 8.19. Principle of the bunch arrival time monitor [26]. A period train of laser pulses is passed through an electro-optical modulator EOM. If a laser pulse coincides with an electron bunch, it is amplitude-modulated by the beam pick-up signal. A high timing accuracy is obtained by working in the zero-crossing scheme

collimated beam with high local charge density is needed. The emittance is a measure of the area in transverse phase occupied by the beam. Loosely speaking, it is the product of transverse beam size and beam divergence. A small emittance means that one can realize a small beam cross section over a long distance, which is very essential in the long undulator magnets of an ultraviolet or X-ray FEL. Usually one normalizes the emittance to the particle momentum

$$\varepsilon_n = \frac{p}{m_e c}\varepsilon \approx \gamma\varepsilon$$

since this quantity is independent of the particle energy (provided there are no disturbances). To illustrate the importance of a small emittance we show in Fig. 8.21 the gain length as a function of emittance for FLASH at an energy of

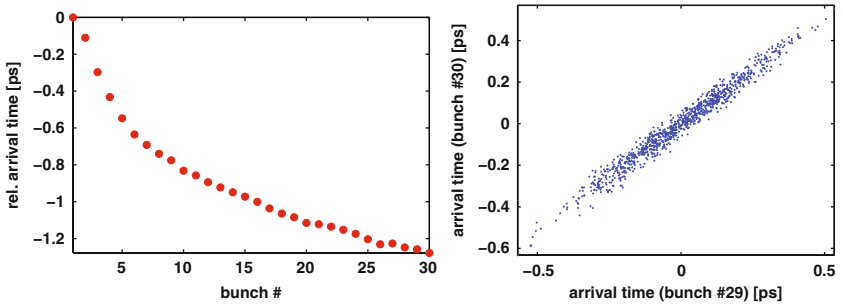

Fig. 8.20. *Left*: arrival time variation in a train of 30 bunches. *Right*: correlation between the arrival times of bunch 29 and bunch 30 (courtesy F. Löhl, DESY)

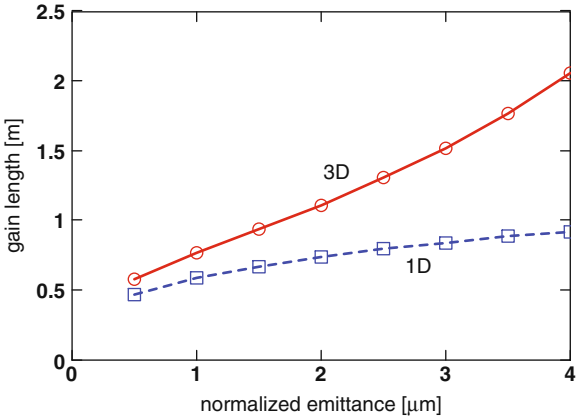

Fig. 8.21. The computed 3D power gain length L_g (*solid red curve and circles*) and the 1D power gain length L_{g0} (*dashed blue curve and squares*) as a function of the normalized emittance. The calculations are done for an energy of 1 GeV in FLASH and are based on (4.53), (6.25) with the following parameters: peak current $I_{\mathrm{peak}} = 2500\,\mathrm{A}$, average beta function $\beta_{\mathrm{av}} = 5\,\mathrm{m}$, energy spread $\sigma_\eta = 0.5\,\rho_{\mathrm{FEL}}$

1 GeV. One can see that the 3D power gain length L_g is rather close to the 1D gain length L_{g0} as long as the emittance criterion (6.20) is fulfilled. For FLASH operating at 1 GeV this corresponds to a normalized emittance $\varepsilon_n \leq 1\,\mu\mathrm{m}$. If the criterion is violated the 3D gain length grows rapidly with increasing beam emittance while the 1D gain length exhibits a moderate growth, $L_{g0} \propto \varepsilon_n^{1/3}$. Reducing the beam emittance is hence of utmost importance.

The value $\varepsilon_n = 2\,\mu\mathrm{m}$ chosen for FLASH is a realistic lower limit of what can be achieved with present-day technology. The emittance criterion (6.20) is fulfilled for $\gamma \leq 1000$ and $\lambda_\ell \geq 23\,\mathrm{nm}$:

$$\varepsilon = \frac{\varepsilon_n}{\gamma} = 2 \cdot 10^{-9}, \quad \frac{\lambda_\ell}{4\pi} = 1.8 \cdot 10^{-9}$$

but at $\gamma = 2000$ and a wavelength of about 6 nm the emittance is a factor of two larger than $\lambda_\ell/(4\pi)$.

Average Emittance of Many Bunches

Emittance measurements are routinely carried out in two diagnostic sections of FLASH. The two-dimensional transverse intensity profile of the beam is imaged by CCD cameras at four locations using optical transition radiation (OTR). From the known beam-optical transfer matrices between the OTR screens the particle distribution in phase space can be reconstructed by tomography using the so-called maximum entropy method, and the beta function

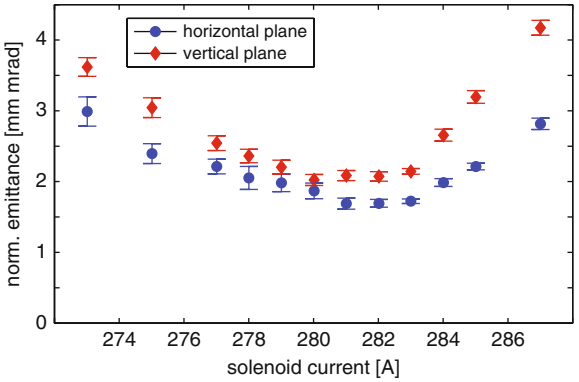

Fig. 8.22. The normalized horizontal resp. vertical emittance as a function of the main solenoid current in the electron gun (courtesy Florian Löhl, DESY). The data were obtained for an uncompressed electron beam (note that 1 mm mrad =1 μm)

and the beam emittance can be determined. Figure 8.22 shows the normalized transverse emittance as a function of the current in the main solenoid magnet of the electron gun. This figure demonstrates how critically the beam focusing in the electron injector depends on the focal properties of the solenoid coil. The emittance shown in Fig. 8.22 is averaged over the longitudinal charge distribution inside the bunch and over many successive bunches.

Slice Emittance

What is really of interest for the SASE FEL is not the average emittance of the entire bunch but the emittance of the high-current region in the bunch head. Standard emittance measurements are incapable of extracting this information. Fortunately, the transverse deflecting RF structure TDS, described above, permits the determination of the emittance in selected time slices of the bunches. For this purpose the quadrupole strengths in the beam optics section between the TDS and the observation screen are varied. This so-called *slice emittance* is shown in Fig. 8.23. The normalized emittance is $\varepsilon_n \approx 10\,\mu\text{m}$ in the head of the bunch and drops to less than $4\,\mu\text{m}$ in the tail of the distribution. This result is surprising at first sight because an emittance of $\varepsilon_n \approx 10\,\mu\text{m}$ is far too large to be compatible with the high FEL gain measured in FLASH.

The complexity of the obtained data is illustrated in Fig. 8.24 where the reconstructed horizontal phase space distribution is shown for a slice in the bunch head region. Large deviations from the ideal elliptic shape are observed. The long wings extend appreciably beyond the central elliptic region towards large values of x and x', and according to (6.10), they contribute strongly

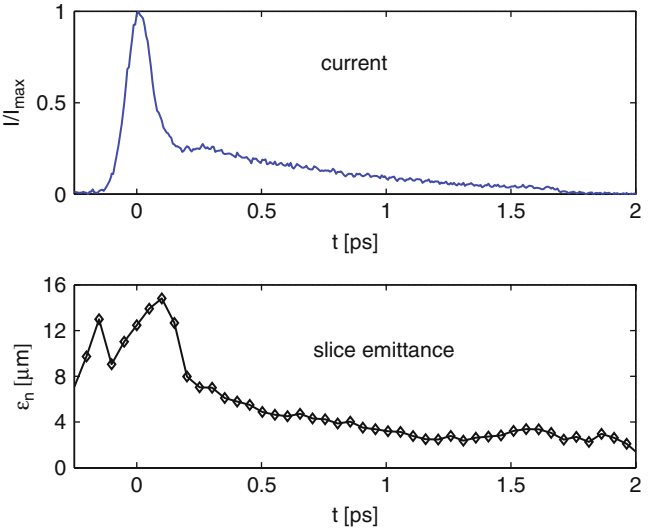

Fig. 8.23. The normalized beam current $I/I_{\max}$ and the normalized horizontal emittance as a function of the temporal position in the bunch [20]. (The maximum current is $I_{\max} = 1.8\,\mathrm{kA}$)

to the large normalized emittance of about 10 μm in the bunch head. These wings have too low a charge density to yield appreciable FEL gain. If we restrict ourselves to the central elliptic region with sufficient charge density (see Fig. 8.25) we obtain a normalized emittance of a few μm at an acceptable peak current of about 1.4 kA. This central region is indeed responsible for the FEL gain.

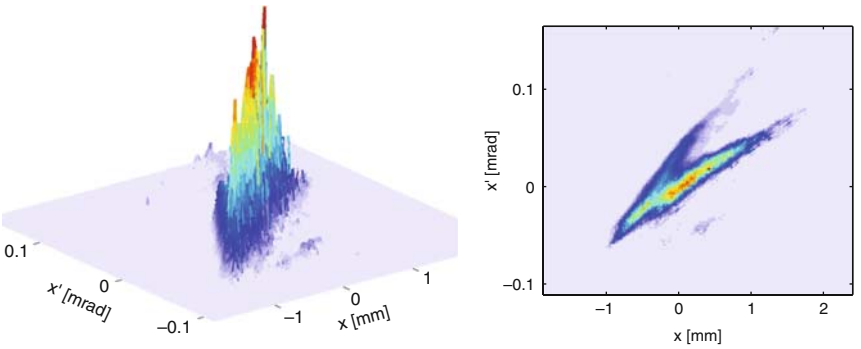

Fig. 8.24. Horizontal phase space distribution in the bunch head region. The long wings extending appreciably beyond the central elliptic region are the main source for the large emittance in the bunch head that is shown in Fig. 8.23 [20]

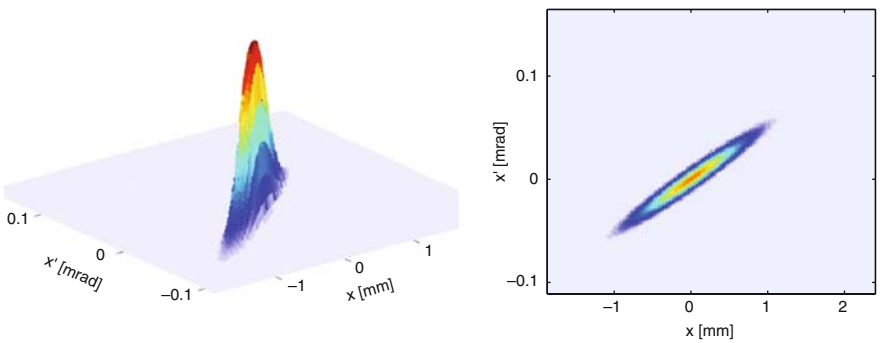

Fig. 8.25. The central elliptic phase space distribution in the bunch head region. The peak current is about 1.4 kA, the normalized emittance is $\varepsilon_n = 4\,\mu$m [20]

References

1. The LCLS Design Study Group, LCLS Design Study Report, http://www-ssrl.slac.stanford.edu/lcls/ 121
2. Lilje, L., et al.: Achievement of 35 MV/m in the superconducting nine-cell cavities for TESLA. Nucl. Instr. Meth. **A 524**, 1 (2004) 121
3. Brinkmann, R., Materlik, G., Rossbach, J., Schneider, J.R., Wiik, B.H.: An X-ray FEL laboratory as part of a linear collider design. Nucl. Instr. Meth. **A 393**, 88 (1997) 121
4. Rossbach, J.: A VUV free electron laser at the TESLA test facility at DESY. Nucl. Instr. Meth. **A 375**, 269 (1996) 121
5. Fraser, J., Sheffield, R., Gray, E.R.: A new high-brightness electron injector for free-electron lasers driven by rf linacs. Nucl. Instr. Meth. **A 250**, 71 (1986) 123
6. Schreiber, S., Will, I., et al.: Running experience with the laser system for the rf gun based injector at the tesla test facility linac. Nucl. Instr. Meth. **A 445**, 427 (2000) 123
7. Will, I., et al.: The upgraded photocathode laser of the TESLA test facility. Nucl. Instr. Meth. **A 541**, 467 (2005) 123
8. Abrahamyan, A., et al.: Characterization of the electron source at the photoinjector test facility at DESY Zeuthen. Nucl. Instr. Meth. **A 528**, 360 (2004) 123, 127
9. Carlsten, B.E.: New photoelectric injector design for the Los Alamos National Laboratory XUV FEL accelerator. Nucl. Instr. Meth. **A 285**, 313 (1989) 127
10. Serafini, L., Rosenzweig, J.B.: Envelope analysis of intense relativistic quasilaminar beams in rf photoinjectors: A theory of emittance compensation. Phys. Rev. **E 55**, 7565 (1997) 127
11. Flöttmann, K.: ASTRA, A Space charge Tracking Algorithm, www.desy.de/∼mpyflo 127
12. Aune, B., et al.: The Superconducting TESLA cavities. Phys. Rev. ST Acc. Beams, PRSTAB **3**, 092001 (2000) 128
13. Schmüser, P.: Superconductivity in high energy particle accelerators. Prog. Part. Nucl. Phys. **49**(1), 155 (2002) 128, 129
14. Ischebeck, R.: Transverse coherence of a VUV free electron laser. Ph.D. Thesis, University of Hamburg 2003, DESY-Thesis-2003-303 131

15. Dohlus, M.: et al.: Start-to-end simulations of the SASE FEL at the TESLA Test Facility phase 1, Nucl. Instr. Meth. **A 530**, 217 (2004) 134
16. Pflüger, J., Hahn, U., Faatz, B., Tischer, M.: Undulator system for the VUV-FEL at the TESLA test facility phase-2. Nucl. Instr. Meth. **A 507**, 228 (2003) 135
17. Chao, A. W.: Physics of Collective Beam Instabilities in High Energy Accelerators. John Wiley, New York 1993 136
18. Krejcik, P., et al.: Commissioning of the SSPS linac bunch compressor. Proc. Part. Acc. Conf. PAC 2003, p. 423, Portland, Oregon 2003 139
19. Akre, R., et al.: Bunch length measurements using a transverse RF deflecting structure in the SLAC linac. Proc. Eur. Part. Acc. Conf. EPAC 2002, Paris 2002 139
20. Röhrs, M.: Investigations of the phase space distributions of electron bunches at the FLASH-linac using a transverse deflecting structure. PhD thesis, University of Hamburg, April 2008 139, 146, 147
21. Steffen, B.: Electro-optic methods for longitudinal bunch diagnostic at FLASH. Ph.D. thesis, University of Hamburg (2007) 141
22. Berden, G., et al.: Benchmarking of electro-optic monitors for femtosecond electron bunches. Phys. Rev. Lett. **99**, 164801 (2007) 140
23. Winter, A., et al.: Towards high-performance optical master oscillators for energy recovery linacs. Nucl. Instr. Meth. **A 557**, 299 (2006) 142
24. Winter, A.: Fiber laser master oscillator for optical synchronization systems. Ph.D. thesis, University of Hamburg, April 2008, DESY-THESIS-2008-010 142
25. Wilcox, R.B., Staples, J.W.: Systems design concepts for optical synchronization in accelerators. Proc. Part. Acc. Conf. PAC, Albuquerque (2007) 142
26. Löhl, F., Hacker, K., Schlarb, H.: A sub-50 femtosecond bunch arrival time monitor system for FLASH. DIPAC (2007) 142, 143

9

Physical and Technological Challenges of an X-Ray FEL

9.1 Brilliance

One of the most exciting aspects of a free-electron laser as compared to alternative X-ray sources is its extreme brightness or brilliance. The expected peak brilliance of the Linac Coherent Light Source and the European XFEL are shown in Fig. 9.1, together with measured values from FLASH and from a selected number of third-generation synchrotron light sources. The spectral brilliance B describes the intensity of a radiation source including its spectral purity and opening angle according to

$$B = \frac{\Phi}{4\pi^2 \Sigma_x \Sigma_{\theta x} \Sigma_y \Sigma_{\theta y}} \,. \tag{9.1}$$

Here Φ is the photon flux, defined as the number of photons per second and within a spectral bandwidth of 0.1%. For radiation sources with only partial transverse coherence (e.g. wigglers and undulators in storage rings), the quantities $\Sigma_x, \ldots$ are calculated from the transverse rms size and angular divergence of the photon and the electron beam

$$\Sigma_x = \sqrt{\sigma_{x,\,ph}^2 + \sigma_{x,\,e}^2} \,, \quad \Sigma_{\theta x} = \sqrt{\sigma_{\theta x,\,ph}^2 + \sigma_{\theta x,\,e}^2}$$

and $\Sigma_y, \Sigma_{\theta y}$ likewise.

For a light source with full transverse coherence, the transverse size and angular divergence are no longer independent. According to (D.14) in Appendix D we get

$$\sigma_x \cdot \sigma_\theta = \frac{\lambda}{4\pi} \tag{9.2}$$

for a photon beam in the fundamental Gaussian mode. In an X-ray FEL equipped with a long undulator the fundamental Gaussian mode will usually dominate, compare Fig. 7.16. If this happens the electron beam properties drop out and one can write

P. Schmüser, et al.: *Physical and Technological Challenges of an X-Ray FEL*, STMP **229**, 149–158 (2008)
DOI 10.1007/978-3-540-79572-8_9

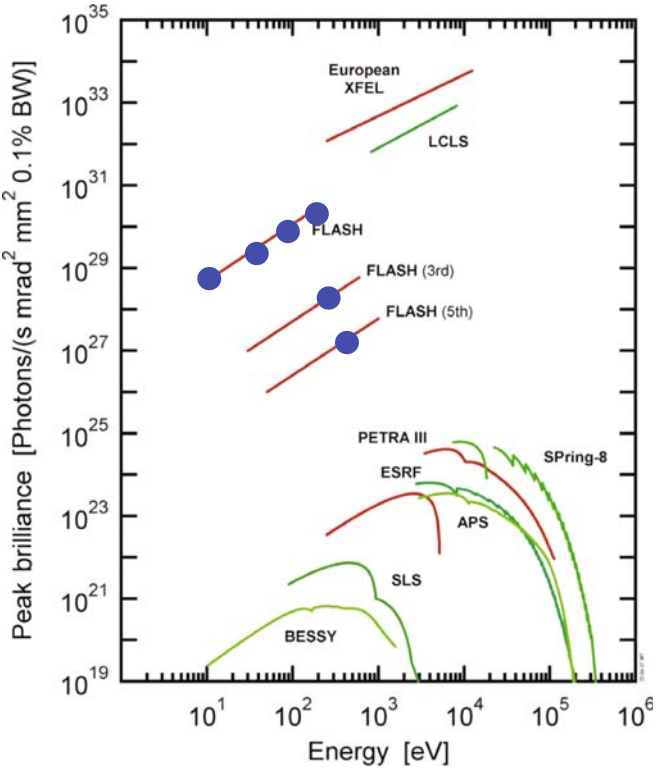

Fig. 9.1. Expected peak brilliance (number of photons per second, mm^2, mrad^2 and 0.1% bandwidth) of the planned X-ray FELs LCLS and XFEL. For comparison the measured peak brilliance of FLASH is shown (*blue dots*) as well as the brilliance achieved in some third-generation synchrotron light sources: APS (USA), BESSY (Germany), ESRF (France), SLS (Switzerland), SPring-8 (Japan). The storage-ring-type X-ray source PETRA III is under construction at DESY

$$\Sigma_x \Sigma_{\theta x} = \Sigma_y \Sigma_{\theta y} = \frac{\lambda_\ell}{4\pi} \, .$$

Hence the brilliance of the FEL is simply inversely proportional to the square of the photon wavelength

$$B_{\mathrm{FEL}} = \frac{4\Phi}{\lambda_\ell^2} \, . \tag{9.3}$$

Indirectly, the electron beam parameters play of course an essential role because stringent upper limits on the transverse size and divergence must be obeyed in order to achieve high FEL gain and the formation of a Gaussian FEL beam.

The peak brilliance at FLASH (this is the brilliance measured during the short duration of the FEL pulse) exceeds that of other existing light sources by some eight orders of magnitude at the wavelength of first harmonic. Two

physical reasons are responsible for the extremely high instantaneous power: the coherent superposition of the radiation fields from a large number of electrons present in each microbunch (this number is responsible for the large total power), and the coherent superposition of radiation fields from all microbunches within a coherence length (this effect is responsible for the small divergence and the narrow spectrum). The brilliance determines how much monochromatic radiation power can be focused onto a tiny spot on the target. The peak brilliance is the essential figure of merit for an entire class of important experiments. It should be noted though, that often also the average brilliance is quoted which is relevant for some applications. Moreover, there are experiments which just need a high X-ray flux. In such cases, an FEL is probably not the adequate source but a storage ring or a recirculating linac might be more appropriate.

While the two quantities peak brilliance and pulse duration make the FEL a unique X-ray source it must be realized that the technical requirements on the FEL facility become more and more demanding with decreasing wavelength and correspondingly increasing particle energy. Here we want to discuss only a few aspects of an X-ray FEL and refer the reader for more information to the technical design reports of the LCLS [1] and the European XFEL [2]. Further valuable information is found in the review articles by Huang and Kim [3] and by Pellegrini and Reiche [4].

9.2 Choice of Electron Energy

From the basic equation

$$\lambda_\ell = \frac{\lambda_u}{2\gamma^2}\left(1 + \frac{K^2}{2}\right) \tag{9.4}$$

we learn that a factor of 10 increase in electron energy yields a reduction of the wavelength by a factor of 100. The power gain length (4.53) depends on the electron energy $\gamma m_e c^2$ and on the particle density n_e in the form

$$L_{\mathrm{g0}} = \frac{1}{\sqrt{3}}\left[\frac{4\gamma_r^3 m_e}{\mu_0 \widehat{K}^2 e^2 k_u n_e}\right]^{1/3}$$

The transverse emittance shrinks inversely proportional to the energy

$$\varepsilon = \frac{\varepsilon_n}{\gamma_r} \quad \Rightarrow \quad n_e \propto \gamma_r$$

Therefore the power gain length scales with energy as:

$$L_{\mathrm{g0}} \propto \gamma_r^{2/3} \tag{9.5}$$

Raising the electron energy from 1 to 10 GeV means that the light wavelength drops by a factor of 100 while the gain length grows by a factor of about

4.6. This is valid under the assumption that the undulator period λ_u and the undulator parameter K are kept constant. Consider as an example the FLASH undulator with $\lambda_u = 27\,\text{mm}$ and $K = 1.18$. Raising the energy of the FLASH linac to 10 GeV would lead to a light wavelength of 0.06 nm which is the below the target value of the European XFEL.

Unfortunately this simple scaling is not always possible. The emittance criterion (6.20) becomes very demanding at small wavelengths. With increasing Lorentz factor of the electrons the transverse emittance shrinks as $1/\gamma$ but the light wavelength shrinks as $1/\gamma^2$. It is obvious that beyond some threshold value of γ the condition

$$\varepsilon \leq \frac{\lambda_\ell}{4\pi}$$

can no longer be fulfilled. They way out is to increase the undulator period λ_u and/or the undulator parameter K so that the light wavelength (9.4) decreases less steeply with energy than $1/\gamma^2$. Such a modification of the undulator has unfortunate consequences: the particle energy must be chosen considerably higher than 10 GeV, and the physical length of the undulator system must be increased. This becomes obvious if one looks at the design parameters of the LCLS at Stanford, USA, the first X-ray FEL to come into operation. They are summarized in Table 9.1. If one were able to use the FLASH undulators at LCLS, an electron energy of 6.5 GeV would suffice for reaching the design wavelength of 0.15 nm. The undulators of LCLS have a parameter $K = 3.5$, significantly larger than that of the FLASH undulator ($K = 1.18$), to fulfill the emittance criterion, and the electron energy is 13.6 GeV.

The power gain length computed with the formula (6.25) is in good agreement with the value $L_g = 5.1\,\text{m}$ quoted in the table. The optimal beta function is closer to 22 m than 30 m, but the difference in gain length is marginal and the predicted saturation power is slightly higher at $\beta_x = 30\,\text{m}$ (we thank P. Emma for this information). The larger beta function was chosen for practical

Table 9.1. Parameters of the linac coherent light source [1]

Electron energy	$W = 13.6\,\text{GeV}$
Bunch duration	200 fs
Bunch current (flat part)	$I_0 = 3400\,\text{A}$
Normalized transverse emittance	$\varepsilon_n = 1.2\,\mu\text{m}$
Average beta function	$\beta_{\text{av}} = 30\,\text{m}$
Undulator period	$\lambda_u = 0.03\,\text{m}$
Undulator field	$B_0 = 1.25\,\text{T}$
Undulator parameter	$K = 3.5$
Active undulator length	$L_u = 112\,\text{m}$
Fundamental wavelength	$\lambda_1 = 0.15\,\text{nm}$
FEL parameter	$\rho_{\text{FEL}} = 4.2 \cdot 10^{-4}$
Power gain length	$L_g = 5.1\,\text{m}$
Saturation power	$P_{\text{sat}} = 8\,\text{GW}$

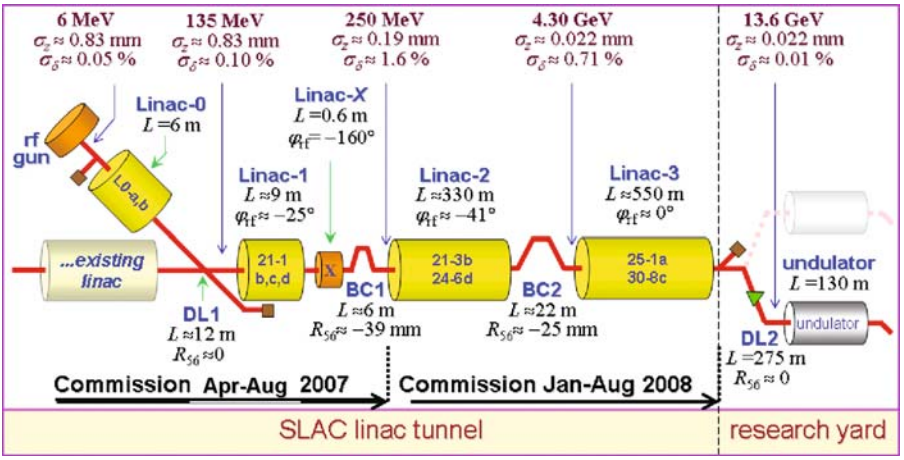

Fig. 9.2. Schematic view of the Linac Coherent Light Source under construction at Stanford (courtesy J. Galayda). Remark: $R_{56} = d\zeta/d\eta$

reasons, such as weaker quadrupole fields and relaxed alignment tolerances. A schematic view of the LCLS facility is shown in Fig. 9.2.

One of the most critical parameters is obviously the transverse emittance, compare also Fig. 8.21. Any progress in reducing the normalized emittance ε_n would have a strong impact on the layout of the FEL facility because the same wavelength could be reached at reduced electron energy, smaller undulator period, and smaller K parameter. This, in turn, would mean reduced overall size and costs. It is therefore not surprising that great efforts are undertaken worldwide to design and build electron sources that are capable of delivering very low emittance beams. Another important task is to preserve the small normalized emittance during acceleration and bunch compression. A breakthrough in these attempts, however, would not mean that the investment in a high-energy linac would turn out unnecessary with hindsight. Indeed, the improved injector performance could then be utilized for reaching even shorter wavelengths in the same accelerator facility.

9.3 Spontaneous Undulator Radiation and Quantum Effects

In addition to the FEL radiation, a large amount of spontaneous undulator radiation is emitted. The total power of spontaneous radiation emitted by a beam of N_e electrons is according to (2.21):

$$P_{\text{spont}} = \frac{N_e e^4 \gamma^2 B_0^2}{12\pi\varepsilon_0 c\, m_e^2} \,. \tag{9.6}$$

It exceeds the FEL saturation power at LCLS by some factor of 10. This is a peculiarity of all FELs driven by multi-GeV electron beams for the following reason. While $P_{\rm spont}$ increases quadratically with beam energy, the FEL saturation power (6.31)

$$P_{\rm sat} \approx 1.6\,\rho_{\rm FEL} P_{\rm beam} \left(\frac{L_{\rm g0}}{L_g}\right)^2$$

increases only rather weakly with energy. The power $P_{\rm beam}$ contained in the electron beam grows linearly with energy while the FEL parameter drops by about a factor of 7 if one compares FLASH ($W = 1\,\mathrm{GeV}$) and LCLS ($W = 13.6\,\mathrm{GeV}$). Thus there is a crossover where the spontaneous power begins to exceed the FEL power when the beam energy is increased. This crossover takes place at around 10 GeV.

Solid Angle and Spectral Width

In view of such a big amount of spontaneous undulator radiation power, the question arises what the benefit of FEL radiation is at all in the X-ray regime. This benefit is in fact present and is very convincing; it results from the fact that FEL radiation is emitted into a tiny solid angle and a narrow spectral band. The solid angle can be estimated as follows. We have seen above that the FEL beam at the end of a long undulator structure is well described by the fundamental Gaussian mode. According to Appendix D the rms divergence angle of a TEM_{00} beam is

$$\sigma_\theta = \frac{\lambda_\ell}{4\pi\sigma_x}$$

If the photon beam is matched in size to the electron beam then

$$\sigma_x = \sqrt{\varepsilon_x \beta_x}$$

With the parameters of LCLS listed in Table 9.1 one obtains a divergence angle of $\sigma_\theta \approx 3 \cdot 10^{-7}$rad and a solid angle of

$$\Delta\Omega_{\rm FEL} < 10^{-12}\,\mathrm{sterad}\,. \tag{9.7}$$

In contrast to this the cone angle containing most of the spontaneous undulator radiation power (2.27) is much larger[1]

$$\theta_{\rm spont} = \frac{K}{\gamma} \approx 1.5 \cdot 10^{-4}\mathrm{rad}\,.$$

The corresponding solid angle is some five orders of magnitude larger than the solid angle of the FEL radiation, so there will a strong suppression of the

[1] We remind the reader that the tight collimation (2.26) of first-harmonic undulator radiation is due to the requirement that the angle-dependent wavelength shift stays within the width of the spectral line observed in forward direction.

spontaneous radiation if one restricts the acceptance range of the detector to the small solid angle $\Delta\Omega_{\rm FEL}$.

Likewise, the spectral width of the entire FEL radiation is very small

$$\left(\frac{\Delta\omega}{\omega}\right)_{\rm FEL} \approx 2\,\rho_{\rm FEL} \approx 10^{-3}$$

while the spectrum of spontaneous undulator radiation is very wide if one integrates over all directions. This is illustrated in Fig. 9.3, where the spectral flux of the spontaneous undulator radiation and the FEL radiation are plotted for LCLS. The FEL radiation contributes very sharp and high spikes at the first and third harmonics.

Electron Energy Loss by Spontaneous Undulator Radiation

The large power of spontaneous radiation has a number of consequences. Firstly, it complicates the commissioning procedure of the X-ray FEL. This procedure normally starts at a rather small FEL gain, far below saturation. The low-level FEL radiation must be discriminated against the large background from spontaneous undulator radiation which is of course always present.

Secondly, the energy loss by spontaneous radiation may drive the electrons out of resonance. The fractional electron energy change due to the emission of spontaneous undulator radiation in an undulator of length L_u can be computed using (2.21). One finds

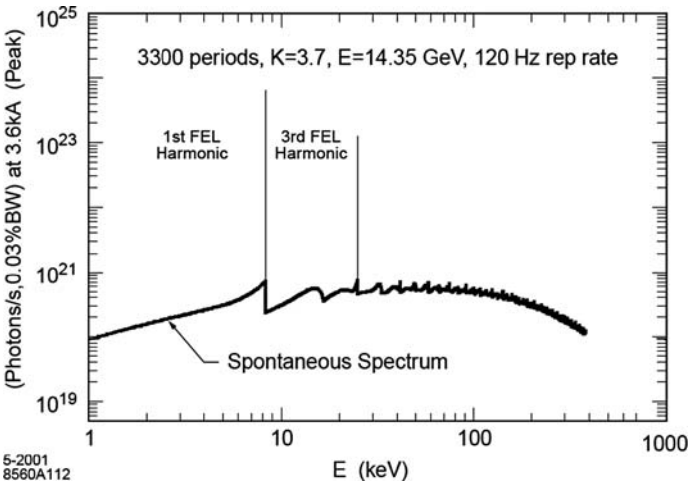

Fig. 9.3. Computed spectral flux of spontaneous undulator and FEL radiation at LCLS. Plotted is the number of photons per second and 0.3% bandwidth as a function of photon energy (courtesy H.-D. Nuhn)

$$\frac{\Delta W}{W} \equiv \frac{\Delta\gamma}{\gamma} = -\frac{e^2\gamma K^2 k_u^2 L_u}{12\pi\varepsilon_0 m_e c^2} \ . \tag{9.8}$$

In the 112 m long undulator of LCLS the fractional energy loss amounts to $1.6 \cdot 10^{-3}$ which is well above the energy bandwidth. One can say that the electrons "fall out of resonance" after having passed through a certain length of the undulator structure. In order to restore the resonance condition one can gradually reduce the undulator parameter with increasing z by reducing the magnetic field, for example by widening the gap in a permanent-magnet undulator or by reducing the coil current in an electromagnetic undulator. This method is often called "undulator tapering".

Quantum Effects and Beam Energy Spread

The classical FEL theory turns out to be adequate for a theoretical description of all existing and proposed FEL facilities. Nevertheless, the quantum nature of the photons, playing an important role for synchrotron radiation in storage rings, must be taken into consideration. When an electron emits a photon its energy will abruptly change, and the question is whether the particle will stay within the FEL gain bandwidth. It is shown in [5] that quantum effects become relevant in a high-gain FEL when the photon energy is comparable to the FEL bandwidth:

$$\hbar\omega \sim \rho_{\mathrm{FEL}}\gamma m_e c^2 \ .$$

Consider as an example the LCLS. For an electron energy of 13.6 GeV and a corresponding FEL photon wavelength of 0.15 nm and photon energy of 8 keV, the fractional energy change of the electron is only $6 \cdot 10^{-7}$, which is far below the FEL bandwidth ($\rho_{\mathrm{FEL}} = 4.2 \cdot 10^{-4}$). So quantum recoil is of no importance if only one photon is emitted. However, the accumulated effect of many photon emissions in the very long undulator of an X-ray FEL may exceed the FEL bandwidth, as we have seen above. The quantum regime of FELs starting from noise is discussed in [6].

Another undesirable effect of incoherent undulator radiation is an additional energy spread in the electron beam which has its origin in the statistical nature of the radiation. This energy spread can be estimated as follows. The growth rate of $(\Delta\gamma)^2$ caused by quantum excitation is calculated to be [7, 8]

$$\frac{d(\Delta\gamma)^2}{dz} = \frac{7e^2\hbar\gamma^4 K^3 k_u^3}{60\pi\varepsilon_0 m_e^2 c^3}\left(1.2 + \frac{1}{K + 1.33K^2 + 0.4K^3}\right) \tag{9.9}$$

where the correction factor in the bracket is derived in [8]. For LCLS the correction factor amounts to 1.22. It turns out that the additional energy spread caused by this so-called "quantum diffusion effect" is of minor importance for FLASH and the planned X-ray FELs and does not lead to an appreciable increase in gain length.

9.4 Photon Beam Lines

The peak intensity of the X-ray beam leaving the undulator is many orders of magnitude higher than what can currently be handled with existing optical technologies. The best method of reducing the power density without degrading the beam quality is to let the photon beam propagate through a long vacuum pipe until it is spread out over a substantially increased area via its natural divergence. Thereby a tolerable level for optical elements like mirrors, lenses and monochromators can be achieved. An alternative is the attenuation of the beam by means of a gas absorption cell which may provide a continuous variation of the power density at the experimental stations.

What matters at the photon beam lines of an X-ray FEL is the high instantaneous energy dose delivered to a thin surface layer of the optical elements. The surface layer is far from thermal equilibrium during the femtosecond X-ray pulse, and it is meaningless to consider equilibrium properties like melting temperatures or expansion coefficients. The tolerable energy dose causing no damage is approximately 0.01 eV/atom (for comparison, graphite requires 0.9 eV/atom for melting). In order to reduce the energy dose, the optical elements are designed to achieve the highest possible reflectivity. For mirrors this can be realized by choosing a grazing incidence geometry, at angles below the critical angle for total external reflection (remember that the refractive index of common materials is slightly less than 1 in the X-ray regime). This is the only way for reaching a reflectivity of more than 90% over a wide range of X-ray wavelengt. A good material combination is a highly polished silicon substrate with carbon coating. For 1 Ångström radiation, such mirrors are operated at a glancing angle of 2 mrad, but still photon beam drift lengths

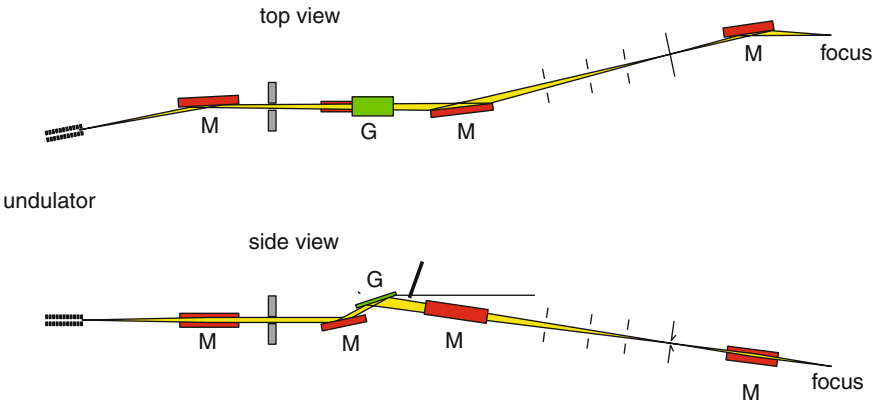

Fig. 9.4. Top view and side view of a 400 m long X-ray beam line equipped with a high-power grating monochromator, foreseen for the European XFEL. M are grazing-incidence mirrors, G is a diffraction grating (courtesy Th. Tschentscher)

of some 100 m are needed to stay below the 0.01 eV/atom limit. The consequence of the grazing incidence geometry and the long drift length is that the mirrors and lenses have to be about 0.5 m long. The surface must be polished to 0.1 nm residual roughness and 0.3 μrad tangential slope errors to preserve the wave fronts of the FEL radiation. As an example, a photon beam line design for the European XFEL is shown in Fig. 9.4.

References

1. The LCLS Design Study Group: LCLS Design Study Report, http://www-ssrl.slac.stanford.edu/lcls/ 151, 152
2. Brinkmann, R., et al.: TESLA XFEL: First stage of the X-ray laser laboratory – Technical design report. http://www.xfel.net 151
3. Huang, Z., Kim, K.-J.: Review of x-ray free-electron laser theory. Phys. Rev. ST Accel. Beams **10**, 034801 (2007) 151
4. Pellegrini, C., Reiche, S.: The Development of X-ray free-electron lasers, IEEE J. Quantum Electron. **10**, 1393, 2004. 151
5. Schroeder, C.B., Pellegrini, C., Chen, P.: Quantum effects in high-gain free-electron lasers. Phys. Rev. E **64**, 056502 (2001) 156
6. Bonifacio, R., Piovella, N., Robb, G.R.M., Schiavi, A.: Quantum regime of free electron lasers starting from noise. Phys. Rev. ST Accel. Beams 9, 090701 (2006) 156
7. Sands, M.: The Physics of Electron Storage Rings – An Introduction. SLAC publication SLAC-121 (1970) 156
8. Saldin, E., Schneidmiller, E., Yurkov, M.: Calculation of energy diffusion due to quantum fluctuations of undulator radiation. Nucl. Instr. Meth. **A 381**, 545 (1996) 156

Further Reading

9. Pellegrini, C. Stöhr, J.: X-ray free-electron lasers – principles, properties and applications. Nucl. Instr. Meth. **A 500**, 33 (2003)

A

Hamiltonian Formalism

A.1 Basic Elements of the Hamilton Formalism

In this appendix we demonstrate how Hamiltonian mechanics can be used to derive the trajectory of an electron in an undulator magnet and the coupling to the radiation field. For a thorough presentation of the Lagrange-Hamilton formulation of classical mechanics we refer to the textbooks by Landau and Lifshitz [1] and Goldstein [2].

A.1.1 Non-Relativistic Hamiltonian

In non-relativistic mechanics the Hamilton function of a particle is the sum of its kinetic and potential energies

$$H(q_j, p_j, t) = W_{\text{kin}} + W_{\text{pot}} \,. \tag{A.1}$$

The q_j and p_j are the generalized coordinates and momenta. The Hamilton equations express the time derivatives of the coordinates and momenta in terms of partial derivatives of the Hamiltonian

$$\dot{q}_i = \frac{\partial H}{\partial p_i} \,, \quad \dot{p}_i = -\frac{\partial H}{\partial q_i} \,. \tag{A.2}$$

The total time derivative of the Hamiltonian is

$$\frac{dH}{dt} = \frac{\partial H}{\partial t} + \sum_j \left[\frac{\partial H}{\partial q_j} \, \dot{q}_j + \frac{\partial H}{\partial p_j} \, \dot{p}_j \right] \,. \tag{A.3}$$

Because of the Hamilton equations the second term vanishes, hence

$$\frac{dH}{dt} = \frac{\partial H}{\partial t} \,. \tag{A.4}$$

P. Schmüser, et al.: *Hamiltonian Formalism*, STMP **229**, 159–168 (2008)
DOI 10.1007/978-3-540-79572-8_A

This means that the total energy of the particle is conserved if the Hamilton function has no explicit time dependence. The implicit time dependence contained in the generalized coordinates and momenta may increase the kinetic energy at the expense of the potential energy, or vice versa, but the sum of both remains invariant.

A.1.2 Example: Mathematical Pendulum

A mechanical example which is of relevance for the FEL is the mathematical pendulum. The mathematical pendulum consists of a mass m attached to a massless bar of length ℓ. In this case the natural choice for the canonical coordinate is the angle ϕ, the conjugated canonical momentum is then the angular momentum L

$$q = \phi\,, \quad p = L = m\ell^2\dot{\phi}\,.$$

The kinetic and potential energies and the Hamiltonian are

$$W_{\rm kin} = \frac{L^2}{2m\ell^2}\,, \quad W_{\rm pot} = m\,g\,\ell(1-\cos\phi)\,,$$
$$H(\phi, L) = \frac{L^2}{2m\ell^2} + m\,g\,\ell(1-\cos\phi) \tag{A.5}$$

where g is the acceleration of gravity. The Hamiltonian is independent of time, and hence the total energy is conserved:

$$W = W_{\rm kin} + W_{\rm pot} = \frac{L^2}{2m\ell^2} + m\,g\,\ell(1-\cos\phi) = \text{const}\,.$$

The Hamilton equations are

$$\frac{d\phi}{dt} = \frac{\partial H}{\partial L} = \frac{L}{m\ell^2}\,, \quad \frac{dL}{dt} = -\frac{\partial H}{\partial \phi} = -m\,g\,\ell\,\sin\phi\,. \tag{A.6}$$

The trajectories in the phase space (ϕ, L) can be easily constructed by writing the coupled differential equations (A.6) as difference equations and solving these in small time steps. These trajectories are the curves of constant Hamiltonian. For small angles, $\sin\phi \approx \phi$ and the pendulum carries out a harmonic oscillation of the form:

$$\phi(t) = \phi_0\cos(\omega t)\,, \quad L(t) = -m\,\ell^2\omega\,\phi_0\sin(\omega t)$$

corresponding to an elliptic phase space curve. With increasing angular momentum the motion becomes unharmonic. At very large angular momentum one gets a rotation (unbounded motion). The two regions of motion are separated by a curve called the separatrix. The equation of the separatrix can be derived from the initial conditions

$$\phi_0 = \pi\,, \quad L_0 = 0 \quad \Rightarrow \quad H_{\rm sep} = m\,g\,\ell(1-\cos\phi_0) = 2\,m\,g\,\ell\,.$$

Since the Hamiltonian is constant on the separatrix the angular momentum as a function of the angle ϕ can be computed from

$$\frac{[L_{\rm sep}(\phi)]^2}{2m\ell^2} = H_{\rm sep} - m\,g\,\ell(1-\cos\phi)$$

from which follows

$$L_{\rm sep}(\phi) = \pm 2m\ell^2\sqrt{g/\ell}\,\cos(\phi/2)\,. \tag{A.7}$$

The phase space picture of the mathematical pendulum is shown in Fig. A.1.

A.1.3 Relativistic Hamiltonian

The relativistic Hamiltonian of a particle of rest mass m_0 moving in a force- and field-free region is

$$H(q_i,p_i) \equiv \gamma m_0 c^2 = c\,\left[\boldsymbol{p}^2 + m_0^2c^2\right]^{1/2}\,. \tag{A.8}$$

The canonical coordinates q_i are taken here as the Cartesian coordinates $\boldsymbol{r} = (x,y,z)$, and the canonical momentum is $\boldsymbol{p} = \gamma m_0\boldsymbol{v}$. The Hamiltonian is identical with the total relativistic energy of the particle, for a free particle it is the sum of kinetic energy $W_{\rm kin}$ and rest energy m_0c^2.

In the presence of an electromagnetic field the Hamiltonian of a particle with charge q must be modified. We characterize the field by its scalar and vector potentials:

$$\boldsymbol{E} = -\boldsymbol{\nabla}\Phi - \frac{\partial\boldsymbol{A}}{\partial t}\,, \qquad \boldsymbol{B} = \boldsymbol{\nabla}\times\boldsymbol{A}\,. \tag{A.9}$$

Remember that we use the SI system in contrast to many articles and books on FEL theory that use Gaussian cgs units. To account for the electromagnetic field we have to add the potential energy $W_{\rm pot} = q\Phi$, and moreover the kinetic momentum $\boldsymbol{p} = \gamma m_0\boldsymbol{v}$ has to be replaced by the canonical momentum

$$\boldsymbol{P} = \boldsymbol{p} + q\,\boldsymbol{A} = \gamma m_0\boldsymbol{v} + q\,\boldsymbol{A}\,. \tag{A.10}$$

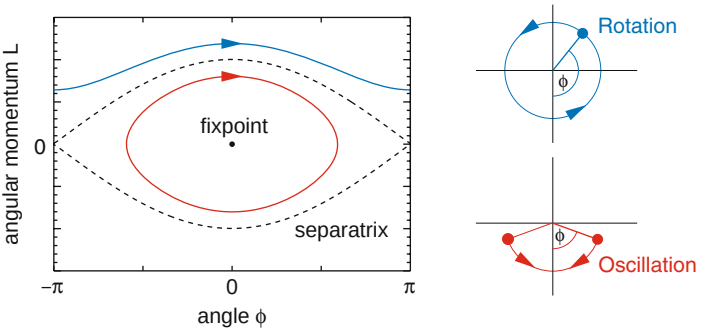

Fig. A.1. Phase space curves of a mathematical pendulum. The separatrix (*dashed curve*) separates the region of bounded motion (*periodic oscillation*) from that of unbounded motion (*rotation*). The point $(0,0)$ is a fixpoint

The relativistic Hamiltonian of a charged particle in an electromagnetic field is thus

$$H(\boldsymbol{r},\boldsymbol{P},t) = c\,\left[(\boldsymbol{P}-q\,\boldsymbol{A})^2 + m_0^2c^2\right]^{1/2} + q\,\Phi\,. \tag{A.11}$$

Again this Hamiltonian is identical with the total relativistic energy of the particle, namely the sum of kinetic energy, potential energy, and rest energy m_0c^2. The Hamiltonian has to be considered a function of the canonical coordinates $\boldsymbol{r} = (x,y,z)$, the canonical momenta $\boldsymbol{P} = (P_x,P_y,P_z)$, and the time t.

In the following we consider an electron (charge $q=-e$, rest mass $m_0 = m_e$) moving in the magnetic field of an undulator magnet and in the electric field of a light wave. Then no scalar potential Φ is present and the Hamilton function has the form

$$H(\boldsymbol{r},\boldsymbol{P},t) = c\,\left[(\boldsymbol{P}+e\,\boldsymbol{A})^2 + m_e^2c^2\right]^{1/2} \equiv \gamma m_e c^2 \tag{A.12}$$

where the vector potential $\boldsymbol{A}(\boldsymbol{r},t)$ comprises both fields. This Hamiltonian is equal to the total energy $W = \gamma m_e c^2$ of the electron and will be time-dependent if the electron exchanges energy with the light wave, in which case the Lorentz factor is a function of time, too. The Hamilton equations are evaluated using the formula

$$\frac{d\sqrt{f(x)}}{dx} = \frac{f'(x)}{2\sqrt{f(x)}}\,.$$

With the help of this formula we find for example

$$\frac{dx}{dt} = \frac{\partial H}{\partial P_x} = \frac{2c(P_x+e\,A_x)}{2\sqrt{(\boldsymbol{P}+e\,\boldsymbol{A})^2+m_e^2c^2}} = \frac{(P_x+e\,A_x)}{\gamma m_e} = \frac{\gamma m_e v_x}{\gamma m_e} = v_x\,. \tag{A.13}$$

Note that one can replace the square root in the denominator by $\gamma m_e c$. The time derivative of the Hamiltonian is found by the same method

$$\frac{\partial H}{\partial t} = \frac{(\boldsymbol{P}+e\,\boldsymbol{A})}{\gamma m_e}\cdot\frac{\partial(e\boldsymbol{A})}{\partial t} = -e\,\boldsymbol{v}\cdot\boldsymbol{E} \tag{A.14}$$

where we have used $\boldsymbol{P}+e\,\boldsymbol{A} = \gamma m_e\boldsymbol{v}$ and $\boldsymbol{E} = -\partial\boldsymbol{A}/\partial t$.

A.2 Electron Motion in a Planar Undulator

The Hamiltonian formulation is now applied to compute the electron trajectory in a planar undulator, following partly the procedure in [3]. The emission of undulator radiation is neglected for the time being. We consider a simplified form of the undulator field, see (2.3)

$$\boldsymbol{B} = -B_0\sin(k_u z)\boldsymbol{e}_y \tag{A.15}$$

which can be derived from the vector potential

$$\boldsymbol{A} = \frac{B_0}{k_u} \cos(k_u z) \boldsymbol{e}_x \,. \tag{A.16}$$

Here $\boldsymbol{e}_x, \boldsymbol{e}_y$ are the unit vectors in x resp. y direction. An electric field is not present in the undulator, hence the potential energy term is missing. We note that the vector potential has only an x component which depends on the single variable z. The Hamiltonian of the electron becomes thus

$$\begin{aligned} H(z, P_x, P_y, P_z) &= c \left[\left(P_x + e \frac{B_0}{k_u} \cos(k_u z) \right)^2 + P_y^2 + P_z^2 + m_e^2 c^2 \right]^{1/2} \\ &\equiv \gamma m_e c^2 \,. \end{aligned} \tag{A.17}$$

The two Hamilton equations

$$\dot{P}_x = -\frac{\partial H}{\partial x} = 0, \quad \dot{P}_y = -\frac{\partial H}{\partial y} = 0$$

imply that $P_x = \gamma m_e v_x - e\, A_x$ and $P_y = \gamma m_e v_y$ are constants of motion. The vector potential A_x vanishes at $z = \lambda_u/4$, right after the beginning of the undulator. Choosing the initial conditions such that $v_x = v_y = 0$ at this position, we obtain $P_x, P_y \equiv 0$ all along the undulator from which follows $v_y(z) \equiv 0$ and

$$v_x(z) = \frac{e\, B_0}{\gamma m_e k_u} \cos(k_u z) = \frac{K\, c}{\gamma} \cos(k_u z) \,. \tag{A.18}$$

This is identical with (2.9) in Chap. 2.
Since the canonical momenta P_x, P_y are zero all along the undulator, the Hamiltonian depends only on z and P_z:

$$H = H(z, P_z) = c \left[\frac{e^2 B_0^2}{k_u^2} \cos^2(k_u z) + P_z^2 + m_e^2 c^2 \right]^{1/2} . \tag{A.19}$$

The Hamilton equations yield (compare (A.13))

$$\dot{z} = \frac{\partial H}{\partial P_z} = \frac{P_z}{\gamma m_e} \,, \quad \dot{P}_z = -\frac{\partial H}{\partial z} = \frac{e^2 B_0^2}{2\gamma m_e k_u} \sin(2k_u z) \,.$$

Using $z(t) \approx \bar{v}_z t$ the second equation can be integrated over time. Inserting the result into the first one we obtain

$$v_z(t) \approx \bar{v}_z - \frac{e^2 B_0^2}{4\gamma^2 m_e^2 k_u^2 c} \cos(2k_u \bar{v}_z t)$$

where the first term comes from the integration constant. By the same consideration as in Chap. 2 we find that the constant velocity term is identical

with the average z speed (2.13). If we define $\omega_u = \bar{v}_z k_u$ the above expression is identical with (2.12). The particle trajectory is, choosing $x(0) = y(0) = 0$,

$$x(t) = \frac{cK}{\gamma\omega_u}\,\sin(\omega_u t)\,, \quad y(t) = 0\,, \quad z(t) = \bar{v}_z t - \frac{cK^2}{8\gamma^2\omega_u}\,\sin(2\omega_u t) \tag{A.20}$$

in agreement with (2.14).

A.3 Electron Motion in a Helical Undulator

Generalizing (A.16) we choose a vector potential

$$\boldsymbol{A} = \frac{B_0}{k_u}\,[\cos(k_u z)\boldsymbol{e}_x + \sin(k_u z)\boldsymbol{e}_y] \tag{A.21}$$

which corresponds to the helical undulator field

$$\boldsymbol{B} = -B_0\,[\cos(k_u z)\boldsymbol{e}_x + \sin(k_u z)\boldsymbol{e}_y]\,. \tag{A.22}$$

This field has the sense of rotation of a right-handed screw. Note that it is a simplified field, not in accordance with the Maxwell equation $\boldsymbol{\nabla} \times \boldsymbol{B} = 0$, but it is a good approximation for the field of a real helical undulator for small deviations from the axis. Again the Hamiltonian does not depend on x and y with the consequence that the corresponding canonical momenta are constants of motion and can be set equal to zero by choosing appropriate initial conditions. Hence we have $P_x \equiv 0$, $P_y \equiv 0$, yielding the important equations:

$$\gamma m_e v_x(z) = e\,A_x(z) = \frac{e\,B_0}{k_u}\cos(k_u z)$$
$$\gamma m_e v_y(z) = e\,A_y(z) = \frac{e\,B_0}{k_u}\sin(k_u z)$$

hence

$$v_x = \frac{c\,K}{\gamma}\,\cos(k_u z)\,, \quad v_y = \frac{c\,K}{\gamma}\,\sin(k_u z)\,. \tag{A.23}$$

Like in the planar undulator the Hamiltonian depends only on z and P_z

$$H = H(z, P_z) = c\left[\frac{e^2 B_0^2}{k_u^2}(\cos^2(k_u z) + \sin^2(k_u z)) + P_z^2 + m_e^2 c^2\right]^{1/2}$$

but now even the z dependence drops out:

$$H = H(P_z) = c\left[\frac{e^2 B_0^2}{k_u^2} + P_z^2 + m_e^2 c^2\right]^{1/2}. \tag{A.24}$$

From this expression follows immediately

$$\dot{P}_z = -\frac{\partial H}{\partial z} = 0 \quad \Rightarrow P_z = \gamma m_e v_z = \text{const} \tag{A.25}$$

so the speed in z direction is a constant. From (A.23) we find

$$v_x^2 + v_y^2 = \frac{K^2 c^2}{\gamma^2}$$

and

$$v_z = \sqrt{v^2 - v_x^2 - v_y^2} = c\sqrt{\beta^2 - K^2/\gamma^2} \approx v_0 \equiv c\left(1 - \frac{1}{2\gamma^2}(1+K^2)\right) \tag{A.26}$$

which differs from the planar undulator case in two aspects: the factor $(1+K^2)$ appears instead of $(1+K^2/2)$, and longitudinal oscillations do not exist. The absence of these oscillations is the reason why helical undulator radiation has no higher harmonics (this applies for radiation in forward direction). The particle trajectory is found by integration of (A.23)

$$x(t) = \frac{e\,B_0}{\gamma m_e k_u^2 v_0}\sin(\omega_u t)\,, \quad y(t) = -\frac{e\,B_0}{\gamma m_e k_u^2 v_0}\cos(\omega_u t)\,, \quad z(t) = v_0 t\,. \tag{A.27}$$

It is a right-handed helix with the radius

$$r_{\text{hel}} = \frac{e\,B_0}{\gamma m_e k_u^2 v_0} \approx \frac{K}{\gamma k_u}\,. \tag{A.28}$$

A.4 Energy Exchange Between Electron and Light Wave

A.4.1 Planar Undulator

We want to demonstrate that the equation (3.5), describing the energy transfer between electron and light wave, can also be obtained in the Hamiltonian formalism. Like in Chap. 3 the radiation field is described by a plane wave with linear horizontal polarization

$$E_x(z,t) = E_0\cos(k_\ell z - \omega_\ell t + \psi_0)\,.$$

The field can be derived from the vector potential

$$\boldsymbol{A}^\ell(z,t) = \frac{E_0}{\omega_\ell}\sin(k_\ell z - \omega_\ell t + \psi_0)\,\boldsymbol{e}_x \tag{A.29}$$

which satisfies the homogeneous wave equation. The total vector potential is the sum of the vector potentials of the undulator (A.16) and the light wave (A.29):

$$\boldsymbol{A}(z,t) = \boldsymbol{A}^u(z) + \boldsymbol{A}^\ell(z,t)\,.$$

It has only an x component but is a function of both z and t. The Hamiltonian of an electron passing a planar undulator in the presence of a horizontally polarized light wave is thus

$$H(\boldsymbol{r},\boldsymbol{P},t) = c\,\left[\left(P_x + e\,A_x^u(z) + e\,A_x^\ell(z,t)\right)^2 + P_y^2 + P_z^2 + m_e^2\right]^{1/2} . \quad \text{(A.30)}$$

The important new feature of this Hamiltonian is its explicit time dependence, brought in by the vector potential of the radiation field. The electron energy is therefore not conserved, which we know already, because there is energy exchange with the radiation field. To find the rate of change dW/dt of the electron energy we compute the partial derivative of H with respect to time using (A.14). The rate of change of the electron energy is

$$\begin{aligned}\frac{dW}{dt} = \frac{\partial H}{\partial t} &= -e\,v_x(z)E_x(z,t) = -\frac{e\,c\,K}{\gamma}\,\cos(k_u z)E_0\cos(k_\ell z - \omega_\ell t + \psi_0) \\ &\equiv -\frac{e\,c\,K E_0}{2\gamma}[\cos\psi + \cos\chi] \end{aligned} \quad \text{(A.31)}$$

which is identical with (3.5). Here $\psi = (k_\ell + k_u)z - \omega_\ell t + \psi_0$ is the ponderomotive phase defined in Chap. 3, and $\chi = (k_\ell - k_u)z - \omega_\ell t + \psi_0$ is the rapidly oscillating phase. Equation (A.31) is only valid in the low-gain regime because we have treated the field amplitude E_0 of the light wave as a constant when computing the time derivative of the Hamiltonian.

It is very easy to understand that vertically polarized radiation cannot couple to the electron: an electric field having only a y component yields a vanishing scalar product with the velocity vector $\boldsymbol{v} = (v_x, 0, v_z)$ of the electron.

A.4.2 Helical Undulator

The helical undulator field (A.22) has a right-handed screw sense. Hence we expect that the helical undulator radiation will be circularly polarized and make the following ansatz for the light wave interacting with the electrons

$$\boldsymbol{E}(z,t) = E_0\,[\cos(k_\ell z - \omega_\ell t)\boldsymbol{e}_x - \sin(k_\ell z - \omega_\ell t)\boldsymbol{e}_y] \quad \text{(A.32)}$$

which derives from the vector potential

$$\boldsymbol{A}^\ell(z,t) = \frac{E_0}{\omega_\ell}\,[\sin(k_\ell z - \omega_\ell t)\boldsymbol{e}_x + \cos(k_\ell z - \omega_\ell t)\boldsymbol{e}_y] \; . \quad \text{(A.33)}$$

A possible constant phase shift ψ_0 has been omitted here. In the language of modern particle physics the photons described by (A.32) are called right-handed and have positive helicity (a positive projection of angular momentum onto the direction of motion). However, in the nomenclature of optics (A.32)

describes a left circularly polarized wave[1]. The vector potential of the undulator magnet is given by (A.21):

$$\boldsymbol{A}^u(z) = \frac{B_0}{k_u}\left[\cos(k_u z)\boldsymbol{e}_x + \sin(k_u z)\boldsymbol{e}_y\right] .$$

We can again use (A.14) to compute the time derivative of the electron energy. The velocities are taken from (A.23).

$$\begin{aligned}\frac{dW}{dt} &= \frac{\partial H}{\partial t} = -e\,v_x(z)E_x(z,t) - e\,v_y(z)E_y(z,t)\\ &= -\frac{e\,c\,K\,E_0}{\gamma}\left[\cos(k_u z)\cos(k_\ell z - \omega_\ell t) - \sin(k_u z)\sin(k_\ell z - \omega_\ell t)\right]\\ \frac{dW}{dt} &= -\frac{e\,c\,KE_0}{\gamma}\cos\psi \end{aligned} \tag{A.34}$$

where $\psi = (k_\ell + k_u)z - \omega_\ell\, t$ is the ponderomotive phase defined in Chap. 3. Sustained energy transfer from the electron to the light wave is obtained if the ponderomotive phase remains constant during the motion through the undulator, the optimum value being $\psi = 0$. From the condition of a stationary phase

$$\dot{\psi} = 0 \quad \Rightarrow \quad (k_\ell + k_u)v_z - k_\ell c = 0$$

and using (A.26) we compute the wavelength of helical undulator radiation:

$$\lambda_\ell = \frac{\lambda_u}{2\gamma^2}\left(1 + K^2\right) . \tag{A.35}$$

What happens if we choose the wrong polarization, i.e. negative helicity resp. right circular polarization? The field is

$$\boldsymbol{E}(z,t) = E_0\left[\cos(k_\ell z - \omega_\ell t)\boldsymbol{e}_x + \sin(k_\ell z - \omega_\ell t)\boldsymbol{e}_y\right]$$

and one gets

$$\begin{aligned}\frac{dW}{dt} &= -\frac{e\,c\,K\,E_0}{\gamma}\left[\cos(k_u z)\cos(k_\ell z - \omega_\ell t) + \sin(k_u z)\sin(k_\ell z - \omega_\ell t)\right]\\ &= -\frac{e\,c\,KE_0}{\gamma}\cos\chi \end{aligned} \tag{A.36}$$

where $\chi = (k_\ell - k_u)z - \omega_\ell\, t$ is the rapidly varying phase defined in Chap. 3. The time derivative of the electron energy averages to zero over half an undulator

[1] In particle physics one looks along the direction of motion of the photon. In that case the electric vector at a fixed spatial position rotates in clockwise direction. In optics the convention is such that the observer is facing into the oncoming wave, and then the field vector at a fixed spatial position rotates counterclockwise, see e.g. [4].

period. This means that no energy transfer happens between electron and light wave; in other words: radiation with the wrong circular polarization will not be emitted. From this observation it is obvious that a helical undulator cannot produce linearly polarized radiation either as this a superposition of left-hand and right-hand circularly polarized waves with 90° relative phase shift. Furthermore we see that it is possible to seed an FEL equipped with a helical undulator with linearly polarized light: a linearly polarized wave can be decomposed into two counter-rotating circularly polarized waves, but only the wave with the correct sense of rotation will be amplified in the FEL. The output light will of course be circularly polarized.

References

1. Landau, L.D., Lifshitz, E.M.: Course of Theoretical Physics, Volume 1: Mechanics. Butterworth-Heinemann, Boston, MA (2003) 159
2. Goldstein, H.: Classical Mechanics. Addison-Wesley, Reading, MA (1959) 159
3. Murphy, J.B., Pellegrini, C.: Introduction to the Physics of the Free Electron Laser. Laser Handbook, vol. 6, p. 11–67. North Holland, Amsterdam, Oxford, New York, Tokyo (1990) 162
4. Jackson, J.D.: Classical Electrodynamics. 3rd ed. John Wiley, New York (1999) 167

B

Low-Gain Limit of the High-Gain FEL Theory

In this appendix we want to demonstrate that the low-gain FEL theory and the Madey theorem are obtained from the high-gain FEL theory if the undulator magnet is short enough. To this end we start from (4.45) in Chap. 4

$$\frac{d\tilde{E}_x}{dz} = i\,k_u\,\frac{\mu_0\widehat{K}n_e e^2}{2m_e\gamma_r^2}\int_0^z [\ldots]\;(z-s)\;\exp\left[-i\,2k_u\eta(z-s)\right]ds$$

with

$$[\ldots] = \left[\frac{\widehat{K}}{2\gamma_r}\tilde{E}_x + i\frac{4\gamma_r c}{\omega_\ell\widehat{K}}\,\frac{d\tilde{E}_x}{dz}\right].$$

In a short undulator the square bracket can be simplified: the electric field can be considered as roughly constant, $\tilde{E}_x \approx E_0$, and its derivative can be neglected in the square bracket. We then get

$$\begin{aligned}\frac{d\tilde{E}_x}{dz} &= i\,k_u\frac{\mu_0\widehat{K}^2 n_e e^2 E_0}{4m_e\gamma_r^3}\int_0^z (z-s)\;\exp\left[-i\,2k_u\eta(z-s)\right]ds \\ &= i\,\Gamma^3 E_0\int_0^z (z-s)\;\exp\left[-i\,2k_u\eta(z-s)\right]ds\,. \qquad \text{(B.1)}\end{aligned}$$

The definite integral yields

$$I(z) \equiv \int_0^z (z-s)\;\exp\left[-i\,2k_u\eta(z-s)\right]ds = \frac{(1+i\,2k_u\eta z)\exp(-i\,2k_u\eta z)-1}{(2k_u\eta)^2}$$

The complex field at the end of an undulator of length L_u is

$$\tilde{E}_x(L_u) = E_0 + i\,\Gamma^3 E_0\int_0^{L_u} I(z)dz \equiv E_0(1+A(L_u))$$

where $A(L_u)$ is defined as

$$A(L_u) = -\frac{i\,\Gamma^3}{(2k_u\eta)^2}\left\{L_u + \frac{i}{k_u\eta} + \left(L_u - \frac{i}{k_u\eta}\right)\exp(-i\,2k_u\eta L_u)\right\}$$

P. Schmüser, et al.: *Low-Gain Limit of the High-Gain FEL Theory*, STMP **229**, 169–170 (2008)
DOI 10.1007/978-3-540-79572-8_B

The absolute square of the field at $z = L_u$ is

$$\left|\tilde{E}_x(L_u)\right|^2 = E_0^2 \left(1 + 2\Re[A(L_u)] + (\Re[A(L_u)])^2 + (\Im[A(L_u)])^2\right) .$$

The quadratic terms can be neglected in a short undulator hence the gain function becomes

$$\begin{aligned} G &= \left|\frac{\tilde{E}_x(L_u)}{E_0}\right|^2 - 1 \approx 2\,\Re[A(L_u)] \\ &= \frac{2\,\Gamma^3}{(2k_u\eta)^2}\left\{\frac{1}{k_u\eta} - \frac{\cos(2k_u\eta L_u)}{k_u\eta} - L_u\sin(2k_u\eta L_u)\right\} \end{aligned}$$

Introducing the variable

$$\xi = k_u\eta L_u$$

the gain function can be written as

$$G(\xi) = -\frac{\Gamma^3 L_u^3}{2}\,\frac{d}{d\xi}\left(\frac{\sin^2\xi}{\xi^2}\right) \tag{B.2}$$

which is the Madey theorem.

C

Non-Periodic First-Order Equations

Our goal is to generalize the first-order equations in such a way that non-periodic processes in the FEL can be handled. Examples are the SASE mechanism where the initial particle distribution is random, FEL seeding with a superposition of harmonic waves of different frequencies, non-uniform charge density profiles in the electron bunches, effects at the head or tail of the electron bunch, slippage between the electrons and the light wave.

In the periodic model, that has been discussed at great length in Sect. 4.6, the slowly varying amplitudes depend only on the position z in the undulator. Field and current density have been written as

$$\tilde{E}_x(z,t) = \tilde{E}_x(z)\exp[i\,k_\ell z - i\,\omega_\ell t]$$
$$\tilde{j}_z(\psi,z) = j_0 + \tilde{j}_1(z)\,\exp\left[i\,(k_\ell + k_u)z - i\,\omega_\ell t\right]\,.$$

In the nonperiodic generalization the current density inside the electron bunch depends in addition on our previously defined internal bunch coordinate

$$\zeta = z - \bar{\beta}\,c\,t = z - \bar{v}_z t$$

and the electric field depends on a corresponding coordinate u inside the FEL pulse

$$u = z - c\,t = \left(1 - \frac{c}{\bar{v}_z}\right)\,z + \frac{c}{\bar{v}_z}\,\zeta\,.$$

Hence the ansatz is made

$$\tilde{E}_x(z,t) = \widehat{E}(z,u)\exp[i\,k_\ell z - i\,\omega_\ell t] \tag{C.1}$$
$$\tilde{j}_z(z,t) = j_0(\zeta) + \widehat{j}_1(z,\zeta)\exp[i\,(k_\ell + k_u)z - i\,\omega_\ell t] \tag{C.2}$$

The complex field amplitude is now denoted with $\widehat{E}(z,u)$, and the subscript x is dropped for simplicity. These expressions are substituted into the wave equation (4.8).

$$\left[\frac{\partial^2}{\partial z^2} - \frac{1}{c^2}\frac{\partial^2}{\partial t^2}\right]\tilde{E}_x(z,t) = \mu_0\frac{\partial\tilde{j}_x}{\partial t} \tag{C.3}$$

P. Schmüser, et al.: *Non-Periodic First-Order Equations*, STMP **229**, 171–174 (2008)
DOI 10.1007/978-3-540-79572-8_C

Then we obtain

$$\begin{aligned}\frac{\partial^2 \tilde{E}_x(z,t)}{\partial z^2} &= \left[\frac{\partial^2}{\partial z^2} + 2\,\frac{\partial^2}{\partial z \partial u} + \frac{\partial^2}{\partial u^2} + 2ik_\ell \left(\frac{\partial}{\partial z} + \frac{\partial}{\partial u}\right) - k_\ell^2\right] \widehat{E}(z,u) \\ &\quad \times \exp[i\,k_\ell z - i\,\omega_\ell t] \\ \frac{\partial^2 \tilde{E}_x(z,t)}{\partial t^2} &= c^2 \left[\frac{\partial^2}{\partial u^2} + 2ik_\ell \frac{\partial}{\partial u} - k_\ell^2\right] \widehat{E}(z,u) \exp[i\,k_\ell z - i\,\omega_\ell t]\,.\end{aligned}$$

In the slowly varying amplitude (SVA) approximation $\widehat{E}(z,u)$ is assumed to be a smooth and slowly varying function of z and u so that its second derivatives can be neglected:

$$\left|\frac{\partial^2 \widehat{E}}{\partial z^2}\right| \ll k_\ell \left|\frac{\partial \widehat{E}}{\partial z}\right|, \quad \left|\frac{\partial^2 \widehat{E}}{\partial z \partial u}\right| \ll k_\ell \left|\frac{\partial \widehat{E}}{\partial z}\right|.$$

Then the left-hand side of the wave equation becomes

$$\left[\frac{\partial^2}{\partial z^2} - \frac{1}{c^2}\frac{\partial^2}{\partial t^2}\right] \tilde{E}_x(z,t) = 2i\,k_\ell \frac{\partial}{\partial z}\widehat{E}(z,u)\, \exp[i\,k_\ell z - i\,\omega_\ell t]\,. \tag{C.4}$$

The current density $\tilde{j}_x$ appearing on the right-hand side of (4.8) is written in the form (compare (4.14))

$$\tilde{j}_x \approx \frac{v_x}{c}\,\tilde{j}_z = \left[j_0(\zeta) + \widehat{j}_1(z,\zeta) \exp[i\,(k_\ell + k_u)z - i\,\omega_\ell t]\right] \frac{K}{\gamma}\,\cos(k_u z)\,.$$

The stimulation by the shape term $j_0(\zeta)$ is far away from the FEL resonance, and hence this term can be dropped when computing the time derivative:

$$\frac{\partial \tilde{j}_x}{\partial t} = -\left[\bar{v}_z \frac{\partial \widehat{j}_1}{\partial \zeta} + i\,\omega_\ell \widehat{j}_1(z,\zeta)\right] \exp[i\,(k_\ell + k_u)z - i\,\omega_\ell t] \frac{K}{\gamma}\,\cos(k_u z)\,.$$

In the SVA approximation

$$\bar{v}_z \left|\frac{\partial \widehat{j}_1}{\partial \zeta}\right| \ll \left|\omega_\ell \widehat{j}_1(z,\zeta)\right|$$

so the wave equation (C.3) reduces to

$$\frac{\partial}{\partial z}\widehat{E}(z,u) = -\frac{\mu_0 c\,K}{2\gamma}\,\widehat{j}_1(z,\zeta) \exp(i\,k_u z)\cos(k_u z)\,.$$

The average value of $\exp(i\,k_u z)\cos(k_u z)$ over one undulator period is $1/2$. Replacing K by $\widehat{K}$ to take the longitudinal oscillation into account we finally obtain the generalization of (4.30d)

$$\frac{\partial}{\partial z}\widehat{E}(z,u) = -\frac{\mu_0 c\widehat{K}}{4\gamma_r}\,\widehat{j}_1(z,\zeta)\,. \tag{C.5}$$

The microscopic expression for the current density is

$$j_z = \frac{Q_b\,\bar{v}_z}{N_t A_b}\sum_{n=1}^{N_t}\delta(\zeta-\zeta_n(z))$$

where $Q_b = -N_t\,e$ is the charge of the bunch, A_b the cross section, and N_t the total number of electrons in the bunch. Since the present FEL codes work with a far smaller number N of test particles, j_z must be approximated by smooth functions $j_0(\zeta)$ and $\widehat{j}_1(z,\zeta)$ that vary slowly in the z coordinate (compared to the undulator period λ_u) and in the ζ coordinate (compared to the FEL wavelength λ_ℓ). Indeed, the conversion of the particle positions ζ_n to smooth functions is a delicate and sensitive part of FEL simulations using macroparticle descriptions. Pseudo-random distributions can be used yielding the same statistical fluctuations that are present in the real electron beam.

In most FEL codes locally periodic conditions are assumed. The bunch is subdivided into slices of length λ_ℓ which are similar the FEL buckets. Within each slice periodic conditions are assumed. The local amplitude of the first harmonic is written as

$$\widehat{j}_1(z,c_m) \approx j_0(c_m)\,\frac{2}{N_m}\sum_{n\in I_m}\exp(-i\,k_\ell\zeta_n) \tag{C.6}$$

where $c_m = m\,\lambda_\ell$ is the center of slice m, N_m the number of particles in that slice, and I_m the index range.

We know from Sect. 5.6 that not all particles stay in their bucket during the FEL gain process but many of them move into the next bucket. In the simulation program this is accounted for by replacing particles leaving a slice on one side by corresponding particles entering the slice from the other side. Further details are beyond the scope of this book. The non-periodic form of the coupled equations is

$$\frac{d\psi_n}{dz} = 2k_u\eta_n\,, \quad n = 1...N \tag{C.7a}$$

$$\frac{d\eta_n}{dz} = \frac{-e}{m_e c^2\gamma_r}\,\Re\left\{\left(\frac{\widehat{K}\,\widehat{E}(z,u_n)}{2\gamma_r} - \frac{i\mu_0 c^2\,\widehat{j}_1(z,\zeta_n)}{\omega_\ell}\right)e^{i\psi_n}\right\} \tag{C.7b}$$

$$\widehat{j}_1(z,c_m) = j_0(c_m)\,\frac{2}{N_m}\sum_{n\in I_m}\exp(-i\,k_\ell\zeta_n), \quad c_m = m\,\lambda_\ell \tag{C.7c}$$

$$\frac{\partial\widehat{E}(z,u)}{\partial z} = -\frac{\mu_0 c\widehat{K}}{4\gamma_r}\,\widehat{j}_1(z,\zeta) \tag{C.7d}$$

with

$$\zeta_n = (\psi_n + \pi/2)\,\lambda_\ell/(2\pi), \quad u_n \approx \zeta_n - (1-\bar{\beta})z\,.$$

In these equations N is the total number of test particles per bunch and not the number of test particles per slice as in the periodic case.

D

Gaussian Modes of Laser Beams

Gaussian beam modes are characteristic of the output of lasers. They are also well suited to describe the beam in a free-electron laser. In this appendix we follow essentially the treatments in [1] and [2].

D.1 Fundamental Gaussian Mode

Laser beams are coherent electromagnetic radiation and obey the Maxwell equations. In a medium with refractive index n the electric field vector satisfies the wave equation

$$\nabla^2 E - \frac{n^2}{c^2}\,\frac{\partial^2 E}{\partial t^2} = 0 \tag{D.1}$$

where $E(x, y, z, t)$ can be any Cartesian component of $\boldsymbol{E}$. We restrict ourselves to homogeneous media ($n = const$) or vacuum ($n = 1$). In the laser literature often quadratic index media are considered, see e.g. [1, 2]. We look for a cylindrically symmetric solution of the wave equation which depends only on $r = \sqrt{x^2 + y^2}$, z, and t, but not on the azimuthal angle. Writing

$$E(x, y, z, t) = f(r, z)\exp(i\,kz - i\,\omega t) \quad \text{with} \quad k = n\,\omega/c$$

we obtain the equation

$$\frac{\partial^2 f}{\partial r^2} + \frac{1}{r}\,\frac{\partial f}{\partial r} + 2\,i\,k\frac{\partial f}{\partial z} = 0 \tag{D.2}$$

In practice the field amplitude varies slowly with z hence the second derivative $\partial^2 f/\partial z^2$ has been neglected in comparison with $2\,i\,k\,\partial f/\partial z$ (SVA approximation).

The simplest solution has no zeros in radial direction. It is convention to write it in the form

$$f(r, z) = \exp\left[i\,P(z) + \frac{i\,k\,r^2}{2q(z)}\right]$$

P. Schmüser, et al.: *Gaussian Modes of Laser Beams*, STMP **229**, 175–180 (2008)
DOI 10.1007/978-3-540-79572-8_D

with two complex functions $P(z)$ and $q(z)$. Substituting this into (D.2) we obtain

$$-\left(\frac{k}{q}\right)^2 r^2 + 2\,i\,\left(\frac{k}{q}\right) - 2\,k\,P' - k^2 r^2\left(\frac{1}{q}\right)' = 0$$

where the prime indicates differentiation with respect to z. This equation holds for all r so the coefficients of different powers of r must vanish:

$$\left(\frac{1}{q}\right)^2 + \left(\frac{1}{q}\right)' = 0\,, \quad P' = \frac{i}{q} \tag{D.3}$$

The solutions are

$$q(z) = z + q_0, \quad P(z) = i\,\ln\left(1 + \frac{z}{q_0}\right) \tag{D.4}$$

with a complex constant q_0. The amplitude function becomes

$$f(r,z) = \exp\left[-\ln\left(1 + \frac{z}{q_0}\right) + \frac{i\,k\,r^2}{2(q_0+z)}\right] \tag{D.5}$$

The amplitude must vanish in the limit $r \to \infty$ for any value of z. At $z = 0$ this is realized if the constant q_0 is purely imaginary. It is expressed in the form

$$q_0 = -i\,z_R \quad \text{with} \quad z_R = \frac{k\,w_0^2}{2} = \frac{\pi w_0^2}{\lambda/n} \tag{D.6}$$

Here z_R is the so-called Rayleigh length, a characteristic length for diffraction, and $\lambda = 2\pi c/\omega$ is the vacuum wavelength. The laser beam is assumed to have a waist of width w_0 at $z = 0$.

Furthermore the following quantities are defined

$$w(z) = w_0\sqrt{1 + (z/z_R)^2} \tag{D.7}$$

$$R(z) = z\left(1 + (z_R/z)^2\right) \tag{D.8}$$

We will see below that the beam width at position z is described by $w(z)$ while $R(z)$ is the radius of curvature of the wave front. Then

$$\frac{1}{q(z)} = \frac{1}{R(z)} + i\,\frac{\lambda/n}{\pi w^2(z)} \tag{D.9}$$

With these quantities the first exponential term in the amplitude function (D.5) can be written in the form

$$\exp\left[-\ln\left(1 + i\,z/z_R\right)\right] = \frac{w_0}{w(z)}\exp(-i\,\chi(z))$$

with the so-called *Gouy phase*

$$\chi(z) = \arctan(z/z_R) \tag{D.10}$$

We have used $\ln(a+i\,b) = \ln(\sqrt{a^2+b^2}) + i\,\arctan(b/a)$. The second exponential term in (D.5) becomes after separating real and imaginary parts

$$\exp\left[\frac{i\,k\,r^2}{2q(z)}\right] = \exp\left[-\frac{r^2}{w^2(z)}\right] \exp\left[\frac{i\,k\,r^2}{2R(z)}\right]$$

The electric field of a horizontally polarized laser wave is thus

$$E_x(r,z,t) = E_0\,\frac{w_0}{w(z)}\,\exp\left[-\frac{r^2}{w^2(z)}\right]\,\exp\left[i\,k\,z - i\,\chi(z) - i\,\omega t\right]\,\exp\left[\frac{i\,k\,r^2}{2R(z)}\right] \tag{D.11}$$

There are many differences to a plane wave:

- The field amplitude drops to $1/e$ of its peak value at a radius $r = w(z)$. The smallest width w_0 is obtained at the waist at $z = 0$.
- The phase velocity is different from that of a plane wave, which is $v_{ph} = \omega/k = c/n$. The presence of the Gouy phase changes the phase velocity of the Gaussian laser wave near a beam waist.
- The phase factor $\exp\left[i\,k\,r^2/(2R(z))\right]$ implies that the wave fronts are curved and of nearly spherical shape.

The beam is sketched in Fig. D.1. The radius of curvature becomes infinite at the waste position $z = 0$ and assumes its minimum value of $R_{min} = 2z_R$ at $z = z_R$. Due to the divergence of the beam the light rays are not exactly parallel to the z axis. As a consequence the electric field has a small z component. This follows also from the first Maxwell equation $\boldsymbol{\nabla} \cdot \boldsymbol{E} = 0$: since $\partial_x E_x \neq 0$, a field component E_z must be present.
The divergence angle of the beam emerging from the waist is

$$\theta_{div} \approx \tan\theta_{div} = \frac{\lambda}{n\,\pi\,w_0} \tag{D.12}$$

The product of beam width and divergence is for a beam in vacuum

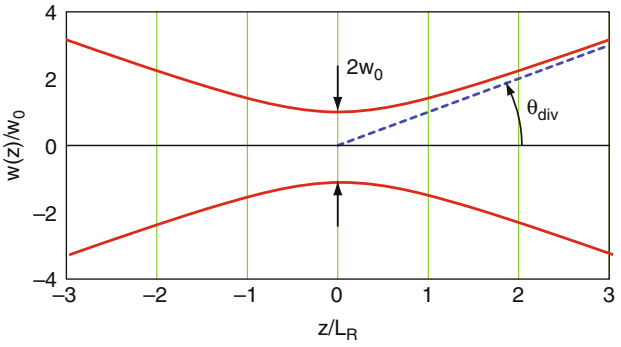

Fig. D.1. The beam envelope $\pm w(z)/w_0$ in the vicinity of a waist. The dotted line indicates the divergence angle θ_{div}

$$w_0 \cdot \theta_{div} = \frac{\lambda}{\pi} \,. \tag{D.13}$$

The intensity of the laser beam is quadratic in the electric field and thus proportional to $\exp\left[-\frac{2r^2}{w^2(z)}\right]$. In terms of Gaussian variances one has therefore

$$\sigma_x = w_0/2, \quad \sigma_\theta = \theta_{div}/2 \,.$$

From (D.13) follows then the fundamental relation between laser beam width and beam divergence

$$\sigma_x \cdot \sigma_\theta = \frac{\lambda}{4\pi} \,. \tag{D.14}$$

In accelerator terminology this product is called the beam emittance.

D.2 High-Order Gaussian Beam Modes

The fundamental Gaussian mode depends only the distance r from the axis and the longitudinal coordinate z. If we do not impose cylindrical symmetry the wave equation (D.1) has solutions of the form [2]

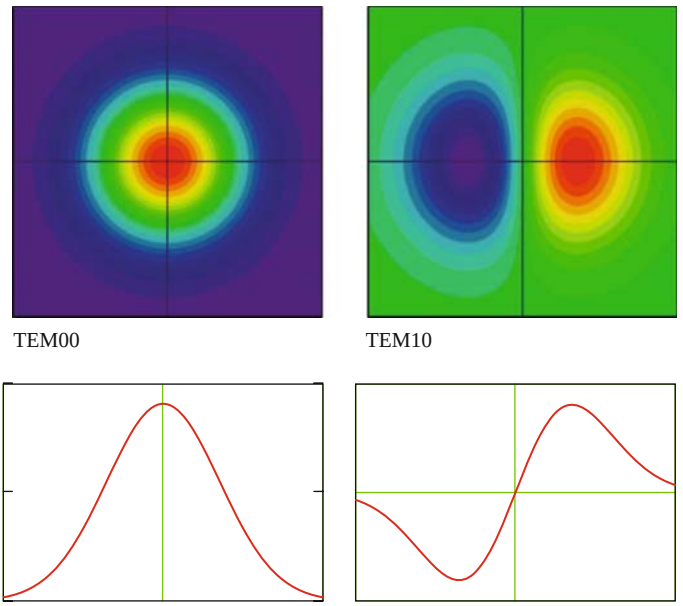

Fig. D.2. *Top*: Electric field distribution of the TEM_{00} and TEM_{10} Hermite-Gaussian laser modes in a plane transverse to the axis of propagation. *Bottom*: the field $E_x(x, 0, 0)$ of the TEM_{00} and TEM_{10} modes as a function of the horizontal coordinate x at $y = z = 0$

$$E_x(x,y,z) = E_0 \frac{w_0}{w(z)} H_m\left(\frac{\sqrt{2}\,x}{w(z)}\right) H_n\left(\frac{\sqrt{2}\,y}{w(z)}\right) \exp\left[-\frac{x^2+y^2}{w^2(z)}\right]$$
$$* \exp\left[i\,k\,z - i\,(m+n+1)\chi(z)\right] \exp\left[\frac{i\,k\,(x^2+y^2)}{2R(z)}\right]. \quad \text{(D.15)}$$

The H_m are the Hermite polynomials. The fundamental mode is the special case $m = n = 0$. The TEM_{00} mode is identical with the fundamental Gaussian mode discussed in the previous section. This mode has its highest intensity on the axis. In an FEL there is optimum overlap between the TEM_{00} mode and the electron beam, and for this reason this mode will be strongly amplified. The higher modes with odd indices have vanishing intensity on the axis and can generally be neglected in the high-gain FEL while the modes with even indices have a finite size on the beam axis. In the TEM_{10} mode the electric field E_x changes sign when going from positive to negative x. This is because $H_1(x)$ is an odd function. Therefore this mode cannot couple to an electron beam with a charge distribution that is symmetric in x. The electric field pattern of the TEM_{00} and TEM_{10} Hermite-Gaussian laser modes is shown in Fig. D.2.

In the TEM_{20} and TEM_{22} modes (see Fig. D.3) the electric field E_x is an even function of x. These modes couple to a symmetric electron beam.

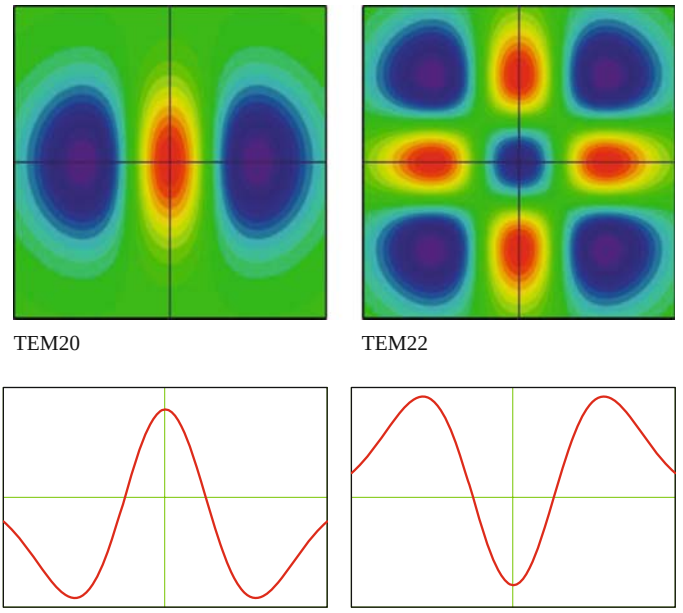

Fig. D.3. Electric field distribution of the TEM_{20} and TEM_{22} Hermite-Gaussian laser modes and the field as a function of x at $y = z = 0$

References

1. Yariv, A.: Optical Electronics in Modern Communications. Oxford University Press, New York, Oxford (1997) 175
2. Meschede, D.: Optik, Licht und Laser. Teubner, Stuttgart, Leipzig (1999) 175, 178

E

Eigenmode Approach

We have seen in Chap. 4 that the third-order equation for the slowly varying field amplitude $\tilde{E}_x(z)$ is solved by an exponential function $\exp(\alpha z)$. For a mono-energetic beam which is on resonance ($\eta = (W - W_r)/W_r = 0$) and for negligible space charge ($k_p = 0$), the three eigenvalues are solutions of the simple cubic equation

$$\alpha_j^3 = i\,\Gamma^3.$$

In this appendix we consider more general cases. For a beam energy different from the resonance energy ($\eta \neq 0$) and with space charge present ($k_p \neq 0$) the third-order equation is still applicable, and for reasonable values of these parameters there exists one eigenvalue α_1 with positive real part leading to exponential growth. The third-order equation is not applicable if beam energy spread is present ($\sigma_\eta > 0$), but then the linear integro-differential equation (4.44) can be used which will usually possess an eigenvalue with $\Re(\alpha_1) > 0$ if σ_η is small enough to preserve the main features of the solutions. The eigenvalue leading to exponential growth will be determined in the following sections. First the general procedure is described resulting in (E.13), and then it is applied to the one-dimensional FEL and a simplified version of the three-dimensional FEL. We will show that in the 1D case the two dimensionless quantities $\sigma_\eta/\rho_{\mathrm{FEL}}$ and k_p/Γ have a significant influence on the FEL gain. In the 3D case the ratio of beam radius r_b to the scale parameter w_0 has to be considered in addition ($r_b/w_0 = r_b/\sqrt{\lambda_\ell L_{\mathrm{g0}}}$).

E.1 General Procedure

In this section we generalize the method for determining the eigenvalues α_j to the 3D case. To this end the full three-dimensional wave equation for the electric field of a horizontally polarized light wave has to be considered

$$\left[\boldsymbol{\nabla}^2 - \frac{1}{c^2}\frac{\partial^2}{\partial t^2}\right] E_x(x,y,z,t) = \mu_0\,\frac{\partial j_x}{\partial t} + \frac{1}{\varepsilon_0}\,\frac{\partial \rho}{\partial x} = \frac{1}{\varepsilon_0}\left(\frac{1}{c^2}\frac{\partial j_x}{\partial t} + \frac{\partial \rho}{\partial x}\right).$$

P. Schmüser, et al.: *Eigenmode Approach*, STMP **229**, 181–190 (2008)
DOI 10.1007/978-3-540-79572-8_E

The second term on the right-hand side can be neglected for two reasons. Its magnitude is small compared to that of the first term:

$$T_1 \equiv \frac{1}{c^2}\left|\frac{\partial j_x}{\partial t}\right| \approx \frac{\omega_\ell \widehat{K}}{c^2\gamma}\left|\tilde{j}_1\right| = \frac{2\pi\widehat{K}}{\gamma\lambda_\ell}\left|\tilde{\rho}_1\right|, \quad T_2 \equiv \left|\frac{\partial \rho}{\partial x}\right| \approx \frac{1}{\sigma_x}\left|\tilde{\rho}_1\right|$$

Typical numbers for FLASH are: Lorentz factor $\gamma = 1000$, wavelength $\lambda_\ell = 30\,\mathrm{nm}$, horizontal beam width $\sigma_x \approx 0.1\,\mathrm{mm}$. Then $T_2/T_1 = \gamma\lambda_\ell/(2\pi\widehat{K}\sigma_x) \approx 0.05$. More importantly, this term has a phase slippage $\exp(ik_u z)$ against the FEL wave and its contribution to the growth rate of the field averages out over one undulator period. This can be seen from the equation

$$\frac{\partial \rho}{\partial x} = \frac{\partial \tilde{\rho}_1}{\partial x}\exp(i\psi) = \frac{\partial \tilde{\rho}_1}{\partial x}\exp(ik_\ell z - i\omega_\ell t)\exp(ik_u z)\,.$$

(In the SVA approximation the phase of $\partial\tilde{\rho}_1/\partial x$ varies slowly and can be taken as constant over one undulator period).

In the present eigenmode approach we neglect the transverse dynamics of the particles (betatron oscillations). The transverse offset $\boldsymbol{r}_\perp = (x, y)$ appears as an independent coordinate in the distribution function and the derivatives with respect to x and y will be dropped in the Vlasov equation. For the transverse electric field the ansatz is made

$$\tilde{E}_x(\boldsymbol{r}_\perp, z, t) = \tilde{E}_x(\boldsymbol{r}_\perp, z)\exp[i(k_\ell z - \omega_\ell t)] \quad \text{with} \quad \boldsymbol{r}_\perp = (x, y)\,. \tag{E.1}$$

Applying the slowly varying amplitude approximation and expressing j_x in terms of $\tilde{j}_1$ this equation assumes the form

$$\left[\boldsymbol{\nabla}_\perp^2 + 2\,i\,k_\ell\frac{\partial}{\partial z}\right]\tilde{E}_x = -\frac{i\,k_\ell\mu_0 c\,\widehat{K}}{2\gamma_r}\tilde{j}_1(\boldsymbol{r}_\perp, z) \quad \text{with} \quad \boldsymbol{\nabla}_\perp^2 = \frac{\partial^2}{\partial x^2} + \frac{\partial^2}{\partial y^2}\,. \tag{E.2}$$

This is the three-dimensional generalization of (4.20).

In the 3D case the distribution function acquires a dependency on the transverse coordinates. To keep the relation to the 1D model an equivalent beam cross section A_b is chosen which is used for normalization purposes but has no influence on absolute (unnormalized) quantities. We set

$$A_b = \frac{I_0}{\max(|j_0|)} \tag{E.3}$$

where I_0 is the magnitude of the dc beam current and $\max(|j_0|)$ the maximum value of the dc current density. For a round beam with constant charge density we get

$$A_b = \pi r_b^2$$

while for a Gaussian beam with $\sigma_x = \sigma_y = \sigma_r$

$$A_b = 2\pi\sigma_r^2\,.$$

The dc beam current is

$$I_0 = n_e A_b \, e \, c \, . \tag{E.4}$$

Generalizing (4.34) the particle distribution function is written as

$$F(\boldsymbol{r}_\perp, \psi, \eta, z) = F_0(\boldsymbol{r}_\perp, \eta) + \Re \left\{ \tilde{F}_1(\boldsymbol{r}_\perp, \eta, z) \cdot e^{i\psi} \right\} . \tag{E.5}$$

The dc current density and the modulated current density are (compare (4.37))

$$j_0(\boldsymbol{r}_\perp) = -I_0 \int_{-\delta}^{\delta} F_0(\boldsymbol{r}_\perp, \eta) \; d\eta, \quad \tilde{j}_1(\boldsymbol{r}_\perp, z) = -I_0 \int_{-\delta}^{\delta} \tilde{F}_1(\boldsymbol{r}_\perp, \eta, z) \, d\eta \tag{E.6}$$

(remember that I_0 is the absolute magnitude of the dc current and thus positive, while j_0 is negative since the electron charge is $q_e = -e$). The modulated distribution function obeys an equation similar to (4.40)

$$(\partial_z + i \, 2k_u \eta) \tilde{F}_1(\boldsymbol{r}_\perp, \eta, z) = \frac{e}{m_e c^2 \gamma_r} \left[\frac{\widehat{K}}{2\gamma_r} \tilde{E}_x(\boldsymbol{r}_\perp, z) + \tilde{E}_z(\boldsymbol{r}_\perp, z) \right] \frac{dF_0}{d\eta} \, . \tag{E.7}$$

The longitudinal space charge field $\tilde{E}_z$ can be computed from the modulated charge density using the Maxwell equation $\boldsymbol{\nabla} \cdot \boldsymbol{E} = \rho/\varepsilon_0$. Neglecting the derivatives with respect to the transverse coordinates x and y and using the SVA approximation one finds as a generalization of (4.17)

$$\tilde{E}_z(\boldsymbol{r}_\perp, z) = -\frac{i\mu_0 c}{k_\ell} \tilde{j}_1(\boldsymbol{r}_\perp, z) = \frac{i\mu_0 c \, I_0}{k_\ell} \int \tilde{F}_1(\boldsymbol{r}_\perp, \eta, z) \, d\eta \, . \tag{E.8}$$

It is the spirit of the eigenmode analysis to assume that $\tilde{E}_x$ and $\tilde{F}_1$ depend exponentially on z:

$$\tilde{E}_x(\boldsymbol{r}_\perp, z) = A(\boldsymbol{r}_\perp) e^{\alpha z}, \quad \tilde{F}_1(\boldsymbol{r}_\perp, \eta, z) = B(\boldsymbol{r}_\perp, \eta) e^{\alpha z}. \tag{E.9}$$

Substitution in (E.2) and (E.7) yields the equations

$$\left[\boldsymbol{\nabla}_\perp^2 + 2 \, i \, k_\ell \alpha \right] A = \frac{i \, k_\ell \mu_0 c \, I_0 \widehat{K}}{2\gamma_r} \int B \, d\eta \tag{E.10}$$

$$\left[\alpha + 2 \, i \, k_u \eta \right] B = \frac{e}{m_e c^2 \gamma_r} \left[\frac{\widehat{K}}{2\gamma_r} \, A + \frac{i\mu_0 c \, I_0}{k_\ell} \int B \, d\eta \right] \frac{dF_0}{d\eta} \, . \tag{E.11}$$

The quantities to be determined are the eigenvalues α_j and the coefficient functions $A(\boldsymbol{r}_\perp)$ and $B(\boldsymbol{r}_\perp, \eta)$. Note that the integral

$$\int B \, d\eta \equiv \int_{-\delta}^{\delta} B(\boldsymbol{r}_\perp, \eta) \, d\eta$$

depends only on the transverse coordinates $\boldsymbol{r}_\perp$ but not on the fractional energy deviation η. This allows us to divide (E.11) by $[\alpha + 2 \, i \, k_u \eta]$ to obtain B, and then to integrate over η:

$$\int_{-\delta}^{\delta} B\, d\eta = \frac{e}{m_e c^2 \gamma_r} \left[\frac{\widehat{K}}{2\gamma_r}\, A + \frac{i\mu_0 c\, I_0}{k_\ell} \int B\, d\eta \right] \int_{-\delta}^{\delta} \frac{1}{[\alpha + 2\, i\, k_u \eta]} \frac{dF_0}{d\eta}\, d\eta\,.$$

We make the assumption that the unmodulated part of the distribution function can be factorized

$$F_0(\boldsymbol{r}_\perp, \eta) = G(\boldsymbol{r}_\perp) H(\eta)\,. \tag{E.12}$$

Integrating by parts and using $H(\pm\delta) = 0$ we obtain

$$\begin{aligned} \int B d\eta &= i\, 2k_u \frac{e}{m_e c^2 \gamma_r} \left[\frac{\widehat{K}}{2\gamma_r}\, A + \frac{i\mu_0 c\, I_0}{k_\ell} \int B\, d\eta \right] G(\boldsymbol{r}_\perp)\; C(\alpha) \\ &= \left[\frac{i\, k_u e\, \widehat{K}}{m_e c^2 \gamma_r^2}\, A - k_p^2\, A_b \int B\, d\eta \right] G(\boldsymbol{r}_\perp)\; C(\alpha) \end{aligned}$$

with the abbreviations

$$C(\alpha) = \int \frac{H(\eta)}{(\alpha + i\ 2k_u \eta)^2} d\eta\,, \quad k_p^2 = \frac{2k_u \mu_0 e}{m_e c\, \gamma_r k_\ell} \frac{I_0}{A_b}\,.$$

Then we can express $\int B d\eta$ in terms of A:

$$\int B d\eta = \frac{i\, k_u\ e\widehat{K}}{m_e c^2 \gamma_r^2} \frac{C\ A_b\ G}{1 + k_p^2\ C\ A_b\ G} \cdot A$$

When this is substituted in (E.10) we get an implicit equation for the determination of the eigenvalues α_j:

$$\left[\boldsymbol{\nabla}_\perp^2 + 2\, i\, k_\ell \alpha \right] A(\boldsymbol{r}_\perp) = (2\, i\, k_\ell) \cdot i\, \Gamma^3 \frac{C(\alpha)\ A_b\ G(\boldsymbol{r}_\perp)}{1 + k_p^2\ C(\alpha)\ A_b\ G(\boldsymbol{r}_\perp)} \cdot A(\boldsymbol{r}_\perp) \tag{E.13}$$

Note that the gain parameter Γ and the space charge parameter k_p are defined in the same way as in the one-dimensional theory, see (4.47).

E.2 One-Dimensional Case

In the 1D case the function $A(\boldsymbol{r}_\perp) \equiv A$ is a constant and the operator $\boldsymbol{\nabla}_\perp^2$ can be omitted from (E.13). Moreover, we can replace $H(\eta)$ by $F_0(\eta)$ and $A_b\ G(\boldsymbol{r}_\perp)$ by 1. Dividing (E.13) by A and ordering terms we obtain the following eigenvalue equation

$$\alpha = \left[i\Gamma^3 - k_p^2 \alpha \right] \int_{-\delta}^{\delta} \frac{F_0(\eta)}{(\alpha + i\, 2k_u \eta)^2}\, d\eta\,. \tag{E.14}$$

Note that this eigenvalue equation is valid for an arbitrary initial energy distribution $F_0(\eta)$ in the beam. An alternative derivation of this result is possible by inserting the eigenmode ansatz $\tilde{E}_x = A\exp(\alpha z)$ into (4.44).

The power growth in the exponential regime is determined by the real part of α_1:

$$P(z) \propto \exp(2\Re(\alpha_1)\, z)\,.$$

The growth rate depends on the mean relative energy offset

$$\langle\eta\rangle = \int_{-\delta}^{\delta} \eta\, F_0(\eta)\, d\eta\,.$$

The maximum value of the function $2\Re(\alpha_1(\eta))$ yields the fastest power rise and is thus directly related to the power gain length. It is therefore obvious to define the power gain length by the equation

$$L_g = \left[\max\{2\Re(\alpha_1(\eta))\}\right]^{-1}\,. \tag{E.15}$$

We can convince ourselves that this expression reduces to the 1D power gain length L_{g0} for a beam with $\eta = 0$ and $k_p = 0$: in that case we have

$$\alpha_1 = (i+\sqrt{3})\Gamma/2 \quad \Rightarrow \quad \left[2\Re[\alpha_1]\right]^{-1} = \frac{1}{\sqrt{3}\,\Gamma} = L_{\mathrm{g0}}\,.$$

The above discussion shows that it is useful to introduce a normalized growth rate function

$$f_{gr}(\eta) = 2\Re(\alpha_1(\eta))\, L_{\mathrm{g0}}\,.$$

The maximum value of this function is identical with the ratio L_{g0}/L_g.

E.2.1 Mono-Energetic Beam Without Space Charge Force

For the special case of a mono-energetic beam of energy W the equation (E.14) becomes

$$\alpha^3 + i\,4k_u\eta\alpha^2 + (k_p^2 - 4k_u^2\eta^2)\alpha - i\,\Gamma^3 = 0\,. \tag{E.16}$$

Alternatively, this result is obtained by inserting the eigenmode ansatz $\tilde{E}_x = A\exp(\alpha z)$ into (4.46). The three roots α_j can in principle be computed analytically, although this may be cumbersome. Often a numerical computation is easier.

An analytical approach is reasonably straightforward for the case $k_p = 0$. Equation (E.16) can be transformed into a normalized algebraic equation

$$a\,(a+i\,b)^2 - i = 0 \quad \text{with} \quad a = \frac{\alpha}{\Gamma} \quad \text{and} \quad b = \frac{\eta}{\rho_{\mathrm{FEL}}}\,. \tag{E.17}$$

The three solutions of this cubic equation are

$$a_1 = \frac{1}{6}\left(u - \frac{4b^2}{u} - i\,4b\right) \tag{E.18}$$

$$a_2 = \frac{1}{6}\left(-\frac{1-i\sqrt{3}}{2}\,u + \frac{2}{1-i\sqrt{3}}\,\frac{4b^2}{u} - i\,4b\right)$$

$$a_3 = \frac{1}{6}\left(-\frac{1+i\sqrt{3}}{2}\,u + \frac{2}{1+i\sqrt{3}}\,\frac{4b^2}{u} - i\,4b\right)$$

where the complex function $u(b)$ is defined by

$$u = u(b) = \sqrt[3]{108\,i - 8i\,b^3 + 12\sqrt{12b^3 - 81}}\,. \tag{E.19}$$

The eigenvalues depend on the relative energy offset $\eta = (W - W_r)/W_r$ through the function $u(b) = u(\eta/\rho_{\mathrm{FEL}})$.

As said above, the maximum value of $2\,\Re\{\alpha_1(\eta)\}$ is equal to the inverse power gain length. The real parts of the eigenvalues α_1 and α_2, multiplied with $2L_{\mathrm{g0}}$, are plotted in Fig. E.1 as a function of η/ρ_{FEL}, the energy detuning η divided by the FEL parameter. The third eigenvalue α_3 remains purely imaginary even for $\eta \neq 0$. The physical relevance of this figure is discussed in Chap. 6. The maximum value of the growth rate function $f_{gr}(\eta) = 2\Re(\alpha_1(\eta))\,L_{\mathrm{g0}}$ is unity which means that in this special case the power gain length L_g is indeed identical with the 1D power gain length L_{g0} of a mono-energetic beam, as expected. In the vicinity of the maximum at $\eta = 0$

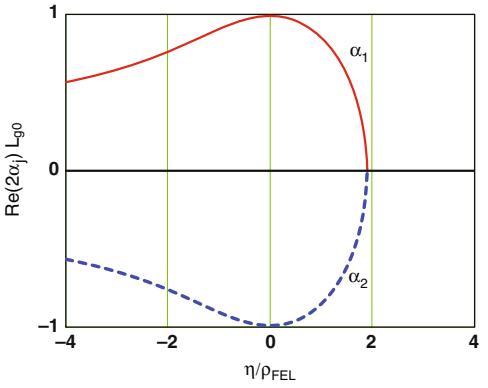

Fig. E.1. The real part of the first and second eigenvalue, multiplied with $2L_{\mathrm{g0}}$, as a function of η/ρ_{FEL}, the relative energy deviation divided by the FEL parameter. Note that $\Re(\alpha_1)$ (*continuous red curve*) is positive, corresponding to exponential growth of the eigensolution $V_1(z) = \exp(\alpha_1 z)$. However, the real part vanishes above $\eta; \approx 1.88\rho_{\mathrm{FEL}}$ which means that the exponential growth stops if the electron energy W exceeds the resonant energy W_r by more than $\Delta W = 1.88\rho_{\mathrm{FEL}} W_r$. The real part of α_2 (*dashed blue curve*) is always negative, hence the eigenfunction $V_2(z)$ drops exponentially. Finally, $\Re(\alpha_3) \equiv 0$, so $V_3(z)$ oscillates along the undulator axis

the growth rate function can be approximated by a parabola

$$2\Re(\alpha_1(\eta))L_{\mathrm{g0}} \approx \left(1 - \frac{\eta^2}{9\,\rho_{\mathrm{FEL}}^2}\right) . \tag{E.20}$$

The imaginary part of α_1 is needed when ones wants to compute the FEL group velocity, which is done in Sect. 6.5. For this purpose the derivative of $\Im(\alpha_1)$ with respect to the light frequency ω has to be calculated. To do this, we express the detuning parameter η in terms of the relative frequency deviation, see (5.7):

$$\eta = \eta(\omega) = -\frac{\omega - \omega_r}{2\omega_r}, \quad b = b(\omega) = -\frac{\omega - \omega_r}{2\omega_r \rho_{\mathrm{FEL}}} .$$

In the vicinity of $\omega = \omega_r$ resp. $\eta = 0$ the derivative of $\Im(\alpha_1)$ is approximately given by

$$\frac{d\Im(\alpha_1)}{d\omega} \approx \left[\frac{d\Im(\alpha_1)}{db}\,\frac{db}{d\omega}\right]_{\omega=\omega_r} = \frac{\Gamma}{3\omega_r \rho_{FEL}} = \frac{2k_u}{3\omega_r} . \tag{E.21}$$

In order to prove this one takes the derivative of (E.17) with respect to $b = \eta/\rho_{\mathrm{FEL}}$, yielding

$$\left(\frac{da}{db}\right)_{b=0} = -\frac{2\,i}{3}$$

and makes use of $\alpha_1 = a_1\Gamma$ and $\eta = -(\omega - \omega_r)/(2\omega_r)$.

E.2.2 Inclusion of Space Charge Force and Beam Energy Spread

If the electron beam has an energy spread σ_η and a non-negligible space charge parameter k_p the determination of the eigenvalue α_1 is possible by solving the integro-differential equation (4.44) with numerical procedures. We call W_0 the mean electron energy and $\eta_0 = (W_0 - W_r)/W_r$ the mean value of η. We show several examples of such numerical studies. In the left part of Fig. E.2 the space charge parameter is raised from $k_p = 0$ to $k_p = 0.5\,\Gamma$ and to $k_p = 1.0\,\Gamma$. The maximum of the growth rate function $2\,\Re(\alpha_1)L_{\mathrm{g0}}$ drops from 1.0 to 0.93 resp. 0.78. Effectively this means that the power gain length will grow by 7% if k_p is equal to $0.5\,\Gamma$, resp. by 28% if $k_p = 1.0\,\Gamma$. Moreover, the width of the FEL gain curve shrinks considerably with increasing space charge. At FLASH $k_p \leq 0.2\Gamma$, so the increase in gain length due to space charge is almost negligible. Beam energy spread is obviously more important. For $\sigma_\eta = 0.5\,\rho_{\mathrm{FEL}}$ the maximum of the growth rate function drops to 0.8 which implies that the corrected gain length is about 25% longer than the ideal length, $L_g \approx 1.25\,L_{\mathrm{g0}}$. At $\sigma_\eta = 1.0\,\rho_{\mathrm{FEL}}$ the gain length increases by more than a factor of two.

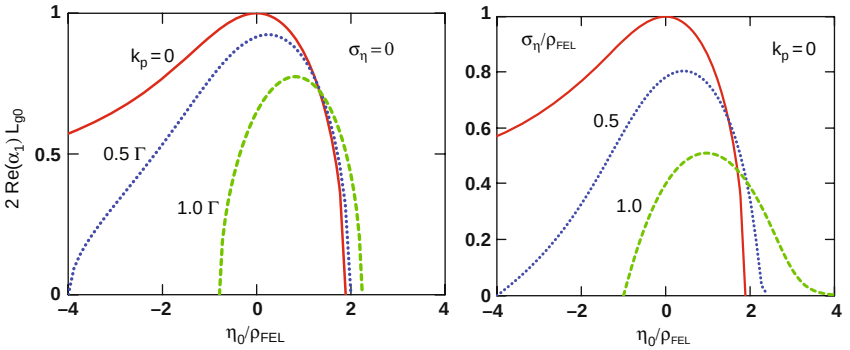

Fig. E.2. *Left*: the growth rate function $f_{gr}(\eta_0) = 2\,\Re(\alpha_1(\eta_0))L_{g0}$ plotted versus $\eta_0/\rho_{\mathrm{FEL}}$ for different values of the space charge parameter k_p. *Continuous red curve*: $k_p = 0$, *dotted blue curve*: $k_p = 0.5\,\Gamma$, *dashed green curve*: $k_p = 1.0\,\Gamma$. The energy spread is put to zero. *Right*: the growth rate function $f_{gr}(\eta_0) = 2\,\Re(\alpha_1(\eta_0))L_{g0}$ is plotted versus $\eta_0/\rho_{\mathrm{FEL}}$ for different values of the relative beam energy spread $\sigma_\eta = \sigma_W/W_r$. *Continuous red curve*: $\sigma_\eta = 0$, *dotted blue curve*: $\sigma_\eta = 0.5\,\rho_{\mathrm{FEL}}$, *dashed green curve*: $\sigma_\eta = 1.0\,\rho_{\mathrm{FEL}}$. Here the space charge parameter is set to zero

E.3 Cylindrical Beam with Constant Charge Density

For simplicity we restrict ourselves to the case of a cylindrical beam with homogeneous charge density. More general beam cross sections are considered in [1]. Cylindrical coordinates (r, ϕ, z) with $r = \sqrt{x^2 + y^2}$ are used and azimuthal symmetry is assumed. Then $A = A(r)$ and

$$G(r) = 1/A_b \quad \text{for} \quad r \le r_b, \quad G = 0 \quad \text{for} \quad r > r_b$$

where r_b is the beam radius. Equation (E.13) reads now

$$A'' + \frac{A'}{r} + i\,2k_\ell\alpha A = \frac{-2\,k_\ell\Gamma^3 C\;GA_b}{1 + k_p^2 C\;GA_b}\;A \tag{E.22}$$

Defining coefficients $u = u(\alpha)$ and $v = v(\alpha)$ by

$$u^2 = \frac{2\,k_\ell\Gamma^3 C(\alpha)}{1 + k_p^2 C(\alpha)} + i\,2k_\ell\alpha, \quad v^2 = -i\,2k_\ell\alpha$$

the differential equation for $A(r)$ can be written as

$$\begin{aligned} A'' + \frac{A'}{r} + u^2 A = 0 \quad &\text{for} \quad r \le r_b \\ A'' + \frac{A'}{r} - v^2 A = 0 \quad &\text{for} \quad r > r_b \end{aligned} \tag{E.23}$$

The solutions which remain finite at $r = 0$ and tend to zero for $r \to \infty$ are

$$A(r) = c_1 J_0(u\ r) \quad \text{for} \quad r \le r_b \qquad \text{(E.24)}$$
$$A(r) = c_2 K_0(v\ r) \quad \text{for} \quad r > r_b$$

Here J_0 and K_0 are Bessel functions. The continuity of A and A' at $r = r_b$ leads to the system of equations

$$c_1 \cdot J_0(u\ r_b) = c_2 \cdot K_0(v\ r_b) \qquad \text{(E.25)}$$
$$c_1 \cdot u\ J_0'(u\ r_b) = c_2 \cdot v\ K_0'(v\ r_b)$$

In order to have a nontrivial solution for the coefficients c_1 and c_2 the determinant must vanish

$$Det = \begin{vmatrix} J_0(u\ r_b) & K_0(v\ r_b) \\ u\, J_0'(u\ r_b) & v\, K_0'(v\ r_b) \end{vmatrix} = 0 \qquad \text{(E.26)}$$

The roots $u = u(\alpha)$, $v = v(\alpha)$ of the equation $Det = 0$ can be found numerically. Note that a whole sequence of roots u_n, v_n of the equation $Det = 0$ exists owing to the oscillatory nature of the Bessel function $J_0(x)$. The first root u_1, v_1 yields an eigenvalue α_1 with a larger positive real part than obtained for the higher roots. This eigenvalue leads to the fastest growth rate and is therefore the most relevant one for the FEL.

It is worthwhile mentioning that a sequence of eigenvalues with positive real part is also obtained for realistic electron beam profiles. The FEL beam can then be characterized in good approximation by the Gaussian modes described in Appendix D. The fundamental TEM_{00} mode has the highest growth rate and dominates in an FEL equipped with a long undulator while higher modes such as TEM_{10}, TEM_{20} etc have a lower growth rate.

E.4 When is the 1D Theory Applicable?

In order to investigate the range of validity of the 1D theory the simplified model of a cylindrical electron beam with constant charge density is not adequate. Instead we consider the most important practical case that the beam has a Gaussian transverse charge distribution. So we assume an amplitude depending on $r = \sqrt{x^2 + y^2}$ in the form

$$A(r) = A_0 \exp\left(-\frac{r^2}{2\,\sigma_r^2}\right)$$

which has cylindrical symmetry, i.e. $\sigma_x = \sigma_y = \sigma_r$. The left-hand side of (E.13) becomes

$$\left[\boldsymbol{\nabla}_\perp^2 + 2\,i\,k_\ell \alpha\right] A(\boldsymbol{r}_\perp) \qquad \text{(E.27)}$$

The magnitude of the derivative is bounded

$$\left|\boldsymbol{\nabla}_\perp^2 A(r)\right| = \left|A'' + \frac{A'}{r}\right| \le \frac{2}{\sigma_r^2}\, A_0\,.$$

To find the magnitude of the second term in (E.27) we insert for α the eigenvalue α_1 of the exponentially growing solution which is roughly given by (4.51):

$$\alpha_1 \approx (i + \sqrt{3})\Gamma/2 \quad |\alpha_1| \approx \Gamma = (\sqrt{3}L_{g0})^{-1} .$$

The derivative term can be disregarded if

$$\frac{2}{\sigma_r^2} \ll 2k_\ell \Gamma .$$

It follows that the rms width of the electron beam has to obey the inequality

$$\sigma_r \gg 0.52 \sqrt{L_{g0}\lambda_\ell} .$$

This is in accordance with our qualitative argumentation in Chap. 6 that the influence of Rayleigh length should exceed twice the power gain length in order to suppress the influence of optical diffraction:

$$z_R = \frac{4\pi\sigma_r^2}{\lambda_\ell} > 2\, L_{g0} \quad \Rightarrow \quad \sigma_r^2 > \frac{L_{g0}\lambda_\ell}{2\pi} .$$

As a rule of thumb one can say that the 1D FEL theory is adequate if the rms electron beam width is much larger than the geometric mean of FEL wavelength and power gain length

$$\sigma_r \gg \sqrt{\lambda_\ell L_{g0}} . \tag{E.28}$$

At FLASH and even more so at the XFEL this criterion cannot be fulfilled if one aims for a short gain length. The obvious conclusion is that a realistic description of UV and X-ray FELs must be based on a 3D theory.

Reference

1. Saldin, E.L., Schneidmiller, E.A., Yurkov, M.V.: The Physics of Free Electron Lasers. Springer, Berlin, Heidelberg (2000) 188

F

Periodic Current Modulation Resulting from Shot Noise

The quantization of charge is the deeper reason why *shot noise* (in German *Schrotrauschen*) is observed in electronic circuits. This type of noise occurs also in the electron beam of an FEL. Our discussion of shot noise follows the lucid presentation in [1].

F.1 Power in Time and Frequency Domain

Consider a real function $A(t)$, for example the current through an ohmic resistor of $R = 1\ \Omega$, and its Fourier transform $a(\omega)$. They are related by

$$A(t) = \frac{1}{2\pi} \int_{-\infty}^{\infty} a(\omega) \exp(-i\ \omega t) d\omega \tag{F.1}$$

$$a(\omega) = \int_{-\infty}^{\infty} A(t) \exp(i\ \omega t) dt. \tag{F.2}$$

Since $A(t)$ is real it follows

$$a(\omega) = a^*(-\omega)\,. \tag{F.3}$$

In practice the measurement time is restricted to a finite duration T. If $A(t)$ is put to zero outside the range $-T/2 \le t \le T/2$ we can define

$$a_T(\omega) = \int_{-T/2}^{T/2} A(t) \exp(i\ \omega t) dt \tag{F.4}$$

which will approach $a(\omega)$ for a sufficiently long time T.

The average power is

$$\begin{aligned} P &= R\,\frac{1}{T} \int_{-T/2}^{T/2} |A(t)|^2\, dt \\ &= R\,\frac{1}{4\pi^2 T} \int_{-T/2}^{T/2} \left[\int_{-\infty}^{\infty} a_T(\omega) \exp(-i\ \omega t) d\omega \int_{-\infty}^{\infty} a_T^*(\omega') \exp(i\ \omega' t) d\omega' \right] dt. \end{aligned}$$

P. Schmüser, et al.: *Periodic Current Modulation Resulting from Shot Noise*, STMP **229**, 191–193 (2008)
DOI 10.1007/978-3-540-79572-8_F

The factor $R = 1\ \Omega$ will be dropped in the following. Interchanging the order of integration and using

$$\int_{-T/2}^{T/2} \exp(i[\omega' - \omega]t)dt \approx \int_{-\infty}^{\infty} \exp(i[\omega' - \omega]t)dt = 2\pi\delta(\omega' - \omega)$$

which is valid for large T we obtain

$$P = \frac{1}{2\pi T} \int_{-\infty}^{\infty} |a_T(\omega)|^2 \, d\omega.$$

This can be written as an integral over positive frequencies

$$P = \frac{1}{\pi T} \int_{0}^{\infty} |a_T(\omega)|^2 \, d\omega. \tag{F.5}$$

If we define the spectral density function as

$$S(\omega) = \lim_{T\to\infty} \frac{1}{\pi T} |a_T(\omega)|^2 \tag{F.6}$$

then $S(\omega)d\omega$ is the average power within the frequency range $[\omega, \omega + d\omega]$, and

$$P = \int_{0}^{\infty} S(\omega)d\omega \tag{F.7}$$

is the total power.

F.2 Shot Noise

We consider relativistic electrons ($v \to c$) that are randomly distributed along the bunch and call N the number of electrons in the time interval T. Then $\dot{N} = N/T$ is the average number of electrons per unit time. The absolute magnitude of the dc beam current is

$$I_0 = e\,\dot{N}.$$

The current seen by a stationary observer has a time dependence

$$I(t) = e \sum_{j=1}^{N} \delta(t - t_j) \quad (-T/2 \le t, t_j \le T/2) \tag{F.8}$$

where the delta functions account for the point-like nature of the electrons in the beam. The average of $I(t)$ over a large sample of identical systems is equal to I_0:

$$\langle I(t) \rangle = eN/T \equiv I_0. \tag{F.9}$$

The Fourier transform of $I(t)$ is

$$i_T(\omega) = \int_{-T/2}^{T/2} I(t) \exp(i\omega t) dt = e \sum_{j=1}^{N} \exp(i\omega t_j). \tag{F.10}$$

According to (F.6) the spectral density function is computed by forming the expression

$$\lim_{T\to\infty} \frac{1}{\pi T} |i_T(\omega)|^2 = \lim_{T\to\infty} \frac{e^2}{\pi T} \left[N + \sum_j \sum_{k\neq j} \exp(i\omega[t_j - t_k]) \right]. \tag{F.11}$$

When we take the average over a large sample of identical systems the double sum in this expression vanishes because the times t_j and t_k are random. Moreover, $N = \dot{N}T$. Hence we obtain for the ensemble-averaged spectral density function

$$S(\omega) = \frac{e\, I_0}{\pi} \tag{F.12}$$

corresponding to a current density $J(\omega)$ whose magnitude is

$$|J(\omega)| = \frac{\sqrt{S(\omega)}}{A_b} = \sqrt{\frac{e\, I_0}{\pi}} \frac{1}{A_b}. \tag{F.13}$$

Owing to the delta-function like shape of the current pulse of a single electron this spectral density is independent of frequency.

The modulated current density $\tilde{j}_1$ that is needed in Sect. 7.1 can be computed from the spectral energy contained in the FEL bandwidth of $\omega_\ell \pm \Delta\omega/2$ which we express in terms of an rms current

$$I_{rms}^2 = S(\omega)\Delta\omega = \frac{e\, I_0}{\pi} \Delta\omega. \tag{F.14}$$

The important result is

$$\tilde{j}_1 = \frac{\sqrt{I_{rms}^2}}{A_b} = \sqrt{\frac{e\, I_0 \Delta\omega}{\pi}} \frac{1}{A_b}. \tag{F.15}$$

Here A_b is the cross sectional area of the electron beam.

Reference

1. Yariv, A.: Optical Electronics in Modern Communications. Oxford Universtity Press, Oxford (1997) 191

G

The Gamma Distribution

In this appendix we study the statistical properties of FEL radiation and demonstrate that the FEL pulse energy obeys the gamma distribution. The one-dimensional approximation is applied, neglecting the dependencies on the transverse coordinates and treating the electromagnetic waves as truncated plane waves. The number of undulator periods N_u is considered as large so that the frequency ω_ℓ of undulator radiation is restricted to a narrow range. We consider two limiting cases:

- (1) The electron bunch is short compared to the length $l_{\rm coh} = c\,\tau_{\rm coh}$ of the optical wavetrains that are produced when the electrons emit undulator radiation. Then the amplitudes of the wavetrains from different electrons must be added and we obtain a single wave packet which is sometimes called a longitudinal mode. In this case the statistical properties of the FEL radiation energy are described by the negative exponential distribution.
- (2) The bunch length is large compared to the length $l_{\rm coh}$ of the optical wavetrains. The wavetrains emitted by electrons of sufficient spatial separation do not overlap. In that case several independent wave packets will be excited, and the total FEL pulse energy obeys the gamma distribution.

G.1 A Single Wave Packet

We consider first an electron bunch which is shorter than the optical wave trains. The electrons are randomly distributed along the bunch axis. Particle j emits a radiation field which we write approximately as a horizontally polarized plane wave

$$E_j(t) = E_0 \exp(-i\omega_\ell t) \exp(i\phi_j) \; . \tag{G.1}$$

The total electric field generated by all electrons in the bunch is

$$E(t) = E_0 \, \exp(-i\omega_\ell t) \sum_j \exp(i\phi_j) \; . \tag{G.2}$$

P. Schmüser, et al.: *The Gamma Distribution*, STMP **229**, 195–199 (2008)
DOI 10.1007/978-3-540-79572-8_G

The time-averaged field energy is

$$U \propto E_0^2 \left| \sum_j \exp(i\phi_j) \right|^2 . \tag{G.3}$$

We are interested in the statistical fluctuations of the energy. To this end, it is useful to realize that the sum of the phase factors $\sum_j \exp(i\phi_j)$ with random phases can be interpreted as a random walk in the complex $(x+iy)$ plane with unit step size, writing the phase factors in the form $\exp(i\phi_j) = x_j + iy_j$ with $x_j^2 + y_j^2 = 1$. Figure G.1 illustrates such random walks for two different sets of random phases. After N steps, the end point of a random walk starting from the origin will have a certain probability to be found in the intervals $[x, x+dx]$ and $[y, y+dy]$. According to the Central Limit Theorem, this probability is given by the two-dimensional Gaussian (see e.g. [1, 2])

$$p(x,y)dxdy = \frac{1}{2\pi\sigma^2} \exp\left(-\frac{x^2+y^2}{2\sigma^2}\right) dxdy \quad \text{with} \quad 2\sigma^2 = N . \tag{G.4}$$

The distance r from the origin is $r = \sqrt{x^2+y^2}$. Using $dxdy = 2\pi r dr$ the probability of finding the end point within a distance interval $[r, r+dr]$ is

$$p(r)dr = \frac{r}{\sigma^2} \exp\left(-\frac{r^2}{2\sigma^2}\right) dr . \tag{G.5}$$

The mean square radius is

$$\langle r^2 \rangle = \int_0^\infty r^2 p(r) dr = 2\sigma^2 = N . \tag{G.6}$$

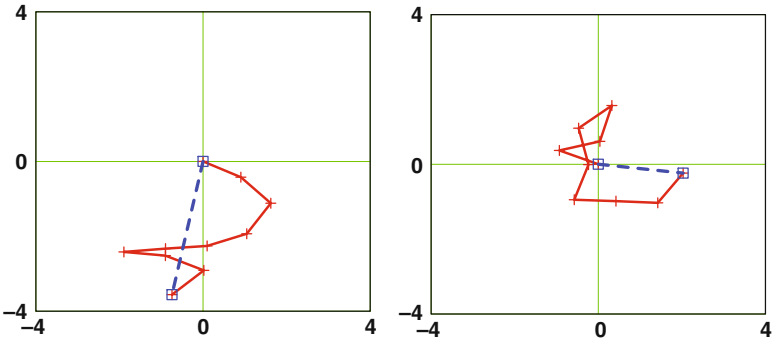

Fig. G.1. Two examples of random walks in the xy plane. The step size is 1, the number of steps is $N = 10$. The start and end points of the walks are indicated by blue boxes

The dimensionless variable

$$\xi = \frac{r^2}{\langle r^2 \rangle}$$

obeys the simple exponential probability distribution

$$p(\xi)d\xi = \exp(-\xi)\, d\xi \tag{G.7}$$

where we have used $d\xi = (2r/\langle r^2 \rangle)\, dr = (r/\sigma^2)\, dr$. Since the radiated field energy U is proportional to the square of the electric field we can conclude from this equation that the probability distribution of the radiation field energy is given by

$$p_1(u)du = \exp(-u)du \quad \text{with} \quad u = \frac{U_1}{\langle U_1 \rangle}. \tag{G.8}$$

Here the index 1 indicates the presence of one wave packet. This is the negative exponential distribution. The most probable value of the FEL pulse energy is zero.

G.2 Many Wave Packets

When the bunch is far longer than the optical wave trains there will be more than one, say M, wave packets. Each of them will obey the exponential distribution (G.8). For sufficient spatial separation these M "modes" are uncorrelated and the respective probability distributions are statistically independent. We want to prove that the probability distribution for the total energy of M independent wave packets is given by the expression

$$p_M(u)du = \frac{u^{M-1}}{\Gamma(M)} \exp(-u)du \tag{G.9}$$

with the gamma function $\Gamma(M)$. The proof is made by complete induction. The statement is true for $M = 1$, then (G.9) is identical with (G.8). Now assume that formula (G.9) has been proved up to some value of M. We make the step from M to $M + 1$:

$$p_{M+1}(u) = \int_0^u p_M(v) \cdot p_1(u - v)dv$$

where we make explicit use of the statistical independence of the wave packets by taking the product of the probability distributions p_M and p_1. Inserting formula (G.9) we get

$$p_{M+1}(u) = \int_0^u \frac{v^{M-1}}{\Gamma(M)} \exp(-v) \cdot \exp(-(u - v))dv = \frac{u^M}{\Gamma(M + 1)} \exp(-u)\,.$$

This completes the proof.

Formula (G.9) is the gamma distribution as defined in the mathematical literature. It is not directly applicable at the SASE FEL but must be modified slightly. From the above derivation it is obvious that the variable u is the ratio of the total FEL pulse energy U_M (summed over all M wave packets), divided by the average energy of a single wave packet. However, the energy contained in a single wave packet is difficult to measure, while its average value is just the measurable total average energy, divided by the number of wave packets:

$$\langle U_1 \rangle = \langle U_M \rangle / M.$$

Hence it is convenient to introduce a modified dimensionless variable $\tilde{u}$

$$\tilde{u} = \frac{U_M}{\langle U_M \rangle} = \frac{u}{M}.$$

Then the gamma distribution can be written in terms of measurable quantities:

$$p_M(\tilde{u})d\tilde{u} = \frac{M^M\, \tilde{u}^{M-1}}{\Gamma(M)} \exp(-M\,\tilde{u})d\tilde{u} \quad \text{with} \quad \tilde{u} = \frac{U_{\rm rad}}{\langle U_{\rm rad} \rangle}\,.$$

Here $U_{\rm rad} \equiv U_M$ is the energy of the entire radiation pulse.

To simplify notation we drop the "tilde" in the following and write the gamma distribution in the form

$$\boxed{p_{_M}(u)du = \frac{M^M\, u^{M-1}}{\Gamma(M)} \exp(-M\,u)du \quad \text{with} \quad u = \frac{U_{\rm rad}}{\langle U_{\rm rad} \rangle}\,.} \tag{G.10}$$

The gamma distribution for $M = 1, 2, 4, 50$ is plotted in Fig. G.2. For very large M it approaches a Gaussian centered at $u = 1$. The distribution is normalized to unity

$$\int_0^\infty p_{_M}(u)du = 1\,. \tag{G.11}$$

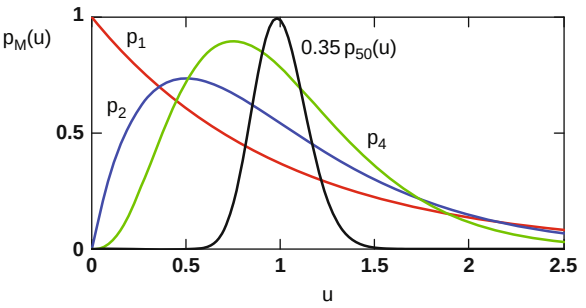

Fig. G.2. The gamma distribution for $M = 1$ (negative exponential distribution) and $M = 2, 4$. For the large value $M = 50$ the distribution is scaled down with the factor 0.35. The area under each of the curves is equal to 1, see (G.11)

The mean value and the variance of the normalized FEL pulse energy are

$$\langle u \rangle = \int_0^\infty u\, p_M(u) du = 1\,, \quad \sigma_u^2 = \left\langle (u - \langle u \rangle)^2 \right\rangle = \frac{1}{M}\,. \tag{G.12}$$

It must be pointed out that only two limiting cases have been considered here: (1) fully overlapping wave trains, yielding a single wave packet (or optical mode), and (2) several perfectly separated modes. In reality partially overlapping wave packets will exist too. One can approximate their probability distribution by a gamma distribution with a non-integer index M. This is done in Chap. 7.

References

1. Reif, F.: Fundamentals of Statistical and Thermal Physics. McGraw Hill, New York (1965) 196
2. Lohrmann, E., Blobel, V.: Statistische und numerische Methoden der Datenanalyse. Teubner Studienbücher (1998) 196

H

Conventions and Frequently Used Symbols

In this book we use the international system of units (SI). Specifically

- $c = 2.9979 \cdot 10^8\,\mathrm{m/s}$ speed of light in vacuum
- $e = 1.60218 \cdot 10^{-19}\,\mathrm{A\,s}$ fundamental charge
- $\varepsilon_0 = 8.854 \cdot 10^{-12}\,\mathrm{A\,s/(V\,m)}$ permittivity of free space
- $\mu_0 = 4\,\pi \cdot 10^{-7}\,\mathrm{V\,s/(A\,m)}$ permeability of free space
- $m_e = 9.109 \cdot 10^{-31}\,\mathrm{kg}$ rest mass of electron
- $\hbar = h/(2\pi) = 1.05 \cdot 10^{-34}\,\mathrm{J\,s}$ Planck's constant

The charge of the electron is written as $q_e = -e$. The electron energy in the accelerator is quoted in MeV or GeV $= 1000\,\mathrm{MeV}$ as usual ($1\,\mathrm{MeV} = 1.602 \cdot 10^{-13}\mathrm{J}$). A right-handed Cartesian coordinate system (x, y, z) is used. The electron beam moves along the z direction, x is the horizontal displacement of an electron from the nominal orbit and y the vertical displacement. Following the usage in many modern physics textbooks we call the field $\boldsymbol{B}$ the magnetic field because it appears in the Lorentz force and is thus directly responsible for the deflection and focusing of the electron beam ($\boldsymbol{H}$ is called the "magnetizing field"). We will often call $\omega = 2\pi f$ the frequency although it is an angular frequency.

In the following Table H.1 we summarize the designation of frequently used quantities, their dimension in SI units, their meaning, and the equation or the chapter where the quantity is introduced.

P. Schmüser, et al.: *Conventions and Frequently Used Symbols*, STMP **229**, 201–203 (2008)
DOI 10.1007/978-3-540-79572-8_H

Table H.1. List of frequently used symbols

symbol	SI units	meaning	Eq./Chap.
$\boldsymbol{A}$	Vs/m	magnetic vector potential	App. A
A_b	m^2	electron beam cross section	Chap. 5
$\alpha_1,\ \alpha_2,\ \alpha_3$	m^{-1}	eigenvalues of third-order eq.	Eq. (4.51)
$\boldsymbol{B}$	T	magnetic field vector	
B_0	T	peak magnetic field of undulator	Chap. 2
$\beta = v/c$	–	normalized velocity of electron	
$\bar{\beta}$	–	averaged normalized velocity	Eq. (2.13)
$\beta_x(z),\ \beta_y(z)$	m	hor./vert. beta function	Sect. 6.3.1
β_{av}	m	average beta function	Eq. (6.11)
β_{opt}	m	optimum beta function	Eq. (6.30)
$\varepsilon_x,\ \varepsilon_y$	m	emittance of electron beam	Eq. (6.10)
ε_n	m	normalized emittance	Eq. (6.12)
$\tilde{E}_x$	V/m	field of light wave	Eqs. (4.1, 4.9)
$\tilde{E}_z$	V/m	space charge field	Eq. (4.17)
η	–	fractional energy deviation	Eq. (3.15)
$F_0(\eta),\ \tilde{F}_1(\eta, z)$	–	particle distribution function	Eq. (4.34)
φ_E	–	phase of field $\tilde{E}_x$	Eq. (5.20)
φ_{j1}	–	phase of current $\tilde{j}_1$	Eq. (5.21)
G	–	gain function of FEL	Eqs. (3.26, 5.3)
γ	–	Lorentz factor of electron	Eq. (1.2)
γ_r	–	resonant value of Lorentz factor	Eq. (3.14)
Γ	m^{-1}	gain parameter	Eq. (4.47)
I_0	A	dc electron beam current	
I_{peak}	A	peak electron beam current	Chap. 5
j_0	$\mathrm{A/m}^2$	dc electron beam current density	Eq. (4.4)
$\tilde{j}_1$	$\mathrm{A/m}^2$	modulated current density	Eq. (4.4)
K	–	undulator parameter	Eq. (2.8)
$\widehat{K}$	–	modified undulator parameter	Eq. (3.31)
k_ℓ	m^{-1}	wave number of FEL radiation	Eq. (3.2)
k_p	m^{-1}	space charge parameter	Eq. (4.47)
k_u	m^{-1}	undulator wave number	Chap. 2

Table H.1. List of frequently used symbols (continued)

symbol	SI units	meaning	Eq./Chap.
λ_ℓ	m	wavelength of undulator/FEL radiation	Eqs. (2.19, 3.9)
λ_u	m	undulator period	Chap. 2
L_{g0}	m	1D power gain length	Eq. (4.53)
L_g	m	3D power gain length	Chap. 6
L_{sat}	m	saturation length	Eq. (7.5)
$p_M(u)$	–	gamma distribution	App. F
P_{sat}	W	saturation power of FEL	Eq. (6.31)
P_{spont}	W	power of undulator radiation	Eq. (2.21)
P_{beam}	W	electron beam power	Eq. (5.15)
ψ	–	ponderomotive phase	Eq. (3.6)
ψ_b	–	bucket center phase	Eq. (5.22)
ψ_m	–	microbunch phase	Eq. (5.23)
r_b	m	radius of electron bunch	Chap. 6
ρ	$\mathrm{C/m^3}$	electron beam charge density	Eq. (4.3)
$\tilde{\rho}_1$	$\mathrm{C/m^3}$	modulated charge density	Eq. (4.3)
ρ_{FEL}	–	FEL parameter	Eq. (4.49)
σ_η	–	normalized rms energy spread	Chap. 6
σ_r	m	rms radius of electron beam	Chap. 6
$\bar{v}_z$	m/s	longitudinal speed	Eq. (2.13)
W	MeV	relativistic electron energy	Chap. 2
W_r	MeV	resonant value of electron energy	Chap. 3
$w(z)$	m	radial width of photon beam	App. D
X_d	–	diffraction parameter	Eq. (6.21)
X_ε	–	angular spread parameter	Eq. (6.21)
X_γ	–	energy spread parameter	Eq. (6.21)
ζ	m	internal bunch coordinate	Eq. (3.12)
z_R	m	Rayleigh length	Eq. (6.15)

Index